THE SYNTHESIS AND CHARACTERIZATION OF NOBLE METAL NANOPARTICLES, THEIR INTERACTION WITH DYES AND USES IN ANTIMICROBIAL SURFACES

PHD IN CHEMISTRY

HAZEL KITCHING
UNIVERSITY COLLEGE LONDON
2017

For Grandpa

‘Mischief managed.’

Declaration

I, Hazel Kitching, confirm that the work presented in this thesis is my own. Where information has been derived from other sources, I confirm that this has been indicated in the thesis.

Abstract

Herein is presented the synthesis and characterization of a range of gold silver and bimetallic nanoparticles using a variety of synthetic routes. Particles of different sizes and shapes were fabricated by using different reaction conditions and capping agents. Mesoscale linear arrangements of tiopronin-capped silver nanoparticles were fabricated using a sonication step. The interaction of all synthesised particles with a range of cationic and anionic dyes was investigated and yielded mixed results. Enhanced absorption of the dye maxima was seen in some cases when combined with citrate-capped gold nanoparticles, with novel dye-nanoparticle combinations which exhibit this behaviour reported. Aggregation of these particles was also observed at high concentrations of cationic dyes. It was established that aggregation was not due to increasing ionic strength of the solution as previously postulated but an attractive charge-charge mechanism between the dye molecules and citrate shell.

It is well known that dye molecules can act as antimicrobial agents. Literature has shown that conjugation of these dyes with a nanoparticle can enhance the bacterial kill rate. The antibacterial capabilities of citrate-stabilised gold and silver nanoparticles were therefore evaluated against gram positive and gram negative organisms. Excellent kill rates were observed for several novel combinations of dye and nanoparticle. Acridine orange with silver nanoparticles, a previously unreported conjugate, delivered complete kill of both *E. coli* and *S. aureus* in five hours both under a white light source and in the dark. This shows potential for further use as a self-sterilising surface due to the potency and rapidity of the bactericidal response.

Novelty of the work

Novel combinations of dyes and nanoparticles that exhibit enhanced optical absorption of the dye maxima were found. Additionally a pre-existing theory concerning the cause of nanoparticle aggregation at high dye concentrations was proven to be incomplete and a new

theory proposed. The new dye-nanoparticle combinations were used for antimicrobial testing with excellent results attained for both gram positive and gram negative organisms. Silver nanoparticles were used in conjunction with dyes to make antimicrobial surfaces for the first time. Light and dark kill rates for acridine orange combined with citrate-capped silver nanoparticles show potential for commercialization as antimicrobial surfaces.

List of publications

'Self-assembly of metallic nanoparticles into one dimensional arrays'

H. Kitching, M. J. Shiers, A. J. Kenyon and I. P. Parkin, *J. Mater. Chem. A.*, 2013, **1**, 6985-6999

'The interaction of gold and silver nanoparticles with a range of anionic and cationic dyes'

H. Kitching, A. J. Kenyon and I. P. Parkin, ***Phys. Chem. Chem. Phys.***, 2014, **16**, 6050-6059

'The antimicrobial capacity of citrate-stabilised silver and gold nanoparticle-dye conjugates for self-sterilising surfaces'

H. Kitching, S. Sehmi, A. J. Kenyon and I. P. Parkin, ***J. Mater. Chem. B.***, 2017, **pending publication**

Acknowledgements

In memory of Dr Russell Binions

21/11/1978 – 13/04/2017

This work would not have been possible without the unending patience and support of Professor Ivan Parkin and Professor Tony Kenyon. I thank them from the bottom of my heart for always being on my side, crashing in with invaluable advice and for bearing with me throughout the good and the bad. Thanks also go to everyone who helped in the lab and with analysis, particularly to Joe Bear, Sandeep Sehmi and Sacha Noimark. The EPSRC is thanked for funding through the EngDoc centre.

I would also like to thank Demus and Annie for their continued excellent friendship, Mum and Rod for their endless and multifaceted support, Alex for his perennially unique perspective, Jarvis and George for the inspiration, Binions for the turkey/life advice and Mike for the inspiration and 'help'. Thanks also to my sister Louise for the good times, the bad ideas and for always keeping The Faith.

I want to thank Simon, my rock, who always makes me challenge myself even when it is uncomfortable to do so. His unquestioning belief in me singlehandedly kept me going through some dark times and his advice, though not sugarcoated, is invaluable. He's also dead good at maths, physics and computers which has saved me (and this file) on multiple occasions, so on behalf of my sanity, this document and everything else on my hard drive – thank you.

Most thanks of all go to my boys, Ben Robinson and Joe Manzi, without whom I could very well not be here. Cheers for the laughs, tears, happy walls, board games, meat binges and common sense. Thanks for keeping your sense of humour when I had lost mine. It has been a privilege to share the ride with you both. Chang on!

List of Abbreviations

AFM: atomic force microscopy

A.U.: arbitrary units

BHI: brain heart infusion

cfu: colony forming units

CNT(s): carbon nanotube(s)

CTAB: cetyltrimethylammonium bromide

DLS: dynamic light scattering

DMF: dimethylformamide

DNA: deoxyribonucleic acid

EBL: electron beam lithography

EDC: 1-(3-dimethylamino)propyl)-3-ethylcarbodiimide methiodide

HAI(s): hospital acquired infection(s)

HEPES: 2-[4-(2-hydroxyethyl)-1-piperazinyl]ethane-sulfonic acid

HIV: human immunodeficiency virus

HpD: haematoporphyrin derivative

HSV: herpes simplex virus

LAAA(s): light activated antimicrobial agent(s)

LED: light emitting diode

MRSA: methicillin resistant *Staphylococcus aureus*

NP(s): nanoparticle(s)

PBS: phosphate buffered saline

PDD: photodynamic diagnosis

PDT: photodynamic therapy

ppb: parts per billion

ppm: parts per million

PVP: Poly(vinyl pyrrolidone)

RNA: ribonucleic acid

ROS: reactive oxygen species

SERS: Surface enhanced Raman scattering

SPR: Surface plasmon resonance

TB: tuberculosis

TEM: transmission electron microscopy

TMV: tobacco mosaic virus

UV: ultraviolet

UV-vis: Ultraviolet-visible spectroscopy

XRD: X-ray diffraction

Table of Figures

Figure 1.1 Image showing the red shift in absorption maximum with increasing aspect ratio of gold nanorods. Image from El-Sayed *et al*.[19] 31

Figure 1.2 TEM images showing extended linear arrays of gold nanoparticles. Scale bars all represent 200 nm. I-III show the structures; IV-V show higher magnification sections of I and II. Figure reproduced with permission from Deng *et al*.[78]Different approaches have been employed to yield similar results. Conductive wires of silver nanoparticles decorated DNA were produced by Braun *et al*.[80] DNA strands were strung between gold electrodes at a separation of 12 µm.[80] Ag^+ ions were then ion exchanged and conjugated with amino groups on the surface of the DNA before being reduced. Repeating the ion exchange and reduction steps resulted in the formation of silver nanoparticles along the DNA wire (Figure 1.3). 38

Figure 1.3 AFM image showing a silver wire templated on DNA connected between gold electrodes at 12 µm separation. Figure reproduced with permission from Braun *et al*.[80] ... 38

Figure 1.4 (a) AFM and (b) TEM images of the ridge-like structure formed by linear assembly of gold nanoparticles on a DNA nanogrid. Figure reproduced with permission from Kiehl *et al*[88]. 39

Figure 1.5 TEM image showing alternating parallel rows of 5 nm and 10 nm gold nanoparticles on a DNA grid. Figure reproduced with permission from Kiehl *et al*.[87] 39

Figure 1.6 TEM images showing (a) double helical arrays of Au nanoparticles on peptide nanofibrils obtained at pH = 3.5, and (b) single chain arrays obtained at pH = 6. Figure reproduced with permission from Wang *et al.*[93] 40

Figure 1.7 TEM image of a single TMV, showing dense coverage of Au nanoparticles. Figure reproduced with permission from Dujardin *et al.*[94]..... 41

Figure 1.8 TEM image of gold nanoparticles on a peptide nanowire. Figure taken with permission from Djalali *et al*.[99] 42

Figure 1.9 TEM images of silver nanoparticles in the central capillary of a carbon nanotube. Scale bars represent 5 nm. Figure reproduced with permission from Ugarte *et al*[107]. 43

Figure 1.10 TEM image showing the self-assembly of gold nanoparticles on the outer surface of a CNT. Figure taken with permission from Fullam *et al*. [108] 44

Figure 1.11 TEM image showing (a) the alignment of gold nanoparticles along the ridges of an amorphous carbon substrate, and (b) a high-magnification image of a single nanoparticle chain showing exceptional linearity. Figure reproduced with permission from Hutchinson *et al*.[122] 45

Figure 1.12 TEM image showing ring-like structures of gold nanoparticles formed on a polylysine support. Image with permission from Dai *et al*. [130] 46

Figure 1.13 TEM image showing a coiled wire of fused silver nanoparticles obtained by treatment with supercritical water at 400 °C at 49 MPa. Reaction time was 60 minutes. Scale bar represents 100 nm. Figure from Chang *et al*.[138] 48

Figure 1.14 Illustration showing the mechanism of formation of linear chains of gold nanoparticles in ethanol. Figure adapted from Liao *et al*.[139] 49

Figure 1.15 TEM images showing (a) 6nm diameter silver wires, and (b) linear arrays of 2nm silver nanoparticles. Figure reproduced with permission from Viau *et al.*[166] 51

Figure 1.16 TEM images showing progressively longer chains of gold nanoparticles encapsulated in amphiphilic poly(styrene-block¬-acrylic acid) by exposure to increasing concentrations of 1-(3-dimethylamino)propyl)-3-ethylcarbodiimide methiodide (EDC): (a) [EDC] = 0 μM; (b) [EDC] = 55 mM; (c) [EDC] = 87 mM. Figure with permission from Kang *et al.*[180] 53

Figure 1.17 High-magnification TEM images of chains of triblocks obtained in the DMF/water mixture with water concentrations of 10 wt% (a) 10 wt% and (b) 15 wt%. The scale bar is 50 nm. Figure with permission from Rubinstein *et al*. [182] 53

Figure 1.18 Image showing the colour change observed on adding mercury ions to a colloidal suspension of peptide-functionalized gold nanoparticles. Image used with permission from Si *et al*.[171] 58

Fig. 1.19 The binding of 1-mercapto-6-hexanol to gold nanoparticle chains measured in real-time. The graph shows the change in resistance when the analyte is added at approx. 50 s. The image above the graph shows numerous chains of gold particles spanning the gap between the electrodes. Graph with permission from Leiterer *et al*.[215] 58

Figure 1.20 Infographic showing the proportion of *S. aureus* bloodstream isolates accounted for by methicillin-resistant species in Europe in 2010. Image with permission from *Antimicrobial resistance surveillance in Europe*, 2010 [228] 61

Figure 1.21 Extensive lupus vulgaris cured after 1 year of heliotherapy. Image with permission from Daniell and Hill.[234] 62

Figure 1.22 Scheme showing the mechanism of photodymanic therapy. Image with permission from Dolmans *et al*.[235] 64

Figure 2.1 The structure of 2-[4-(2-hydroxyethyl)-1-piperazinyl]ethane-sulfonic acid (HEPES) showing the piperazine ring..... 75

Figure 2.2 UV-vis spectrum of gold nanoparticles made using the Turkevich citrate reduction method..... 80

Figure 2.3 TEM images showing gold nanoparticles synthesised by the Turkevich method 81

Figure 2.4 UV-vis spectrum of silver nanoparticles synthesised by the Turkevich citrate reduction method 82

Figure 2.5 TEM images showing silver nanoparticles synthesised by the Turkevich method. Irregularities are seen in particle size and morphology..... 82

Figure 2.6 Photograph showing the progression in colour as molar ratio of gold to silver changes in solutions of citrate-stabilised gold-silver nanoparticles. A = pure silver, B = 1:3 Au:Ag, C = 1:1 Au:Ag, D = 3:1 Au:Ag, E = pure gold. 83

Figure 2.7 UV-vis absorption spectra showing the mean spectrum of silver-gold nanoparticles synthesised *via* the citrate reduction method. Particles had molar ratios of 1:3, 1:1 and 3:1 gold:silver. 84

Figure 2.8 Graph showing the change in position of the SPR maximum as molar ratio of gold to silver increases 86

Figure 2.9 Illustration showing different types of gold-silver particles that can form. A: silver core, gold shell; B: gold core, silver shell; C: silver-rich alloy core, gold-rich alloy shell; D: alloyed; E: gold-rich alloy core, silver-rich alloy shell. 86

Figure 2.10 TEM images showing bimetallic silver-gold particles synthesised using a molar ratio of 1:3 Au:Ag 88

Figure 2.11 TEM images showing bimetallic silver-gold particles synthesised using a molar ratio of 1:1 Au:Ag 89

Figure 2.12 TEM images showing bimetallic silver-gold particles synthesised using a molar ratio of 3:1 Au:Ag 89

Figure 2.13 UV-vis spectrum of tiopronin-capped silver nanoparticles dissolved in water at a rate of 1 mg/mL. 91

Figure 2.14 TEM image showing as-prepared tiopronin-capped silver nanoparticles. Scale bar corresponds to 100 nm. 91

Figure 2.15 TEM image showing as-prepared tiopronin-capped silver nanoparticles. Scale bar corresponds to 1 µm. 92

Figure 2.16 TEM images showing linear arrays of tiopronin-capped silver particles formed as a result of sonication 93

Figure 2.17 UV-vis spectrum of CTAB-stabilised gold nanorods synthesised by a seed-mediated growth method. 94

Figure 2.18 TEM images of gold nanorods obtained by a seed and growth synthesis, showing A&B: gold nanorods; C: a variety of differently shaped particles within the same sample; D: lattice planes of crystalline gold within a rod. 96

Figure 2.19 UV-vis absorption spectrum of a solution of gold branched nanocrystals (AuBNCs) 97

Figure 2.20 TEM images of branched gold nanocrystals produced by reduction of auric acid using a HEPES buffer. 98

Figure 3.1 UV-vis absorption spectra of malachite green in a solution of gold nanoparticles. 'Dye' corresponds to the absorption spectrum of 20 μM malachite green dye on its own; 'Au NPs' to the absorption spectrum of 5 mM gold nanoparticle solution only. '1 mL' corresponds to the absorption spectrum of 1 mL 20 μM malachite green in 16 mL 5 mM gold nanoparticle solution. 2 mL corresponds to the absorption spectrum of 2 mL malachite green in 16 mL nanoparticle solution etc. Shoulder indicative of aggregation is indicated by the black arrow. 107

Figure 3.2 UV-vis absorption spectra of rhodamine 6G in a solution of gold nanoparticles. 'Dye' corresponds to the absorption spectrum of 20 μM rhodamine dye on its own; 'Au NPs' to the absorption spectrum of 5 mM gold nanoparticle solution only. '1 mL' corresponds to the absorption spectrum of 1 mL 20 μM rhodamine in 16 mL 5 mM gold nanoparticle solution. 2 mL corresponds to the absorption spectrum of 2 mL rhodamine in 16 mL nanoparticle solution etc. The peak that forms as nanoparticles aggregate is indicated by a black arrow. 108

Figure 3.3 UV-vis absorption spectra of toluidine blue in a solution of gold nanoparticles. 'Dye' corresponds to the absorption spectrum of 5 μM toluidine blue dye on its own; 'Au NPs' to the absorption spectrum of 5 mM gold nanoparticle solution only. '1 mL' corresponds to the absorption spectrum of 1 mL 5 μM toluidine blue in 16 mL 5 mM gold nanoparticle solution. 2 mL corresponds to the absorption spectrum of 2 mL toluidine blue in 16 mL nanoparticles,

etc. Black arrow indicates maximum enhancement of the absorption after 6 mL of toluidine blue had been added. Dotted grey arrow indicates decrease in absorbance of the nanoparticle peak as a function of dilution; dashed grey line shows the increase in absorbance of the dye from the start of the experiment to the enhanced absorption observed at 6 mL dye added. Solid grey arrow shows the decrease in intensity and slight red shift of the aggregation peak as further aliquots of toluidine blue after 6 mL are added. 109
Figure 3.4 Graph comparing the UV-vis absorption spectra of toluidine blue at 1.36 μM (blue line), gold nanoparticle solution at 3.63 mM (red line), the spectra of toluidine blue (1.36 μM) and gold nanoparticle solution (3.63 mM) added together to give a mathematical estimate of the absorption spectrum that could be expected if there were no electronic interaction between toluidine blue and the gold particles (green line), and finally the enhanced absorption of toluidine observed experimentally (purple line)..... 110
Figure 3.5 UV-vis absorption spectra of crystal violet in a solution of gold nanoparticles. Maximum enhancement of the absorption after 7 mL crystal violet had been added is indicated by a black arrow. Grey dotted arrow shows the decrease in absorption of the nanoparticles as a function of dilution; dashed grey arrow shows the increase in absorption of the dye from the start of the experiment to the enhanced absorption observed at 7 mL dye added. Solid grey arrow shows the decrease in intensity and slight red shift of the aggregation peak as further aliquots of crystal violet after 7 mL are added..... 111
Figure 3.6 Graph comparing the UV-vis absorption spectra of crystal violet at 1.52 μM (blue line), gold nanoparticle solution at 3.48 mM (red line), the spectra of crystal violet (1.52 μM) and gold nanoparticle solution (3.48 mM) added together to give a mathematical estimate of the absorption spectrum that could be expected if there were no electronic interaction between crystal violet and the gold particles (green line), and finally the enhanced absorption of crystal violet observed experimentally (purple line). 112

Figure 3.7 UV-vis absorption spectra of acridine orange with a solution of gold nanoparticles. Black arrow indicates the new peak that forms after 3 aliquots of acridine orange have been added. Dashed grey arrow shows the increase in absorption and red shift from the start of the experiment to the enhanced absorption observed at 3 mL dye added. Solid grey arrow shows the decrease in intensity and slight red shift of the aggregation peak as further aliquots of acridine orange after 3 mL are added. 113

Figure 3.8 Graph comparing the UV-vis absorption spectra of acridine orange at 3.75 μM (blue line), gold nanoparticle solution at 4.21 mM (red line), the spectra of acridine orange (3.75 μM) and gold nanoparticle solution (4.21 mM) added together to give a mathematical estimate of the absorption spectrum that could be expected if there were no electronic interaction acridine orange and the gold particles (green line), and finally the enhanced absorption of crystal violet observed experimentally (purple line). 114

Figure 3.9 A generalised scheme depicting the changes observed in the UV-vis spectra as a cationic dye is added to a solution of gold nanoparticles. Arrows on spectra indicate general trends observed in peak intensity and red shift. 115

Figure 3.10 UV-vis absorption spectra of rose bengal with a solution of gold nanoparticles. Isosbestic points are indicated by black arrows. 117

Figure 3.11 UV-vis absorption spectra of naphthol green with a solution of gold nanoparticles. Isosbestic points are indicated by black arrows. 117

Figure 3.12 UV-vis absorption spectra of 2, 7-dichlorofluorescein with a solution of gold nanoparticles. 118

Figure 3.13 UV-vis spectra showing the effect of titrating aqueous 5 μM potassium chloride solution against a solution of citrate-capped gold nanoparticles. 119

Figure 3.14 UV-vis spectra showing the effect of titrating aqueous 20 μM potassium chloride solution against a solution of citrate-capped gold nanoparticles. 119

Figure 3.15 Naphthol green and silver nanoparticles. Isosbestic points indicated by black arrows. 120

Figure 3.16 Rose bengal and silver nanoparticles. Isosbestic points indicated by black arrows. 121

Figure 3.17 2, 7-dichlorofluorescein with silver nanoparticles. Isosbestic points indicated by black arrows. 121

Figure 3.18 UV-vis absorption spectra of malachite green with a solution of silver nanoparticles. Isosbestic points shown by black arrows. 122

Figure 3.19 UV-vis absorption spectra of rhodamine 6G with a solution of silver nanoparticles. Isosbestic points indicated by black arrows. 122

Figure 3.20 UV-vis absorption spectra of toluidine blue with a solution of silver nanoparticles 123

Figure 3.21 UV-vis absorption spectra of crystal violet with a solution of silver nanoparticles. Isosbestic points indicated by black arrows 123

Figure 3.22 UV-vis absorption spectra of acridine orange with a solution of silver nanoparticles 124

Figure 3.23 UV-vis spectra showing the titration of 5 mM toluidine blue with a solution of citrate stabilised silver-gold nanoparticles made using a gold to silver ratio of 1:3. 127

Figure 3.24 UV-vis spectra showing the titration of 5 mM crystal violet with a solution of citrate stabilised silver-gold nanoparticles made using a gold to silver ratio of 1:3. A second peak was seen to develop at ~680 nm as the titration progressed. 127

Figure 3.25 UV-vis spectra showing the titration of 20 µM naphthol green with a solution of citrate stabilised silver-gold nanoparticles made using a gold to silver ratio of 1:3 128

Figure 3.26 UV-vis spectra showing the titration of 5 mM toluidine blue with a solution of citrate stabilised silver-gold nanoparticles made using a gold to silver ratio of 1:1 129

Figure 3.27 UV-vis spectra showing the titration of 5 mM crystal violet with a solution of citrate stabilised silver-gold nanoparticles made using a gold to silver ratio of 1:1 129
Figure 3.28 UV-vis spectra showing the titration of 20 μM naphthol green with a solution of citrate stabilised silver-gold nanoparticles made using a gold to silver ratio of 1:1 130
Figure 3.29 UV-vis spectra showing the titration of 5 mM toluidine blue with a solution of citrate stabilised silver-gold nanoparticles made using a gold to silver ratio of 3:1 131
Figure 3.30 UV-vis spectra showing the titration of 5 μM crystal violet with a solution of citrate stabilised silver-gold nanoparticles made using a gold to silver ratio of 3:1 132
Figure 3.31 UV-vis spectra showing the titration of 20 μM naphthol green with a solution of citrate stabilised silver-gold nanoparticles made using a gold to silver ratio of 3:1 132
Figure 3.32 UV-vis spectrum of gold branched nanocrystals synthesised using the HEPES buffer and a solution of auric acid. Two SPR peaks are seen at 339 and 546 nm. 134
Figure 3.33 UV-vis spectrum of the titration between gold branched nanocrystals and toluidine blue 136
Figure 3.34 UV-vis spectrum of the titration between branched gold nanocrystals (AUBNCs) and crystal violet 136
Figure 3.35 UV-vis spectrum of the titration between branched gold nanocrystals and rose bengal 137
Figure 3.36 UV-vis spectrum of the titration between branched gold nanocrystals and naphthol green 137
Figure 3.37 The structure of 2-[4-(2-hydroxyethyl)piperazin-1-yl]ethanesulfonic acid (HEPES) 138
Figure 3.38 UV-vis spectra showing the titration between CTAB-stabilised gold nanorods and 5 μM toluidine blue 139
Figure 3.39 UV-vis spectra showing the titration between CTAB-stabilised gold nanorods and 20 μM acridine orange. 140

Figure 3.40 The structure of cetyltrimethylammonium bromide (CTAB)..... 141
Figure 3.41 UV-vis spectra showing the titration between CTAB-stabilised gold nanorods and 20 µM naphthol green. 141
Figure 3.42 UV-vis spectrum of the titration of tiopronin-capped silver nanoparticles (Ag-tio NPs) with acridine orange..... 142
Figure 3.43 UV-vis spectrum of the titration of tiopronin-capped silver nanoparticles (Ag-tio NPs) with crystal violet 143
Figure 3.44 UV-vis spectrum of the titration of tiopronin-capped silver nanoparticles (Ag-tio NPs) with rhodamine 6G..... 143
Figure 3.45 UV-vis spectrum of the titration of tiopronin-capped silver nanoparticles (Ag-tio NPs) with 2, 7-dichlorofluorescein..... 144
Figure 3.46 The structure of 2-mercaptopropionylglycine (tiopronin)..... 145
Figure 3.47 TEM image showing gold nanoparticles synthesised by the Turkevich method 146
Figure 3.48 TEM images showing (a) gold nanoparticles made by the Turkevich method before dye solutions were added; (b) gold nanoparticles to which 4 mL of toluidine blue had been added; (c) gold nanoparticles to which 5 mL toluidine blue had been added; (d) gold nanoparticles to which 6 mL toluidine blue had been added. 147
Figure 3.49 TEM images showing the formation of aggregates as crystal violet is added to a solution of gold nanoparticles: (a) 3 mL crystal violet added; (b) 6 mL crystal violet added; (c) and (d) 10 mL crystal violet added..... 148
Figure 3.50 TEM images showing the formation of aggregates of nanoparticles as acridine orange was added to a solution of gold nanoparticles: (a) 1 mL acridine orange added; (b) 3 mL acridine orange added; (c) 7 mL acridine orange added; (d) 10 mL acridine orange added. 149

Figure 3.51 TEM images showing the formation of aggregates as malachite green was added to a solution of gold nanoparticles: (a) 3 mL malachite green added; (b) 6 mL malachite green added. 150

Figure 3.52 Graph showing the increase in observed hydrodynamic radius of gold nanoparticles as dyes are added to the nanoparticle solution. 150

Figure 4.1 TEM images showing A) citrate capped gold nanoparticles showing good uniformity of size and shape, and B) citrate-capped silver nanoparticles produced by the same method showing a greater spread of particle sizes and less regular shape. 165

Figure 4.2 Graphs showing the UV-vis spectra of A) citrate-capped gold nanoparticles, showing characteristic SPR band at 519 nm, and B) citrate-capped silver nanoparticles showing SPR band at 402 nm. 165

Figure 4.3 Graph showing the UV-vis absorption spectra of (i) solvent-treated polyurethane, (ii) polyurethane with citrate-capped gold nanoparticles and (iii) polyurethane with citrate-capped silver nanoparticles. 167

Figure 4.4 Graph showing the UV-vis absorption spectra of (i) solvent-treated polyurethane, (ii) polyurethane post-coated with 0.1 M aqueous crystal violet (CV), (iii) polyurethane treated with solvent and acridine orange (AO), (iv) polyurethane post-coated with 0.1 M aqueous malachite green (MG), (v) polyurethane treated with solvent and naphthol green (NG). 168

Figure 4.5 Graph showing the UV-vis absorption spectra of (i) solvent-treated polyurethane with citrate-capped gold nanoparticles (AuNPs), (ii) polyurethane embedded with gold nanoparticles and post-coated with 0.1 M aqueous crystal violet (AuCV), (iii) polyurethane embedded with gold nanoparticles then treated with solvent and acridine orange (AuAO), (iv) polyurethane embedded with gold nanoparticles then post-coated with 0.1 M aqueous malachite green (AuMG), (v) polyurethane embedded with gold nanoparticles treated with solvent and naphthol green (AuNG). 169

Figure 4.6 Graph showing the UV-vis absorption spectra of (i) solvent-treated polyurethane with citrate-capped silver nanoparticles (AuNPs), (ii) polyurethane embedded with silver nanoparticles and post-coated with 0.1 M aqueous crystal violet (AgCV), (iii) polyurethane embedded with silver nanoparticles then treated with solvent and acridine orange (AgAO), (iv) polyurethane embedded with silver nanoparticles then post-coated with 0.1 M aqueous malachite green (AgMG), (v) polyurethane embedded with silver nanoparticles treated with solvent and naphthol green (AgNG). 170

Figure 4.7 Images showing the water contact angles acheived on (a) solvent treated polyurethane; (b) polyurethane containing tiopronin-capped silver particles and naphthol green; (c) polyurethane containing citrate-capped silver particles and malachite green... 171

Figure 4.8 Graph showing viable counts of *S. aureus* after a 5 hour incubation on dye-modified polyurethane, incubated either in the dark or illuminated by a white light source (of 6600 ± 990 lux at a distance of 25 cm). 172

Figure 4.9 Graph showing viable counts of *S. aureus* after a 5 hour incubation on gold nanoparticle and dye-modified polyurethane, incubated either in the dark or illuminated by a white light source (of 6600 ± 990 lux at a distance of 25 cm.). A dot indicates that the bacterial numbers were reduced below the detection limit of 100 cfu/mL for that sample. 173

Figure 4.10 Graph showing viable counts of *S. aureus* after a 5 hour incubation on silver nanoparticle and dye-modified polyurethane, incubated either in the dark or illuminated by a white light source (of 6600 ± 990 lux at a distance of 25 cm.). A dot indicates that the bacterial numbers were reduced below the detection limit of 100 cfu/mL for that sample. 175

Figure 4.11 Graph showing viable counts of *S. aureus* after a 2 hour incubation on silver nanoparticle and acridine orange-modified polyurethane, incubated either in the dark or illuminated by a white light source (of 6600 ± 990 lux at a distance of 25 cm.). A dot indicates

that the bacterial numbers were reduced below the detection limit of 100 cfu/mL for that sample. 175

Figure 4.12 Graph showing viable counts of *E. coli* after a 5 hour incubation on dye-modified polyurethane, incubated either in the dark or illuminated by a white light source (of 6600 ± 990 lux at a distance of 25 cm). 176

Figure 4.13 Graph showing viable counts of *E. coli* after a 5 hour incubation on gold nanoparticle and dye-modified polyurethane, incubated either in the dark or illuminated by a white light source (of 6600 ± 990 lux at a distance of 25 cm). 177

Figure 4.14 Graph showing viable counts of *E. coli* after a 5 hour incubation on silver nanoparticle and dye-modified polyurethane, incubated either in the dark or illuminated by a white light source (of 6600 ± 990 lux at a distance of 25 cm.). A dot indicates that the bacterial numbers were reduced below the detection limit of 100 cfu/mL for that sample. 178

Figure 4.15 Graph showing viable counts of *E. coli* after a 2 hour incubation on silver nanoparticle and dye-modified polyurethane, incubated either in the dark or illuminated by a white light source (of 6600 ± 990 lux at a distance of 25 cm.). 179

Table of Contents

Abstract 2

Novelty of the work 2

List of publications 4

Acknowledgements 5

Table of Figures 8

Table of Contents 21

Chapter 1 : Introduction and literature review 28

1.1 Noble metal nanoparticles: their importance, properties and synthesis 28

1.1.1 Surface plasmon resonance 30

1.1.2 Synthetic routes to noble metal nanoparticles 31

1.1.2.1 The Turkevich synthesis of charge-stabilised nanoparticles 33

1.1.2.2 Seeding methods 34

1.1.2.3 Two-phase reactions 34

1.1.3 Assemblies of multiple nanoparticles 35

1.2 Self-assembly of metallic nanoparticles into one dimensional arrays 35

1.2.1 Methods of preparation of 1D assemblies of nanoparticles 36

1.2.1.1 Templated assembly 36

1.2.1.1.1 DNA 37

1.2.1.1.2 Other biomolecules 40

1.2.1.1.3 Carbon nanotubes 42

1.2.1.1.4 Other templates 44

1.2.1.2 Template-free assembly 46

1.2.1.2.1 Supercritical fluids 47

1.2.1.2.2 Dipole-dipole interactions 48

1.2.1.2.3 Linker molecules 50

1.2.1.2.4 Magnetic interactions 51

1.2.1.2.5 Oriented aggregation 51

1.2.1.2.6 Non-uniform stabiliser distributions 52

1.2.1.2.7 Electron beam lithography 52

1.2.1.2.8 Micelles 52

1.2.1.2.9 Hydrophobic/hydrophilic interactions 53

1.2.1.2.10 Electric fields 53

1.2.2 Properties and applications of 1D nanoparticle arrays 54

1.2.2.1 Optical properties 54

1.2.2.2 Magnetic and electrical properties 56

1.2.2.3 Sensing applications 57

1.2.3 Future challenges 60

1.3 Introduction to photodynamic therapy 60

1.3.1 History of PDT 62

1.3.2 Photosensitizers and the mechanism of PDT 63

1.3.3 Oncological applications of PDT 64

1.3.4 PDT to treat viruses, bacteria and fungi 65

1.3.5 Conjugation of photosensitizers with nanoparticles 67

1.3.6 Photosensitizers for antimicrobial surfaces 67

1.3.6.1 Photosensitizer-nanoparticle conjugates for antimicrobial surfaces 69

Chapter 2 : The synthesis and characterization of gold and silver nanoparticles 72

2.1 Aims 72

2.2 Introduction to the synthesis and properties of noble metal nanoparticles 72

2.3 Experimental methods 75

2.3.1 Modified Turkevich synthesis of gold and silver nanoparticles 75

2.3.1.1 Synthesis of citrate-stabilised gold nanoparticles 76

2.3.1.2 Synthesis of citrate-stabilised silver nanoparticles 76

2.3.1.3 Synthesis of citrate-stabilised silver-gold nanoparticles 76

2.3.2 Synthesis of 2-mercaptopropionylglycine-capped silver nanoparticles and fabrication of 1D chains 77

2.3.2.1 Synthesis of 2-mercaptopropionylglycine-capped silver nanoparticles 77

2.3.2.2 Synthesis of high-aspect ratio 2-mercaptopropionylglycine-capped silver nanoparticle chains 77

2.3.3Synthesis of gold nanorods using seed and growth solutions 78

2.3.3.1 Stock solutions 78

2.3.3.2 Synthesis of gold nanorods 78

2.3.4 Synthesis of branched gold nanocrystals 79

2.3.5 Characterization techniques 79

2.3.5.1 TEM 79

2.3.5.2 UV-vis absorption measurements 79

2.4 Results and discussion 80

2.4.1 Modified Turkevich synthesis of noble metal nanoparticles 80

2.4.1.1 Citrate-stabilised gold nanoparticles 80

2.4.1.2 Citrate-stabilised silver nanoparticles 81

2.4.1.3 Citrate-stabilised bimetallic silver-gold nanoparticles 82

2.4.2 Synthesis of 2-mercaptopropionylglycine capped silver nanoparticles 90

2.4.2.1 2-mercaptopropionylglycine capped silver nanoparticle chains 92

2.4.3 Synthesis of gold nanorods 93

2.4.4 Synthesis of branched gold nanocrystals 96

2.5 Conclusions 98

Chapter 3 : The interaction of cationic and anionic dyes with gold and silver nanoparticles 100

3.1 Aims 100

3.2 Motivations and an introduction to photodynamic therapy 101

3.2.1 Combination of photosensitizers with nanoparticles 102

3.3 Experimental methods 103

3.3.1 Modified Turkevich synthesis of gold and silver nanoparticles 103

3.3.1.1 Synthesis of citrate-stabilised gold nanoparticles 103

3.3.1.2 Synthesis of citrate-stabilised silver nanoparticles 103

3.3.1.3 Synthesis of citrate-stabilised silver-gold nanoparticles 103

3.3.2 Synthesis of 2-mercaptopropionylglycine-capped silver nanoparticles 103

3.3.2.1 Synthesis of high-aspect ratio 2-mercaptopropionylglycine-capped silver nanoparticle chains 103
3.3.3 Synthesis of gold nanorods 104
3.3.4 Synthesis of branched gold nanocrystals 104
3.3.5 Titration experiments 104
3.3.6 UV-vis absorption measurements 106
3.3.7 Particle size measurements 106
3.3.7.1 Zetasizer measurements 106
3.3.7.2 TEM 106
3.4 Results and discussion 107
3.4.1 UV-vis studies 107
3.4.1.1 Citrate-stabilised gold nanoparticles with cationic dyes 107
3.4.1.2 Citrate-stabilised gold nanoparticles with anionic dyes 116
3.4.1.3 Citrate-stabilised silver nanoparticles with anionic dyes 120
3.4.1.4 Citrate-stabilised silver nanoparticles with cationic dyes 121
3.4.1.5 Citrate-stabilised silver-gold nanoparticles with cationic and anionic dyes 125
3.4.1.5.1 1:3 Au:Ag nanoparticles 125
3.4.1.5.2 1:1 Au:Ag nanoparticles 128
3.4.1.5.3 3:1 Au:Ag nanoparticles 130
3.4.1.6 Branched gold nanocrystals with anionic and cationic dyes 133
3.4.1.7 Gold nanorods with anionic and cationic dyes 138

3.4.1.8 2-mercaptopropionylglycine-capped silver nanoparticles with cationic and anionic dyes 141

3.4.2 Particle size measurements for citrate-capped gold nanoparticles: TEM studies and Zetasizer 145

3.5 Conclusions 150

Chapter 4 : The antimicrobial capacity of citrate-stabilised gold and silver nanoparticle-dye conjugates in polyurethane 153

4.1 Aims 153

4.2 Introduction and motivations 153

4.2.1 Nosocomial infections 153

4.2.2 Light activated antimicrobial surfaces 154

4.2.3 Conjugation of LAAAs and nanomaterials 156

4.3 Experimental methods 159

4.3.1 Synthesis of nanoparticles 159

4.3.1.1 Synthesis of gold and silver citrate stabilised nanoparticles. 159

4.3.1.2 Nanoparticle characterisation techniques 159

4.3.2 Preparation of dye solutions 159

4.3.3 Polymer samples for antimicrobial testing 160

4.3.3.1 Characterisation of polymer samples 162

4.3.4 Antimicrobial activity assays 163

4.4 Results and discussion 164

4.4.1 Nanoparticle synthesis 164

4.4.2 Polymer samples 165

4.4.2.1 UV-vis studies 166

4.4.2.2 Water contact angle measurements 170

4.4.3 Antibacterial testing 171

4.4.3.1 Staphylococcus aureus 171

4.4.3.2 E. coli 176

4.5 Conclusions 179

Chapter 5 : Concluding Remarks 182

5.1 Synthesis of gold and silver nanoparticles 182

5.2 Interaction of gold and silver nanoparticles with anionic and cationic dyes 183

5.3 Incorporation of dyes and nanoparticles into polyurethane for antimicrobial surfaces 184

5.4 Future work 186

Bibliography 188

CHAPTER 1 : INTRODUCTION AND LITERATURE REVIEW

This work presents the successful synthesis and characterisation of a range of noble metal nanoparticles using a range of synthetic techniques. Nanoparticles varied in shape, size, capping agent and supraparticular arrangement: rods, stars and spheres of different sizes were successfully synthesised, with highly linear anisotropic chains of some particles formed. The ability of the synthesised nanoparticles to enhance the absorption and activity of a range of photosensitising dyes was then investigated, producing novel dye-nanoparticles combinations not previously reported. It has been reported that dye-nanoparticle combinations which show enhanced activity compared to dye alone can act as highly potent antimicrobial agents for photodynamic therapy or self-sterilising surfaces. The antibacterial capabilities of dye-nanoparticle conjugates against *S. aureus* and *E. coli* was therefore investigated with excellent kill rates observed for novel combinations. Total kill of both bacterial species in light and dark conditions was observed in five hours using a new pairing of acridine orange with citrate-stabilised silver nanoparticles. This represents an exciting possibility for the development of new self-sterilising surfaces that are active under both ambient light and in the dark, a property which is paramount to maximise the benefit of antimicrobial surfaces.

A literature review outlining the background, motivations and theory behind these fields follows.

1.1 Noble metal nanoparticles: their importance, properties and synthesis

Nanoparticles of metals and inorganic materials have been known for many years. They are loosely defined as a particle in the size range 1-100 nm that exhibits properties not found in

the bulk material.[1] From accidental colouration of glass in the Roman era by throwing golden coins into the melt[2] to cutting edge technological applications now, they have always been at the forefront of science and their unique properties, innumerable uses and sheer beauty mean they still enjoy much attention.

Nanoparticles exhibit a number of unique features. Due to their small size they show behaviour not found by non-nanoscale particles with the same composition. Their atypical surface structure, very high surface area to volume ratio and consequent increased reactivity make them useful in many commercial applications.[3–5] Small nanoparticles (below ~30 nm) are characterised by a surfeit of energy at the surface and are thermodynamically unstable.[6] Crystallographic changes such as expansion or contraction of the lattice, a change in morphology, the appearance of defects or rearrangement of the atoms at the surface have all been observed to happen in an effort to lower the surface energy of the unstable particles .[7–9] Another distinctive property of small nanoparticles is the size dependence of their optical behaviour in a phenomenon called surface plasmon resonance, which is discussed more fully in Section 1.1.1. The physical properties of nanoparticles can also be size dependent, with thermal properties being among the easiest to measure. Particles of indium show a 120 °C drop in melting point when the diameter of the particle is reduced from 100 to 10 nm.[10] Particles of tin exhibit an 80 °C reduction under the same parameters.[11] The electrical properties of nanoparticles can also be related to their size – the Curie temperature for ferromagnetic $MnFe_2O_4$ and $MgFe_2O_4$ is changeable dependent on the diameter of the particles tested.[12–14]

The size and shape dependence of nanoparticles' properties offers excellent tuneability of their behaviour, making them ideal for applications such as catalysis[15] and surface enhanced Raman scattering (SERS) where very specific performance is required.[16] In both the above

cases, altering the shape of the nanocrystal from spherical to many-edged and nanorods respectively causes an enhancement in their ability to carry out the required function.

1.1.1 Surface plasmon resonance

Surface plasmon resonance (SPR) is a phenomenon exhibited by gold, silver and limited other nanoparticles. It originates from the presence of the free d electrons in metallic lattices which are free to travel through the material. The mean free path in gold and silver is approximately 50 nm, thus in a nanoparticle smaller than this no scattering is expected from the bulk and consequently the interaction of light is only with the surface. When the wavelength of incident light is much larger than the diameter of the nanoparticle standing resonance conditions can be set up. Light which is in resonance with the oscillations of the surface plasmon causes the free electrons to oscillate with the light's frequency, causing a standing oscillation.[17] This effect produces solutions of nanoparticles with very strong characteristic colourations and is a useful diagnostic tool, as the SPR of the nanoparticles is highly size and shape dependent.[18,19] Thus, the colour of a gold colloid can give an accurate idea of the size of the nanoparticles it contains. Increasing the diameter of gold particles from 10 nm to 100 nm sees the SPR band undergo red shift from 515-520 nm to 572 nm, an increase of about 50 nm. Increasing the aspect ratio of particles can have a much stronger effect; increasing the aspect ratio of gold nanorods from 2.4 – 5.7 is concurrent with a red shift of 300-350 nm for the longitudinal plasmon (Figure 1.1).[20]

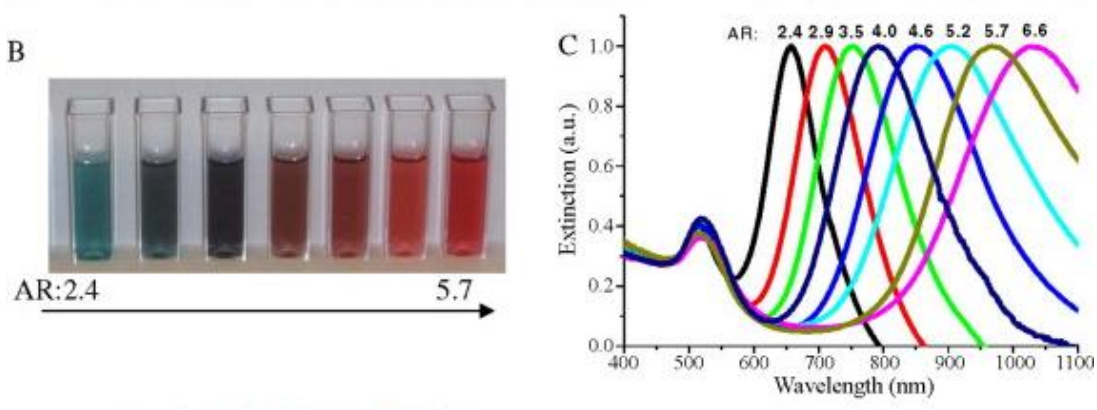

Figure 1.1 Image showing the red shift in absorption maximum with increasing aspect ratio of gold nanorods. Image from El-Sayed *et al*.[20]

The SPR of a nanoparticle is also very sensitive to change in the dielectric constant of the surrounding material. Changing the solvent is a facile way to do this, but choice of ligand or capping molecule is by far the most important consideration in altering the plasmon resonance electrically. Molecules which are covalently bonded to the surface of the metallic nanoparticle affect the electron density found there, resulting in a shift in the observed SPR maximum.[21] In this manner nanoparticles can act as simple chemical sensors, an application discussed more thoroughly in Section 1.2.2.3.

1.1.2 Synthetic routes to noble metal nanoparticles

There are myriad ways to achieve nanoparticles of gold and silver with many papers published on the topic. Broadly speaking, however, all synthetic routes to gold and silver nanoparticles fall into one of two general categories: top down or bottom up approaches.

Top down methods start with a bulk material and remove the excess to leave the desired nanostructures. Common approaches include electron beam lithography and photolithography.[22–25] Though excellent results can and have been achieved by both techniques, top-down methods suffer from the obligation to remove large quantities of material which is then wasted. There are also hard limits on the size of the nanostructures

that can be generated, as photolithography is bound by the diffraction limit of the available lasers. Current technology allows features as in the range 20-100 nm to be generated and this is ever improving as laser pulses with shorter wavelengths are developed, but even if this hurdle can be overcome photolithography requires expensive, highly specialised equipment.[26] Electron beam lithography also requires costly instrumentation, though it does allow smaller nanostructures (in the region of 10 nm) to be generated compared to photolithography.[27]

Bottom-up techniques have garnered more interest as they are more adaptable and tend to require less specialist apparatus. The general approach is to use a reducing agent to reduce gold or silver ions in solution, then assemble the atoms into nanostructures. Techniques in this area are many and varied, including templating, chemical, sono- electro- and photochemical and thermal reductions.[17] Bottom-up methods allow very small nanostructures to be fabricated (1 nm upwards) but usually require an arresting agent to stop particle growth at the desired point.[28] Monodispersity can also be difficult to achieve using these methods. As such, capping molecules or ligands are usually employed to coat the surface of the particles which renders them much more stable to aggregation and falling out of solution than bare particles alone.[29]

Bottom up methods allow great control over the shape and size of the nanoparticles produced by close control of reaction parameters such as time, temperature, reducing agent and capping molecule.[30] Though most nanoparticles are spherical, different reaction conditions and methods have produced rods, cubes, wires, tubes, one to eight pointed stars, prismatic and tetrahedral nanoparticles from gold, silver and platinum.[31–35]

One downside of bottom up techniques is the slight variance in each experimental run. Nanoparticles synthesised by the same methods will always vary from batch to batch as the particles are extremely sensitive to tiny fluctuations in temperature, pH, time etc., so

extreme care should be taken to keep reaction conditions as similar as possible to minimise this.

A brief overview and explanation of the common bottom up techniques used in the following chapters is given below.

1.1.2.1 The Turkevich synthesis of charge-stabilised nanoparticles

The Turkevich synthesis of noble metal nanoparticles is widely used and well known. The method uses citrate ions to reduce a hot solution of auric acid or silver nitrate to give a stable solution of small, well-formed, citrate-stabilised nanoparticles.[36] This method is unusual among bottom-up techniques as the citrate plays the dual role of reductant and stabilizer; usually, two separate reactants are required to achieve this.[37] Control over the size and morphology of the particles can be exercised by altering temperature,[38] pH[39] and concentration of citrate ions.[37] Increasing the concentration of citrate ions in the reaction mixture produces smaller particles which are more stable to aggregation.[40]

The citrate reduction of metal salts is a redox system. Oxidation of the citrate forms acetone dicarboxylic acid, which reduces the gold ions from Au^{3+} to Au^{0} (Or Ag^{+} to Ag^{0} for silver particles) and forms a supersaturated solution. Nucleation followed by condensation of more gold onto the surface of the nuclei results in nanoparticles forming.[41] As the particles grow the SPR develops, allowing the solution to take on the distinctive strong colouration of gold and silver colloids. SPR was discussed in more detail in Section 1.1.1. The nuclei prior to the growth step are too small (~1nm) to produce an SPR band in the visible region.

Once the nanoparticles have formed citrate ions remain bound to the surface, forming a negatively charged capping layer.[42] Thus the particles carry an overall negative charge. It is presumed that at the surface of the particle there are both donor and acceptor sites – neutral metal that donates electrons to acceptor molecules and gold complexes in a high oxidation

state which are reduced by donors. The capping citrate ligands are bound at the surface of the particle where the oxidation state of the gold is +1.

The nanoparticles for the main part of this work were synthesised by a slightly modified Turkevich method as used by Narband *et al*.[43]

1.1.2.2 Seeding methods

Another common approach to making nanoparticles is the seeding approach, whereby a strong reducing agent (commonly $NaBH_4$) is used to make very small, spherical particles. These particles are then added to a growth solution containing more metal ions and a surfactant to promote directional growth. The growth solution uses a weaker reducing agent such as ascorbic acid to reduce the metal ions to a halfway, intermediate state, allowing catalysed reduction and condensation of metal on the surface of the seed particles.[44]

This method is used with very specific surfactant and seed conditions to grow nanorods in solution.[31,45,46] Steric inhibition by the surfactant (chosen to be a large, bulky molecule; cetyltrimethylammonium bromide (CTAB) is a common choice) of growth along the long sides of the rod allows for anisotropic growth on the short sides only, forming a particle with a distinct aspect ratio.

1.1.2.3 Two-phase reactions

Very small (1 – 5 nm) nanoparticles can be produced using a two-phase approach.[47] The first stage of these reactions uses a surfactant to transfer the gold or silver ions into the organic phase. The surfactant of choice is usually a thiol, as the gold- or silver-thiol bond is strong and stabilises the growing particles. Addition of sodium borohydride to the aqueous phase followed by vigorous stirring promotes the growth of nanoparticles in the organic phase, which will start to colourise as particles grow and develop SPR bands. Particles produced in this way are small and very stable when isolated, allowing storage for long periods.

1.1.3 Assemblies of multiple nanoparticles

The unique optical,[48–50] electronic,[51,52] magnetic[53] and catalytic[54–56] properties of metallic nanoparticles has made them the focus of intensive study by both the scientific and engineering communities. Though the properties and applications of noble metal nanoparticles are numerous, a fascinating quirk they possess is that the collective behaviour of a group of particles can be very different to the individual. As such, careful assembly of the particles into groups – be it thin films, arrays or composites - allows us the possibility of tweaking their behaviour to suit a prospective application. The potential of these assemblies to facilitate the miniaturisation of existing electronic components (such as LEDs and photoconductive devices[57]) is huge; consequently there is a large body of literature devoted to their understanding and applications.

Assemblies of nanoparticles are classified as being either one-, two- or three-dimensional. The latter two are well covered by several existing reviews and are not discussed herein.[58–60] By contrast, the former is less thoroughly reported in the literature owing to difficulties concerning their preparation, isolation and analysis whilst maintaining their anisotropic character. The next section of this review outlines these problems and presents a comprehensive overview of the methods used to prepare 1D arrays of metallic nanoparticles along with a summary of their properties and applications.

1.2 Self-assembly of metallic nanoparticles into one dimensional arrays

Though relatively facile to prepare, unsupported anisotropic arrays of discrete nanoparticles have a tendency to undergo sintering without charge-induced stabilisation or the physical support of a template. Their remaining as unconnected particles can also be effected by wrapping the array in stabilising molecules or using another form of external coating. All of these methods of stabilising the arrays can make isolation for analysis difficult.

Owing to the difficulties outlined above, metallic nanowires would seem a sensible compromise when an application calls for a 1D nanoparticle array. Indeed, they share some similar functional properties which mean they could be substituted in certain applications and tend to be easier to produce, isolate and analyse.[61] However they lack the unique inter-particle photonic, electronic and energy transfer[62,63] properties of 1D arrays of particles which make them so interesting for producing modernised electronic components and devices.

The unique properties of 1D arrays are dependent upon our ability to control and manipulate the interparticle spacing. For example, nanoparticles of copper,[64,65] silver[66–69] and gold[19,70,71] show SPR effects which give rise to enhanced absorption, reflection and remarkably strong colouration.[72] The ability to tailor the spatial coupling of the nanoparticles in these cases therefore allows extremely close control of optical and electronic properties,[73] essential for efficient and repeatable device manufacture.

The next section of this review covers the reported methods used to produce 1D arrays of metallic nanoparticles, both template and template-free. Section 1.2.2 sets out the novel properties exhibited by these assemblies and discusses their current uses and scope for the future.

1.2.1 Methods of preparation of 1D assemblies of nanoparticles

1.2.1.1 Templated assembly

By far the most common way of producing 1D arrays if nanoparticles is to use an appropriately shaped template to guide the particles into the desired configuration. Some template-free methods have been reported and are discussed in Section 1.2.1.2. Templates can be divided into two loose categories: 'hard', such as carbon nanotubes, facetted substrates and inorganic wires, or 'soft' examples such as DNA, peptides and other biopolymers.[74]

1.2.1.1.1 DNA

By far the most widely studied template for nanoparticle assembly is DNA. It boasts several features which make it a champion in this field – peerless molecular recognition and the ease with which nanoparticles can be functionalized with DNA 'tags' of complementary sequences to template attachment points, taking advantage of the specific bonding of DNA base pairs. As it is itself a nanoscale material (possessing a diameter of 2 nm and an inter-base spacing of 3.4 Å)[75] it allows facile production of components that are themselves on the nanoscale. The biospecificity of the DNA system allows a high degree of control over ordering, structure and features in the nanoparticles assemblies.[76] Metallisation of DNA templates has been widely reported and is discussed in more detail below.[77]

Directed assembly of nanoparticles using a DNA template has been studied over the past two decades, first brought to prominence by Schulz *et al.* in 1996.[78] Though their dimeric structures were proof of concept for functionalising nanoparticles and selective attachment to a DNA template, it was not until almost ten years later that the first report of linear nanoparticles assemblies was published.[79] Deng *et al*. functionalised phosphine-capped gold nanoparticles with DNA-1 fragments to produce gold-DNA conjugates. They then used rolling circle polymerisation (a biological technique in which a circular DNA oligonucleotide revolves and is used to produce long strands of DNA up to 12000 nucleotides in length)[80] to assemble the conjugates into arrays, which were isolated by gel electrophoresis. TEM and AFM images confirmed the presence of micrometre-scale linear arrays, comprised of well-separated gold nanoparticles spaced along the DNA backbone at an average spacing of 18.5 nm (Figure 1.2). Similar processes have since produced arrays of nanoparticles of different metals, including silver,[81,82] gold,[83,84] platinum[85] and palladium.[86]

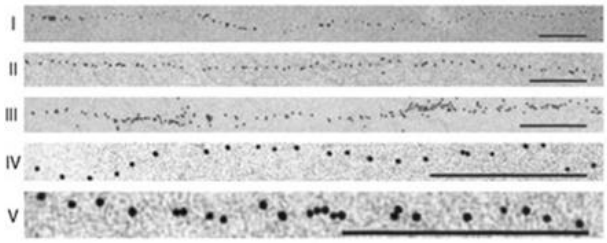

Figure 1.2 TEM images showing extended linear arrays of gold nanoparticles. Scale bars all represent 200 nm. I-III show the structures; IV-V show higher magnification sections of I and II. Figure reproduced with permission from Deng *et al*.[79]Different approaches have been employed to yield similar results. Conductive wires of silver nanoparticles decorated DNA were produced by Braun *et al*.[81] DNA strands were strung between gold electrodes at a separation of 12 µm.[81] Ag^+ ions were then ion exchanged and conjugated with amino groups on the surface of the DNA before being reduced. Repeating the ion exchange and reduction steps resulted in the formation of silver nanoparticles along the DNA wire (Figure 1.3).

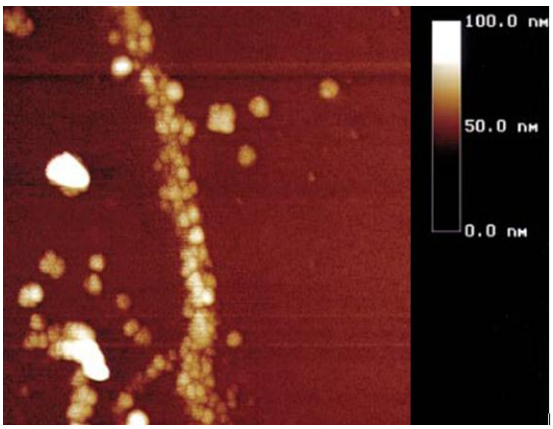

Figure 1.3 AFM image showing a silver wire templated on DNA connected between gold electrodes at 12 µm separation. Figure reproduced with permission from Braun *et al*.[81]

2D crystals of DNA have also been used to produce anisotropic nanoparticle arrays.[87] A nanogrid of DNA was functionalised with coded attachment points in linear patterns. It was then exposed to gold nanoparticles that were conjugated with complementary thiolated DNA. AFM results showed a pattern of corrugations on the surface of the grid corresponding to the linear attachment of nanoparticles (Figure 1.4). A more complex approach yielded

nanogrids with two differently-coded attachments points.[88] On exposure to a mixture of nanoparticles (5 nm and 10nm, each size tagged with differently-coded DNA) parallel rows of alternating small and large particles were observed (Figure 1.5). This facile approach uses DNA's exceptional biospecificity to allow control of both size and position of nanoparticles within a component.

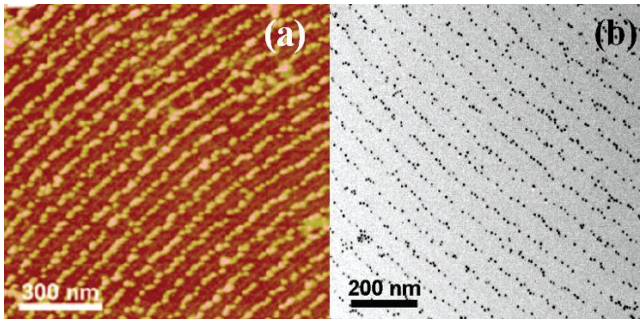

Figure 1.4 (a) AFM and (b) TEM images of the ridge-like structure formed by linear assembly of gold nanoparticles on a DNA nanogrid. Figure reproduced with permission from Kiehl *et al*[89].

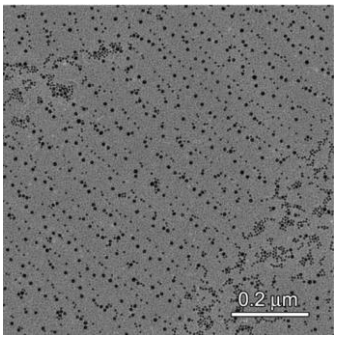

Figure 1.5 TEM image showing alternating parallel rows of 5 nm and 10 nm gold nanoparticles on a DNA grid. Figure reproduced with permission from Kiehl *et al*.[88]

DNA has also been used to mediate the assembly of gold nanoparticles into quasi-1D, cyclical structures.[90] Gold nanoparticles functionalised with thiolated DNA were conjugated with support DNA to produce 'building blocks'. These blocks then underwent hybridisation to produce a cyclical DNA backbone decorated with nanoparticles. Though novel, functional properties of these structures have yet to be reported.

1.2.1.1.2 Other biomolecules

Peptide fibrils have shown great ability to produce linear arrays of nanoparticles. One method reported by Wang *et al*. used protonation of the nitrogen groups along the length of the fibril to attach anionically-stabilised gold nanoparticles *via* electrostatic interaction.[91] Varying the pH resulted in single nanoparticle width assemblies forming at low pH (Figure 1.6b) and double helical arrangements at higher pH (Figure 1.6a). Analogous experiments produced comparable arrays of palladium nanoparticles. Utilising antibody-antigen and streptavidin-biotin specificity on fibre-recruiting peptides has also successfully produced anisotropic arrays of gold particles on the micrometre scale.[92] Dextran can be used similarly to achieve analogous results.[93]

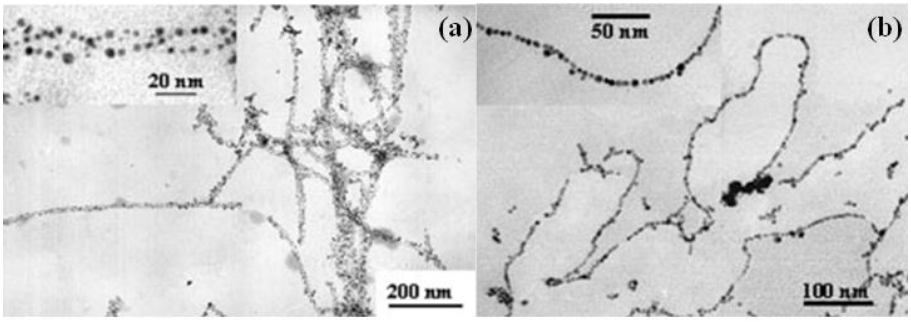

Figure 1.6 TEM images showing (a) double helical arrays of Au nanoparticles on peptide nanofibrils obtained at pH = 3.5, and (b) single chain arrays obtained at pH = 6. Figure reproduced with permission from Wang *et al.*[94]

Viruses can also be used to this end. The tobacco mosaic virus (TMV) is a tubular molecule with a length of 300 nm and an inner diameter of 4 nm, making it an ideal template to align small nanoparticles into chains. Dujardin *et al*.[95] published the first report of metallic nanoparticles on the TMV, using silver, gold and platinum. Silver experiments comprised exposing the virus to silver nitrate then reducing it under UV light. This yielded nanoparticles 2-4 nm in diameter spaced along the internal channel of the virus. Gold and platinum studies used $HAuCl_4$ and $[PtCl_6]^{2i}$ ions (the latter stabilised by Na^+ or K^+) reduced by hydrazine hydrate

and generated spherical nanoparticles densely packed along the external surface of the virus (Figure 1.7). Similar results have been produced using highly specialised bacteriophages.[96] The TMV has also been used to assemble semiconducting quantum dots into anisotropic arrays dots[97,98] and a modified version of the virus yielded quasi 1-D cyclical arrangements of gold particles.[99]

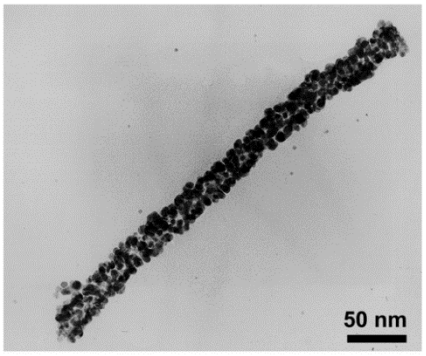

Figure 1.7 TEM image of a single TMV, showing dense coverage of Au nanoparticles. Figure reproduced with permission from Dujardin *et al.*[95]

Sequenced histidine-rich peptide nanotubes show similar molecular recognition to DNA and therefore offer a further biomolecular approach to synthesising 1D arrays of nanoparticles. Functionalising gold nanoparticles with complementary peptide tags allows a dense coverage of particles on the surface of the peptide wire (Figure 1.8).[100] Interparticle spacing was 6.4 nm, consistent with the distance between peptide attachment points. Nanotubes of heterodimeric tubulin have been shown to arrange palladium nanoparticles into highly ordered chains.[101] Some size control over the nanoparticles produced was afforded by the reducing agent used. Silicified bolaphospholipid nanofibrils have also been successfully employed to arrange gold nanoparticles into linear assemblies.[102]

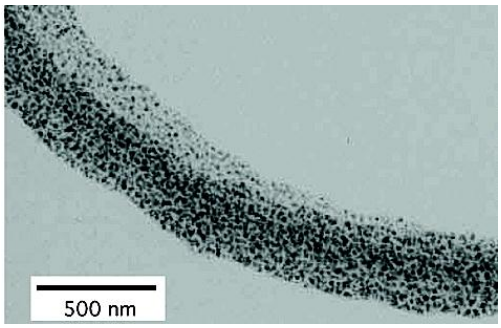

Figure 1.8 TEM image of gold nanoparticles on a peptide nanowire. Figure taken with permission from Djalali *et al*.[100]

As mentioned above, genetically modified bacteriophages provide excellent scaffolds for nanoparticle assembly. Alloyed particles of CoPt and FePt were produced on these supports,[103] though it has also successfully been used to produce nanoparticles of semiconducting materials.[97,98] Modified yeast cells have been used to form belts of gold and silver nanoparticles 100 nm wide.[104] The belts produced in these experiments exhibit excellent conductivity, similar to that of a solid metal wire.

Cellulose molecules contain a large amount of oxygen and can therefore stabilise bare nanoparticles in a similar way to crown ethers. This eliminates the need for stabilising ligands on the particles themselves. Nanoparticles of bare silver, gold and platinum have been produced using this template, aligning themselves along the length of the cellulose fibrils to give highly linear arrays.[105]

1.2.1.1.3 Carbon nanotubes

Carbon nanotubes (CNTs) are widely used for the purpose of aligning particles, and are known as 'hard' templates owing to their inflexibility and toughness. They hold an advantage over biomolecules in cases where harsh reaction conditions are required, as they tolerate extremes of temperature, pH and oxidation/reduction much better than biological tissues. They also offer two options for alignments of particles: either decorated on the outer surface or aligned along the interior, capillary-like cavity.

One elegant system for filling the central capillaries of the CNTs is nanotube wetting. This technique was reported using low melting point metals (Pb, [106] Ni and UO_x[107]) but as a general point suffered with poor filling efficiency of the capillary. The work of Ugarte *et al*. using silver nitrate, however, produced discrete nanoparticles of metallic silver along the internal cavity after prolonged electron irradiation (Figure 1.9).[108] Thermal decomposition of the silver nitrate produced a continuous wire within the capillary.

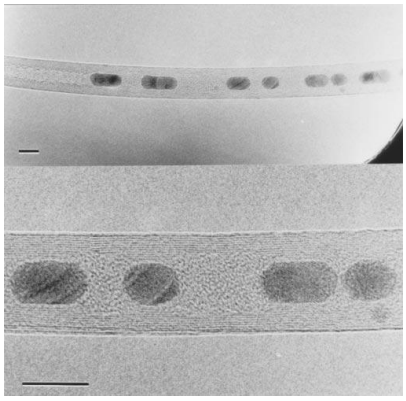

Figure 1.9 TEM images of silver nanoparticles in the central capillary of a carbon nanotube. Scale bars represent 5 nm. Figure reproduced with permission from Ugarte *et al*[108].

Sol-gel methods have been widely explored to deposit nanoparticles from colloidal solution onto the outer surface of CNTs. Precipitation of CNTs from a highly concentrated solution of gold colloid yields CNTs with monolayer coverage of gold particles on the surface (Figure 1.10).[109] 1D gold structures produced in this way were up to 10 µm in length. DNA[110] and organic capping agents[111] can also be used to functionalise both the CNT walls and the nanoparticles, resulting in coverage of the outer walls. Similar approaches have been used to produce comparable structures from gold,[112] silver,[113] platinum,[114–116] palladium,[117] tin,[117] and copper.[118] Rhodium nanoparticles have also been prepared on CNTs[119] and have been proven to exhibit exceptional catalytic activity.[120]

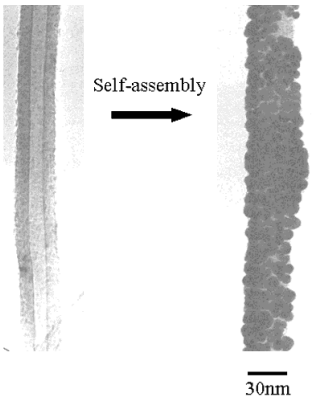

Figure 1.10 TEM image showing the self-assembly of gold nanoparticles on the outer surface of a CNT. Figure taken with permission from Fullam *et al*. [109]

Electrodepostion has also been used with some success to deposit gold, palladium and platinum nanoparticles on single-walled CNTs.[121] Coverage was found to be dependent on a myriad of factors including salt concentration, potential and deposition time. This therefore offers an inexpensive method to control the coverage and tune it for purpose. CNTs functionalised with 1-pyrenesulfonic acid can initiate the assembly of gold nanoparticles along their length to produce 1D structures.[122] This can be followed by a heating step to induce nanowelding.

1.2.1.1.4 Other templates

Ridged and facetted sheet substrates present another method of preparing high aspect ratio chains of nanoparticles. Slow evaporation of a colloidal gold solution onto ridged amorphous carbon results in spontaneous arrangement of the particles along the step edges of the substrate (Figure 1.11).[123] This is thought to be due to entropic force fields generated at the ridges of the carbon sheet. Pulsed laser deposition of silver onto facetted alumina has also be shown to produce linear arrangements of nanoparticles.[124] The grooves in the surface of the alumina sheet provide high-coordination binding sites to which the silver nanoparticle will preferentially attach.[125] Physical vapour deposition of silver onto highly ordered pyrolytic

graphite can be used to similar effect, generating chains of silver nanoparticles in excess of 100 µm in length along the step edges of the graphite. [126]

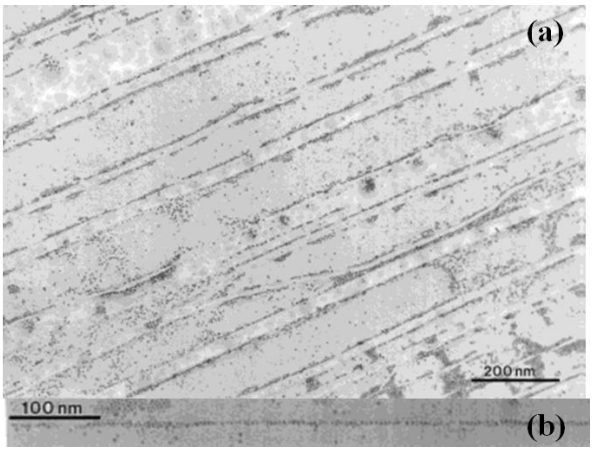

Figure 1.11 TEM image showing (a) the alignment of gold nanoparticles along the ridges of an amorphous carbon substrate, and (b) a high-magnification image of a single nanoparticle chain showing exceptional linearity. Figure reproduced with permission from Hutchinson *et al*.[123]

The internal linear cavities of zeolites and other mesoporous zeolite-type materials can be used to efficiently align metallic nanoparticles. Monodisperse chains of gold or platinum nanoparticles have been generated by saturating mesoporous organosilicas with the appropriate metal salt, followed by reduction under dry hydrogen gas.[127] Thermal decomposition of silver nitrate in the pores of SBA-15 produces nanowires of metallic silver,[128] with similar techniques producing analogous structures of platinum[129] and palladium.[130]

Polymerisation reactions between monomer units has also been reported to form quasi-1D nanoparticle structures. Carboxylic acid functionalised gold nanoparticles were joined to a polylysine support. Inducing closure of the polylysine ring generated rings of gold nanoparticles held on a cyclic template (Figure 1.12).[131] Slightly different approaches to this have used polymer units: gold nanoparticles functionalised with thiolated poly(ethylene oxide) form large aggregates of particles when mixed with polymers. Linear arrays of particles

up to several hundred nanometres in length can be induced to form by adding chondroitin sulphate-c-sodium salt to the aggregates.[132] Polyvinylpyrrolidone produces 1D, branched arrays of gold nanoparticles in a similar way.[133]

Figure 1.12 TEM image showing ring-like structures of gold nanoparticles formed on a polylysine support. Image with permission from Dai *et al*. [131]

The grain boundaries of ice provide a less obvious way of templating nanoparticles. Chen *et al.* showed that upon freezing a colloidal solution of gold the nanoparticles will be excluded from the ice crystals, creating 1D arrays of nanoparticles within the veins between grains.[134] These chains could extend over several micrometres.

Liquid crystals can also yield 1D arrays of particles. The intrinsically linear arrangement of liquid crystals into matrices can produce 1D structural defects, which can trap small gold nanoparticles (~5 nm in diameter). Spatial coupling (both interparticle spacing and chain thickness) could be easily controlled by altering the concentration of the colloidal solution.[135]

1.2.1.2 Template-free assembly

Template free assembly of nanoparticles, though perhaps less facile than templated, does present a true bottom-up technique to produce linear arrays of particles whilst avoiding some of the problems that template assembly can produce. Generally harsh reaction conditions are required to remove a nanoparticle chain from its support, which can disturb or destroy the chains' structure. Conversely, if the chains are not removed from the template

then the substrate can have a great effect on the electrical properties of the array. Thus, exploiting the intrinsic preferences of some nanoparticles to align presents a method of achieving anisotropic arrangements of metallic particles whilst circumventing the need for a template. The major methods of attaining this are reported below.

1.2.1.2.1 Supercritical fluids

Supercritical fluids offer the advantages of tuneable solvation with tiny changes in pressure and temperature, meaning their effect can be minutely controlled. This makes them ideal for the fine control needed to synthesise and modify nanostructures, and have already proven invaluable in the synthesis of carbon nanotubes,[136] metal oxide nanoparticles[137] and silicon nanowires.[138]

Supercritical water has been shown to organise silver aggregates into nanoparticles and 1D wires sponatenously.[139] Ag_2O was decomposed in an argon atmosphere before being transferred to the supercritical water reaction vessel. Small changes in the temperature and pressure of the water were found to radically alter the morphologies that resulted: low pressures (<49 MPa) gave rise to in discrete nanoparticles, whereas higher pressures (>49 MPa) caused the particles to aggregate and assemble into coiled wires (Figure 1.13). Investigation of intermediate steps in the wires' formation shows they are composed of nanoparticles that fuse and crystallize together into the anisotropic arrays. The chains were more easily polarisable longitudinally, thus aggregation tended to occur on the ends of the wires to minimise coulombic repulsion.

Figure 1.13 TEM image showing a coiled wire of fused silver nanoparticles obtained by treatment with supercritical water at 400 °C at 49 MPa. Reaction time was 60 minutes. Scale bar represents 100 nm. Figure from Chang *et al*.[139]

1.2.1.2.2 Dipole-dipole interactions

Linear aggregation of gold nanoparticles in ethanol has been shown.[140] 10 nm gold nanoparticles synthesised in aqueous solution, sonicated in ethanol for 1 h then immobilised on silicon resulted in closely spaced lines of discrete nanoparticles. Observation of the nanoparticles in the ethanol solution showed similar results, giving credence to the theory that aggregation happens in solution due to dipole-dipole interactions than due to drying effects on the silicon. It is proposed that due to the change of medium in this study excess stabiliser was removed from the solution, allowing aggregation of the particles where previously electrostatic repulsion would have forbidden it. Coupled with the difference in polarity of water *vs.* ethanol molecules, the former being able to counteract asymmetric charges on the surface of the gold particles and the latter not, there is a compelling argument for dipole-dipole interaction in solution being the cause of the anisotropic wires. Liao *et al*. proposed a mechanism for this, whereby the formation of asymmetric charges on nanoparticles lead them to become dimers.[140] The integrative dipole moment of a dimer is

greater than that of a lone particle thus they will attract nanoparticles more strongly, causing growth of the chain (Figure 1.14).

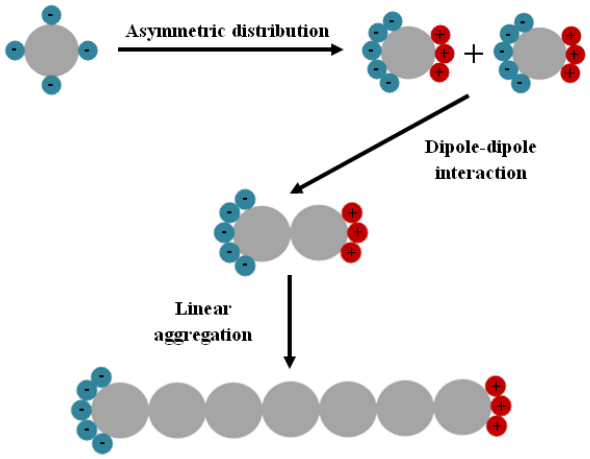

Figure 1.14 Illustration showing the mechanism of formation of linear chains of gold nanoparticles in ethanol. Figure adapted from Liao *et al*.[140]

Further work by a different group suggests that this dipole-dipole mechanism could also be dependent on the salt concentration in the solution.[141] Dipole-dipole interactions induced by exchange of negatively charged citrate ligands with neutral thiourea has also been reported to trigger assembly of gold particles into 1D arrays.[142] Similar methods have been employed by other groups.[143] There is still, however, some dispute over the true processes at work and ongoing research by computational[144] and experimental groups[145, 146] aims to clarify this.

Superparamagnetic iron particles have been reported to spontaneously align into randomly oriented 1D structures.[147] There is a clear-cut transition from single nanoparticles to chains as particle size increases and the dipole charges become sufficient to induce aggregation.

Electrochemistry can be used to exploit dipoles and align gold particles into short 1D structures. A colloid of spherical gold particles (approx. 18 nm in diameter) was added to a mixed organic/aqueous electrolytic solution. A current of 20 mA was applied for 20 min

whilst the solution underwent ultrasonication. TEM images showed chain-like aggregations of nanoparticles.[148]

1.2.1.2.3 Linker molecules

Due to their nature, nanoparticles lack any capacity for specific directional bonding. However, placing 'linker molecules' at opposing positions on nanoparticles allows them to behave as divalent building blocks, which can undergo pseudo-polymerisation reactions to form chains. This was first reported in 2007 using 11-mercaptoundecanoic acid placed on gold nanoparticles, forming chains of between 3 – 20 particles.[149] The chains were highly regular and lacked any branching, suggesting successful diametric functionalisation. Interparticle spacing could be easily controlled by using linker molecules of different carbon chain lengths. Similar approaches using a wide range of linker molecules followed, including alkanedithiol molecules,[150] biotin disulfide and streptavidin,[151] DNA and heavy metal-chelation reactions,[152] a biocompatible polymer called chitosan,[153] amide linkages,[154] halogen donor ligands[155] and histidine.[156] Chains resulting from this method tend to be reasonably stable and also offer an easy way to alter spatial coupling of the particles, essential for photonic and electrical applications.

Comparable studies using 2-mercaptobenzimidazole functionalised silver particles in a 1:1 water/ethanol mixture gave linear arrays, though the chains were found to be held together by hydrogen bonding rather than covalently.[157] tiopronin-capped silver particles have been shown to organise spontaneously into chains under ultrasonication – again, it is thought that hydrogen bonding between the carboxylic acid groups on the tiopronin molecule is the cause.[158] Analogous gold experiments gave similar results.[159] The electrostatic interactions between adsorbed cysteine molecules can also yield linear arrangements of gold nanorods.[160]

1.2.1.2.4 Magnetic interactions

The inherent anisotropy in magnetic nanoparticles can be exploited to align them into 1D arrays.[59,161] thermal decomposition of iron pentacarbonyl was found to form single domain ferromagnetic iron nanoparticles. The particles assembled themselves into chains extending up to 300 µm due to the intrinsic magnetic forces present. .[162] Similar results have been reported computationally for cobalt, iron and nickel particles. [163]

1.2.1.2.5 Oriented aggregation

'The crystallographically specific self-assembly of primary nanocrystals' is known as oriented aggregation. [164] It involves the self-assembly of nanocrystals followed by crystallographic reorganization, then subsequent aggregation into oriented aggregates.[165] This phenomenon was first investigated using titania,[164,166] with silver being the first purely metallic nanoparticles to be proven to behave in this way.[167] Silver nitrate was reduced by a polyol in the presence of a thiol stabiliser. Silver wires with high aspect ratios were formed in this way, spanning from the nano- to micrometre scale in length and 2-6 nm in diameter. TEM studies showed the wires to be an anisotropic coalescence of crystalline silver particles (Figure 1.15). Giersig *et al*. produced similar results also using silver: silver wires were grown by the spatially directed aggregation of silver along the (100) and (111) crystallographic planes.[168] Palladium in toluene has been shown to form nanoribbons in a comparable manner.[169]

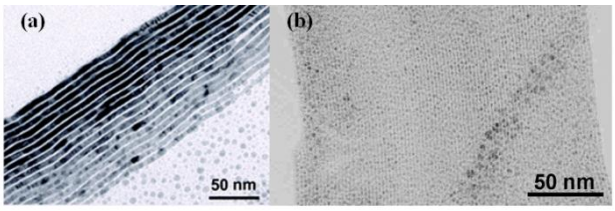

Figure 1.15 TEM images showing (a) 6nm diameter silver wires, and (b) linear arrays of 2nm silver nanoparticles. Figure reproduced with permission from Viau *et al.*[167]

1.2.1.2.6 Non-uniform stabiliser distributions

The uneven adsorption of stabilising ligands on the surface of nanocrystals is most often seen in composite particles (such as CdSe[170,171], silver sulphide[172] and titania[173]). However, the different crystallographic planes exhibited on pure metallic nanoparticles can also present surfaces with different affinities for a chosen ligand, though this phenomenon has only been reported for silver to the best of our knowledge. Poly(vinyl pyrrolidone) (PVP) shows differing affinities for the silver {100} and {111} crystallographic planes, and varying the ratio of silver nitrate precursor to PVP has resulted in anisotropic silver wires.[174]

1.2.1.2.7 Electron beam lithography

Electron beam lithography (EBL) is a well-known technique that has been used to form periodic arrays of nanoparticles on a substrate, be that 1- or 2D.[26,175–179] Palladium is one of many metals that has been used in conjunction with EBL to form periodic arrays of nanoparticles.[179] Despite EBL's ability to produce linear chains of particles it is not a bottom-up self-assembly process and therefore is not covered in any detail here.

1.2.1.2.8 Micelles

Block copolymer micelles, exposed to a change in salt concentration or pH, can undergo a transition from spherical to ribbon-like structures.[180] Similar observations have been made about gold nanoparticles encapsulated in amphiphilic poly(styrene-block-acrylic acid) exposed to increasing acetic acid or salt concentration, forming chains of discrete particles (Figure 1.16).[181] An inversion of charge at the surface-liquid interface is thought to be the driving force behind this. Chains up to 300 nanoparticles long have been produced by a similar method.[182]

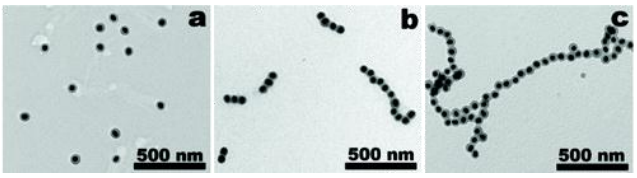

Figure 1.16 TEM images showing progressively longer chains of gold nanoparticles encapsulated in amphiphilic poly(styrene-block¬-acrylic acid) by exposure to increasing concentrations of 1-(3-dimethylamino)propyl)-3-ethylcarbodiimide methiodide (EDC): (a) [EDC] = 0 µM; (b) [EDC] = 55 mM; (c) [EDC] = 87 mM. Figure with permission from Kang *et al.* [181]

1.2.1.2.9 Hydrophobic/hydrophilic interactions

Utilising the inherent hydrophobic/hydrophilic nature of different ligands can cause oriented assembly of nanoparticles. Gold nanorods (8 x 42 nm) in an organic medium were capped with CTAB along the long sides and a hydrophobic polymer on the ends.[183] Exposure to water in the organic medium caused the now amphiphilic nanorods to self-assemble into chains between 10-100 blocks in length (Figure 1.17).

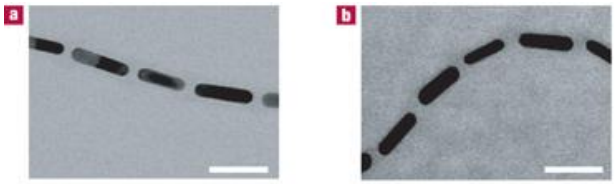

Figure 1.17 High-magnification TEM images of chains of triblocks obtained in the DMF/water mixture with water concentrations of 10 wt% (a) 10 wt% and (b) 15 wt%. The scale bar is 50 nm. Figure with permission from Rubinstein *et al*. [183]

1.2.1.2.10 Electric fields

Polarizing conductive nanoparticles can bring about their organization along field lines, forming 1D chains. [74,184] Facile control of chain length was afforded by tuning the concentration of particles in the colloid, strength of the field and the dielectric permittivity of the medium.

1.2.2 Properties and applications of 1D nanoparticle arrays

Anisotropic arrays of nanoparticles often display very different optical, electrical and magnetic properties to their discrete counterparts, whilst simultaneously showing excellent sensing capabilities. These properties and their current and potential uses are presented below.

1.2.2.1 Optical properties

Optical properties of 1D arrays of metallic particles have been observed both theoretically and experimentally as they exhibit extremely interesting group behaviours. Strong dichroism in the absorption spectrum of linear arrays of silver particles has been observed.[185] Different resonant plasmon wavelengths were recorded depending upon the direction of polarization, either perpendicular or parallel.

Plasmonics is the study of controlling and manipulating the interaction between the free electrons in metals and incident light.[186,187] Within plasmonics, waveguiding is one of the most promising fields of interest. Waveguides are nanostructures of metal that transmit light from one location to another with extreme precision. As waveguiding is possible due to the strong interaction of light with the free electrons in the nanostructure, altering the shape and size of the waveguiding structures is a powerful method of controlling the light and in some cases can effect sub-wavelength manipulation.[188,189]

Though waveguiding is still somewhat in its infancy, silver has attracted the most attention for both computational and experimental study.[190–193] Nanowires of silver have been proven to transmit light over distances of 10 μm,[194] in addition to being capable of directing light through multiple changes of angle and fanning the light out from a single wire to many branches.[195–197] Integration of plasmonic silver with optical polymer waveguides achieves close control over coupling by altering the polarization of the incident light. Quantum dots

can be conjugated with silver nanowires to make simple plasmonic circuits.[198] Silver nanorods have been reported to produce 2D waveguides.[199]

Though interesting, silver nanowires do not fit completely within the remit of this review. Chains of discrete silver nanoparticles show potential in waveguiding applications, though have only more recently been studied. In 2003 the transfer of a plasmon along a closely-spaced chain of silver nanoparticles was measured by Maier *et al*.[200] Though propagation distance was short (several hundred nanometres) the plasmon lost intensity, adding observed experimental evidence to pre-existing theoretical predictions concerning dampening of plasmon transmission along waveguides.[193] Silver nanoparticle chains have shown the ability to propagate light along the array at 10% the speed of light, with speed of transmission dependent upon shape and size of the particles – this offers a facile method of controlling propagation velocity. Gold nanoparticles in anisotropic arrays have been shown to behave in a similar manner.[181,201–203] Additionally, DNA-assembled chains of nanoparticles have great promise in plasmonic applications as the helicity of the DNA introduces chirality into the assembly which could hold potential in nanoscale electrical components.[204,205]

Integration of chains of gold nanoparticles with silicon waveguides has met with good success. Depositing 700 nm chains of gold particles and exciting them through the evanescent field of the silicon substrate showed transfer of a large proportion of the transverse electric mode energy to the resonant gold particles.[206] The system was found to be highly sensitive to changes in the physical environment, showing potential for biological or chemical sensing.

Another group utilised the strong electromagnetic coupling between close-packed gold particles to trigger the formation of sub-radiant plasmons.[207] The loss low associated with this system allowed light to be propagated over several micrometres. This work highlighted

the advantage of disorder in the nanoparticles and opens the gates for nanoscale optoelectronic applications.

1.2.2.2 Magnetic and electrical properties

The electrical properties of aggregations of nanoparticles are not necessarily an extrapolation of the behaviour of the single particle. Braun *et al*. showed that wires of silver nanoparticles showed non-linear electrical behaviour rather than ohmic.[81] The current-voltage curves seen were asymmetric with respect to zero bias, with some dependence on scan directionality. At high resistance (>1013 Ω) a zero current plateau was observed at zero bias. However at higher biases the silver wire became very conductive which has great potential for electrical components, even if the origins of this effect are as yet unclear.

The collective magnetic properties exhibited by metallic nanoparticle arrays can be vastly different to the sum of their parts. Evaporation of a cobalt containing solution onto highly ordered pyrolytic graphite substrates in a strong magnetic field was shown to produce linear arrays of 8 nm nanoparticles.[208] Hysteresis studies showed a significant increase in remnant magnetisation and coercivity of the linear chains of cobalt particles compared to a disordered system of comparable particles (chains of particles 0.60 and 0.14 T respectively, compared to the disordered systems 0.52 and 0.13 T). This was accredited to improved orientation of the magnetic moments in the direction of the applied magnetic field. A perpendicularly applied field resulted in a large drop in remnant magnetisation and coercivity. This was not observed during hysteresis studies of disordered systems of the same cobalt particles. Similar phenomena have been observed in nickel, with chains of nickel particles exhibiting magnetic coercivity two orders of magnitude greater than the bulk metal.[209] Coercivity was shown to decrease with increasing size of the nickel particles.[210] Manganese particles organised into chains and supported on CuN substrates have also been proven to exhibit weak ferromagnetism, compared to the paramagnetism seen in bulk manganese metal.[211]

1D arrays of polyelectrolyte-stabilised magnetite particles have found practical application as a contrast agent in MRI scanning.[212] The magnetic fluid, when injected directly into rats' brains, has given scan results with vastly enhanced detail, allowing more accurate diagnoses. Additionally they have shown superb biocompatibility and are cleared from the body quickly, potentially due to the morphology of the chains allowing easy passage through the blood vessels. This also has potential for detecting irregularities within the circulatory system such as blocked blood vessels.

Quasi-1D rings of magnetic cobalt nanoparticles have recently been shown to have a vortex state in the centre of the system which can be stable at room temperature.[213] If the chirality of the vortex can be controlled and switched easily it has great potential in next-generation, ultradense data storage.[214]

1.2.2.3 Sensing applications

Sensing applications of 1D arrays of nanoparticles is one of the fastest-growing and most applicable fields. Gold nanoparticle surfaces functionalised with peptide molecules have been shown to self-assemble into linear chains when exposed to mercury ions.[215] This spontaneous assembly is marked by a noticeable colour change of the solution from red to blue or purple, depending on the concentration of mercury ions present (Figure 1.18). This was shown to be due to the formation of a new SPR band at 670 nm. This method enables the facile detection of low concentrations Hg^{2+} ions (up to 4 ppm) in water by the naked eye, proving a useful test for heavy metal contamination. Thiourea has been detected in a similar colorimetric assay by utilising the assembly of gold nanoparticles in the presence of sensitising sodium hydrogen sulphate, allowing concentrations of thiourea as low as 15 ppb to be detected with the human eye.[142]

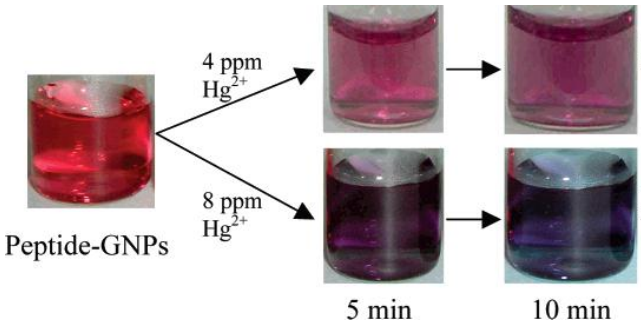

Figure 1.18 Image showing the colour change observed on adding mercury ions to a colloidal suspension of peptide-functionalized gold nanoparticles. Image used with permission from Si *et al*.[171]

Potential nanosensors to detect thiols have been produced by stringing chains of gold nanoparticles between two electrodes.[216] The resistance across the nanoparticle chain was observed to change significantly on the binding of 1-mercapto-6-hexanol, possibly due to the thiol molecules affecting the tunnelling barriers between nanoparticles. Measurements taken in real time using an ampere meter of the thiol binding event show this change in resistance clearly (Figure 1.19). This is a facile sensing method using readily available equipment for detection, thus showing promise for commercialization.

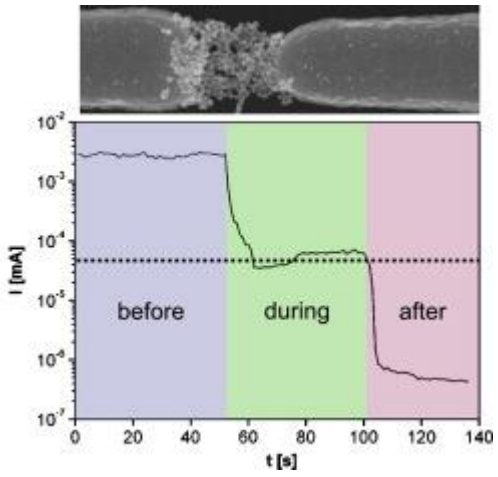

Fig. 1.19 The binding of 1-mercapto-6-hexanol to gold nanoparticle chains measured in real-time. The graph shows the change in resistance when the analyte is added at approx. 50 s. The image

above the graph shows numerous chains of gold particles spanning the gap between the electrodes. Graph with permission from Leiterer *et al*.[216]

A similar measurable drop in resistance has been used to sense gaseous hydrogen utilising palladium nanoparticle chains adsorbed on cyanoacrylate.[217] Exposure to H_2 caused a reversible drop in the resistance of the palladium chains in under 75 ms, attributed to the palladium crystal lattice expanding as dihydrogen molecules are adsorbed. The reversibility of this response credits this system with the potential for producing reusable sensors.

Decoration of existing gas sensors with palladium nanochains has proved an effective strategy to increase the sensitivity of their sensing capabilities. Alignment of palladium nanoparticles along zinc oxide nanorods resulted in a 4-6 fold increase in ability of the system to sense carbon monoxide.[218] Particles of alloyed silver and palladium on carbon fibres have shown the ability to sense hydrogen at concentrations as low as 0.2 % whilst retaining reversibility and offering good stability.[219]

Gaseous organic molecules have been successfully sensed by alkanethiol-capped gold particles.[220] A range of alkene, alkane and alcohol vapours were detected. A range of alkanethiols were used with carbon chain length ranging from 4-11. Longer carbon chain length in the capping agents were associated with heightened sensitivity of response to the gases.

Carbon nanotubes with gold nanoparticles arranged on the outer walls are capable of detecting hydrogen sulphide at notable low concentrations in the region of parts per billion.[122] Gold nanoparticles capped with amino acids have shown similar promise in sensing H_2S.[221] This work yielded detection limits sub-ppm and a response time of *ca.* 20 seconds at room temperature, proving viability for commercialization.

1.2.3 Future challenges

For chains of nanoparticles to realise their potential in commercial applications, control over the interparticle spacing must be achieved. Distance-dependent photonic and electronic transfer is vital in many electronic and photonic devices, sensors and telecommunication applications therefore precise control over the spacing between nanoparticles is essential. 1D arrays of mixed nanoparticles could also be investigated, such as the combination of metallic and semiconducting particles to produce nanoscale diodes.

A fuller understanding of template-free assembly methods is also needed if we are to exercise more control over the preparation, spacing and resultant properties of the chains. There is some debate over whether the model of spherical particles with a monolayer cover of ligands is accurate.[222] This feeds into a separate debate as to the extent to which the removal or rearrangement of stabilising ligands is necessary to create a dipole on the particles to induce self-assembly mechanisms. There is also evidence that points to intermolecular forces between the ligands that make up the monolayer could be at least partially responsible for inducing alignment of particles.[223] Clarifying these issues would lead to a more thorough explanation and understanding of the self-assembly processes behind forming anisotropic arrangements of nanoparticles and therefore allow a more focused and informed push towards commercialization.

The next section of this introduction covers photodynamic therapy, a thriving area of research on the boundaries of chemistry and medicine. Recent advances in the field have started to integrate pre-existing therapies with nanoparticle research to great effect, generating exciting results which are reported below.

1.3 Introduction to photodynamic therapy

The emergent and ongoing epidemic of infections caused by antibiotic resistant strains of common bacteria is a modern day plague on the global healthcare industry. Antibiotic

resistant strains of the bacteria that cause once easily-controlled infections such as tuberculosis and pneumonia,[224] gonhorrea,[225] diarrhoea-causing *C. difficile*[226] and food poisoning pathogens *E. coli*[227] and *Salmonella*[228] are now commonplace. In several European countries methicillin-resistant *Staphylcoccus aureus* (MRSA) accounts for up to 50% of tested *S. aureus* bloodstream isolates (Figure 1.20).[229] We desperately require innovative alternative treatments for when standard antibiotic therapy fails, as is increasingly the case.

One potential treatment to replace or complement antibiotics is photodynamic therapy (PDT). PDT can be used to kill bacteria for effective infection control or somatic cells for cancer therapies.[230]

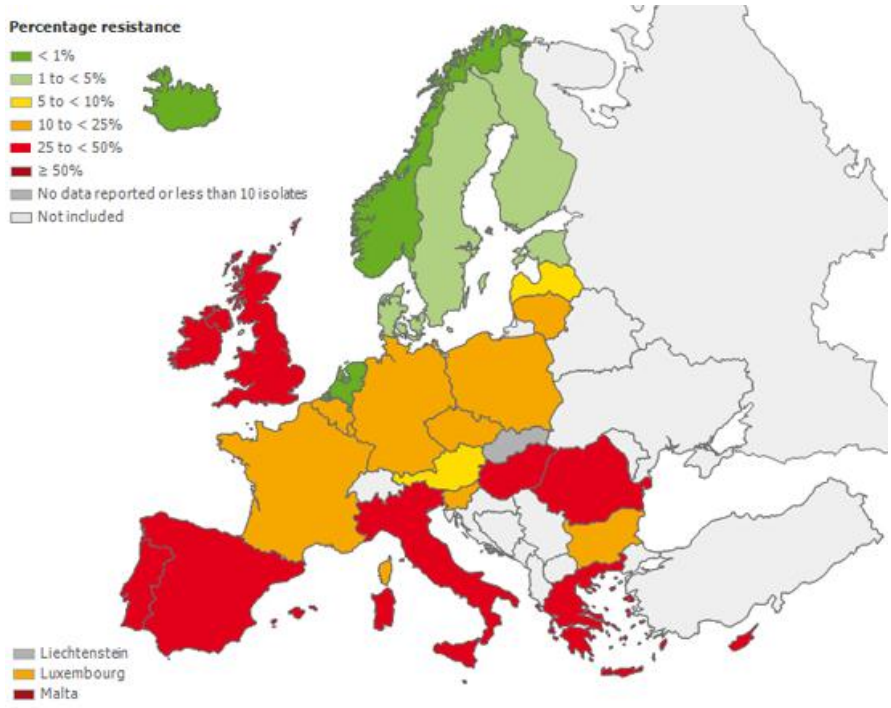

Figure 1.20 Infographic showing the proportion of *S. aureus* bloodstream isolates accounted for by methicillin-resistant species in Europe in 2010. Image with permission from *Antimicrobial resistance surveillance in Europe*, 2010 [229]

1.3.1 History of PDT

Heliotherapy (the therapeutic use of light) is an ancient technique dating back over three thousand years to early Chinese, Indian, Egyptian and Greek civilisations, when it was used in the absence of effective drug therapies to treat a range of diseases such as rickets and vitiligo.[231] Though effective, heliotherapy was somewhat forgotten about until it was introduced into western medicine at the end of the 19th century. Niels Finsen, a Danish physician and scientist, showed that exposure to red wavelengths was an effective treatment to prevent the formation and discharge of pustules associated with smallpox.[232] Cutaneous infection by the TB bacterium (lupus vulgaris; Figure 1.21) was also successfully treated using UV light filtered from the sun, leading to Finsen's being awarded the Nobel prize for Physiology in 1903.[233] Now brought into prominence, many different conditions were reported as being treatable using heliotherapy such as psoriasis, skin ulcers and peritoneal tuberculosis. [231,233] Quartz lamps producing large amounts of UV light allowed more intensive therapy to be applied to various skin conditions and was a popular method of treatment up until the 1940s, when antibiotics began to take precedence.[234]

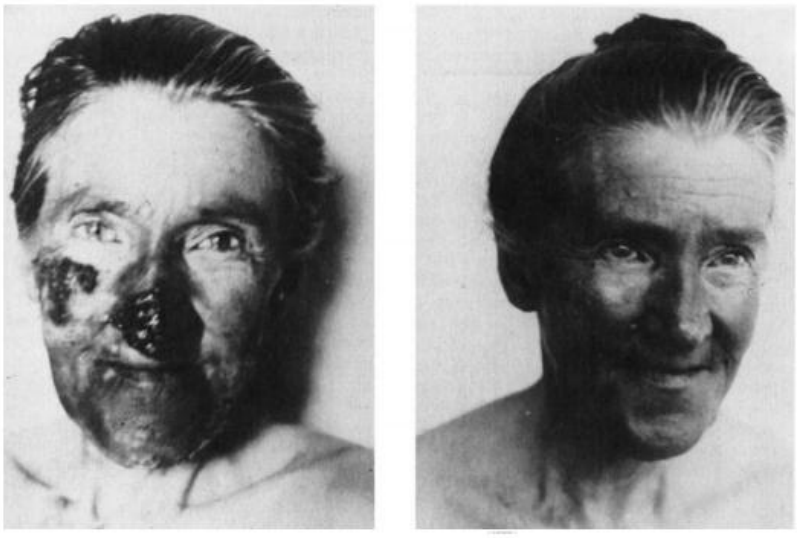

Figure 1.21 Extensive lupus vulgaris cured after 1 year of heliotherapy. Image with permission from Daniell and Hill.[235]

The early years of last century brought the realisation that certain chemicals could, when exposed to light of the right frequency, cause cellular death. Infusoria in the presence of acridine dye were shown to be killed when exposed to certain wavelengths of light.[236] Ingestion of eosine was found to induce dermatitis on skin that was exposed to sunlight,[237] as well as being used topically to treat skin tumours.[238] This singular property was named 'photodynamic action', with the agents that caused it termed 'photosensitizers'. Modern PDT sprang from extensive testing of different photosensitizer-light combinations in these years.

1.3.2 Photosensitizers and the mechanism of PDT

For PDT photosensitizers are typically localised to the target area, tissues or cells. This provides an advantage over traditional surgical and chemotherapeutic techniques, as the pathogens or malignant cells can be targeted and killed with little collateral damage to surrounding tissues. Localisation can be achieved by injection, topical application or by functionalisation with microbe- or cell-recognising moieties.

During the PDT process the photosensitizer is exposed to light of a specific frequency and absorbs a photon, thus is promoted to a high energy triplet state. This excited state transfers energy to molecular oxygen which in turn generates singlet oxygen, a metastable form of the O_2 molecule. Excited singlet oxygen is approximately 1 V more oxidising than the ground state and consequently is much more electrophilic, allowing it to oxidise substrates that are unaffected by oxygen in its lowest energy form.[239] Singlet oxygen will react rapidly with carbon-carbon double bonds, neutral nucleophiles (e.g. amines) and anions. As a consequence of this it is highly cytotoxic, destroying cells by damaging cell walls, membranes and DNA.[240] This process is illustrated in Figure 1.22.

There are various well-studied families of photosensitizers used including phthalocyanines, chlorophyll derivatives, porphyrins and associated macrocycles and dyes.[241] The thiazine family of dyes are also used as photosensitizers and includes methylene blue, azures A, B and

C, toluidine blue and thionin. There have already been many studies which confirm their ability to act as photosensitizers in PDT.[242–244] Methylene blue has been shown to be successful against a range of pathogenic species and tumour cells. Topical application to an MRSA infected wound followed by irradiation with 670 nm light gives a 25-fold reduction in the number of viable MRSA bacteria.[245] Good results have been obtained against *E. coli*[246] and malignant cells.[247] The latter study combines effective *in vivo* kill of tumour cells with very little damage to surrounding healthy tissues by coupling methylene blue to a recognition moiety.

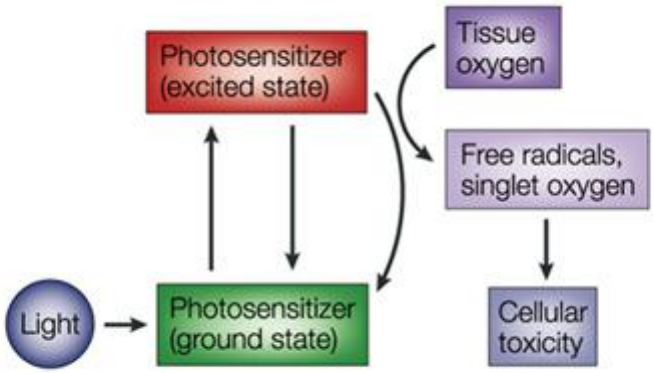

Figure 1.22 Scheme showing the mechanism of photodymanic therapy. Image with permission from Dolmans *et al*.[236]

1.3.3 Oncological applications of PDT

One of the most promising applications for PDT is the *in vivo* targeted treatment of cancers. First reported in 1972 using haematoporphyrin-sensitized glioma cells in rats,[248] fluorescein[249] and acridine[250] were quickly shown to be similarly effective. Clinical trials in humans followed shortly, injecting haematoporphyrin derivative (HpD) into cutaneous or sub-cutaneous tumours and irradiating them with 600-700 nm light.[251] 111 out of 113 lesions showed a complete or partial response to this treatment. Moreover, no tumour type investigated (including carcinomas of the prostate, breast, endometrium and colon;

melanomas; angio- and chondrosarcomas) was found to be unresponsive. This offers an enormous advantage over current chemo- and radiotherapy, which is extremely specialised and must be tailored to specific tumour types. Similar studies have since shown that HpD-mediated PDT is also effective in the treatment of cancers of the lung,[252,253] bladder,[254,255] head and neck[256,257] and glioma.[258,259] Purified HpD in the form of photofrin II has also shown potential.[260–263]

More recently, photodynamic diagnosis (PDD) has been used to obtain early diagnosis of premalignant oral lesions. Topical application of 5-aminolevulinic acid in combination with fluorescence imaging for this purpose was reported in 2006.[264] Precursor lesions to squamous cell carcinoma have been similarly diagnosed.[265] With great sensitivity and almost faultless accuracy, PDD is a vital tool in the early diagnosis of these aggressive and common cancers, allowing the greatest possible chance of successful treatment as well as improved cost effectiveness, monitoring ability, patient tolerance and a low invasiveness compared to traditional diagnosis *via* surgical biopsy.

1.3.4 PDT to treat viruses, bacteria and fungi

Outside the field of oncology PDT is a phenomenally useful technique to combat pathogenic viruses, bacteria and fungi. Methylene blue can be used to kill the herpes (HSV 1) virus by blocking viral DNA replication.[266] The same dye can be used topically under 660 nm laser illumination for relief from herpes lesions.[267] Strikingly, low concentrations of both methylene blue and toluidine blue have both been shown to photoinactivate the HIV-1 virus in blood plasma.[268] It was later shown that inactivation of the virus was due to destruction of the viral RNA.[269] This has real potential for purification of donor blood. A 99% reduction in the virus titre of cells infected by HIV and HSV viruses was also achieved by treatment with 5-aminolevulinic acid and irradiation.[270]

Many common fungal conditions can be addressed using PDT. Ringworm-causing *Trichophyton mentagrophytes* and *Microsporum gypseum* can be killed using methylene blue and illumination with white light.[271] Candiosis, a common recurrent infection in immunocompromised patients, is caused by a species of yeast called *Candida albicans* and is easily killed by topical application of either methylene or toluidine blue followed by illumination with a low-energy laser.[272] Topical applications of methylene blue (concentration 450-500 μg/mL) completely removed *C. albicans* from the oral cavity in mice, showing great promise for treatment of this opportunistic infection without aggressive drugs.[273]

Periodontal disease and other bacterial infections of the mouth have been treated with great success with PDT. Aluminium disulphonated phthalocyanine in conjunction with a GaAs laser has been shown to kill cariogenic bacteria in a convenient clinical time frame (30-90 s).[274] Chlorin e6 has been shown to induce lethal photoinactivation of *P. gingivalis, F. nucleatum* and *C. gingivalis* – three of the leading causes of periodontal disease.[275]

PDT has been used extensively to treat bacterial skin infections. MRSA in particular has been shown to be killed by a variety of photosensitizers. Burn wounds on mice infected with *S. aureus* were successfully treated with porphyrins to reduce the bacterial count.[276] Polyethylenimine-ce6 in conjunction with non-coherent red light accelerated the healing of MRSA-infected abrasions by 8.6 days compared to untreated wounds.[277] Selective killing of MRSA in a mixture with *E. coli* has been achieved by functionalising the photosensitizer with a MRSA-recognising antibody for the specific strain, a treatment which shows potential to treat infections caused by pathogenic species without disturbing the normal microbial ecology of the skin.[278]

For situations where non-specific kill is desirable, methylene blue has proven itself a useful broad-spectrum photosensitizer against a range of common problematic bacteria including those species that cause acne and erythrasma.[279] Kill was induced by exposure to white light,

meaning the cost of the treatment would be minimal. This, the non-specificity of the kill and the improbability of the bacteria to develop resistance to this treatment in the manner of antibiotic resistant pathogens means the technique holds real promise in clinical situations.

1.3.5 Conjugation of photosensitizers with nanoparticles

It has been recently reported that combining a photosensitizer with a nanoparticle to form a conjugate can greatly increase their photosensitizing capacity.[280,281] The toluidine blue-induced lethal photosensitization of *S. aureus* can be increased by an order of magnitude by conjugating the dye with gold nanoparticles.[282] Further work by the same group on this topic showed that conjugation with gold nanoparticles enhanced the UV-visible (UV-vis) absorption of toluidine blue and methylene blue at a 'critical concentration', increasing the extinction coefficient ten-fold compared to a solution of the dye alone.[43] This work is expanded upon in Chapter 3 of this thesis, with novel results being obtained.

It is worth noting that whilst scant literature is available on the subject of silver-dye conjugates, both bulk and colloidal silver show inherent antimicrobial activity in the form of a silver ion release mechanism.[283] Ion release, though temperature and pH dependent, is not reliant upon a photoactivated mechanism so kill of bacteria is seen both light and dark conditions.[284] Thus, combination of silver nanoparticles with photosensitizing dyes is an interesting and relatively unexplored avenue of approach for lethal photosensitization of pathogenic bacterial species.

1.3.6 Photosensitizers for antimicrobial surfaces

One very promising application of the bactericidal ability of photosensitizers is in making functional surfaces.[285] Instead of topical or *in vivo* application of the photosensitizer it is encapsulated within a material and immobilised there. The surface can then be irradiated as in PDT and bacteria which have colonised the surface will be killed *via* the singlet oxygen mechanism outlined in Figure 1.22. Materials which have this capability have great potential

in medical applications, as a large number of hospital acquired infections (HAIs) are transmitted by touch after contact with heavily contaminated, frequently touched 'reservoir' surfaces such as bed rails, door handles and telephones.[286,287] HAIs are estimated to affect more than 1 in 10 hospital patients and over half all hospitalization complications.[288] These preventable infections are a huge drain on health care resources worldwide, costing an estimated £1 billion per year in the UK alone.[289] Thus if these reservoir surfaces in hospitals could be fabricated from functional, antimicrobial materials the overall number of viable bacteria on them could be significantly reduced and transmission rates lessened. This presents an elegant scheme to reduce the number of HAIs and reduce associated cost, benefitting patients and healthcare system.

A number of different surfaces such as glass[290] and titania[291] have been investigated for the application of functional antimicrobial surfaces, but polymers have emerged as by far the most popular due to their flexibility, ease of modification, low cost and durability.[292] Different polymers have been trialled, including silicone,[293,294] cellulose acetate,[295,296] resins[297] and polyurethane.[298–300] Combinations of these polymers with different photosensitising dyes – particularly from the triarylmethyl and phenothiazine groups – showed good general photobactericidal effect against both gram positive and gram negative organisms, though broadly speaking better and quicker kill rates were observed against the former. Activation of the photobactericidal effects of the photosensitizer-modified polymers can either be by laser[301] or a non-specific white light source.[298] Though laser illumination tends to induce quicker kill rates it is also more expensive and requires specialist equipment, therefore it is advantageous if the modified polymers exhibit good antimicrobial activity under a standard white light source to minimise the cost and expertise required.

Additional essential criteria for these functional surfaces to fulfil include high durability, resistant to leaching under routine cleaning/washing conditions and benign to both humans

and the environment. Non-toxicity towards humans can be achieved either by choosing photosensitizers which are known to be safe or by ensuring the photosensitizer is sufficiently well contained within the polymer that it cannot leach out. Several methods of incorporating dyes into polymers have been reported. Simple covalent attachment to the surface can be used but can be hard to achieve as polymers used in medical settings tend to be reasonably inert. Another easy method is to use a swell-encapsulation-shrink method to allow dye molecules to be held within the bulk polymer rather than sitting on the surface.[298] This method uses a solvent to swell the polymer in the presence of the desired dye molecule. The dye molecules can diffuse into the polymer matrix under these conditions and move into the bulk. Upon removal from the swelling solution the solvent evaporates and the polymer shrinks back to its original size, trapping the dye molecules within. In this way the dye molecules are immobilised within the polymer framework and are resistant to leaching under aqueous conditions, an important property if the antimicrobial polymers are to be both long lasting and non-toxic to humans.

Though toxicity of the chosen photosensitizer should be carefully considered, it has been shown that the concentrations of photosensitizers and illumination times which exhibit excellent bacterial cytotoxicity do not possess sufficient power to damage larger mammalian cells.[302,303] The high vulnerability of bacterial cells to lethal photosensitization allowed surfaces to be fabricated that not only kill bacteria on the polymer itself but also up to 0.65 mm away from it, a huge distance in the nanoworld.[304] This protective 'aura' provided by antimicrobial surfaces shows excellent potential in medical applications by providing a potent barrier to biofilm formation.

1.3.6.1 Photosensitizer-nanoparticle conjugates for antimicrobial surfaces

As discussed in Section 1.3.5, the efficiency of a photosensitizer in solution can be increased by combining it with a nanomaterial, particularly a nanoparticle. Similar phenomena have

been recorded in polymer-encapsulated systems. Methylene blue has been shown to exhibit enhanced bacterial kill rates when combined with gold nanoparticles in silicone, compared to methylene blue-modified silicone only. [298,305,306] Great specificity was seen as to the size of the nanoparticles incorporated into the system – gold particles over 20 nm in diameter decreased the photobactericidal kill rates whereas very small particles (~2 nm) increased activity significantly, increasing the kill of gram negative *E. coli* by a factor of 1log10 and reducing numbers of gram positive *S. epidermis* to below the detection limit, corresponding to a 99.99% kill.[305]. Silicone samples containing the same ~2 nm gold particles did not show any antimicrobial ability, thus the enhanced kill rates seen on the addition of these particles to methylene blue was thought to be due to a cooperative effect between the particle and the dye. Similar studies have shown that the number of viable *S. epidermis* colonies can be reduced by half using silicone modified with methylene blue and gold nanoparticles when the surface is illuminated by a laser for 10 minutes per hour.[307]

Metal oxide nanoparticles have also shown good antimicrobial ability when combined with crystal violet. Semiconducting zinc oxide particles, fabricated from the thermal decomposition of a metal-oleate precursor, were incorporated into medical grade polyurethane sheets along with crystal violet.[308] The resultant modified polymer showed excellent bactericidal activity against both gram positive and negative organisms, exhibiting complete kill of *S. aureus* in 1 hour and a 2.5 log10 reduction of *E. coli* counts in 2 hours. Interestingly the crystal violet-zinc oxide nanoparticle system also had a potent dark kill effect, achieving 99.9% kill against *E. coli* in 4 hours and *S. aureus* in 2 hours when incubated in dark conditions. The ability to destroy bacteria under a non-specialised white light source combined with good dark kill ability make this system very promising for medical applications.

The conjugation of photosensitizers with nanoparticles is, then, an exciting topic with much scope to provide real benefit in many healthcare settings. Chapter 4 of this thesis is dedicated to results gained from the conjugation of both silver and gold nanoparticles with a range of dyes to excellent effect, producing antimicrobial polymers with potent light and dark kill.

The next chapter of this thesis exemplifies the techniques used to synthesize a range of gold and silver nanoparticles to be used in the later chapters' investigations.

CHAPTER 2 : THE SYNTHESIS AND CHARACTERIZATION OF GOLD AND SILVER NANOPARTICLES

2.1 Aims

In this chapter we aimed to synthesise a range of gold, silver and bimetallic nanoparticles. Particles were fabricated *via* a variety of synthetic routes and using a number of different capping agents to produce particles with different compositions and shapes. The properties and behaviour of metallic nanoparticles varies greatly according to shape, size, composition and capping ligand, thus the ability to control the morphology of particles is paramount in the quest for tuneable behaviour. We present the synthesis of pure silver, pure gold and silver-gold bimetallic citrate-stabilised spherical particles using a modified Turkevich (citrate reduction) method. The synthesis of 2-mercaptopropionylglycine-capped silver particles is also presented. These particles were subsequently caused to self-arrange into long, high aspect ratio chains *via* a sonication treatment. Anisotropic gold nanorods were also synthesised using a seeding method, producing particles with a defined aspect ratio. Multi-branched gold nanocrystals were made by reduction of auric acid by a 2-[4-(2-hydroxyethyl)-1-piperazinyl]ethane-sulfonic acid (HEPES) buffer solution, forming 'nanourchins' under very mild reaction conditions. Particles were studied by UV-vis spectroscopy to obtain the SPR for each type. TEM was also used to provide visual confirmation of unique morphologies.

2.2 Introduction to the synthesis and properties of noble metal nanoparticles

Synthetic routes to noble metal nanoparticles have been widely reported since the fifties. The fascinating properties of nanoparticles make them the focus of intense study in both chemical and physical fields as they have many uses in commercial, medical and technological applications.[20,72,309] One of the most interesting things about nanoparticles is the size, shape

and dielectric medium-dependence of their properties; that is, altering the morphology of a particle or its capping agent can have notable effects on its optical, electrical and magnetic behaviour, a phenomenon discussed more fully in Section1.1.[12,30,48,50] This level of achievable tuneability can be vital in engineering novel nanoparticles for new applications. The method of synthesis of a nanoparticle, be it bottom-up or top-down, and selection of the capping agent are crucial to producing the different shapes, sizes and properties desired.

As already noted in Section 1.1.2, bottom-up methods of nanoparticle synthesis dominate the literature, not only due to their ease and flexibility but also as they do not require the specialist instrumentation needed for top-down approaches and consequently tend to be much cheaper. Most bottom-up techniques use a reducing agent such as sodium borohydride or citric acid to reduce gold or silver ions in solution, resulting in particles of the neutral metal forming. Capping molecules are usually used in the reaction mixture to aid monodispersity and stabilise the particles, which have a high surface energy, from precipitating out of solution.[310,311]

Great control over size, shape and properties of nanoparticles can be achieved by altering reaction parameters. Though susceptible to variation in each batch, control of reaction time, choice of reducing agent or method, temperature and selection of capping molecule can all dictate the morphology of the resultant particles.[17,46,312] A wide variety of particle shapes such as stars, cubes, triangles, wires and tubes have been produced in addition to regular nanospheres.[30,33,34,44,313]

The work in this chapter uses some common bottom-up synthesis techniques, successfully synthesising a range of gold, silver and bimetallic particles of different shapes and sizes for use in further investigations. We report the successful synthesis of citrate-stabilised gold and silver nanoparticles using a Turkevich-style citrate reduction method (discussed in Section 1.1.2.1), producing excellent, well-formed particles. Bimetallic particles of gold and silver

were produced using analogous methods. Tiopronin-capped silver nanoparticles were also generated using a Brust synthesis, utilising sodium borohydride as a reducing agent to give regular, spherical particles of small size. These particles were then used to fabricate high aspect ratio arrays of discrete particles by a sonication step. Gold nanorods were synthesised using a seed-mediated growth mechanism (seeding methods are reported on in Section 1.1.2.2), producing particles with defined quadrilateral shape with a range of aspect ratios.

Branched gold nanocrystals were also successfully produced using a HEPES buffer solution to reduce aqueous auric acid to produce branched nanocrystals of crystalline gold. By contrast with the spherical or anisotropic particles described above, branched nanocrystals are comparatively poorly covered in literature owing to the difficulties in generating branched structures from highly symmetrical, face-centred cubic noble metals by a homogenous nucleation and growth process. Several methods for producing branched or asymmetric nanostructures by seeding methods have been reported,[314–319] though all required multistep seeding procedures and/or the use of polymers and surfactants to induce directional growth. Such molecules can be difficult to remove from the surface of the nanoparticles without harsh reaction conditions which can also damage the desired nanocrystals. The method used herein was adapted from Lee *et al*. and is both seedless and surfactantless, utilising a 2-[4-(2-hydroxyethyl)-1-piperazinyl]ethane-sulfonic acid (HEPES) buffer to reduce an aqueous solution of auric acid to produce branched gold nanocrystals.[320] HEPES contains a piperazine ring (Figure 2.1) which is capable of producing nitrogen-centred free radicals, which in turn are capable of reducing the $AuCl_4^-$ ions in aqueous auric acid. HEPES also preferentially adsorbs on the {100} face of gold, thus directs growth along the {111} plane and results in multiple branches forming.

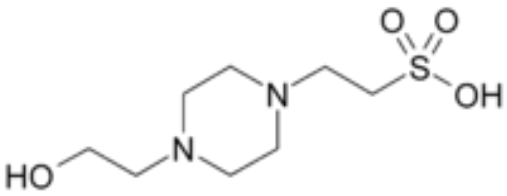

Figure 2.1 The structure of 2-[4-(2-hydroxyethyl)-1-piperazinyl]ethane-sulfonic acid (HEPES) showing the piperazine ring.

All particles synthesised in this chapter were studied using UV-vis to obtain the SPR band value for each sample. SPR (discussed in detail Section 1.1.1) is a useful diagnostic tool when synthesising colloids as different metals exhibit characteristic colours which are variable with size. The shape, size and monodispersity of the particles were observed using transmission electron microscopy (TEM).

2.3 Experimental methods

All water used was deionised (resistivity ≥ 15 MΩ cm). All glassware was washed with aqua regia before use, then rinsed with copious quantities of deionised water and air dried.

2.3.1 Modified Turkevich synthesis of gold and silver nanoparticles

Stock solutions were made up as follows:

Solution 1: $HAuCl_4.3H_2O$ (170 mg, 0.445 mmol) was dissolved in deionised water (100 mL) giving a ~4.5 mM solution. Solution was a clear bright yellow.

Solution 2: $AgNO_3$ (85 mg, 0.500 mmol) was dissolved in deionised water (100 mL) giving a ~5 mM solution. Solution was colourless.

Solution 3: $Na_3C_6H_5O_7.2H_2O$ (250 mg, 0.969 mmol) was dissolved in deionised water (50 mL) giving a ~20 mM solution. Solution was colourless.

2.3.1.1 Synthesis of citrate-stabilised gold nanoparticles

Solution 1 (2 mL) was diluted in deionised water (16 mL). The pale yellow solution was heated in a mantle and boiled for 2 min. *Solution 3* (2 mL) was added dropwise over 45-60 s. Solution was boiled for 1 min, during which time a rapid colour change from colourless to grey to pinkish red to deep crimson was observed. Solutions were allowed to cool.

2.3.1.2 Synthesis of citrate-stabilised silver nanoparticles

Solution 2 (2 mL) was diluted in deionised water (16 mL). The colourless mixture was brought to reflux. *Solution 3* (2 mL) was added dropwise over 45-60 s. The mixture was refluxed for 30 min, during which time a gradual colour change from colourless to slightly cloudy, greyish yellow was observed. Solutions were allowed to cool.

2.3.1.3 Synthesis of citrate-stabilised silver-gold nanoparticles

Three different ratios of 5 mM $HAuCl_4.3H_2O$ (*solution 1*) to 5 mM $AgNO_3$ (*solution 2*) were used:

i. 0.5 mL *solution* 1 and 1.5 mL *solution 2*; gold to silver ratio of 1:3
ii. 1 mL *solution* 1 and 1 mL *solution 2*; gold to silver ratio of 1:1
iii. 1.5 mL *solution* 1 and 0.5 mL *solution 2*; gold to silver ratio of 3:1

Each ratio used an analogous method. The example given is for (ii) 1:1. The results of (i) - (iii) are summarised in Table 1.

Solutions 1 (1 mL) *2* (1 mL) were dissolved in deionised water (16 mL). The pale yellow solution was brought to the boil. *Solution 3* (2 mL) was injected and the mixture boiled for a further 2 minutes. A colour change from pale yellow to grey to a purplish red was observed.

Table 2.1 the ratios of gold to silver used to make citrate-stabilised silver-gold particles and the colour of the resultant solution of nanoparticles

Sample	Vol. *solution 1* (mL)	Vol. *solution 2* (mL)	Ratio gold : silver	Colour of solution
(i)	0.5	1.5	1:3	Peach

(ii)	1	1	1:1	Red/purple
(iii)	1.5	0.5	3:1	Lilac

2.3.2 Synthesis of 2-mercaptopropionylglycine-capped silver nanoparticles and fabrication of 1D chains

2.3.2.1 Synthesis of 2-mercaptopropionylglycine-capped silver nanoparticles

Silver nitrate (0.5092 g, 3.00 mmol) and of 2-mercaptopropionylglycine (0.9499 g, 5.82 mmol) were dissolved in deionised water (25 ml and 10 ml respectively). The two solutions were cooled separately to below 5 °C before being combined to give a cloudy yellow solution. Sodium borohydride (0.2563 g, 6.78 mmol) was dissolved in deionised water (10 ml) and added dropwise to the yellow solution over ~5min with vigorous stirring. The temperature was kept below 5 °C throughout this addition. A colour change from yellow to orange to a dark red-brown was observed. This solution was allowed to come to room temperature.

Methanol (*ca.* 100 mL) was added to precipitate the particles. The reddish brown suspension was filtered under vacuum and the particles collected on a Millipore 0.45 µm membrane filter. The dark brown cake of isolate was washed sequentially with methanol, ethanol and acetone before being allowed to dry in air.

2.3.2.2 Synthesis of high-aspect ratio 2-mercaptopropionylglycine-capped silver nanoparticle chains

To make the silver nanoparticle chains the dried tiopronin capped silver nanoparticles were added to deionised water at a concentration of 0.5 mg/mL. The flask was sonicated for 2 hours in an ultrasonic bath to produce the silver nanoparticle assemblies in solution. The solution was a dark amber colour.

2.3.3Synthesis of gold nanorods using seed and growth solutions

2.3.3.1 Stock solutions

Stock solutions were made up as follows:

Solution A: $HAuCl_4.3H_2O$ (0.5 mL of a 5 mM solution) was dissolved in 4.5 mL deionised water to give a 0.5 mM solution

Solution B: $(C_{16}H_{33})N(CH_3)_3Br$ (cetyltrimethylammonium bromide [CTAB]; 0.7337 g) was dissolved in deionised water (10 mL) to give a 0.2 M solution.

Solution C: $NaBH_4$ (0.0039 g) was dissolved in deionised water (10 mL) to give a 0.01 M solution.

Solution D: $AgNO_3$ (0.0068 g) was dissolved in deionised water (10 mL) to give a 0.004 M solution.

Solution E: $HAuCl_4.3H_2O$ (1 mL of a 5 mM solution) was dissolved in 4 mL deionised water to give a 1 mM solution

Solution F: Ascorbic acid (0.1377 g) was dissolved in deionised water (10 mL) to give a 0.0788 M solution.

2.3.3.2 Synthesis of gold nanorods

Seed solution: *Solution A* (5 mL) was added to *Solution B* (5 mL) and stirred for 15 min. *Solution C* was cooled in ice. *Solution C* (0.6 mL, 3 °C) was added to the CTAB/gold solution with vigorous stirring. A colour change from milky yellow to opaque brown was observed. The solution was stirred and heated to 50 °C in a water bath to promote dissolution of CTAB. Once fully dissolved (~5 min) the solution was removed from the water bath.

Growth solution*: Solution E* (0.2 mL) was added to *Solution B* (5 mL). *Solution F* (5 mL) was added and a colour change from colourless to yellow-amber was observed on gentle mixing.

Solution F (70 µL) was added to the mixture. A colour change from yellow to colourless was observed.

Synthesis of nanorods: 20 µL seed solution was added to the growth solution. This mixture was incubated at 30 °C. A colour change from colourless to smoky grey was observed after ~5 min and to dark blue after 1 h. Incubation overnight resulted in dark indigo solutions that were removed from the water bath and allowed to come to room temperature.

2.3.4 Synthesis of branched gold nanocrystals

A buffer solution of 2-[4-(2-hydroxyethyl)-1-piperazinyl]ethane-sulfonic acid (HEPES) was made up by dissolving 0.4747 g HEPES in deionised water (20 mL). The pH of this was adjusted to 7.4 ± 0.1 using 1 M NaOH. 2 mL of the buffer was dissolved in deionised water (3 mL) and 20 mM $HAuCl_4.3H_20$ (50 µL) was added. This mixture was agitated and left to stand at room temperature for 1 h. A colour change from clear, extremely faint yellow to blue-purple was observed.

2.3.5 Characterization techniques

2.3.5.1 TEM

Samples of the particles were prepared by evaporating drops of the nanoparticle solution onto carbon coated copper grids and allowing them to air dry in a dust-free environment. A Jeol 200 kV microscope was used to obtain images of all particles other than as-prepared 2-mercaptopropionylglycine-capped silver nanoparticles, for which a Jeol-1010 microscope at 80 kV was used.

2.3.5.2 UV-vis absorption measurements

UV-vis absorption spectra were recorded using a Shimadzu UV-1800 Spectrophotometer. Plastic cuvettes with a light path length of 10 mm were used. Absorption was measured over the spectral range 200 – 1000 nm.

2.4 Results and discussion

2.4.1 Modified Turkevich synthesis of noble metal nanoparticles

2.4.1.1 Citrate-stabilised gold nanoparticles

Synthesis of gold nanoparticles using the citrate reduction method outlined above resulted in ruby red, clear solutions forming. UV-vis studies of these showed a single, clear absorption in the visible range at 527 nm (Figure 2.2), typical for gold colloids formed by this method.[28] TEM studies of the same particles showed well-formed, spherical particles arranged singly or in small groups (Figure 2.3). Average particle diameter was found to be 11 nm.

The synthesis was very robust and repeatable with little variation in colour observed for each experimental run. Solutions were stable for long periods of time (> 2 years) with no change in colour or transparency.

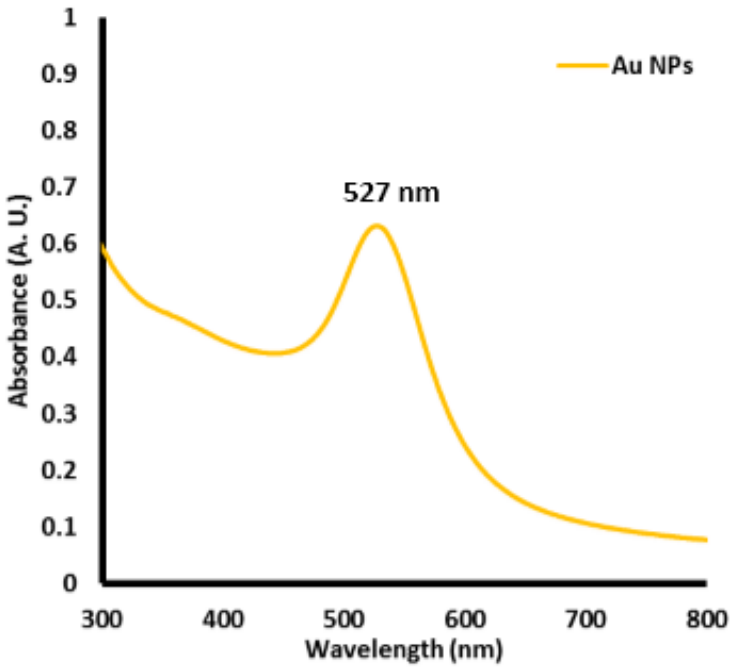

Figure 2.2 UV-vis spectrum of gold nanoparticles made using the Turkevich citrate reduction method.

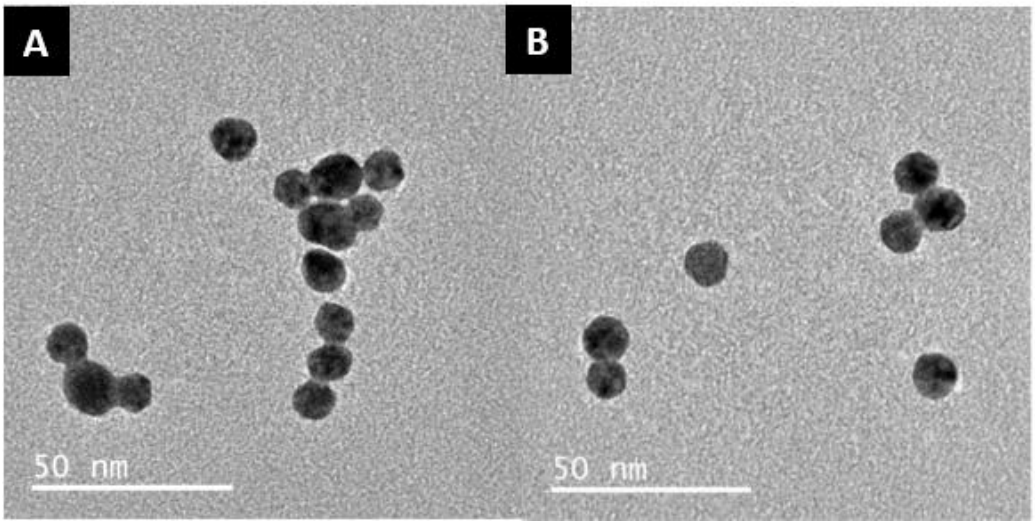

Figure 2.3 TEM images showing gold nanoparticles synthesised by the Turkevich method

2.4.1.2 Citrate-stabilised silver nanoparticles

Synthesis of silver nanoparticles using the citrate reduction method gave pale yellow solutions that were occasionally greyish and slightly turbid, mostly likely a consequence of partial oxidation of the surface of the silver particles. UV-vis studies of these showed a single absorption in the visible range at ~402 nm (Figure 2.4), though the peak was somewhat broader than the sharp absorption seen for the gold particles synthesised in the same way. This is indicative of a less tightly arranged distribution of particle sizes and could also be due to the extra scattering caused by the slight turbidity of the silver colloids compared to the gold. TEM studies of the silver particles showed particles that were predominantly spherical with some ellipsoidal entities. Some less regular shapes were also observed (Figure 2.5). A greater range of particle sizes was observed than in the gold samples, spanning the range 5-40 nm. The increased range of particle sizes, less regular shape and larger average size of the silver crystallites formed by this method as opposed to analogous gold experiments is documented in literature.[37] Average particle size could not be accurately calculated due to the irregular morphology of the silver nanoparticles.

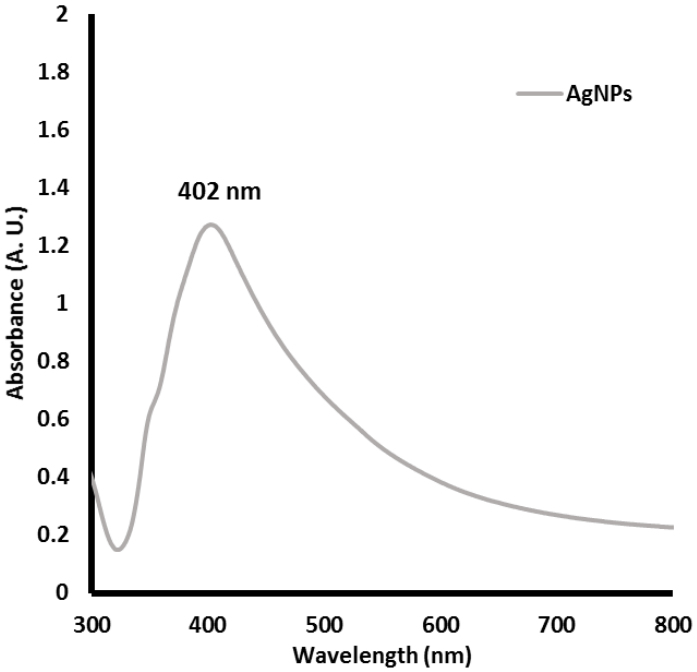

Figure 2.4 UV-vis spectrum of silver nanoparticles synthesised by the Turkevich citrate reduction method

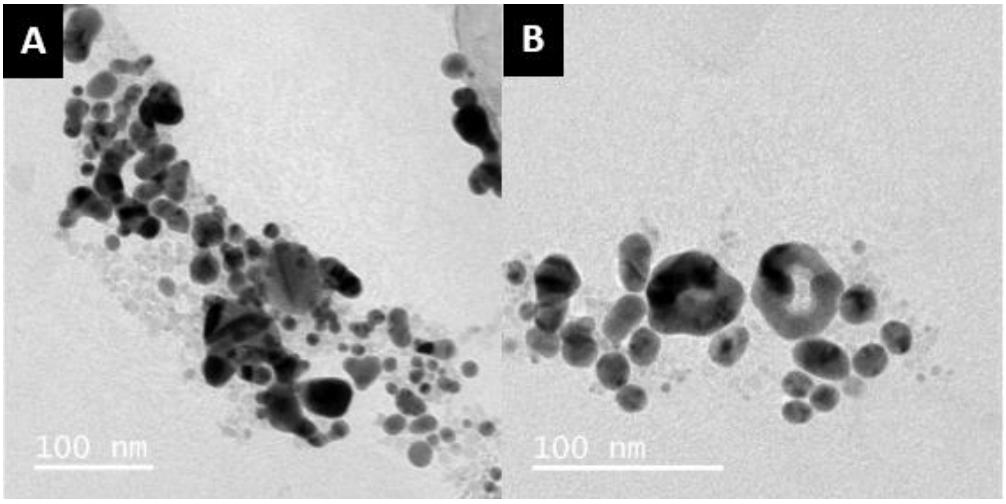

Figure 2.5 TEM images showing silver nanoparticles synthesised by the Turkevich method. Irregularities are seen in particle size and morphology.

2.4.1.3 Citrate-stabilised bimetallic silver-gold nanoparticles

Particles of silver and gold were synthesised using the citrate reduction method. Three different ratios of silver to gold stock were used, as summarised in Table 2.1. All samples of all molar ratios of gold and silver gave one absorption in the visible range of the UV-vis

spectrum, indicative of a gold-silver hybrid particle forming rather than two separate particles of pure gold and pure silver, which would give rise to a double peaked spectrum. Colours of the colloids ranged from dark yellow (Ag only) through peach (1:3 Au:Ag), red-purple (1:1 Ag:Au), lilac (3:1 Au:Ag) to red (Au only). This can be seen in Figure 2.6. It should be noted that these solutions were of the modal colour and that repeats at the same molar ratios exhibited variation in hue. Bimetallic samples were less stable than pure silver or pure gold synthesised in the same manner and fell out of solution after ~24-48 hrs.

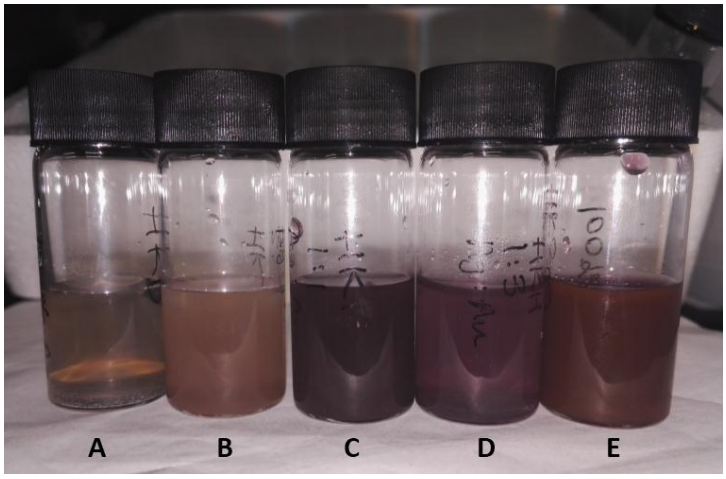

Figure 2.6 Photograph showing the progression in colour as molar ratio of gold to silver changes in solutions of citrate-stabilised gold-silver nanoparticles. A = pure silver, B = 1:3 Au:Ag, C = 1:1 Au:Ag, D = 3:1 Au:Ag, E = pure gold.

UV-vis absorption spectra of all silver-gold particles gave single absorption in the UV-vis. The location of the maximum of this point varied with each run. As such, a mathematical average of all samples of each molar ration was calculated to give a more representative view. The spectra of these are shown in Figure 2.7. The SPR maxima vary with changing molar ratios of gold to silver, though not in a linear way: 3:1 Au:Ag particles had an average SPR band located at 531 nm, .1:1 Au:Ag at 534 nm and 1:3 Au:Ag at 526 nm. The SPR peaks are tabulated in Table 2.2 and also marked on Figure 2.7. Absorptions for 3:1 and 1:3 Au:Ag particles were reasonably sharp, whereas the absorption for 1:1 Au:Ag particles was broader and less symmetrical.

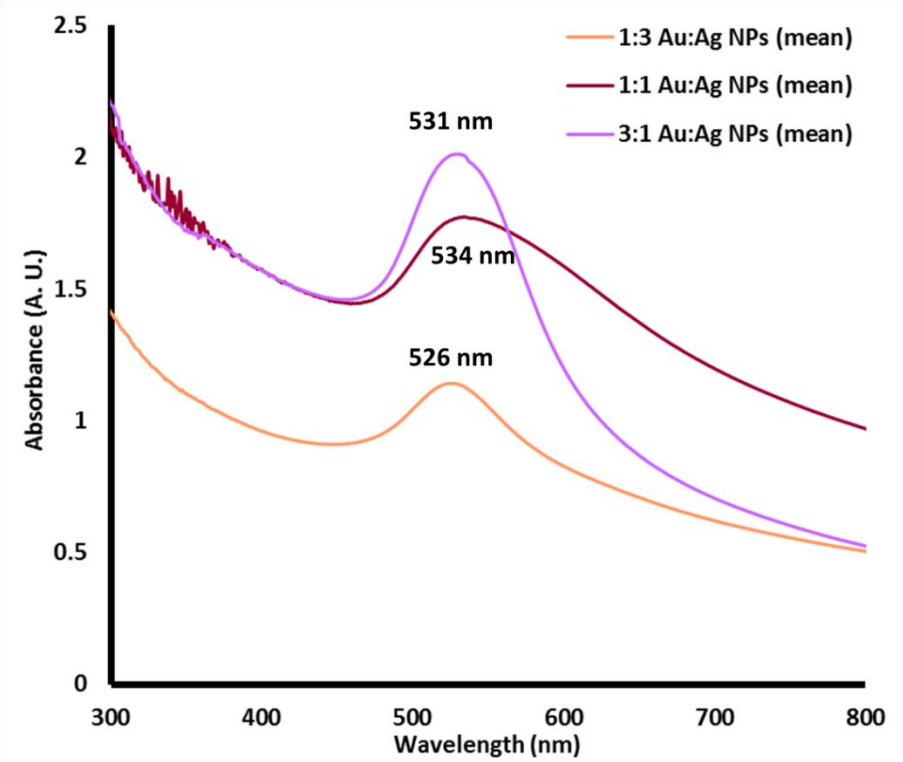

Figure 2.7 UV-vis absorption spectra showing the mean spectra of silver-gold nanoparticles synthesised *via* the citrate reduction method. Particles had molar ratios of 1:3, 1:1 and 3:1 gold:silver.

Table 2.2 Table showing the colour and the average location of the SPR peak for alloyed particles of different gold to silver molar ratios.

Sample	Molar ratio gold : silver	Colour of solution	Average SPR peak maximum (nm)
Pure Ag	0:1	Yellow	402
1:3 Au:Ag	1:3	Peach	531
1:1 Au:Ag	1:1	Red/purple	534
3:1 Au:Ag	3:1	Lilac	526
Pure Au	1:0	Red	527

It has been reported in the literature that if bimetallic Au-Ag particles form alloys the relationship between the SPR band and the changing Au:Ag ratio is linear.[321] Alloys of gold and silver can form favourably with little surface segregation as they have the same face-centred cubic packing structure and very similar lattice constants of ~4.088 Å (silver) and

4.073 Å (gold), thus minimising lattice strain.[30] It has also been shown that core-shell particles exhibit a non-linear, but progressive, relationship as the Au:Ag content changes.[322] The particles in this experiment exhibit neither type of behaviour, as is shown in Figure 2.8. Position of the average SPR red shifts dramatically from the pure silver position (402 nm) at even low gold content, then fluctuates as gold content continues to increase. SPR bands for all gold to silver ratios were above that of the pure gold samples (527 nm) with the exception of 3:1 Au:Ag particles, which had a maximum at 526 nm. No predictable relationship between molar ratio of gold to silver and average SPR was observed. Failure of the SPR to behave either linearly or predictably non-linearly suggests a structure which is neither core-shell nor a true, homogenous alloy. It is possible that particles formed with a core shell structure whereby both core and shell are alloys of gold and silver, but rich in one or the other. A visualisation of this is shown in Figure 2.9. If this is true, differing levels of silver or gold in the core or shell of the particles could explain the fluctuations observed in SPR maxima for each molar ratio. Alternatively it is possibly that no core-shell structure exists but that different regions of gold- or silver-rich alloy make up the particles randomly, giving a different 'patchwork' effect with each and explaining the unsystematic SPR results. It is possible that very high resolution XRD could be used to resolve this issue. High resolution XRD has been successfully used in other cases to prove the existence of homogenous gold-silver alloys in nanoparticles so its use in this instance could prove useful,[323] however the isolation of particles as a powder would be necessary and these samples were of insufficient concentrations to achieve this.

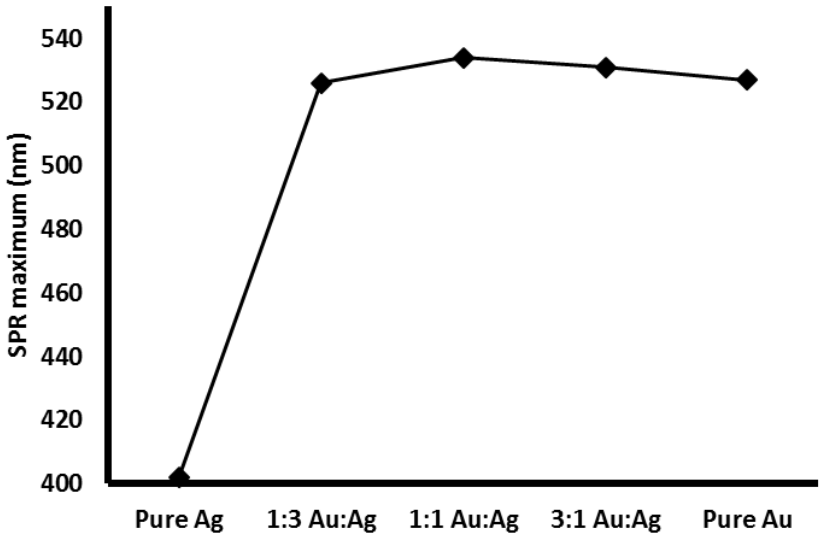

Figure 2.8 Graph showing the change in position of the SPR maximum as molar ratio of gold to silver increases.

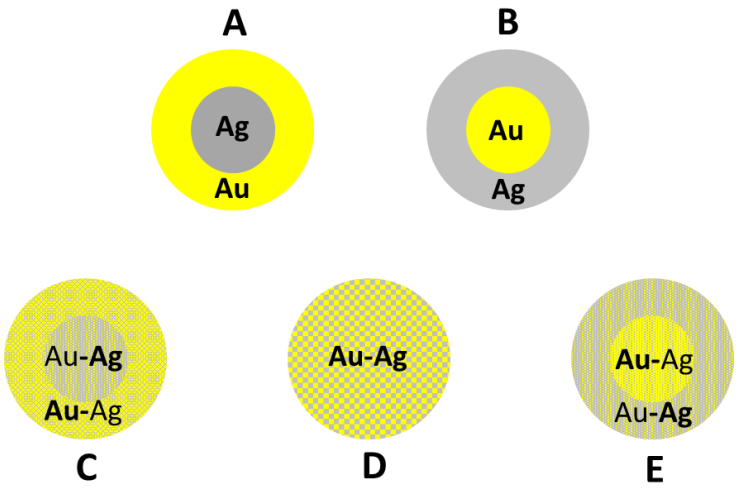

Figure 2.9 Illustration showing different types of gold-silver particles that can form. A: silver core, gold shell; B: gold core, silver shell; C: silver-rich alloy core, gold-rich alloy shell; D: alloyed; E: gold-rich alloy core, silver-rich alloy shell.

TEM analysis of 1:3 Au:Ag particles showed a range of particles sizes and shapes (Figure 2.10). The average diameter of discrete particles was found to be 10.5 nm, though particles from 2 nm to 30 nm were observed (Figure 2.10A and B). Regions of densely packed particles and larger, cloudy agglomerations were observed (Figure 2.10C). Discrete particles were observed to be of crystalline metal as lattice planes were seen under high magnification

(Figure 2.10D), though not to be single crystals - grain boundaries were seen. This suggests different regions of growth, probably as a result of the mix of metals used in synthesis, and supports the assertion that a patchwork of silver- or gold-rich alloys makes up the particles synthesised in this manner. Images of 1:1 Au:Ag particles reveal similar patterns: a range of particles with irregular sizes and shapes (Figure 2.11 A and B) exhibiting regions of both discrete particles and large agglomerations of particles and less well-formed cloudy matter extending over several micrometres (Figure 2.11C). Particles were again found to be crystalline under high magnifications, showing areas of differently-orientated lattice planes indicative of aggregated crystallites. Average particle size was 10.1 nm with a size range of 2-35 nm, showing little difference to the 1:3 Au:Ag particles. 3:1 Au:Ag particles yielded very similar results (Figure 2.12) though particle size was found to be somewhat smaller, showing a range from 2-15 nm and an average diameter of 8 nm. Particles were also observed to be more regular in shape, likely a consequence of the increased gold content in the reaction mixture as silver particles synthesised by a citrate reduction tend to be larger and less regular than gold.[324]

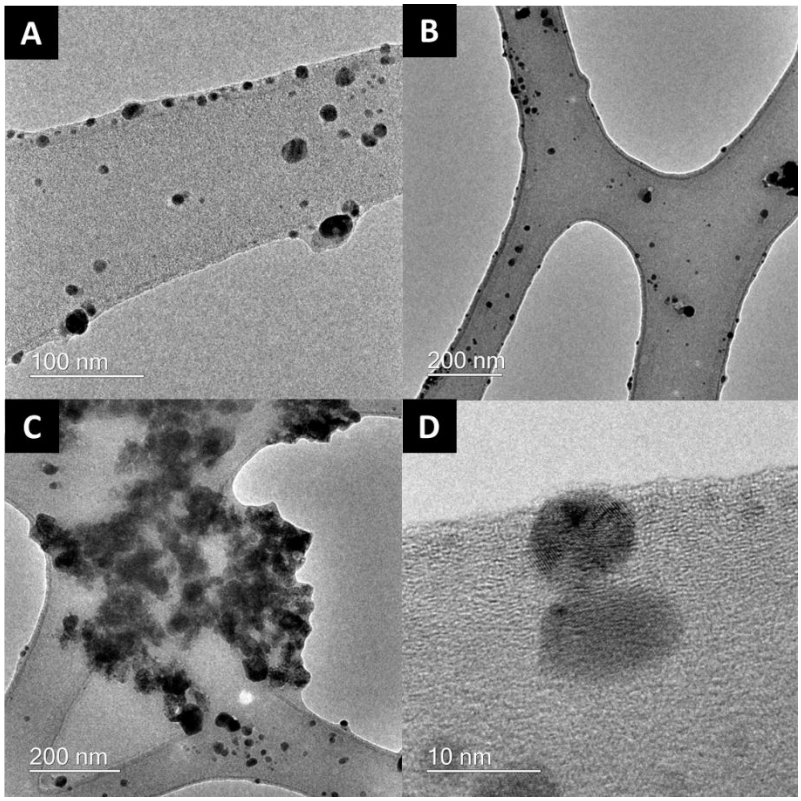

Figure 2.10 TEM images showing bimetallic silver-gold particles synthesised using a molar ratio of 1:3 Au:Ag

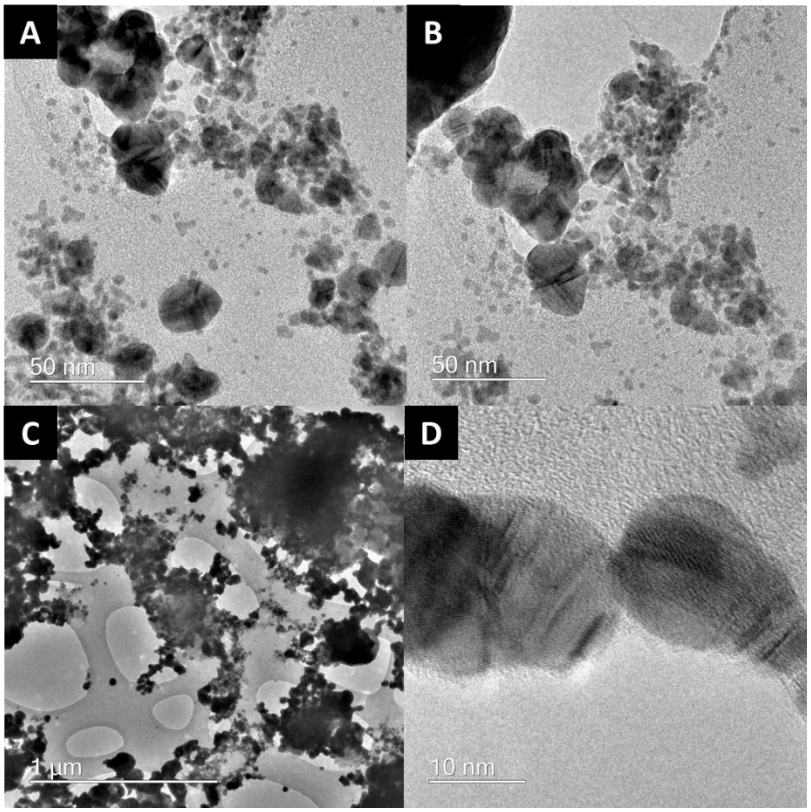

Figure 2.11 TEM images showing bimetallic silver-gold particles synthesised using a molar ratio of 1:1 Au:Ag

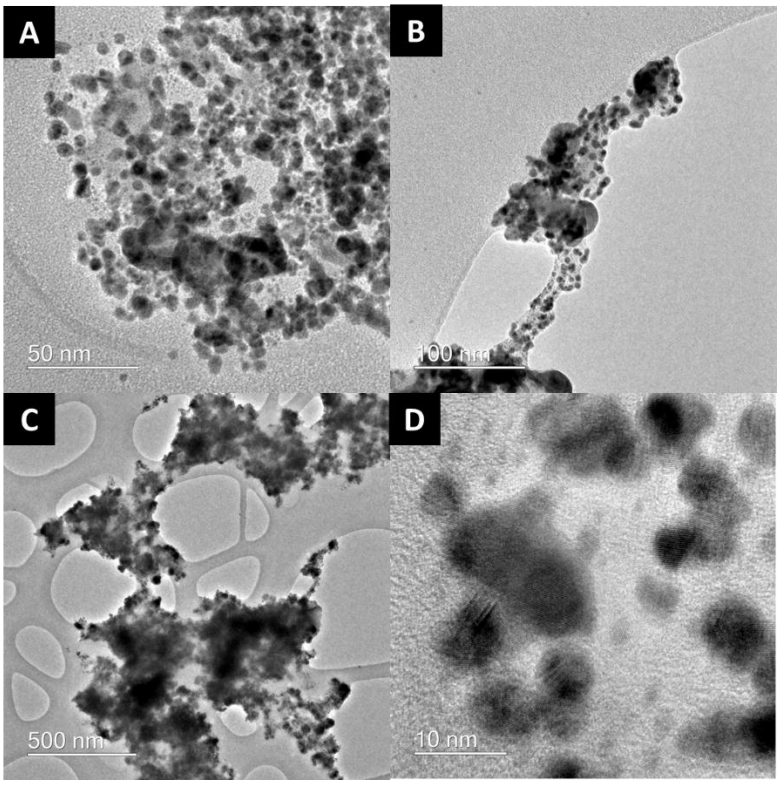

Figure 2.12 TEM images showing bimetallic silver-gold particles synthesised using a molar ratio of 3:1 Au:Ag

2.4.2 Synthesis of 2-mercaptopropionylglycine capped silver nanoparticles

Synthesis of silver nanoparticles capped with 2-mercaptopropionylglycine (tiopronin) was successfully achieved using a Brust sodium borohydride reduction of silver nitrate. Isolated nanoparticles produced by this method were a solid, dark red-brown powder. Upon dissolution in deionised water at a rate of 1 mg/mL dark amber solutions were obtained. A UV-vis spectrum of a typical solution prepared thus is shown in Figure 2.13 below. A distinct shoulder is seen at ~377 nm.

Examination of as-prepared samples of nanoparticles under the electron microscope showed discrete particles with a variety of sizes present on the grid (Figures 2.14 and 2.15). Particle size varied from 3 nm to approximately 15 nm, though smaller particles were most common. Particles were predominantly spherical, typically well-formed and closely packed. Average particle size was 6 nm. Particles in the as-prepared samples were observed to be predominantly in densely-packed agglomerations rather than dispersed, as shown in the micrograph in Figures 2.14 and 2.15. There is no evidence of the formation of chains of nanoparticles in the as-prepared samples.

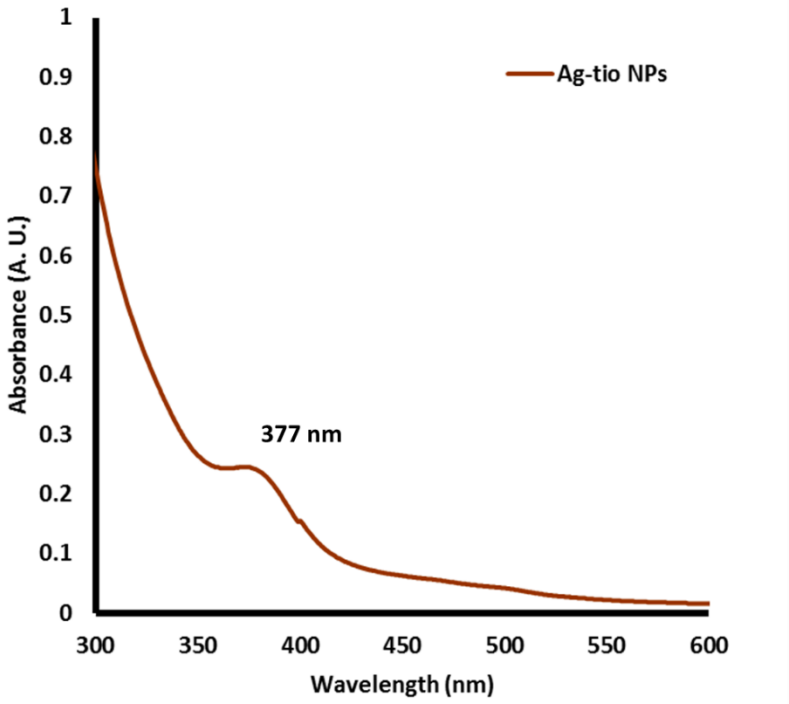

Figure 2.13 UV-vis spectrum of tiopronin-capped silver nanoparticles dissolved in water at a rate of 1 mg/mL.

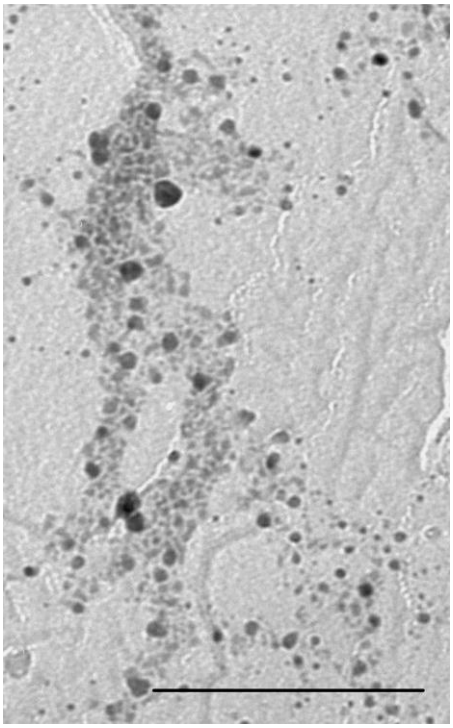

Figure 2.14 TEM image showing as-prepared tiopronin-capped silver nanoparticles. Scale bar corresponds to 100 nm.

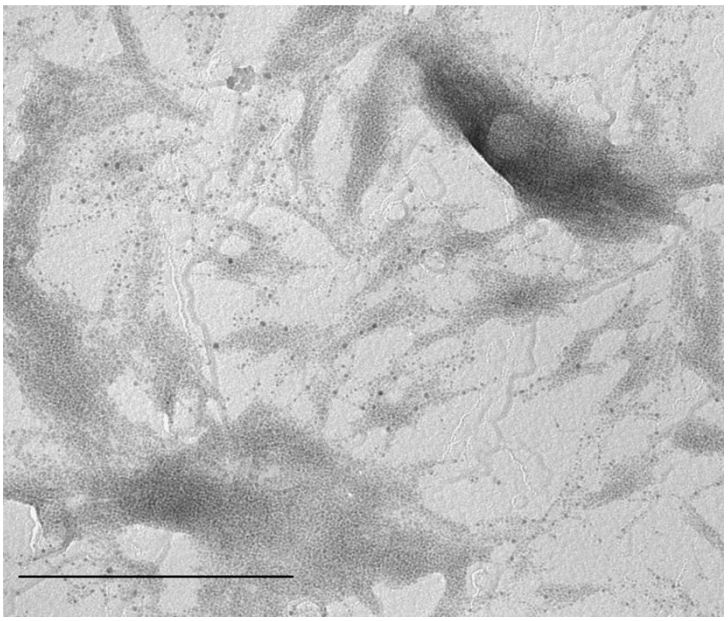

Figure 2.15 TEM image showing as-prepared tiopronin-capped silver nanoparticles. Scale bar corresponds to 1 µm.

2.4.2.1 2-mercaptopropionylglycine capped silver nanoparticle chains

After isolation of the dry nanoparticles, high aspect ratio chains of particles were fabricated. For this, a small quantity of the dry nanoparticle powder (typically ~0.5 mg/mL) was dispersed in deionised water. The vial was then placed in an ultrasonic bath and sonicated for ~2 hours. TEM studies of these samples showed small particles aligned into long chains of good linearity. The width and length of these assemblies varied widely, from single-nanoparticle width chains to ribbon- and belt-like assemblies. The length of these assemblies typically extended over several micrometres (Figure 2.16). All arrays of nanoparticles observed were reasonably linear and continuous. Notably, post-sonication the particle size distribution was much narrower, with only small (~4 nm) particles seen. This effect has also been observed in the work of Shiers *et al*. and has been attributed to digestive ripening, possibly driven by acoustic cavitation caused by sonication. The increased surface energy of the particles as a result of acoustic cavitation is believed to provide the necessary thermodynamic impetus to promote the digestive ripening process to minimise surface energy.[325]

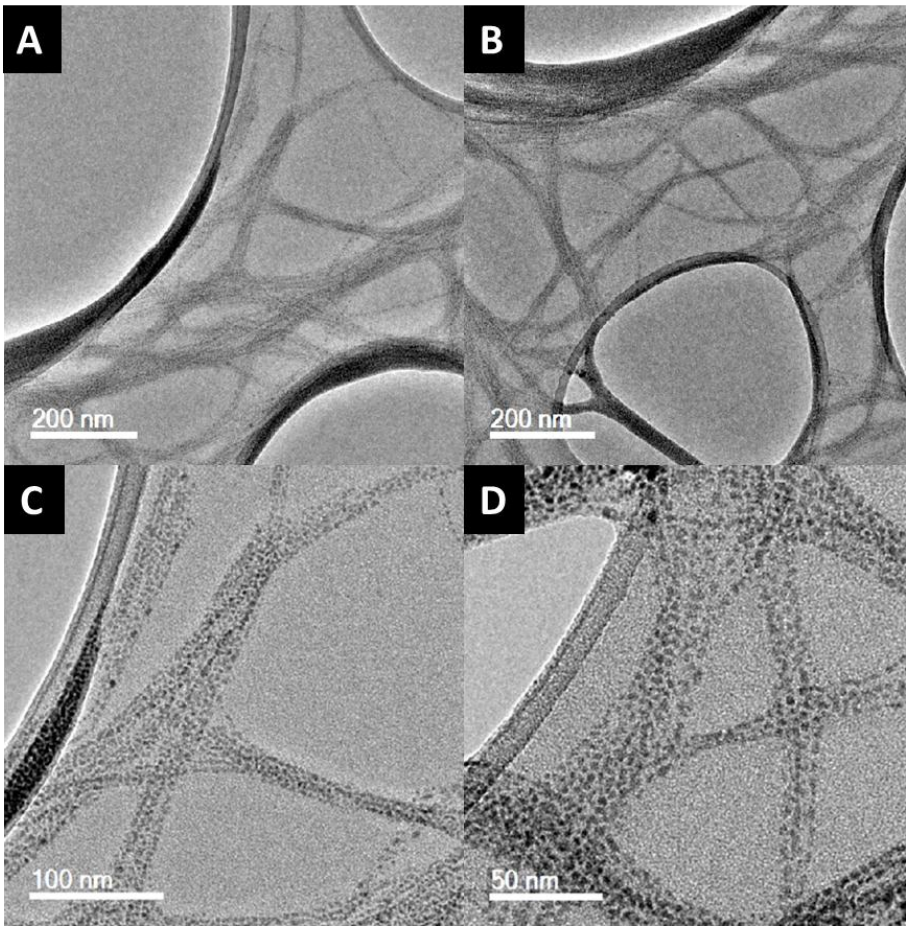

Figure 2.16 TEM images showing linear arrays of tiopronin-capped silver particles formed as a result of sonication.

2.4.3 Synthesis of gold nanorods

Nanorods were successfully synthesised using a two-step seed and growth mechanism as reported in literature. Though facile, the resultant colours of solutions of nanorods produced by this method were not completely consistent indicating a sensitivity to minute changes in reaction conditions. Solutions range from pale greyish blue to dark blue after overnight incubation at 30 °C.

UV-vis studies of the gold nanorod solutions produced by this method showed samples with a large, very broad absorption centred around 658 nm, corresponding to the longitudinal plasmon (Figure 2.17). In literature, the longitudinal plasmon has been reported to be affected by the aspect ratio of the rods. It has been shown that as aspect ratio increases from ~2 to 9 the maximum of the longitudinal plasmon increases from ~700 – 1250 nm.[31] As the

plasmon for the presented samples is ~650-660 nm, we would expect this to correlate to an aspect ratio of below 2. This was confirmed by TEM, as shown in Figure 2.18. There was a lack of a distinct transverse plasmon peak in the typical UV-vis spectrum of a nanorod sample, though a slight increase in absorption at 350-450 nm was observed. It is possible that the lack of sharp transverse plasmon peak originates from the extremely short aspect ratio of the synthesised nanorods.

The background of the UV-vis spectrum of nanorods was high in general, probably due to the dissolved CTAB still in solution affecting light scattering. In general there was also variation in the colour and translucency of the samples; due to the protected, anisotropic growth patterns, nanorods synthesis is extremely sensitive to tiny changes in concentration of both silver- and gold-ions , as reported in literature.[45]

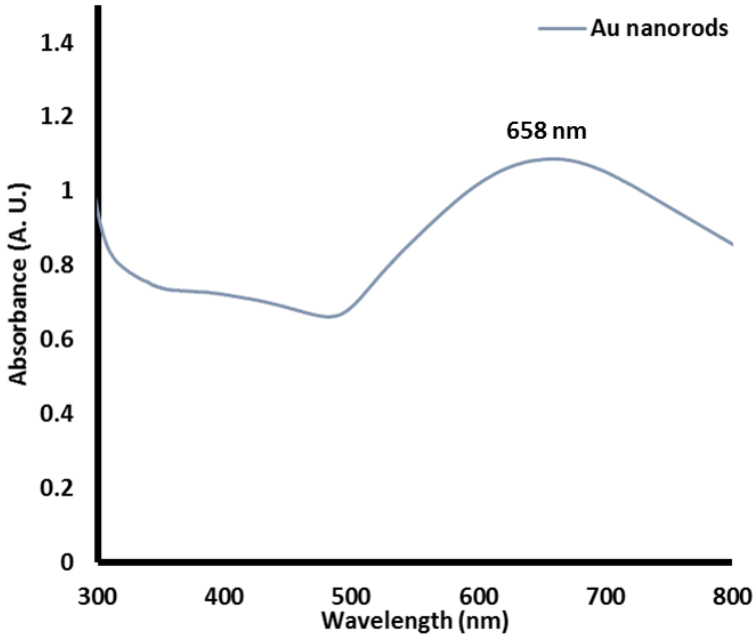

Figure 2.17 UV-vis spectrum of CTAB-stabilised gold nanorods synthesised by a seed-mediated growth method.

TEM micrographs of samples produced by this synthesis showed consistently cylindrical particles with squared-off ends, typically ~40 nm long by 15-20 nm wide (Figures 2.18A and 2.18B). A significant variation was seen in the size, shape and aspect ratio of rods produced

by this method, even within the same sample, with some cubic particles observed as well as longer, thinner rods with less well squared-off ends (Figure 2.18C). Despite some variation in morphology particles were well-formed and of crystalline gold, as evidenced by observed lattice planes at high magnification (Figure 2.18D). Average aspect ratio was found to be 1.9, which agrees closely with the ratio expected by analysis of UV-vis spectra of the sample.

Why a variety of different aspect ratios was observed in the same samples is unclear. According to literature the aspect ratio of seed-mediated nanorods grown in this manner is control by the concentration of silver ions in the seed solution.[31] Though consistency is hard to achieve from batch to batch even with minute care, it would be expected that nanorods within the same reaction sample should be comparable. Within the same sample (as illustrated in Figure 2.18C) rods with aspect ratios ranging from 1 to 2.9 were observed. It is possible that incubation without stirring resulted in small, localised fluctuations in temperature or local concentration of seed/growth solutions and these tiny differences in reaction condition in the immediate surroundings of a seed particle caused the observed differences, though previously in literature this has not been reported to be the case.

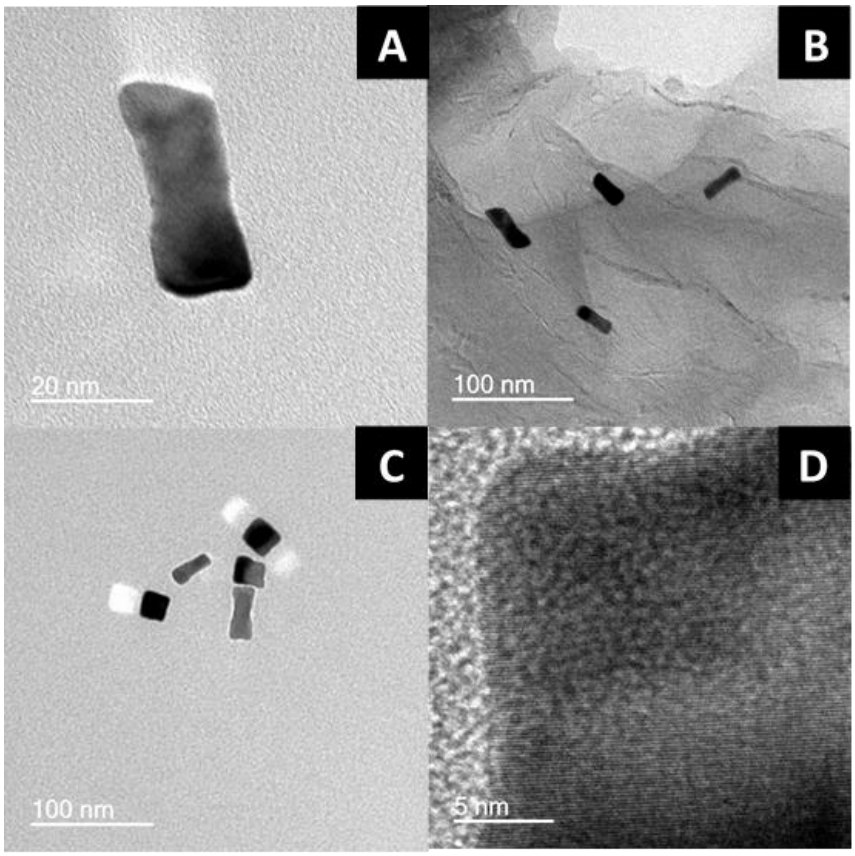

Figure 2.18 TEM images of gold nanorods obtained by a seed and growth synthesis, showing A&B: gold nanorods; C: a variety of differently shaped particles within the same sample; D: lattice planes of crystalline gold within a rod.

2.4.4 Synthesis of branched gold nanocrystals

Branched gold nanocrystals were synthesised as described in Section 2.3.4. This synthesis was found to be difficult to repeat with accuracy, as the method was strongly affected by tiny changes in temperature, concentration and volume and would often fail. Solutions were most often dark blue in colour. UV-vis studies on a typical solution show two absorptions, one at ~550 nm in the visible range and another at 344 nm, just into the ultraviolet range (Figure 2.16). This corresponds well with literature examples for branched gold nanocrystals: the absorption in the visible range is the longitudinal plasmon and gives the solution its colour (in this case blue/purple) and the absorption at the edge of the ultraviolet reason corresponds to the transverse plasmon, present in elongated particles. It is well known both theoretically and experimentally that anisotropic nanoparticles exhibit this characteristic two-peak spectrum.[31,201]

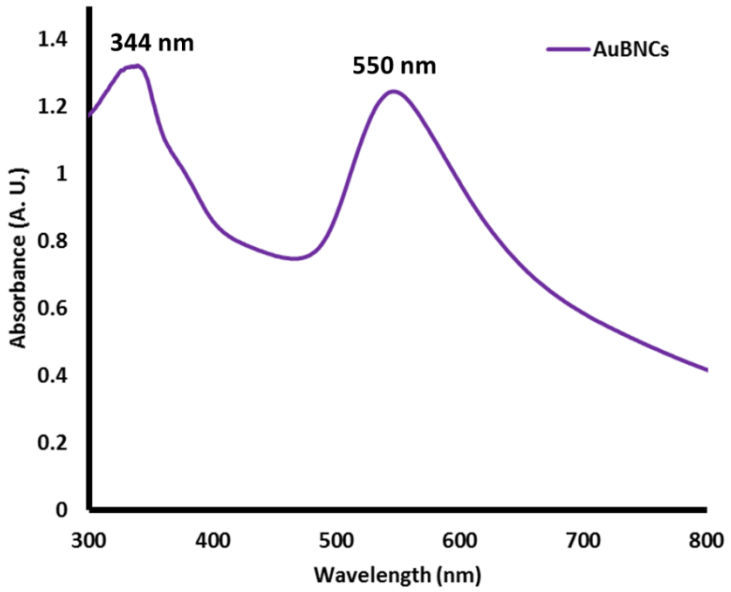

Figure 2.19 UV-vis absorption spectrum of a solution of gold branched nanocrystals (AuBNCs)

TEM images of these samples show multi-branched crystals of roughly spherical overall shape with diameters between 20-80 nm (Images shown in Figure 2.20). Particles were reasonably monodisperse, occasionally being found in small clusters of 2-6. The crystals exhibited many fine points and appeared rather urchin-like in shape. Though unusual in shape the particles were crystalline gold, as evidenced by visible lattice planes under high magnification (Figure 2.20F). These urchin-like particles have been reported in literature before, though not using the HEPES method.[319,326] Previous studies have shown a large increase in light intensity around the tips of the branches and consequent potential in SERS, so if these effects can be replicated this represents an easy, quick and extremely mild method of fabricating branched crystals for this use.

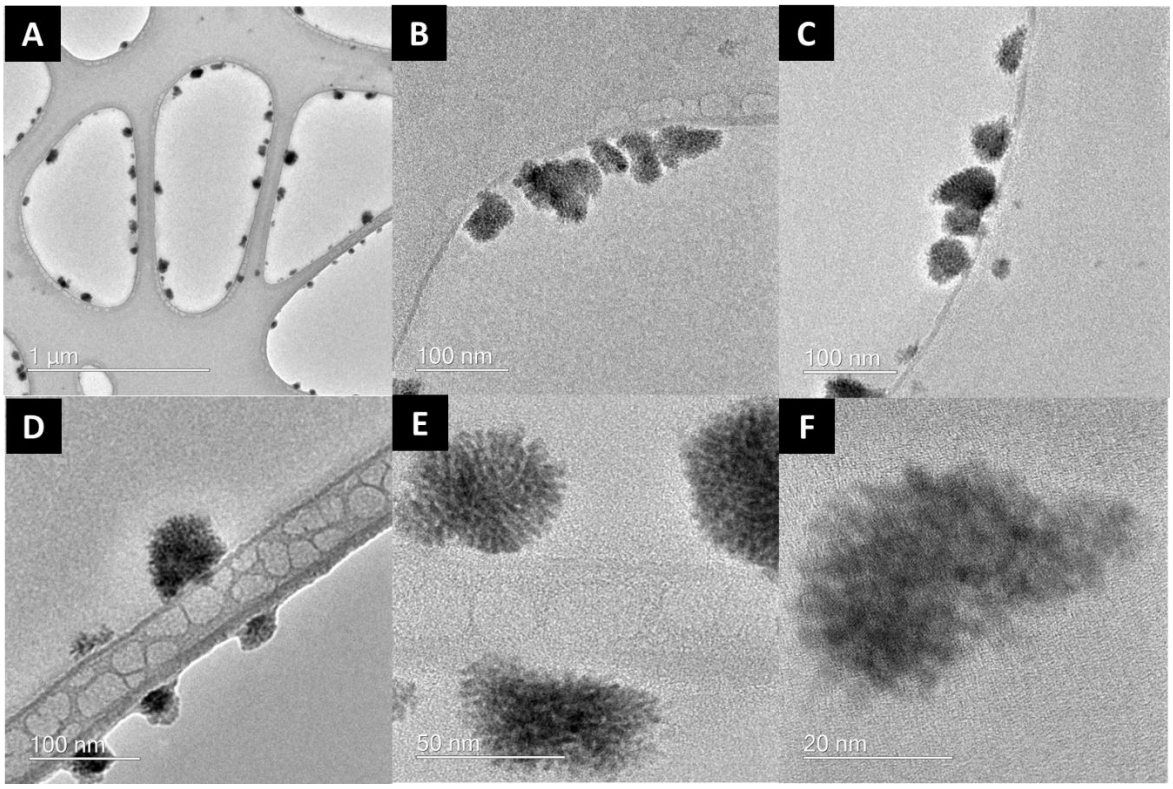

Figure 2.20 TEM images of branched gold nanocrystals produced by reduction of auric acid using a HEPES buffer.

2.5 Conclusions

A range of noble metal nanoparticles was successfully synthesised *via* a variety of methods. Citrate-capped gold and silver particles were made using a well-known citrate reduction method. Gold particles made by this method were found to be well-formed, spherical and regular in size, with an average particle diameter of ~11 nm. Silver particles formed by this method were somewhat larger (ranging from 5 – 40 nm) and possessed a diversity of morphologies. Silver-gold particles of different molar ratios were also synthesised using the citrate reduction method. All molar ratios of gold to silver showed distinct SPR bands, though the position of this varied on each run. No relationship between molar ratio and position of the SPR band was drawn.

Small, spherical silver particles capped with tiopronin with an average particle diameter of 6 nm were synthesised by a borohydride reduction. These were caused to self-arrange into

chains *via* sonication, forming very high aspect ratio arrays of good linearity. Particles in chains were smaller and had a narrower size distribution (~4 nm average diameter, all particles in the range of 3-5 nm) than in the as-prepared samples, a phenomenon attributed to digestive ripening during ultrasonication treatment. CTAB-stabilised gold nanorods were synthesised, though average aspect ratio was quite short (< 2). Nevertheless the rods showed defined cylindrical shape and definite anisotropic growth patterns. Branched gold nanocrystals were synthesised using a HEPES buffer solution as both reducing agent and growth director, leading to samples that showed a distinct two-peak UV-vis spectrum and multiple points in the TEM images.

The next section of this work took the successfully synthesised nanoparticles and titrated them with a range of anionic and cationic dyes. Differences in behaviour between nanoparticles of differing shapes and capping agents were seen, with new, novel dye-nanoparticle combinations being observed to give enhanced absorption of the dye maxima.

CHAPTER 3 : THE INTERACTION OF CATIONIC AND ANIONIC DYES WITH GOLD AND SILVER NANOPARTICLES

3.1 Aims

Noble metal nanoparticles not only show a wealth of unique properties, they have the ability to affect the properties of molecules they are conjugated with. This chapter presents an investigation of the behaviour of the range of noble metal nanoparticles synthesised in Chapter 2 with both cationic and anionic dyes with the ultimate aim of utilising such combinations for antimicrobial purposes. Titration of dyes against solutions of nanoparticles was carried out to observe consequent changes to the UV-vis spectrum including red shift of peaks, new peaks emerging and enhanced absorption of the dye; all of which indicate interaction between the dye and the nanoparticle in question. Literature has shown that conjugation of dyes with nanomaterials can create potent antimicrobial agents which can be used for medical purposes, either in photodynamic therapy or as antimicrobial surfaces. These applications, discussed in the following section, have potential to combat the rise of antibiotic resistance in common pathogens.

Titration of citrate-stabilised gold nanoparticles with cationic dyes was found to interact strongly, triggering aggregation of the particles and also exhibiting enhanced absorption of crystal violet, toluidine blue and acridine orange. Enhanced absorption had not, to the best of our knowledge, been reported for acridine orange before. Anionic dyes were not seen to show the same behaviour. Citrate-capped silver nanoparticles, made by identical methodology to their gold analogues, did not exhibit the same interaction with cationic dyes. Citrate-stabilised bimetallic particles of different gold to silver molar ratios showed erratic behaviour, possibly a consequence of the variation in size, shape and surface composition of the particles synthesised by this method. Tiopronin-capped silver and branched gold nanocrystals all showed no interaction with either class of dye. CTAB-stabilised gold

nanorods showed a small interaction with anionic naphthol green, though no enhanced absorption was seen.

3.2 Motivations and an introduction to photodynamic therapy

The continuing explosion in the number of antibiotic resistant strains of bacteria is a major concern for the scientific and medical communities.[327] Rapidly increasing numbers of infections caused by resistant strains of common bacteria such as Salmonella,[228] *E. coli,*[227] *S. aureus,*[278] *C. difficile*[226] and *M. tuberculosis*[328] amongst many others has produced a desperate need for alternative treatments when established antibiotic therapies fail. As previously stated, photodynamic therapy (PDT) has been widely studied as one such process that could help to gain control over the epidemic of resistant pathogens.

PDT is a well-known technique which involves exciting a photosensitizer with a known wavelength of light.[329] The photosensitizer absorbs a photon of specific frequency and is promoted to a high energy triplet state. This excited state transfers energy to molecular oxygen to create singlet oxygen, a cytotoxic species which is highly reactive towards organic compounds and can kill pro- and eukaryotic cells by destroying cell walls, membranes and DNA.[330] This mechanism is shown in Scheme 3.1.

Photodynamic therapy relies on an efficient photosensitizer, the molecule that is able to absorb light. There is a wide variety of photosensitizers in use today, including phthalocyanines, chlorophyll derivatives, porphyrins and associated macrocycles and dyes.[241] The dyes from the thiazine family are also used as photosensitizers and include methylene blue, azures A, B and C, toluidine blue and thionin. There have already been many studies which confirm the thiazines' ability to act as photosensitizers in PDT.[242–244] Within this work we use a range of dyes (a list of which can be found below in Table 3.1) from the thiazine family and other groups.

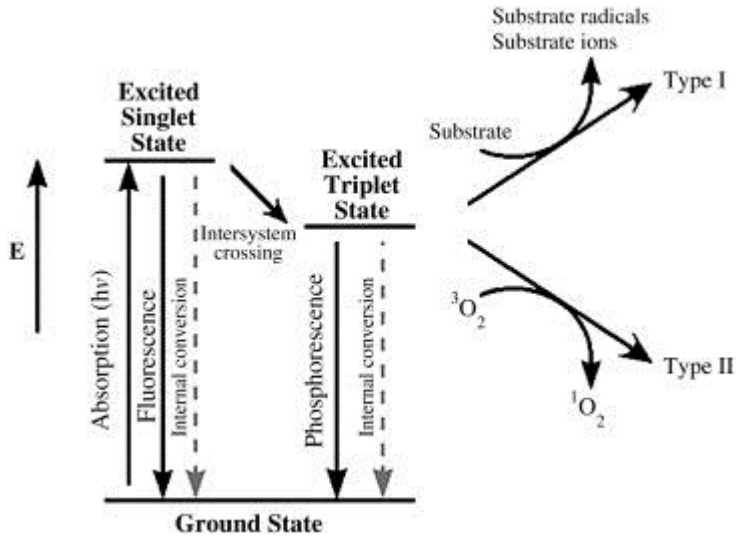

Scheme 3.1 Illustration showing the mechanism of photodynamic therapy.

3.2.1 Combination of photosensitizers with nanoparticles

The efficacy of photodynamic therapy has been shown to be increased upon conjugation with a nanoparticle or nanostructured material.[298,309] Studies on the toluidine blue-induced lethal photosensitization of *Staphylococcus aureus* showed that conjugation of the dye molecule with a gold nanoparticle increased the kill rate by an order of magnitude.[282] The same system exhibited enhanced absorption of the toluidine blue maximum absorption in the UV-vis spectrum when combined with gold nanoparticles. The increased photosensitizing capacity of the dye when combined with nanoparticles is potentially very exciting for clinical applications.

It is possible that dyes other than toluidine blue possess this ability and would behave similarly under UV-vis studies, thus this work tests a range of dyes (a list of which is given in Table 3.2) with citrate-capped gold nanoparticles to assess any analogous behaviour. The selected range of dyes was also tested with both citrate-capped- and tiopronin-capped silver nanoparticles to see how different nanoparticle composition affects these behaviours. Citrate-capped gold-silver hybrid particles were also synthesised and tested, in addition to branched gold nanocrystals synthesised using a seedless, surfactantless method and CTAB-

stabilised seed-mediated gold nanorods. All particles were tested with cationic and anionic dyes. The results of these investigations are reported below.

3.3 Experimental methods

3.3.1 Modified Turkevich synthesis of gold and silver nanoparticles

Stock solutions were made up as in Section 2.3.1.

3.3.1.1 Synthesis of citrate-stabilised gold nanoparticles

Citrate-stabilised gold particles were synthesised as described in Section 2.3.1.1. Cooled nanoparticle solutions were used in titration experiments as described in Section 3.3.5.

3.3.1.2 Synthesis of citrate-stabilised silver nanoparticles

Citrate-stabilised silver particles were synthesised as described in Section 2.3.1.2. Cooled nanoparticle solutions were used in titration experiments as described in Section 3.3.5.

3.3.1.3 Synthesis of citrate-stabilised silver-gold nanoparticles

Citrate-stabilised silver-gold particles were synthesised as described in Section 2.3.1.3. Cooled nanoparticle solutions were used in titration experiments as described in Section 3.3.5.

3.3.2 Synthesis of 2-mercaptopropionylglycine-capped silver nanoparticles

2-mercaptopropionylglycine-capped silver nanoparticles were synthesised as described in Section 2.3.2.1.

3.3.2.1 Synthesis of high-aspect ratio 2-mercaptopropionylglycine-capped silver nanoparticle chains

2-mercaptopropionylglycine-capped silver nanoparticle chains were fabricated as described in Section 2.3.2.2. These solutions were used in the titration experiments outlined in Section 3.3.5.

3.3.3 Synthesis of gold nanorods

CTAB-stabilised gold nanorods were synthesised using the methods outlined in Section 2.3.3. The resultant solutions were used in titration experiments described in Section 3.3.5.

3.3.4 Synthesis of branched gold nanocrystals

Branched gold nanocrystals were synthesised by the methods described in Section 2.3.4. The resultant solutions were used in the titration experiments as described in Section 3.3.5 below.

3.3.5 Titration experiments

Firstly, solutions of dyes were made by dissolving a known mass of the solid dye in deionised water. The full list of dyes used in these experiments, their respective concentrations and structures are shown in Table 3.1.

UV-vis spectra of nanoparticle solutions and dye solutions were obtained separately. For each dye to be studied, 16 mL of nanoparticle solution was used. 1 mL dye was added to the nanoparticle solution and stirred. A cuvette was filled and the UV-vis spectrum of this mixture was obtained. The sample solution was returned to the original mixture and a further 1 mL of dye was added. The UV-vis sample of this mixture was recorded. This process was repeated 15 times until 15 mL of dye solution total had been added to the nanoparticle solution.

This titration experiment was repeated for each dye.

Table 3.1 Dyes used in the titration experiments, their structures and concentrations.

Dye	Structure	Concentration (μM)
	Cationic dyes	
Toluidine blue O	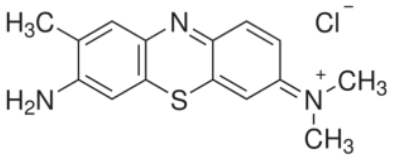	5

Malachite green	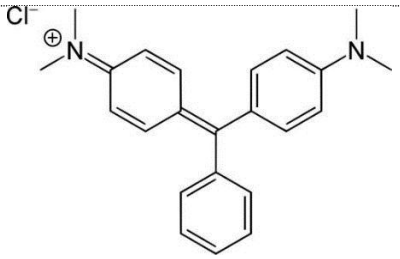	20
Rhodamine 6G	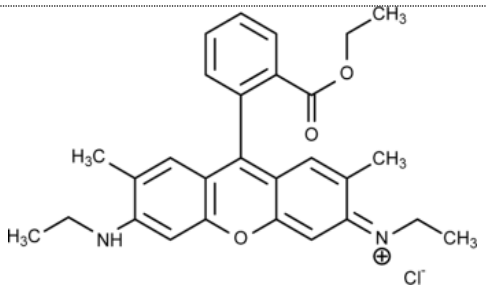	20
Crystal violet	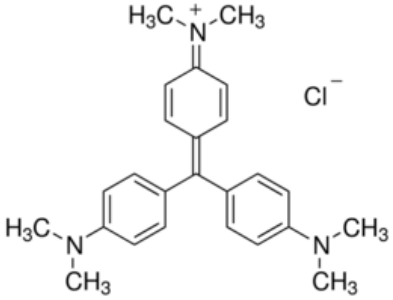	5
Acridine Orange	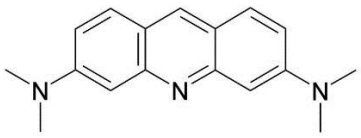	20
	Anionic dyes	
Rose bengal	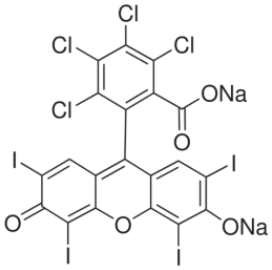	20
Naphthol green B	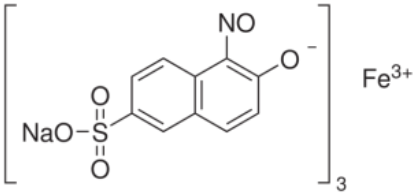	20

2',7'-Dichlorofluorescein	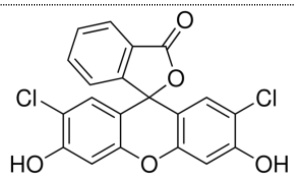	20

3.3.6 UV-vis absorption measurements

UV-vis absorption spectra were recorded using a Shimadzu UV-1800 Spectrophotometer. Plastic cuvettes with a light path length of 10 mm were used. Absorption was measured over the spectral range 200 – 1000 nm.

3.3.7 Particle size measurements

The size of nanoparticles which showed interaction with dyes in the UV-vis was monitored before, during and after the titration experiments using the following two techniques.

3.3.7.1 Zetasizer measurements

The hydrodynamic radius of the particles was measured using photon correlation spectroscopy on a Zetasizer 3000 (Malvern, UK). Experiments were carried out at 25 °C using plastic cuvettes with a path length of 10 mm.

3.3.7.2 TEM

A Jeol 200 kV TEM was used to measure the size of nanoparticles before and during the titration experiments. Samples of the particles without dyes were prepared by evaporating drops of the nanoparticle solution onto carbon coated copper grids. Further samples were prepared at points through the titration procedure so the physical effect of increasing dye concentration could be seen and compared to the nanoparticle-only specimens.

3.4 Results and discussion

3.4.1 UV-vis studies

3.4.1.1 Citrate-stabilised gold nanoparticles with cationic dyes

During titration experiments with citrate-capped gold nanoparticles all the cationic dyes studied (see Table 3.1) showed formation of a new peak in the UV-vis absorption spectra at approximately 630-690 nm. This peak (separate to that of the dye or nanoparticle solution) was typically found at a large red shift thus was indicative of the aggregation of the nanoparticles into large agglomerates. This assertion was confirmed using TEM and Zetasizer studies to observe changes in particle size, as discussed in Section 3.4.2. The effect was more pronounced for certain cationic dyes. The UV-vis absorption spectrum of the titration of malachite green with gold particles showed only a small shoulder at 685 nm (Figure 3.1). It is proposed that some of the 'new' absorption presented at 685 nm could be being masked by the absorption peak corresponding to the dye solution alone, which is found at 617 nm for malachite green. TEM analysis for this sample (Figure 3.51) revealed limited aggregation however, explaining the lack of intensity observed in the agglomeration peak.

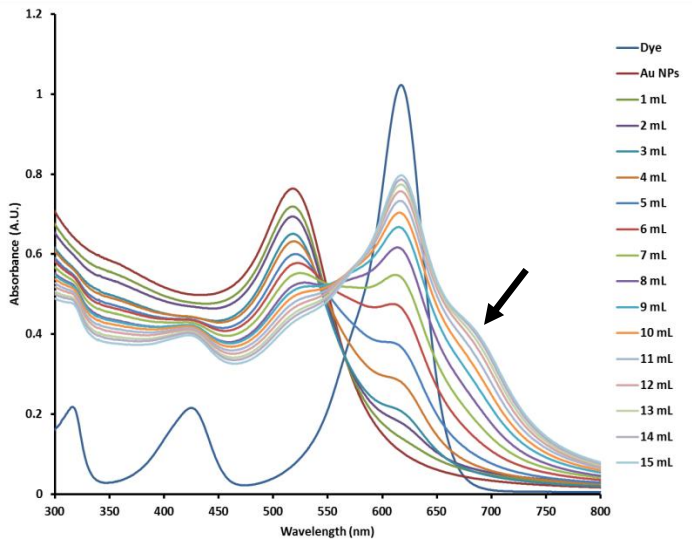

Figure 3.1 UV-vis absorption spectra of malachite green in a solution of gold nanoparticles. 'Dye' corresponds to the absorption spectrum of 20 µM malachite green dye on its own; 'Au NPs' to the absorption spectrum of 5 mM gold nanoparticle solution only. '1 mL' corresponds to the absorption spectrum of 1 mL 20 µM malachite green in 16 mL 5 mM gold nanoparticle solution. 2 mL

corresponds to the absorption spectrum of 2 mL malachite green in 16 mL nanoparticle solution etc. Shoulder indicative of aggregation is indicated by the black arrow.

Rhodamine 6G titrated with gold nanoparticle showed a very distinct peak forming at 640 nm, indicating aggregation in a similar manner (Figure 3.2). The dye maximum for rhodamine is located at 527 nm, thus a much clearer and more distinct peak is seen in the absorption spectrum when the aggregation peak emerges. The aggregation peak reached maximum intensity after 6 mL of rhodamine had been added to the nanoparticle solution. Increasing dye concentration further with additional aliquots of rhodamine up to 15 mL resulted in a decrease in the absorption maxima of the aggregation peak accompanied by slight red shift, indicating further nominal aggregation.

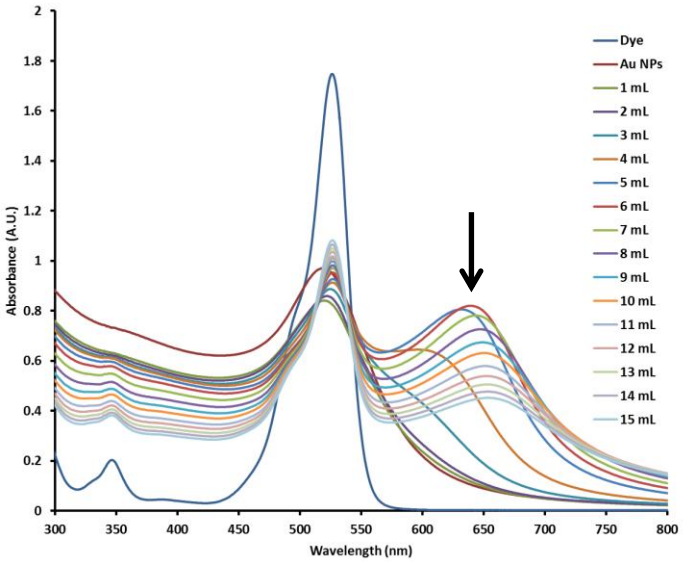

Figure 3.2 UV-vis absorption spectra of rhodamine 6G in a solution of gold nanoparticles. 'Dye' corresponds to the absorption spectrum of 20 µM rhodamine dye on its own; 'Au NPs' to the absorption spectrum of 5 mM gold nanoparticle solution only. '1 mL' corresponds to the absorption spectrum of 1 mL 20 µM rhodamine in 16 mL 5 mM gold nanoparticle solution. 2 mL corresponds to the absorption spectrum of 2 mL rhodamine in 16 mL nanoparticle solution etc. The peak that forms as nanoparticles aggregate is indicated by a black arrow.

The three remaining cationic dyes in this study – toluidine blue, crystal violet and acridine orange - show similar features in the UV-vis studies of their titrations with gold nanoparticles. Additionally they show an enhanced absorption in the aggregation peak; that is, an absorption above the intensity of the dye peak alone.

The absorption spectra of toluidine blue and gold nanoparticles show enhanced absorption at a critical concentration, as reported in the literature (Figure 3.3).[43,331] Dilution of the absorption peak corresponding to gold nanoparticles (SPR band at approx. 510 nm) was observed as expected, due to the decreasing overall concentration of gold nanoparticles in the solution as total volume increases (shown by the dotted grey arrow in Figure 3.3). Alongside this, enhancement of the absorption at 630 nm was observed. Maximum enhancement was seen after 6 mL of toluidine blue had been added, corresponding to a dye concentration of 1.36 µM in the reaction mixture. Each aliquot of dye added subsequently resulted in a decrease of the intensity of the aggregation absorption peak with slight red shift, indicating further minimal agglomeration.

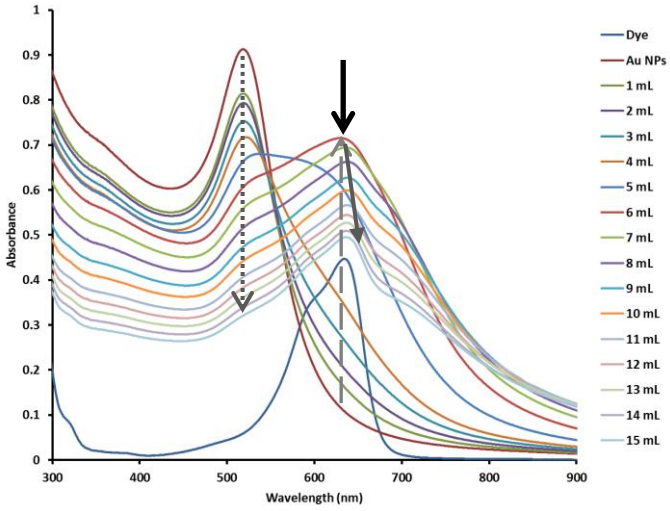

Figure 3.3 UV-vis absorption spectra of toluidine blue in a solution of gold nanoparticles. 'Dye' corresponds to the absorption spectrum of 5 µM toluidine blue dye on its own; 'Au NPs' to the absorption spectrum of 5 mM gold nanoparticle solution only. '1 mL' corresponds to the absorption spectrum of 1 mL 5 µM toluidine blue in 16 mL 5 mM gold nanoparticle solution. 2 mL corresponds to the absorption spectrum of 2 mL toluidine blue in 16 mL nanoparticles, etc. Black arrow indicates maximum enhancement of the absorption after 6 mL of toluidine blue had been added. Dotted grey arrow indicates decrease in absorbance of the nanoparticle peak as a function of dilution; dashed grey line shows the increase in absorbance of the dye from the start of the experiment to the enhanced absorption observed at 6 mL dye added. Solid grey arrow shows the decrease in intensity and slight red shift of the aggregation peak as further aliquots of toluidine blue after 6 mL are added.

The concentrations of toluidine blue and gold nanoparticles at the point where maximum dye absorption enhancement was observed were calculated to be 1.36 µM and 3.63 mM respectively. Solutions of these concentrations were made up and the UV-vis spectra taken

separately. The two curves (1.36 µM toluidine blue and 3.63 mM gold nanoparticles) were then mathematically combined, giving the absorption curve that could be expected if the two solutions were to show zero interaction with each other. The UV-vis spectrum from the titration experiment with corresponding concentration showing enhanced absortion was plotted on the same axes to give a comparison. This study is shown in Figure 3.4. It is clearly seen that the maximum absorption of the calculated UV-vis spectrum of the mixed nanoparticle-dye solution (green line) is far lower than the experimentally observed curve for a solution of identical concentration (purple line); the former being 0.23 A. U. and the latter 0.74 A. U. This roughly three-fold increase in maximum absorption is the largest recorded in this data set. It is also clear that the calculated spectrum is a strikingly different shape to the experimentally observed curve: the experimental spectrum clearly exhibits decreased intensity at 520 nm due to consumption of the initial gold nanoparticles to form aggregates.

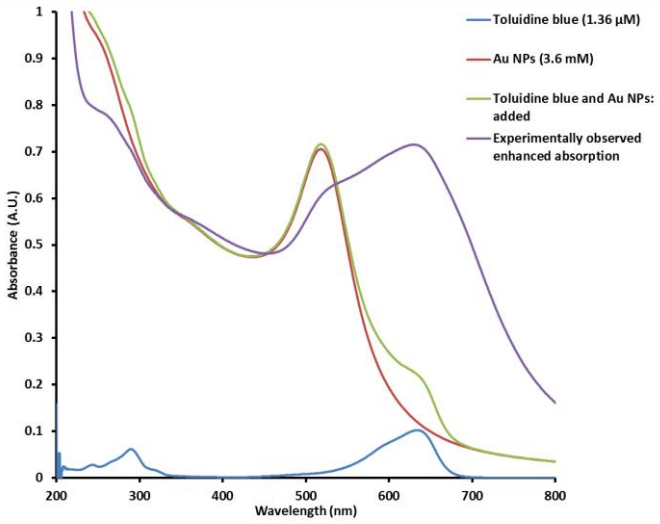

Figure 3.4 Graph comparing the UV-vis absorption spectra of toluidine blue at 1.36 µM (blue line), gold nanoparticle solution at 3.63 mM (red line), the spectra of toluidine blue (1.36 µM) and gold nanoparticle solution (3.63 mM) added together to give a mathematical estimate of the absorption spectrum that could be expected if there were no electronic interaction between toluidine blue and the gold particles (green line), and finally the enhanced absorption of toluidine observed experimentally (purple line).

Analogous results were obtained during the titration experiment between gold nanoparticles and crystal violet (Figure 3.5). As the concentration of crystal violet in the solution was

increased an aggregation peak began to develop at approximately 680-700 nm, as opposed to the dye-only absorption maximum at 590 nm. Maximum enhanced absortion was recorded after 7 mL of crystal violet had been added to the gold nanoparticle solution, corresponding to a dye concentration of 1.52 µM. Further additions of dye after this point caused a decrease in the absorption at 680 nm along with further slight red shift to ~700 nm, as seen in the toludine blue-gold nanoparticle titration.

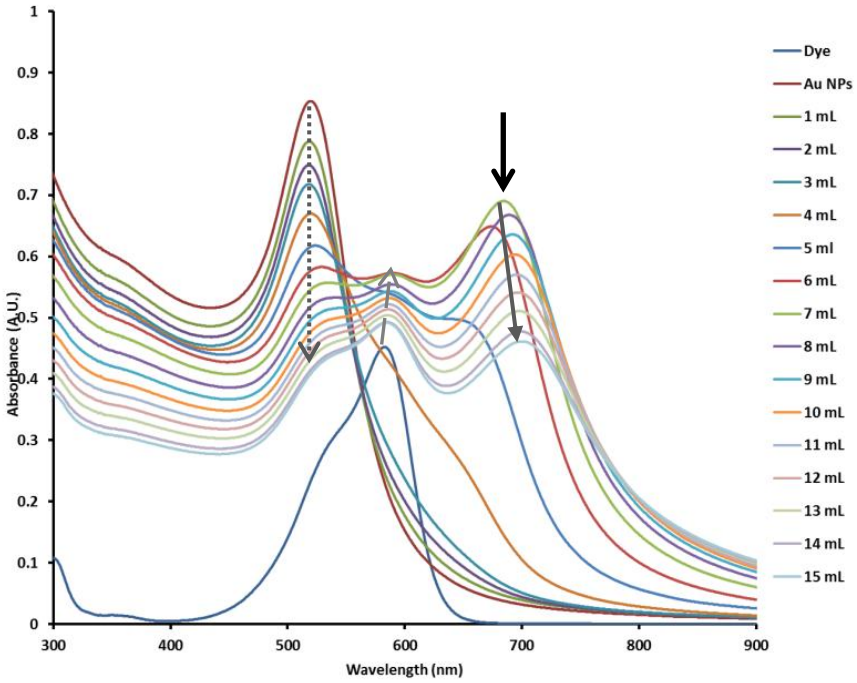

Figure 3.5 UV-vis absorption spectra of crystal violet in a solution of gold nanoparticles. Maximum enhancement of the absorption after 7 mL crystal violet had been added is indicated by a black arrow. Grey dotted arrow shows the decrease in absorption of the nanoparticles as a function of dilution; dashed grey arrow shows the increase in absorption of the dye from the start of the experiment to the enhanced absorption observed at 7 mL dye added. Solid grey arrow shows the decrease in intensity and slight red shift of the aggregation peak as further aliquots of crystal violet after 7 mL are added.

The concentrations of crystal violet and gold nanoparticles at the point where maximum dye absorption enhancement was observed were calculated to be 1.52 µM and 3.48 mM respectively. As with the toluidine blue – gold nanoparticle experiment, solutions of these concentrations were made up and the UV-vis spectra taken separately. The two curves were then mathematically combined to give the absorption curve that could be expected if the two solutions were to show zero interaction with each other. The UV-vis spectrum from the

crystal violet-gold nanoparticle titration experiment with corresponding concentration showing enhanced absortion was plotted on the same axes. This study is shown in Figure 3.6. Again, it is obvious that the calculated spectrum (green) differs greatly from the experimentally observed curve (purple): the calculated absorption spectrum shows no aggregation peak at longer wavelengths, indicating a definite interaction between the nanoparticles and dye molecules.

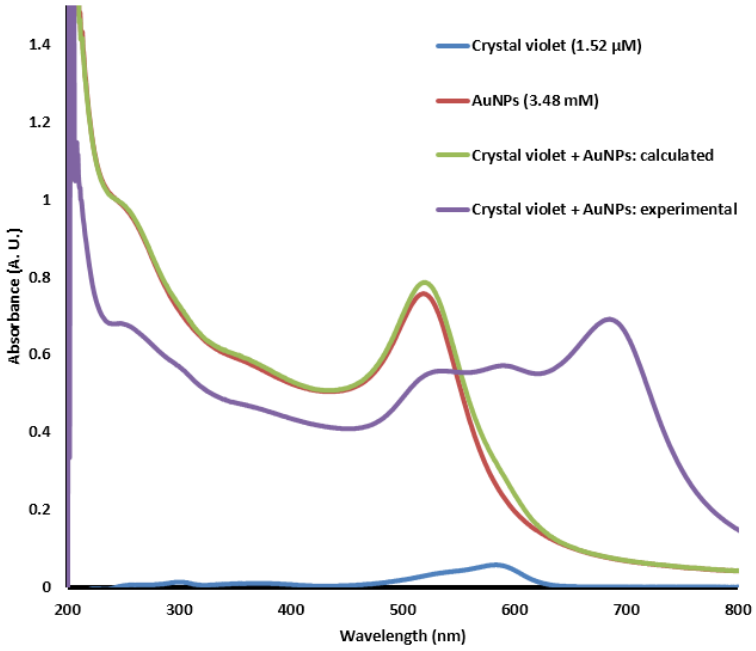

Figure 3.6 Graph comparing the UV-vis absorption spectra of crystal violet at 1.52 µM (blue line), gold nanoparticle solution at 3.48 mM (red line), the spectra of crystal violet (1.52 µM) and gold nanoparticle solution (3.48 mM) added together to give a mathematical estimate of the absorption spectrum that could be expected if there were no electronic interaction between crystal violet and the gold particles (green line), and finally the enhanced absorption of crystal violet observed experimentally (purple line).

Similar results were obtained when the titration was carried out between gold nanoparticles and acridine orange, though the enhanced absorption observed was much less pronounced (Figure 3.7). An aggregation peak was seen to form at 630 nm (indicated by the black arrow). Maximum enhancement was observed after 3 mL of 20 mM acridine orange had been added to the nanoparticle solution, corresponding to a dye concentration of 3.75 µM in the reaction mixture. Further addition of dye caused the expected decrease in absorption of the

aggregation peak accompanied by slight red shift, as seen with both toluidine blue and crystal violet.

The critical concentration of acridine orange in the reaction mixture when maximum absorption was recorded was 3.75 µM. The concentration of gold nanoparticles was 4.21 mM. The calculated spectrum if there were zero interaction between the two solutions is compared with the experimentally observed spectrum in Figure 3.8.

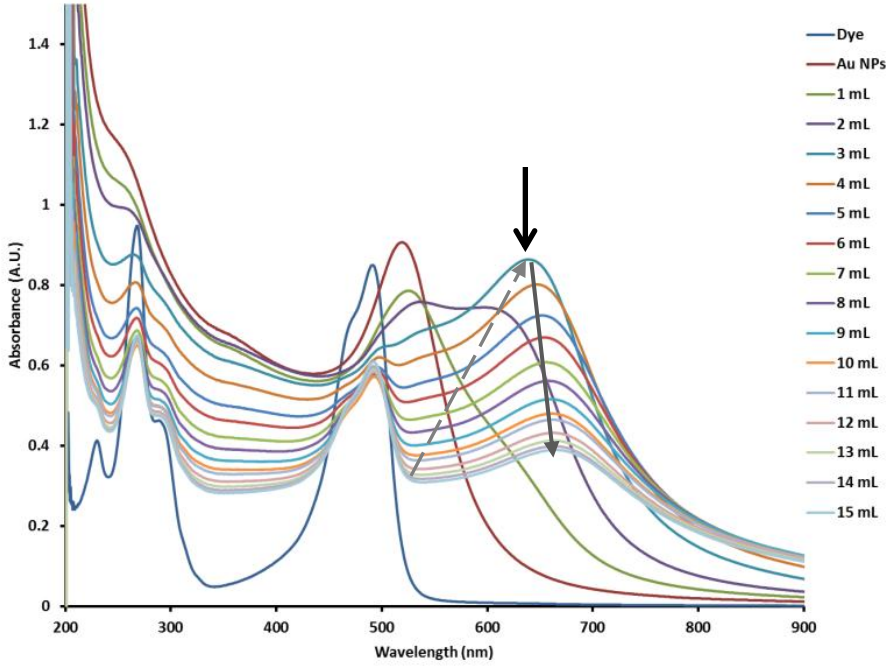

Figure 3.7 UV-vis absorption spectra of acridine orange with a solution of gold nanoparticles. Black arrow indicates the new peak that forms after 3 aliquots of acridine orange have been added. Dashed grey arrow shows the increase in absorption and red shift from the start of the experiment to the enhanced absorption observed at 3 mL dye added. Solid grey arrow shows the decrease in intensity and slight red shift of the aggregation peak as further aliquots of acridine orange after 3 mL are added.

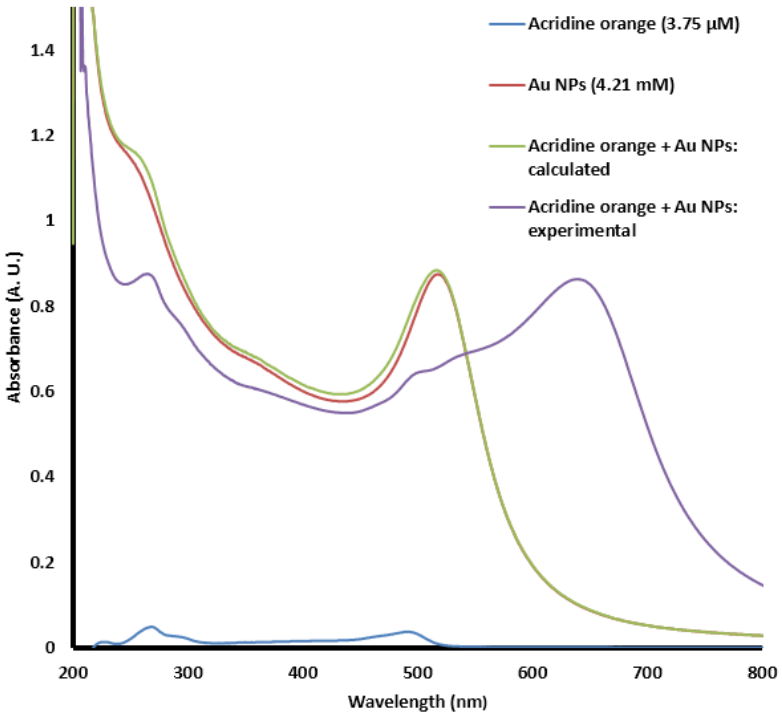

Figure 3.8 Graph comparing the UV-vis absorption spectra of acridine orange at 3.75 µM (blue line), gold nanoparticle solution at 4.21 mM (red line), the spectra of acridine orange (3.75 µM) and gold nanoparticle solution (4.21 mM) added together to give a mathematical estimate of the absorption spectrum that could be expected if there were no electronic interaction acridine orange and the gold particles (green line), and finally the enhanced absorption of crystal violet observed experimentally (purple line).

A general outline to illustrate what is observed when a cationic dye is added to a solution of citrate-capped gold nanoparticles is shown in Figure 3.9.

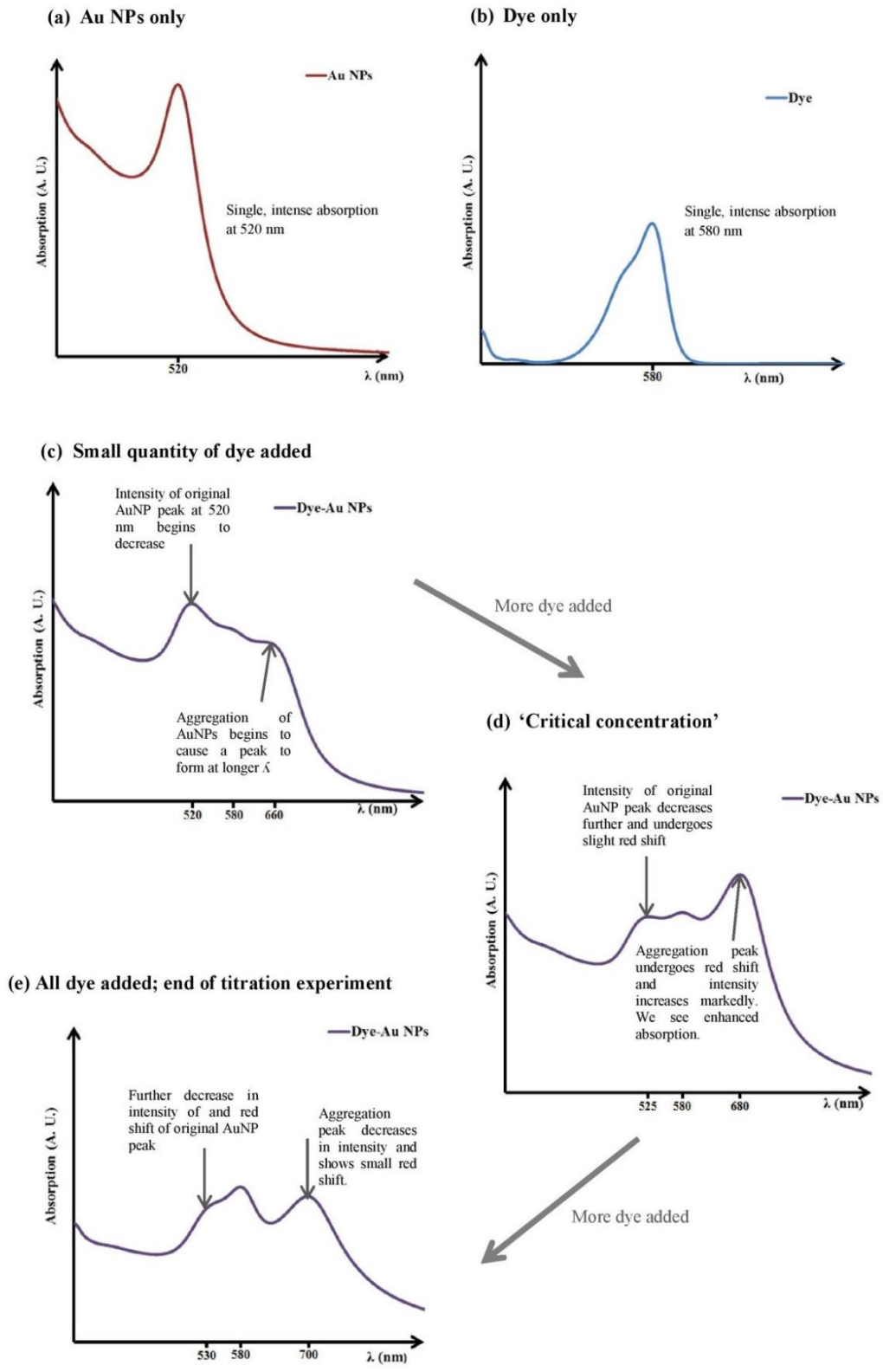

Figure 3.9 A generalised scheme depicting the changes observed in the UV-vis spectra as a cationic dye is added to a solution of gold nanoparticles. Arrows on spectra indicate general trends observed in peak intensity and red shift.

In the case of toluidine blue and crystal violet the dye absorption maxima lie close to the aggregation peak. The maximum absorbance for toluidine blue alone is found at 630 nm which perfectly overlaps the aggregation peak that forms. In this case then we do not see a 'new' peak forming in the UV-vis, merely an enhancement of the dye absorption. Similarly, crystal violet's maximum absorption is located at 578 nm, close to the aggregation peak at 685 nm. In this case we do see the aggregation peak emerge separately as it is not masked by the dye absorption, but the two lie sufficiently close that the aggregation peak 'borrows' some intensity from the dye peak to produce the enhanced absorption we observe.

3.4.1.2 Citrate-stabilised gold nanoparticles with anionic dyes

Spectra with no enhancement of absorption and no interaction between the dye molecules and gold nanoparticles were observed for all the anionic dyes used in this work: rose bengal (Figure 3.10), naphthol green (Figure 3.11) and 2,7-dichlorofluorescein (Figure 3.12). All three spectra showed the increase in the intensity of the dye absorption as it becomes more concentrated in the titration mixture and the expected decrease in intensity of the nanoparticle peak as the titration experiment progresses as a function of dilution. None showed red-shifted peaks forming at longer wavelengths that would indicate aggregation of the particles, nor did they show any enhancement of the dye absorption. The spectra of gold nanoparticles with rose bengal and naphthol green show clear isosbestic points (a wavelength at which the absorption of light by a mixed solution remains constant as the equilibrium between the components in the solution changes), which are indicative of zero electronic interaction between the particle and the dye molecules.

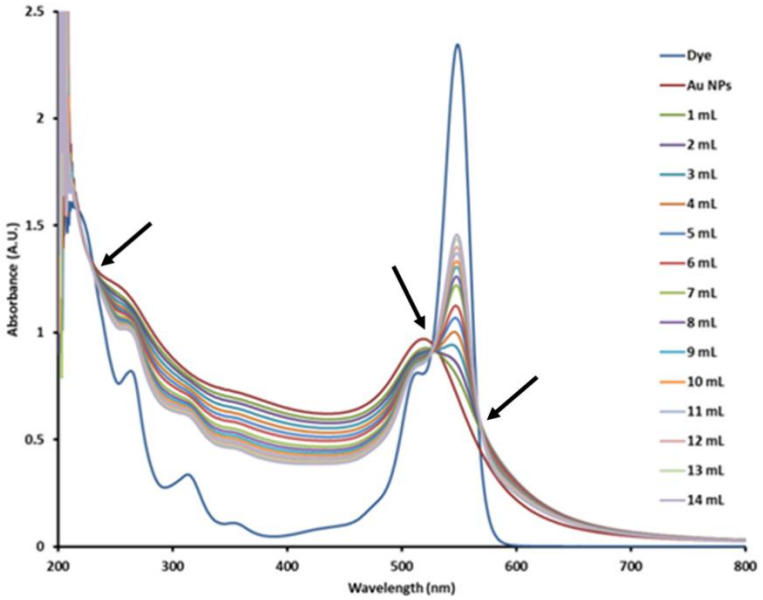

Figure 3.10 UV-vis absorption spectra of rose bengal with a solution of gold nanoparticles. Isosbestic points are indicated by black arrows.

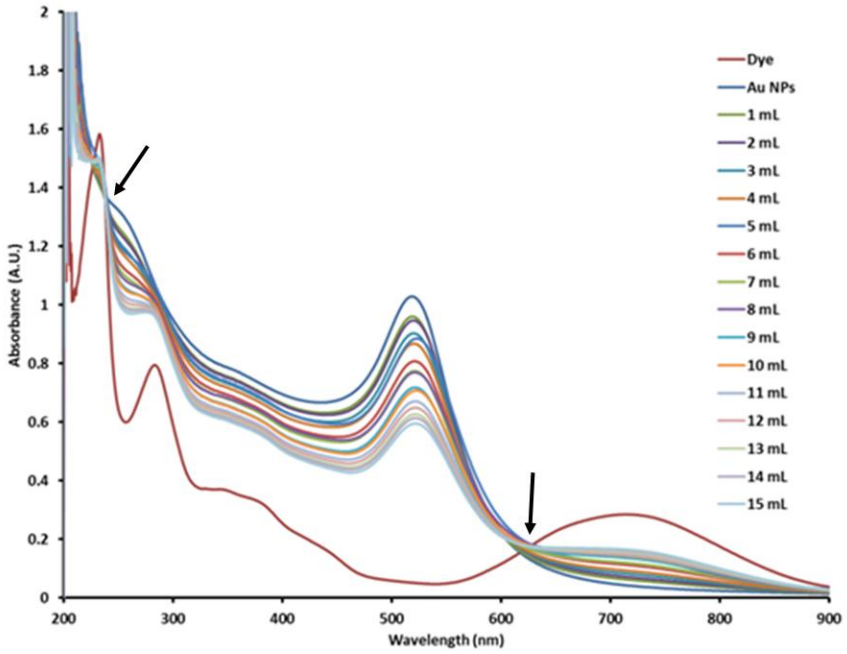

Figure 3.11 UV-vis absorption spectra of naphthol green with a solution of gold nanoparticles. Isosbestic points are indicated by black arrows.

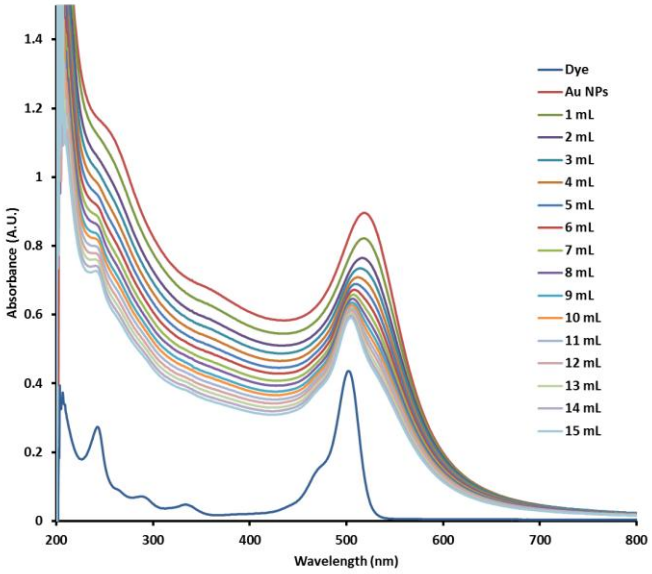

Figure 3.12 UV-vis absorption spectra of 2, 7-dichlorofluorescein with a solution of gold nanoparticles.

The lack of interaction exhibited by anionic dyes and gold nanoparticles does present a strong challenge to the previously suggested theory that the agglomeration of gold nanoparticles is solely due to increasing the ionic strength of the reaction solution.[43,332] Were this true, anionic dyes should trigger aggregation of the particles in the same manner as the cationic dyes in this study, as should the introduction of other ions into the titration mixture. To test this, analogous titration experiments were performed using the same citrate-capped gold nanoparticle samples but using potassium chloride in place of the dyes. Titrations were performed using KCl concentrations of 5 µM and 20 µM to mimic the concentrations of the dyes used. UV-vis spectra showing the results of these can be found in Figures 3.13 and 3.14 respectively. In each case we observe only the expected dilution effects upon the SPR band of the gold nanoparticles – the intensity of absorption decreases with each additional aliquot of KCl solution added. No enhanced absorption is seen and no new peaks form on the UV-vis, indicating no aggregation or change in effective particle size. Solutions remained the characteristic ruby red, merely diluted so slightly paler in saturation.

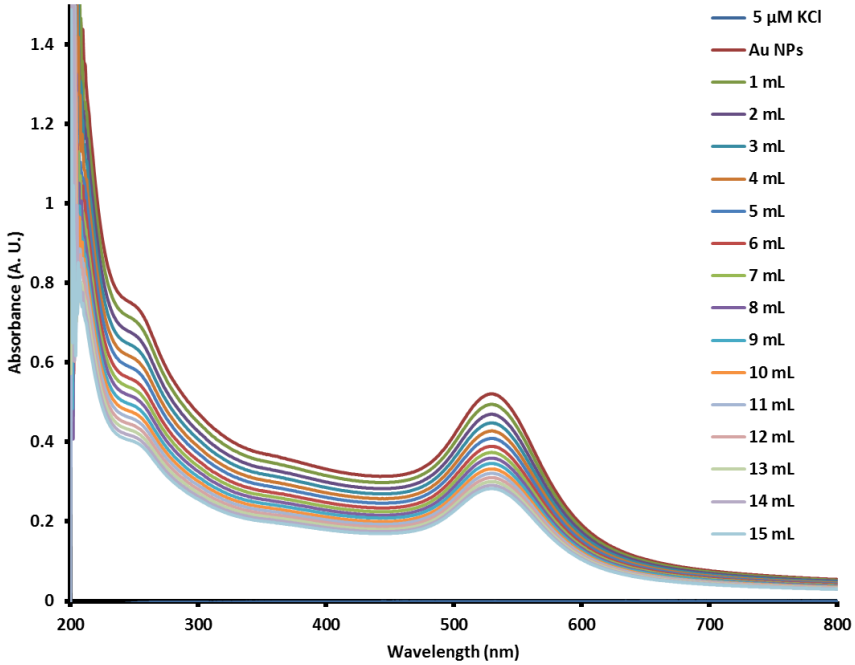

Figure 3.13 UV-vis spectra showing the effect of titrating aqueous 5 µM potassium chloride solution against a solution of citrate-capped gold nanoparticles.

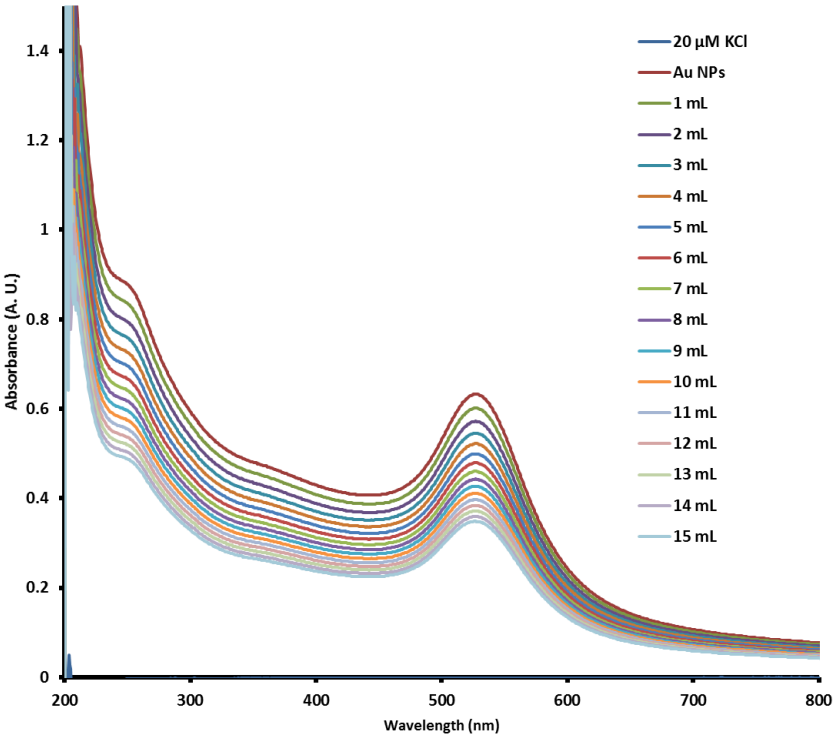

Figure 3.14 UV-vis spectra showing the effect of titrating aqueous 20 µM potassium chloride solution against a solution of citrate-capped gold nanoparticles.

It is therefore clear that the charge on the dye molecules and consequently the way they interact with the surface of the nanoparticle or the citrate shell is important. It is suggested that the electrostatic repulsion between the anionic dyes and the negatively charged citrate capping ligands prevents them coming close enough to form aggregates. The positively charged cationic dyes would, however, be attracted to the net-negative citrate shell and undergo ligand exchange, allowing coordination with the surface of the gold. From this position there is the potential for the dye molecules to act as linker molecules (a well-documented phenomenon; see Section 1.2.1.2.3) and to chelate numerous nanoparticles, driving the formation of the large aggregates that were observed.

3.4.1.3 Citrate-stabilised silver nanoparticles with anionic dyes

Titration of the three anionic dyes with silver nanoparticles also showed no electronic interaction with well-formed isosbestic points being observed. The spectra of naphthol green, rose bengal and 2, 7-dichlorofluorescein with silver nanoparticles are shown below (Figures 3.15, 3.16 and 3.17 respectively).

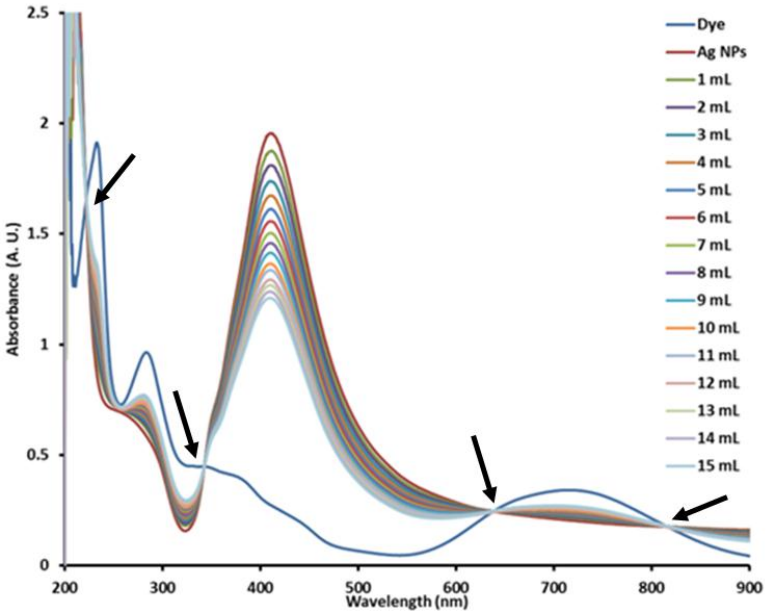

Figure 3.15 Naphthol green and silver nanoparticles. Isosbestic points indicated by black arrows.

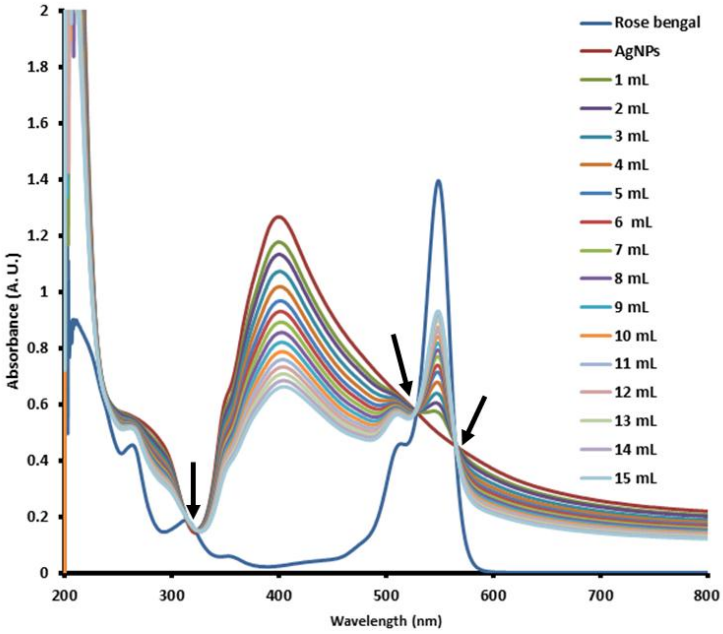

Figure 3.16 Rose bengal and silver nanoparticles. Isosbestic points indicated by black arrows.

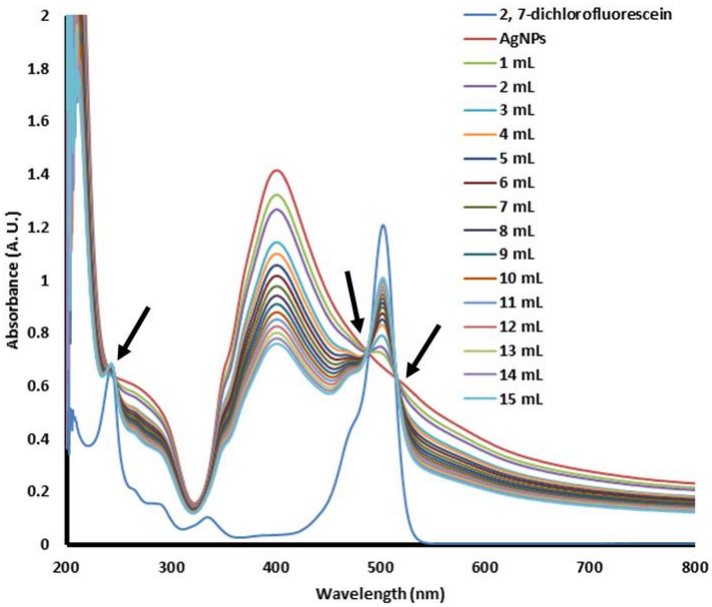

Figure 3.17 2, 7-dichlorofluorescein with silver nanoparticles. Isosbestic points indicated by black arrows.

3.4.1.4 Citrate-stabilised silver nanoparticles with cationic dyes

Interestingly, titration experiments using silver nanoparticles and cationic dyes also produced UV-vis spectra with no enhanced absorption and a series of clearly formed isosbestic points. This indicates no electronic interaction in these cases either. The spectra of malachite green

(Figure 3.18), rhodamine 6G (Figure 3.19), toluidine blue (Figure 3.20), crystal violet (Figure 3.21) and acridine orange (Figure 3.22) are shown.

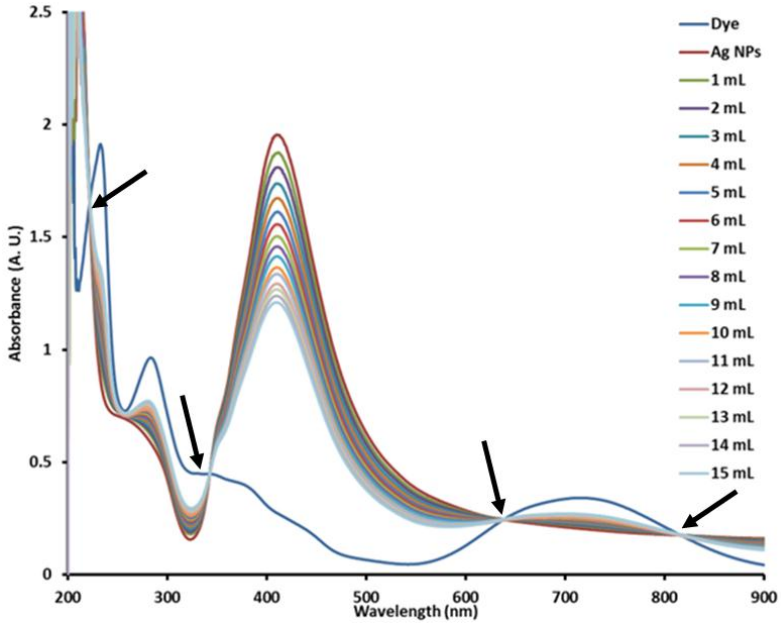

Figure 3.18 UV-vis absorption spectra of malachite green with a solution of silver nanoparticles. Isosbestic points shown by black arrows.

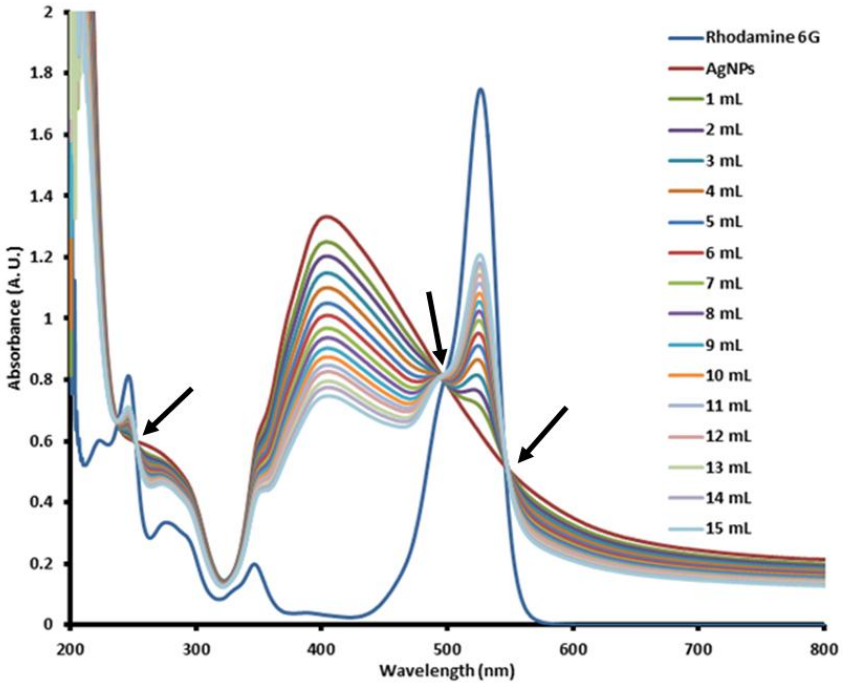

Figure 3.19 UV-vis absorption spectra of rhodamine 6G with a solution of silver nanoparticles. Isosbestic points indicated by black arrows.

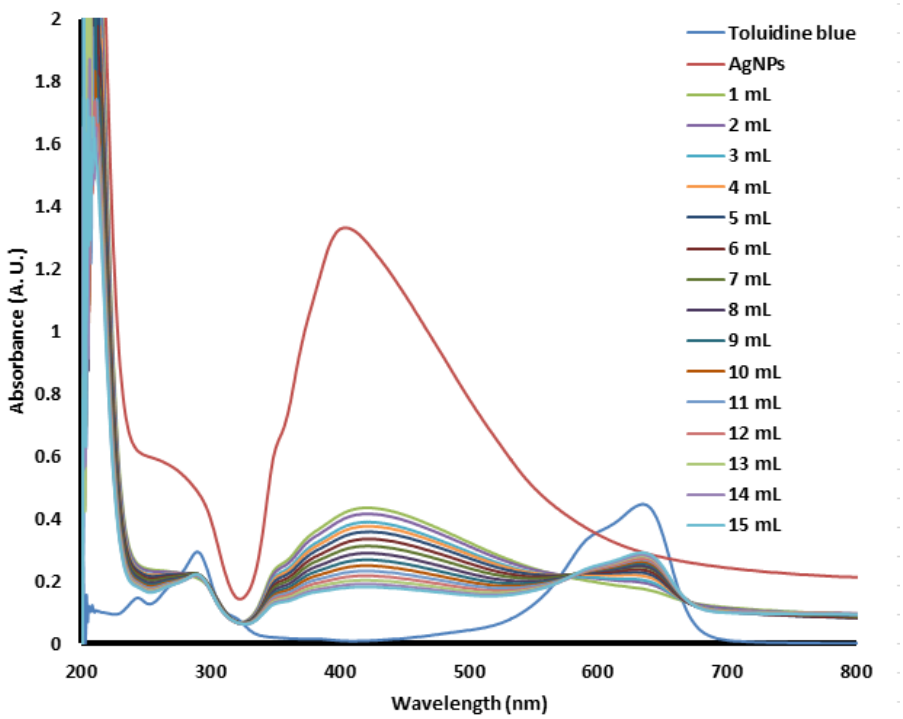

Figure 3.20 UV-vis absorption spectra of toluidine blue with a solution of silver nanoparticles

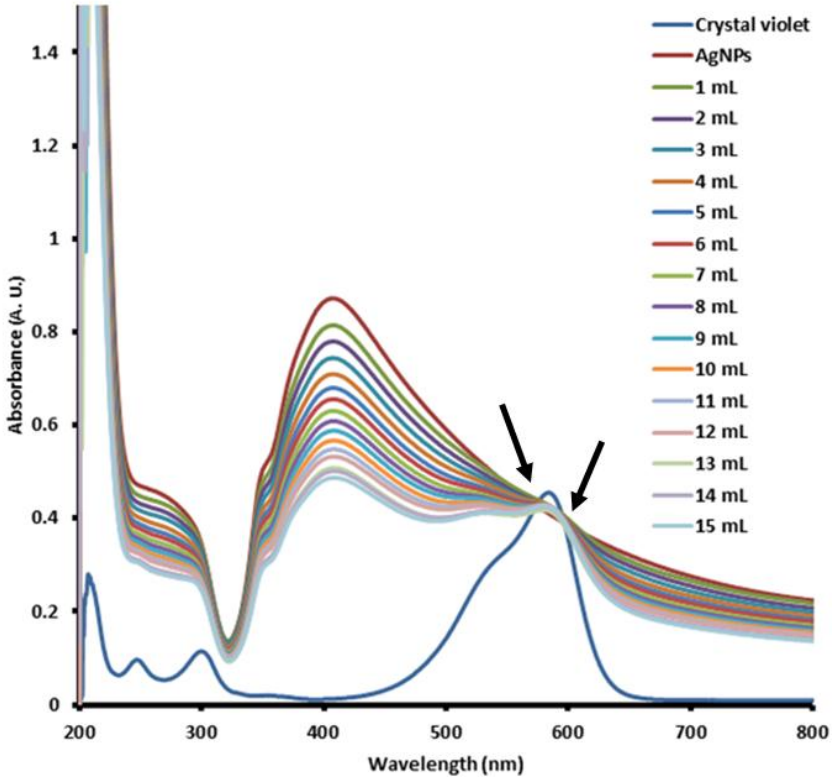

Figure 3.21 UV-vis absorption spectra of crystal violet with a solution of silver nanoparticles. Isosbestic points indicated by black arrows.

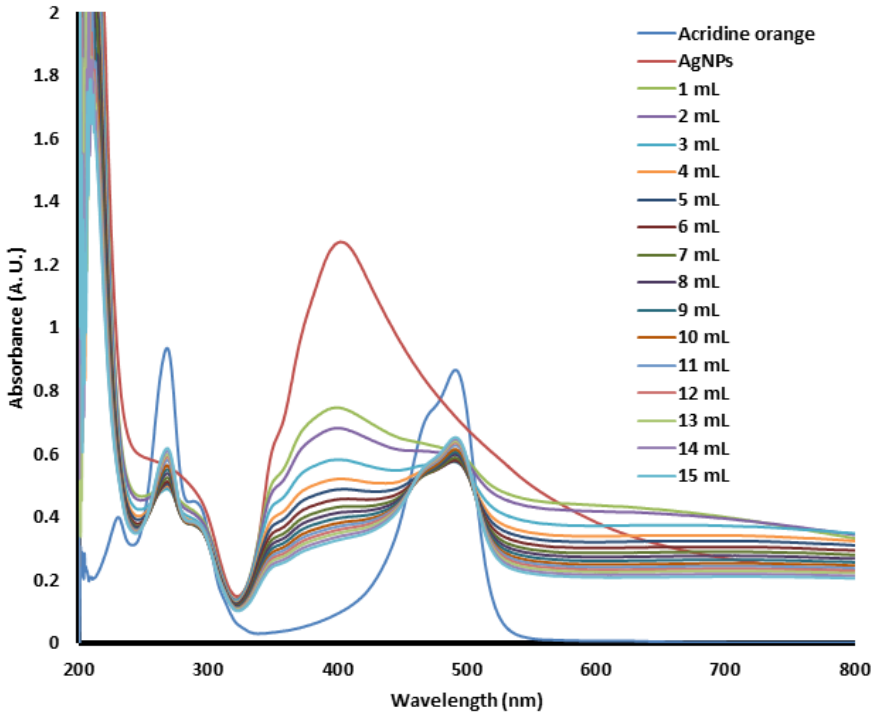

Figure 3.22 UV-vis absorption spectra of acridine orange with a solution of silver nanoparticles

It is unclear why enhanced absorption coupled with aggregation was observed only when cationic dyes were titrated with gold nanoparticles. The method used to synthesis both the silver and gold particles results in a nanoparticle with positive surface charge stabilised by citrate ions, creating a negatively charged capping shell. Theoretically then the two particles should behave analogously when titrated with the same dyes.

Although not proven at present, it is thought that the dyes used interact with the surface of the nanoparticle through the amine group (all cationic dyes used in this work have an amine group in common; see Table 3.2 for structures). Amine groups have been shown to be aurophilic.[333,334] Amines will also complex with silver, though their affinity for silver is comparatively weaker than for gold. Thus, silver-amine complexes are less stable than gold-amine complexes.[335] The capping citrate ions coordinate to the metal through oxygen atoms. Gold-oxygen bonds are weaker (223 kJ mol^{-1}) than silver-oxygen analogues (238 kJ mol^{-1}),[336] therefore it is probable that the stronger Ag-O interaction cannot be overcome by the weaker affinity of amines for silver, whereas the gold particles will prefentially bind amine-containing

dyes over oxygen-containing citrate. This allows ligand exchange to occur for dyes and gold particles, where the relative stability of the gold-citrate complexes is lower, but not for the same dyes and silver particles.

In the case of toluidine blue it is possible that the dye is coordinating through a sulphur atom, as sulphur is well-known to be exceptionally aurophilic.[337,338] This could explain the large enhancement seen in the UV-vis spectrum of gold-toluidine blue. However sulphur has also been shown to be argentophilic,[339] so why there is a failure of toluidine blue to react with the silver particles is unclear. Regardless of coordinating atom it has not been established whether the interaction between the dyes and the nanoparticle surface is covalent or electrostatic. It is possible that a slightly lower surface charge on the silver nanoparticles or partial surface oxidation could alter their behaviour towards the cationic dyes compared to their gold analogues. Further work would help to clarify the mechanisms driving this. Density functional theory (DFT) calcuations could potentially be used to map the electron density of the system and elucidate the nature of the bonding, though this would be the subject of future work.

3.4.1.5 Citrate-stabilised silver-gold nanoparticles with cationic and anionic dyes

3.4.1.5.1 1:3 Au:Ag nanoparticles

Titration of silver-gold alloy particles with cationic dyes gave inconsistent results. As reported in the previous chapter consistency in colour (and therefore size and shape) was impossible to achieve. As such, titration of the nanoparticles consisting of different ratios of gold to silver with cationic dyes gave varied results as exemplified briefly below.

Titration of gold-silver particles with a ratio of 1:3 Au:Ag with toluidine blue showed no interaction (Figure 3.23). Dilution of the nanoparticle peak at 526 nm was observed as the total volume of the dye/nanoparticle solution increased, as expected. No further features of interest were present on the spectrum. Titration of particles using the same molar ratio of

gold to silver with crystal violet, however, showed a distinct aggregation peak which formed at longer wavelengths (670-680 nm, a red shift of ~140 nm), reaching its maximum after 14 aliquots of crystal violet had been added to the nanoparticle solution (Figure 3.24). This is attributed to aggregation, as in the case of the citrate-stabilised gold nanoparticles with cationic dyes in Section 3.4.1.1. It is unclear why these particles interacted with crystal violet but not toluidine blue, though it is postulated that the differences in SPR observed for particles of the same molar ratio in the previous chapter (Section 2.4.1.3) is due to core-shell structures of silver- or gold-rich alloys forming. If this is the case, it is possible that the samples titrated with crystal violet simply had a shell which was richer in gold (which is known to interact with crystal violet, as shown above) than the sample which was titrated with toluidine blue, causing the observed differences.

Titration of these particles with anionic naphthol green (Figure 3.25) showed expected dilution effects as the titration progressed up to 10 aliquots of dyes added, after which the measured intensity fluctuated rather than decreasing steadily with each additional portion of dye added. No red shift was observed and no additional peaks were seen on the spectrum. In this case it is to be expected that the surface presence of silver- or gold-rich alloys would make no difference, as anionic naphthol green interacted with neither type of metal.

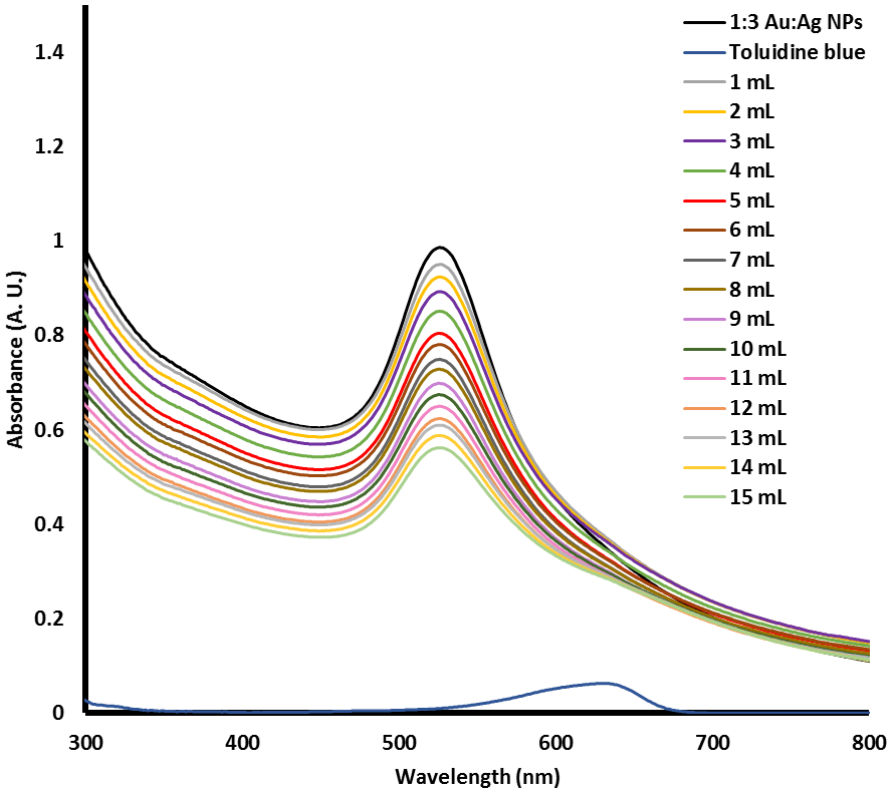

Figure 3.23 UV-vis spectra showing the titration of 5 mM toluidine blue with a solution of citrate stabilised silver-gold nanoparticles made using a gold to silver ratio of 1:3.

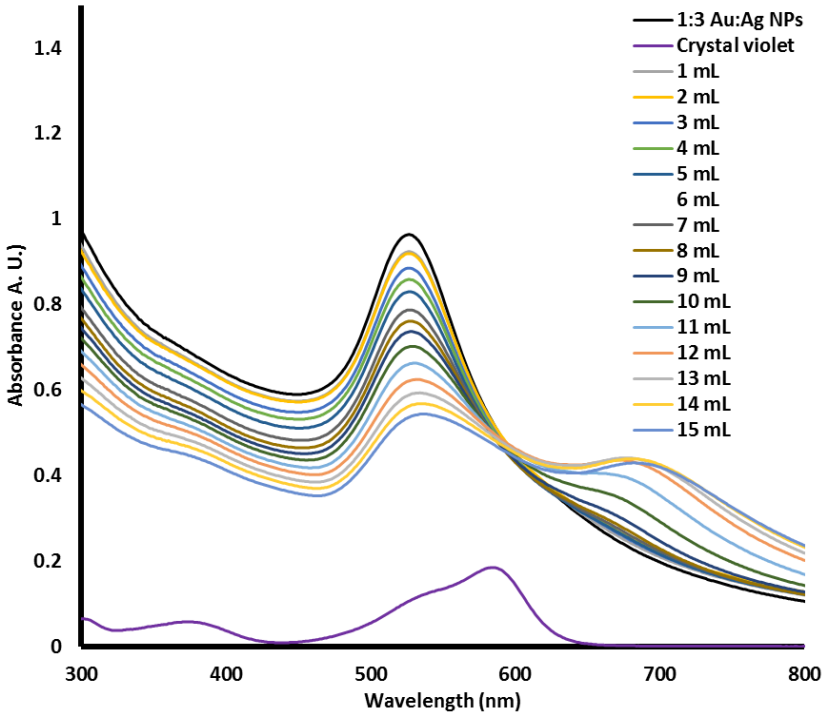

Figure 3.24 UV-vis spectra showing the titration of 5 mM crystal violet with a solution of citrate stabilised silver-gold nanoparticles made using a gold to silver ratio of 1:3. A second peak was seen to develop at ~680 nm as the titration progressed.

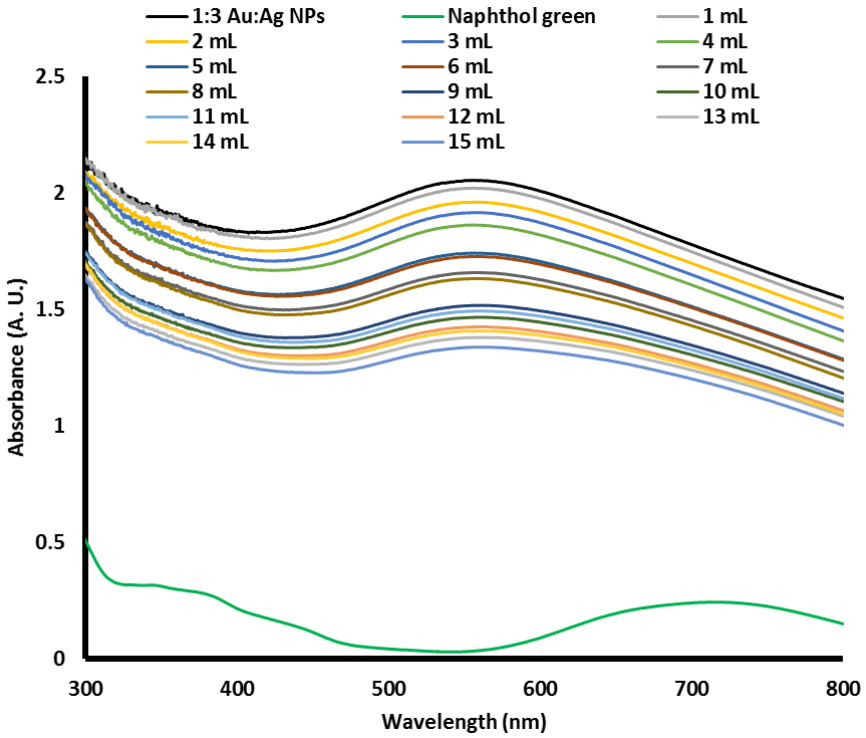

Figure 3.25 UV-vis spectra showing the titration of 20 µM naphthol green with a solution of citrate stabilised silver-gold nanoparticles made using a gold to silver ratio of 1:3

3.4.1.5.2 1:1 Au:Ag nanoparticles

Titration of silver-gold particles synthesised using a 1:1 molar ratio of gold to silver with toluidine blue again produced no interaction; the only noteworthy feature on the UV-vis spectrum being dilution of the nanoparticle peak (Figure 3.26). Unlike the 1:3 Au:Ag particles discussed above, however, the 1:1 Au:Ag particles also showed no extra peak in the UV-vis when titrated with with crystal violet (Figure 3.27); there was a marginal uniform increase in absorption on the first addition of dye, then a steady, stepwise decrease throughout the whole experiment. Titration of 1:1 Au:Ag particles with anionic naphthol green also showed zero interaction, merely the dilution of the nanoparticle peak as the titration progresses (Figure 3.28).

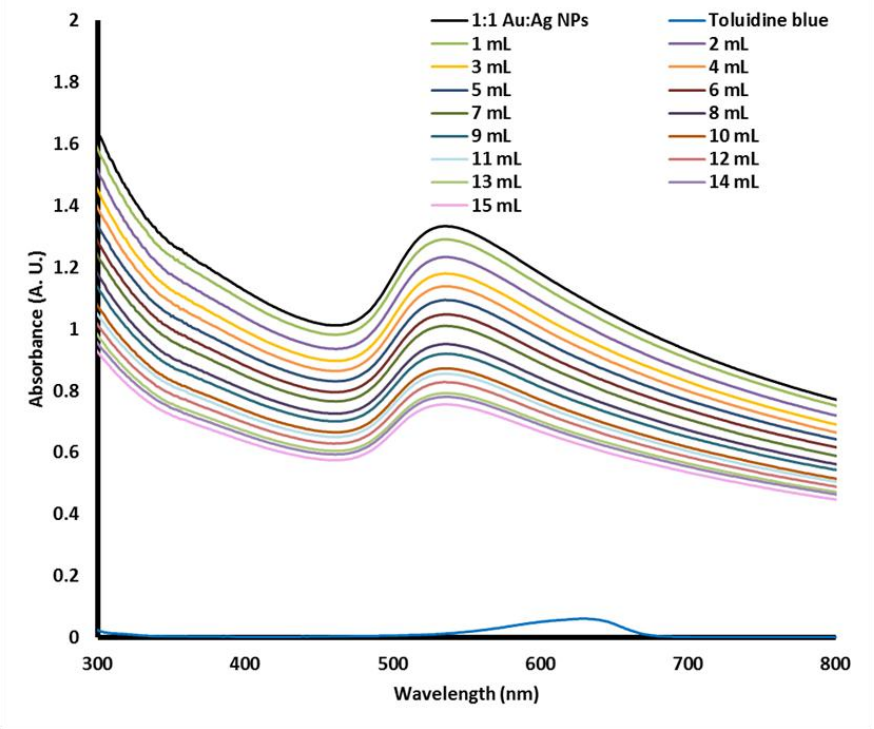

Figure 3.26 UV-vis spectra showing the titration of 5 mM toluidine blue with a solution of citrate stabilised silver-gold nanoparticles made using a gold to silver ratio of 1:1

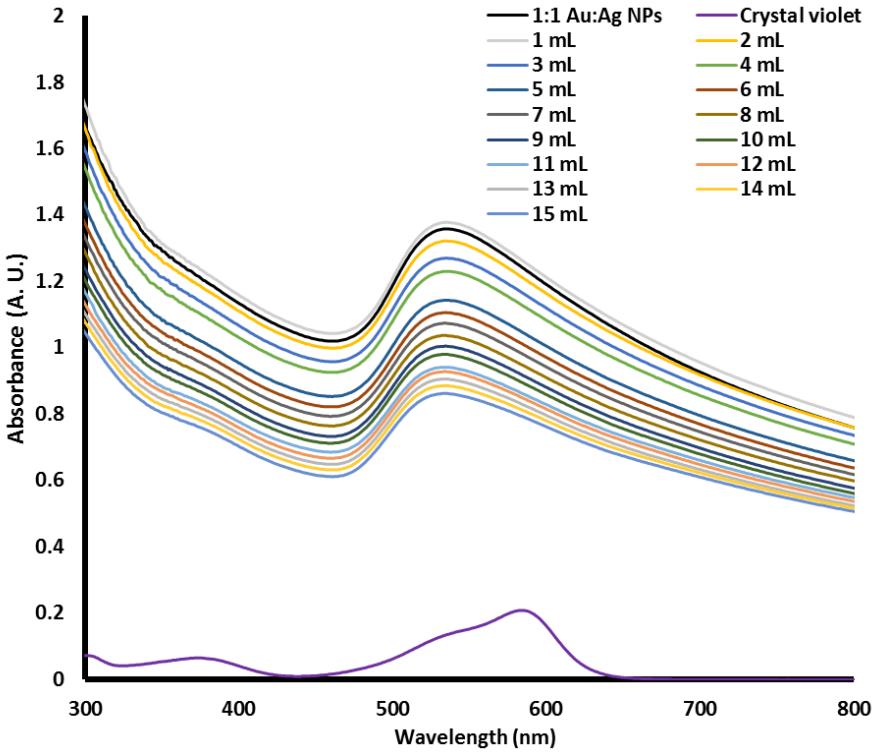

Figure 3.27 UV-vis spectra showing the titration of 5 mM crystal violet with a solution of citrate stabilised silver-gold nanoparticles made using a gold to silver ratio of 1:1

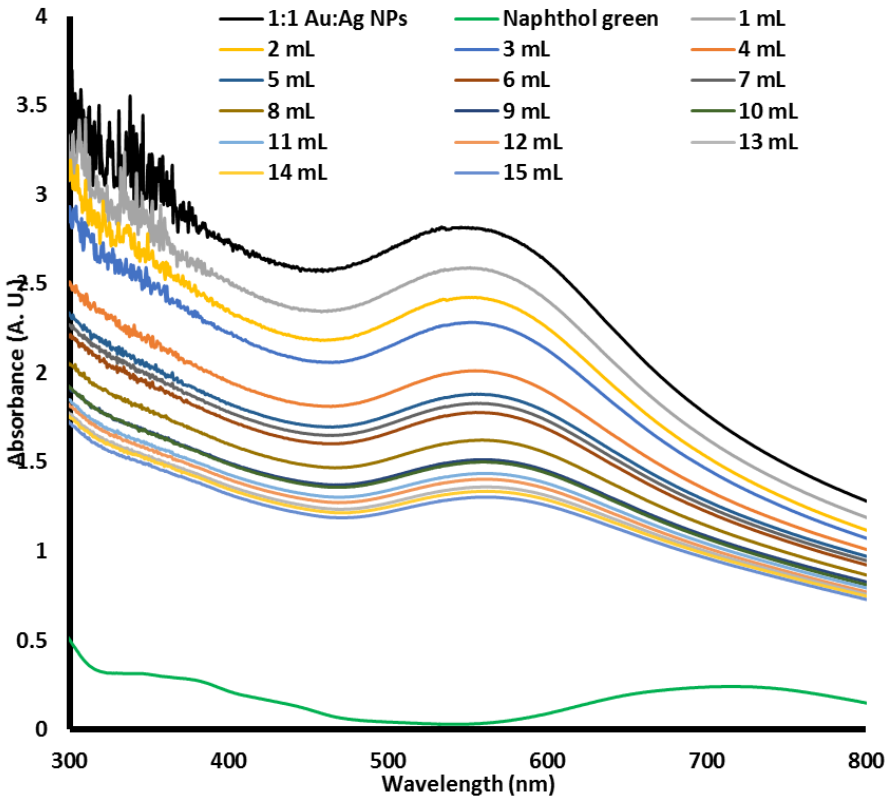

Figure 3.28 UV-vis spectra showing the titration of 20 µM naphthol green with a solution of citrate stabilised silver-gold nanoparticles made using a gold to silver ratio of 1:1

3.4.1.5.3 3:1 Au:Ag nanoparticles

Titration of particles made using a 3:1 ratio of Au:Ag with toluidine blue and crystal violet showed different results again. Titration of these particles with toluidine blue showed erratic behaviour; exhibiting a dilution effect after 1 mL dye had been added to the nanoparticle solution then jumping in intensity to show enhanced absorption after 2 aliquots were added (Figure 3.29, grey and yellow lines respectively). Addition of a third millilitre of dye caused a drop in intensity of nearly 1 A. U., before fourth and fifth additions provoked another increase to above the intensity for the nanoparticles alone. This erratic behaviour continued as further portions of dye were added, though the variations became less pronounced.

Titration of the same particles with crystal violet also showed irregular behaviour. Aliquots 1-4 caused a simple dilution effect be observed (Figure 3.30). Aliquot 5 then showed an increase in absorption compared to 4, though not above the observed maximum for the

particles alone. 6 and 7 showed a further minimal increase in absorption before 8 decreased slightly. Addition of a ninth aliquot of toluidine blue caused a bigger drop in intensity. 10 mL of dye brought the intensity back up to be almost the same as 8 mL (line mostly obscured on graph). A steady decrease in intensity was then seen from 11 mL dye until the end of the experiment. No red shift was seen and no extra peaks formed as the titration progressed. All peaks regardless of intensity were centred around 527 nm, the same as the nanoparticle peak alone.

Titration of 3:1 Au:Ag particles with anionic naphthol green showed no aggregation or red shift of peaks (Figure 3.31). A large drop in absorption was observed on addition of the first aliquot of dye. Each aliquot added thereafter caused very small drops in intensity.

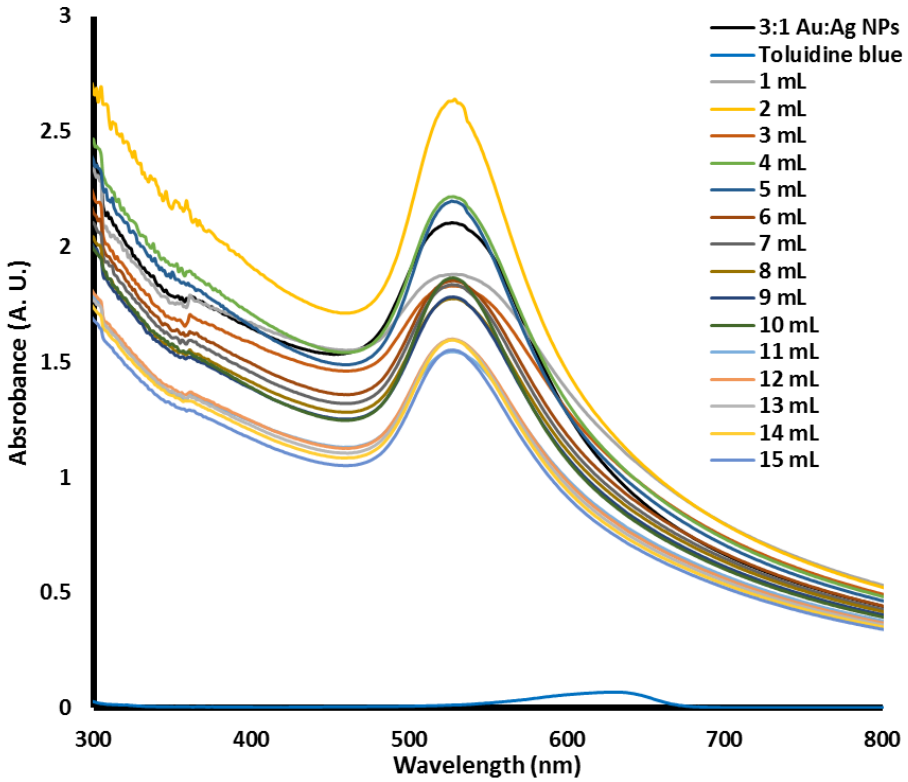

Figure 3.29 UV-vis spectra showing the titration of 5 mM toluidine blue with a solution of citrate stabilised silver-gold nanoparticles made using a gold to silver ratio of 3:1

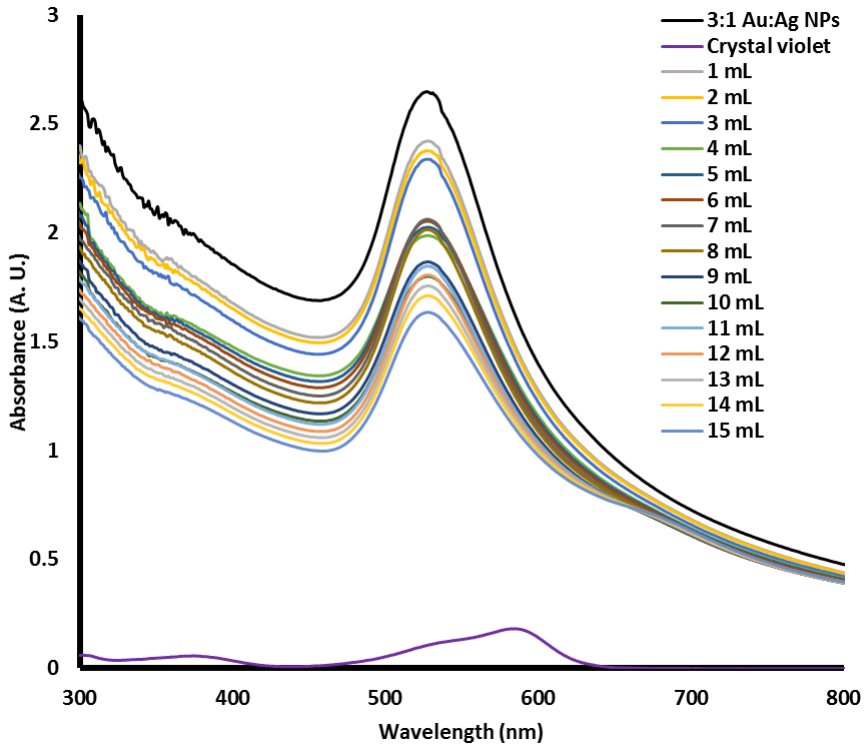

Figure 3.30 UV-vis spectra showing the titration of 5 µM crystal violet with a solution of citrate stabilised silver-gold nanoparticles made using a gold to silver ratio of 3:1

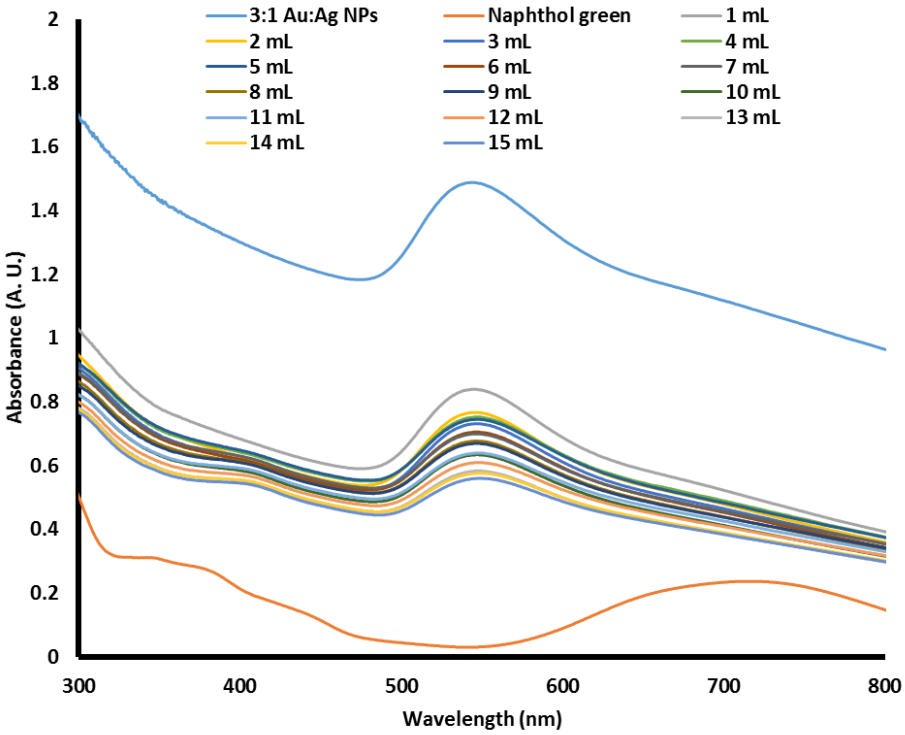

Figure 3.31 UV-vis spectra showing the titration of 20 µM naphthol green with a solution of citrate stabilised silver-gold nanoparticles made using a gold to silver ratio of 3:1

The strange behaviour exhibited by bimetallic particles of all molar ratios of gold to silver is testament to the irregularity and irreproducibility seen during the synthesis of these particles. It is well documented that nanoparticles can be very sensitive to small changes in temperature, pressure, concentration and pH.[28] Though the Turkevich synthesis for gold is facile and easily repeatable it is much less so for silver – as evidenced by the irregular shapes and sizes of silver particles obtained by this method (see Section 2.4.1.2). The proposed core-shell structure with silver-rich and gold-rich alloys and fluctuations in composition between each sample could explain the erratic and unpredictable results gathered here, by providing zones of different reactivity towards the dye molecules for particles synthesised using the same molar ratios and even within the same sample.

3.4.1.6 Branched gold nanocrystals with anionic and cationic dyes

Branched gold nanocrystals were synthesised using a HEPES buffer and auric acid, resulting in particles which exhibited multiple points (see Section 2.4.4). UV-vis on the resultant blue-purple solutions showed two peaks at 344 and 550 nm, typical of the double peak spectrum given by branched nanocrystals in literature (Figure 3.32).[320] Samples were most often purple but some variation in colour was seen.

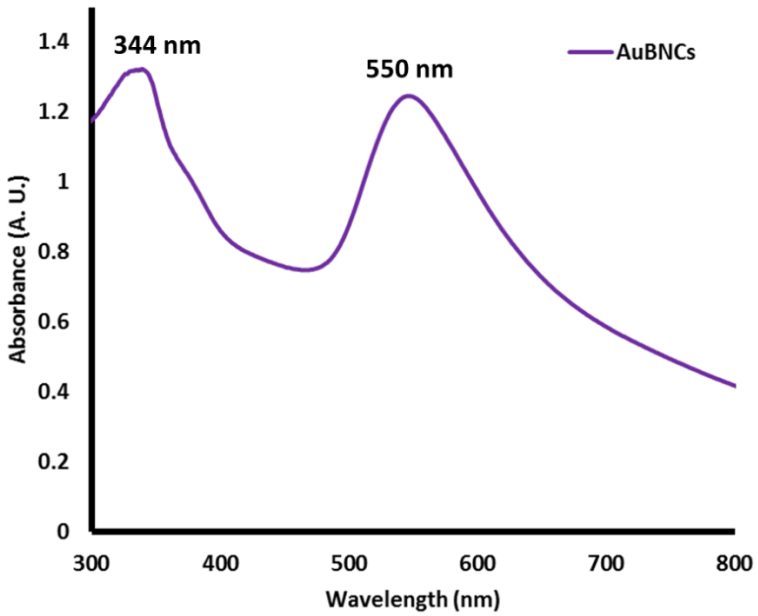

Figure 3.32 UV-vis spectrum of gold branched nanocrystals synthesised using the HEPES buffer and a solution of auric acid. Two SPR peaks are seen at 339 and 546 nm.

Titration of solutions of branched gold nanocrystals with both anionic and cationic dyes showed no interaction in the manner of the citrate-stabilised spherical particles. Spectra for all dyes with the branched particles showed simple dilution effects where the intensity of the nanostar peak decreased as more aliquots of toluidine blue were added. The spectra of the cationic dyes toluidine blue and crystal violet titrated with gold branched crystals are shown in Figures 3.33 and 3.34 respectively. It clearly seen that as dilution occurs on the addition of dye solution the shape of the branched nanoparticle peaks remained constant, indicative of no change in effective particle size and therefore no aggregation. There was also no red/blue shift of the peaks. There was also no disproportionate decrease in either peak, indicative of retention of the branched morphology as both longitudinal and transverse plasmon peaks were maintained, albeit diluted. Similar results were seen for branched gold crystals titrated with anionic dyes (the spectra of the titration with rose bengal and naphthol green are shown in Figure 3.35 and 3.36 respectively). The failure of either class of dye to interact with branched gold nanocrystals is likely due to the nature of the interaction between the shape-directing HEPES ligands and the surface of the gold – the HEPES molecule binds to the surface

of the gold through a sulphur atom (structure of HEPES shown in Figure 3.37). It is known that gold-thiol bonds are very strong (Au-S dissociation energy is 254 kJ mol^{-1}) thus are unlikely to be displaced by dyes coordinating either through a nitrogen (Au-N bond energy unquantified, but reportedly a comparatively weak covalent interaction compared to the strong Au-S covalent bond[340]) or oxygen atom (Au-O 223 kJ mol^{-1}).

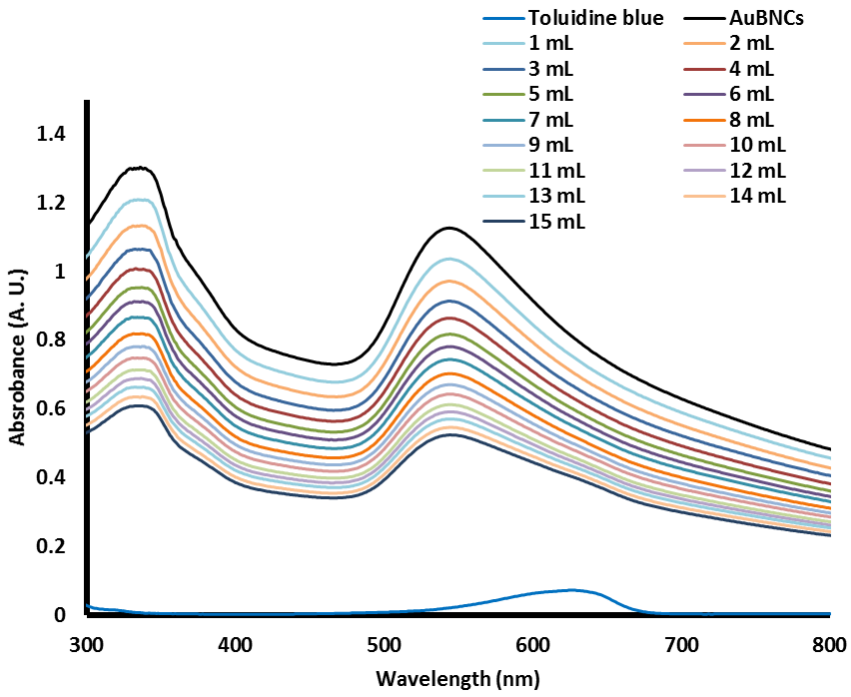

Figure 3.33 UV-vis spectrum of the titration between gold branched nanocrystals and toluidine blue

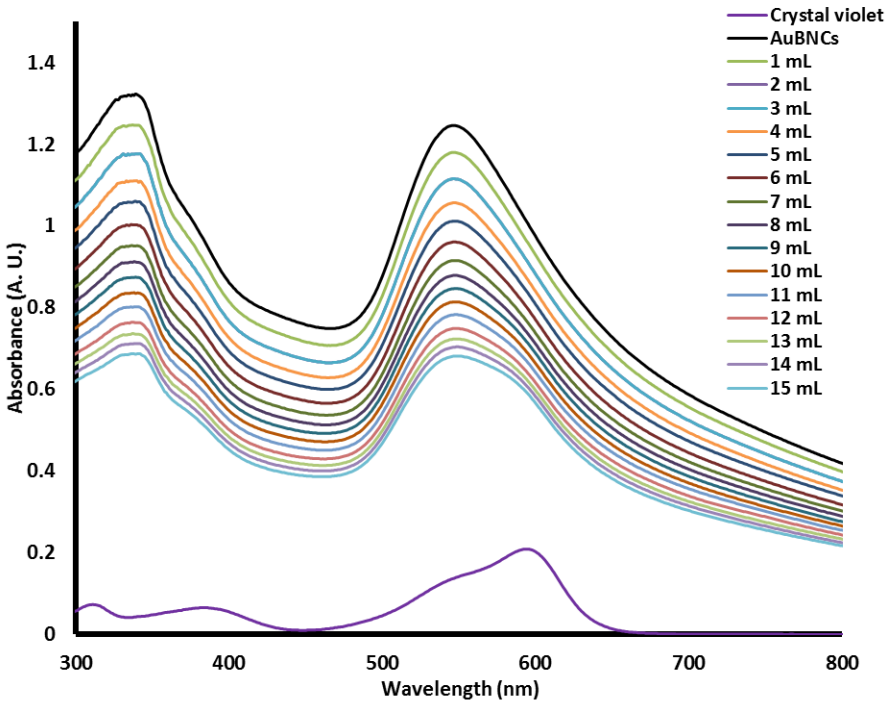

Figure 3.34 UV-vis spectrum of the titration between branched gold nanocrystals (AUBNCs) and crystal violet

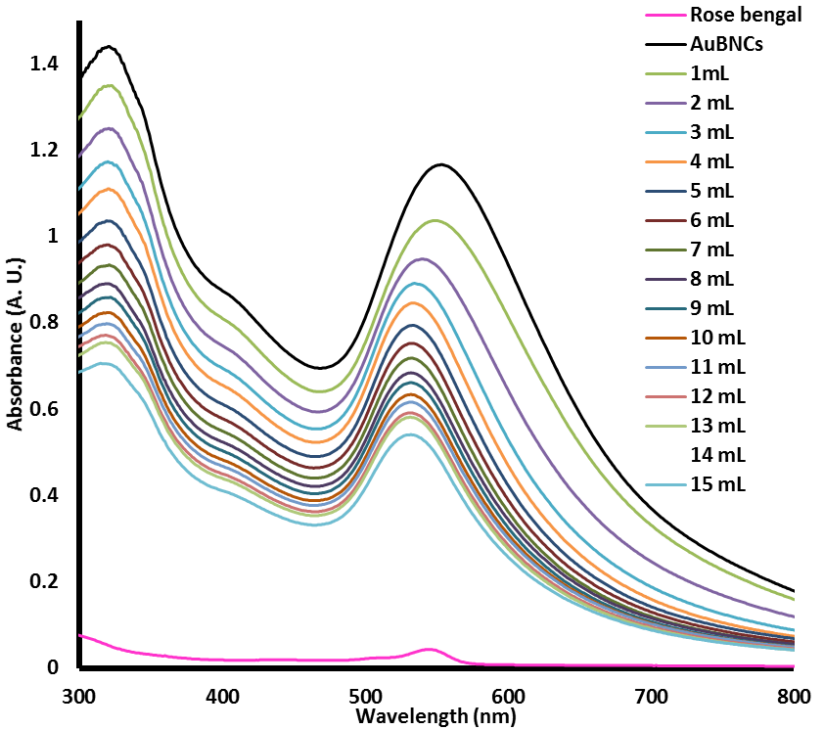

Figure 3.35 UV-vis spectrum of the titration between branched gold nanocrystals and rose bengal

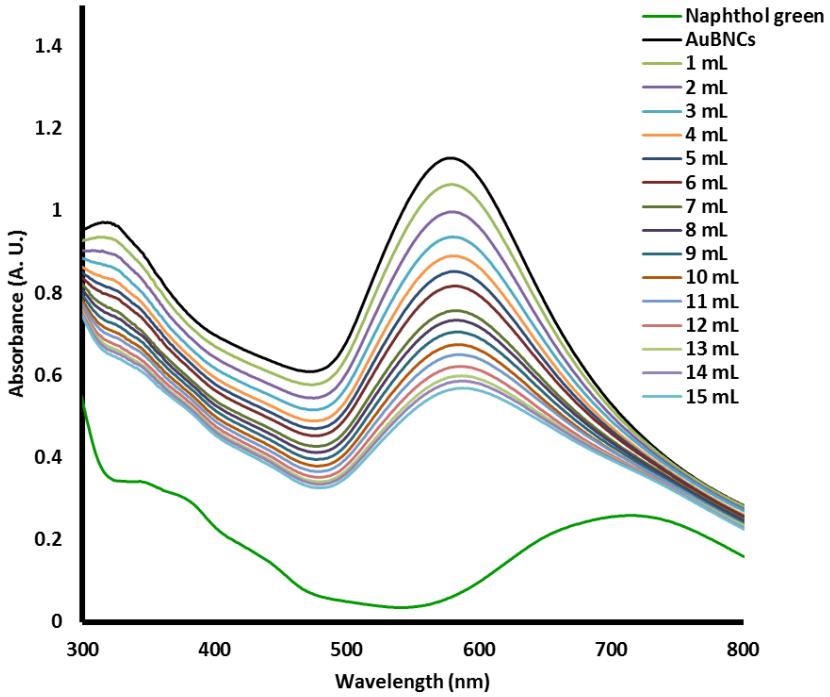

Figure 3.36 UV-vis spectrum of the titration between branched gold nanocrystals and naphthol green

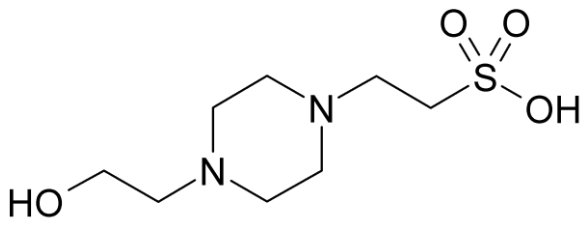

Figure 3.37 The structure of 2-[4-(2-hydroxyethyl)piperazin-1-yl]ethanesulfonic acid (HEPES)

3.4.1.7 Gold nanorods with anionic and cationic dyes

Titration of CTAB-stabilised gold nanorods with cationic dyes showed only expected dilution effects. Examples of the titration of gold nanorods with toluidine blue and acridine orange are shown below (Figures 3.38 and 3.39 respectively). It is clearly seen in the spectrum of toluidine blue and nanorods that there is a steady decrease in intensity of the nanorods absorption (black line) as the titration progresses. In the spectrum of acridine orange and nanorods we see dilution of the nanorods absorption and also an increase in the peak corresponding to the dye as the concentration of dye in the reaction mixture increases. Isosbestic points are also seen on this spectrum. These features, coupled with the conspicuous absence of enhanced dye absorption or red-shifted peaks, indicate there is no interaction between the cationic dyes and gold nanorods.

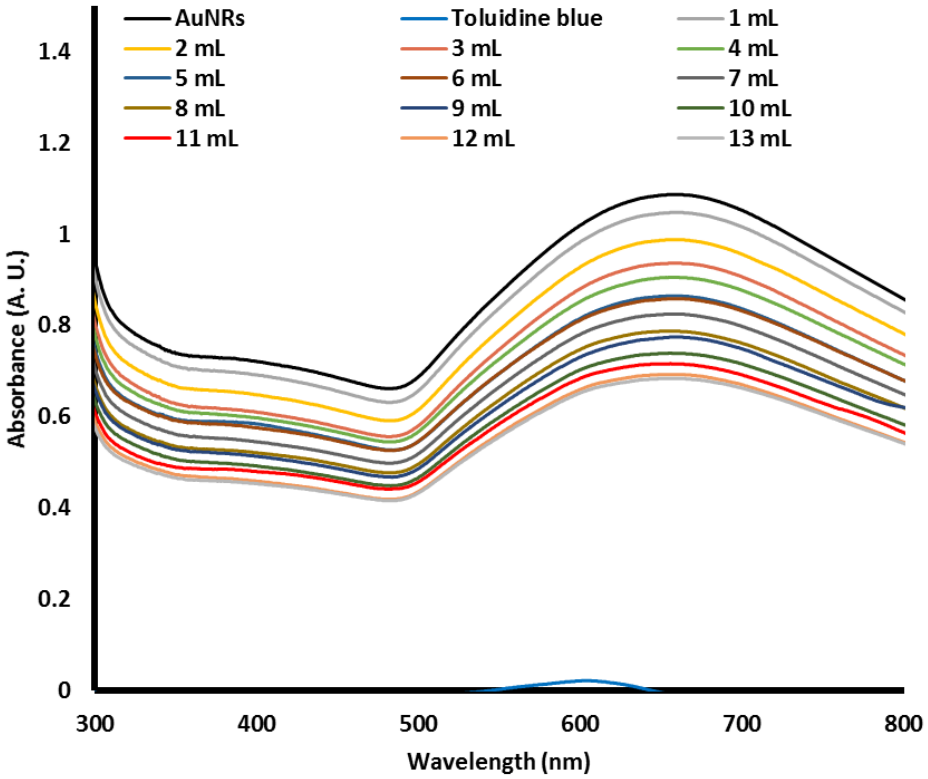

Figure 3.38 UV-vis spectra showing the titration between CTAB-stabilised gold nanorods and 5 µM toluidine blue.

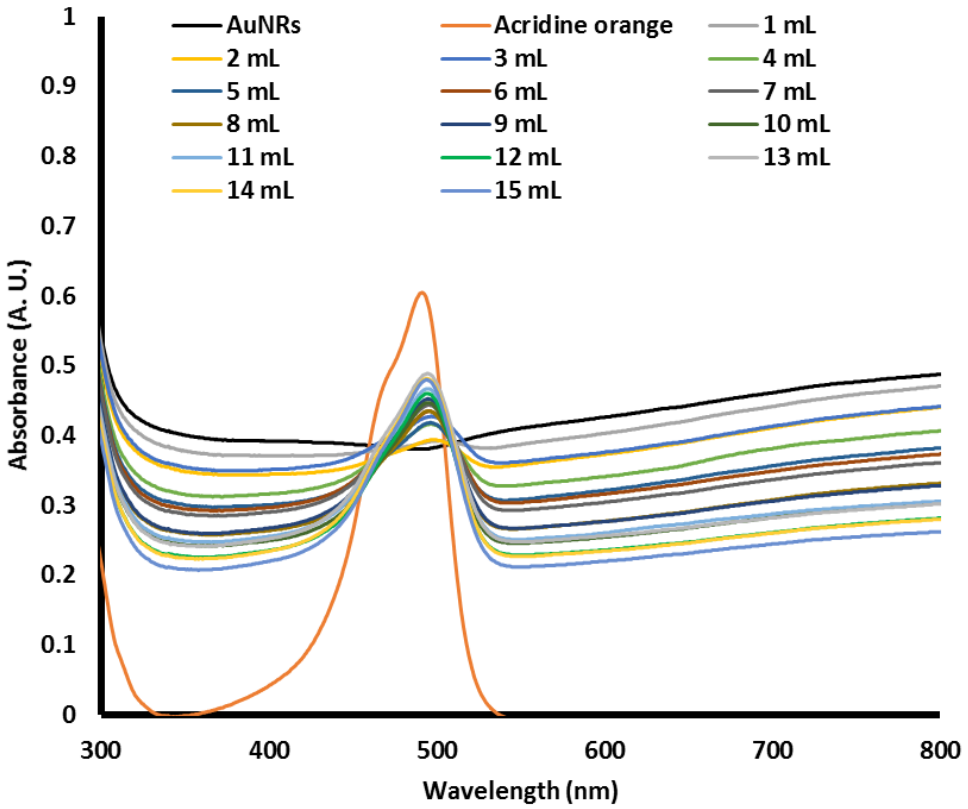

Figure 3.39 UV-vis spectra showing the titration between CTAB-stabilised gold nanorods and 20 µM acridine orange.

Titration between gold nanorods and the anionic dye naphthol green (Figure 3.41) showed different behaviour. Absorption of the nanorods was uniformly increased on addition of one aliquot of naphthol green, followed by a slow decrease in absorption for each subsequent addition. No aggregation peak was seen and no shift of the initial peak was seen, indicating no change in effective particle size. This slight interaction is most likely a result of the nature of stabilising CTAB molecules, which by contrast to citrate carry an overall positive charge (see Figure 3.40 for structure of CTAB). As such, positively charged naphthol green will not be repelled from the ligand shell in the way that the cationic dyes are, resulting in limited interaction between the dye molecule and the surface of the gold.

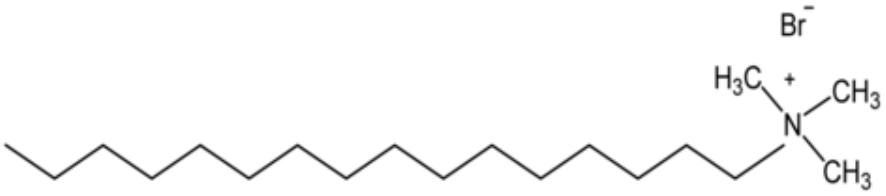

Figure 3.40 The structure of cetyltrimethylammonium bromide (CTAB)

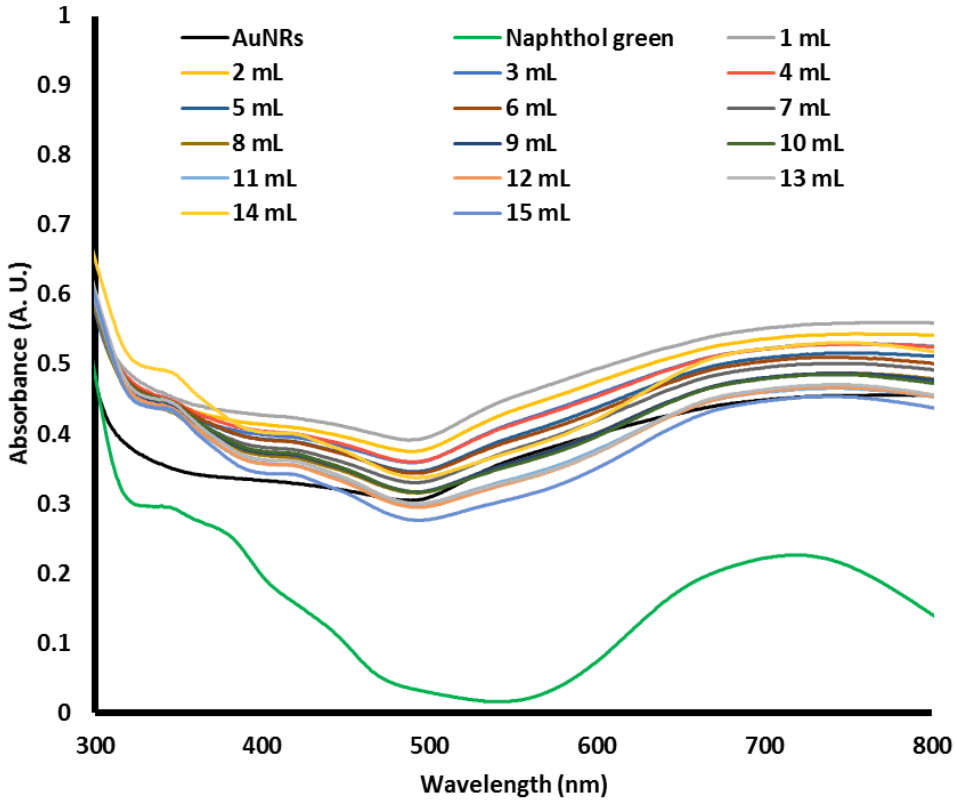

Figure 3.41 UV-vis spectra showing the titration between CTAB-stabilised gold nanorods and 20 µM naphthol green.

3.4.1.8 2-mercaptopropionylglycine-capped silver nanoparticles with cationic and anionic dyes

Synthesis of 2-mercaptopropionylglycine-capped (tiopronin-capped) silver nanoparticles resulted in a dark brown powder. When redispersed in water at a rate of 0.5 mg/mL dark amber solutions formed (see Section 2.4.2). Titration of these solutions with cationic dyes showed zero interaction between the particles and the dyes. No enhanced absorption nor aggregation peaks were seen. The only effects observed were the expected dilution of the

nanoparticle peak as the titration progressed to completion. Example spectra of tiopronin-capped silver particles with the cationic dyes acridine orange (Figure 3.42) and crystal violet (Figure 3.43) are shown, though all cationic dyes tested produced similar graphs. Anionic dyes too showed no interaction with the tiopronin-capped silver particles (Figures 3.44 and 3.45; Ag-tio NPs with rhodamine 6G and 2, 7-dichlorofluorescein respectively). All spectra show isosbestic points, indicating no electronic interaction between nanoparticle and any dyes.

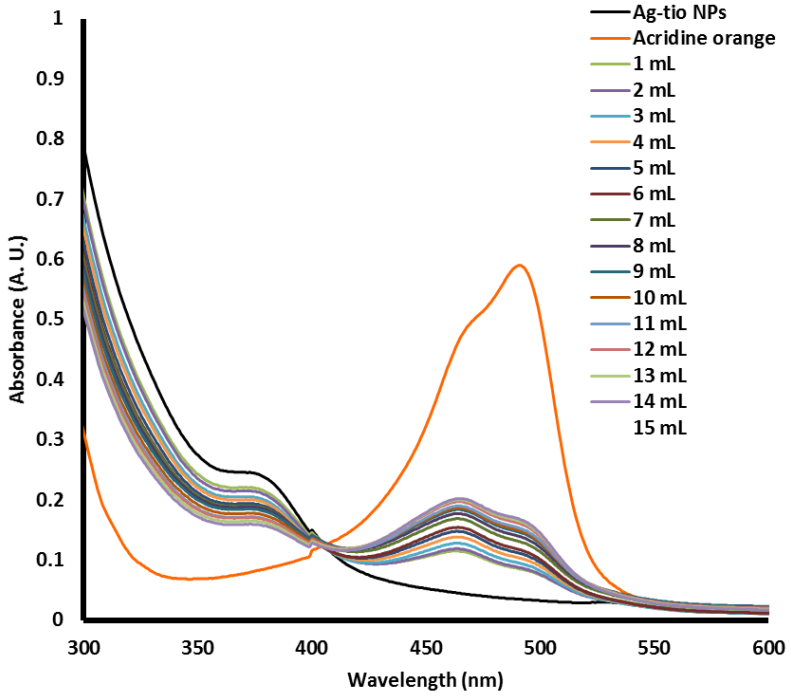

Figure 3.42 UV-vis spectrum of the titration of tiopronin-capped silver nanoparticles (Ag-tio NPs) with acridine orange

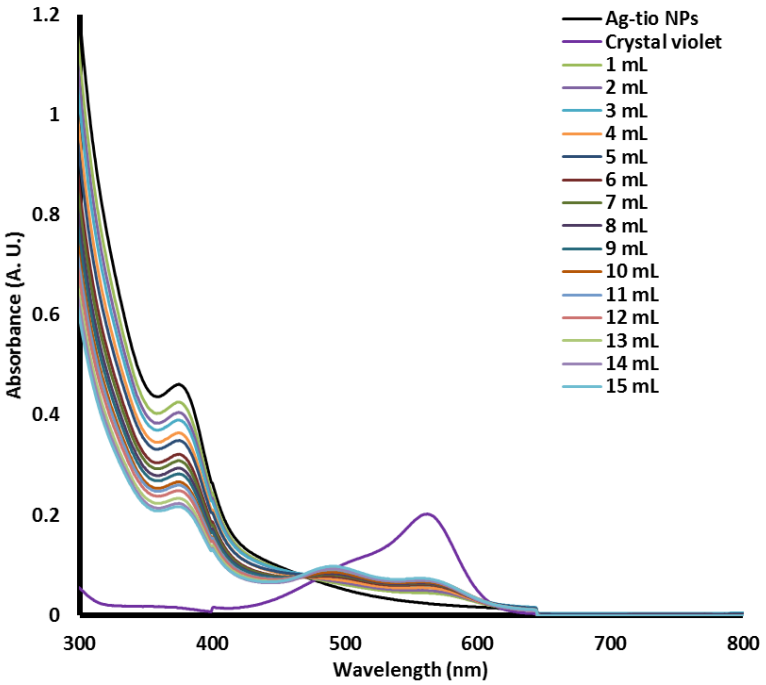

Figure 3.43 UV-vis spectrum of the titration of tiopronin-capped silver nanoparticles (Ag-tio NPs) with crystal violet

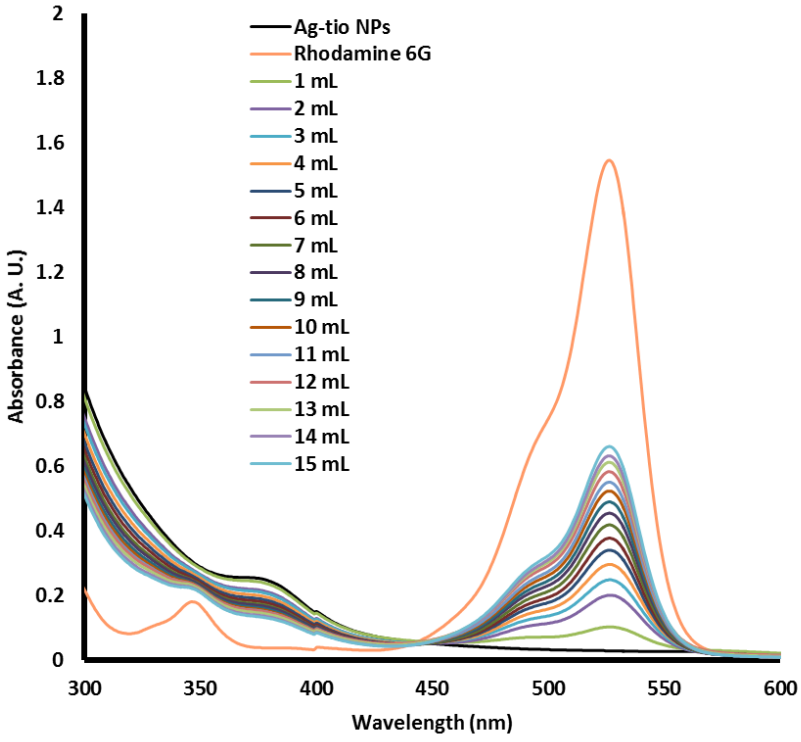

Figure 3.44 UV-vis spectrum of the titration of tiopronin-capped silver nanoparticles (Ag-tio NPs) with rhodamine 6G

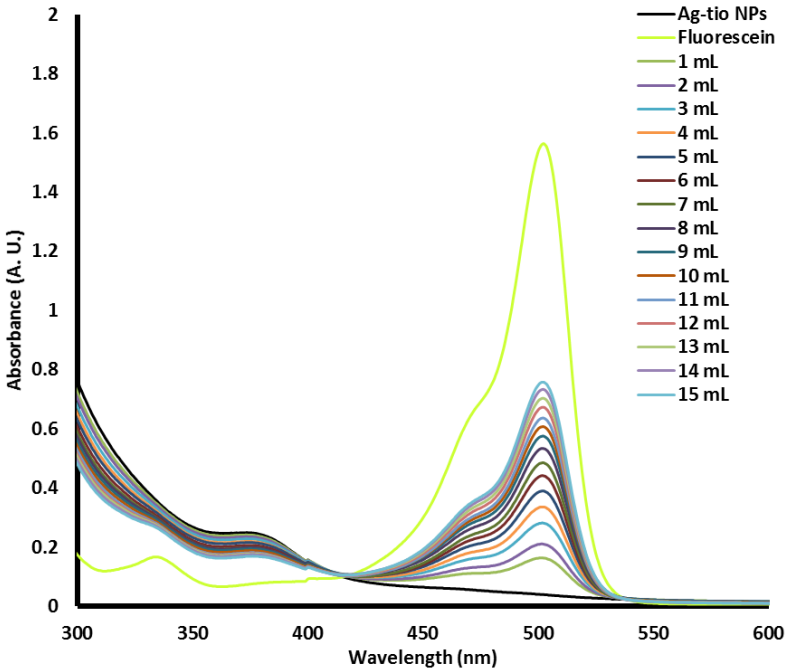

Figure 3.45 UV-vis spectrum of the titration of tiopronin-capped silver nanoparticles (Ag-tio NPs) with 2, 7-dichlorofluorescein

Failure of either cationic or anionic dyes to interact in any way with tiopronin-capped silver particles raises interesting questions. Tiopronin coordinates to the surface of the silver through a sulphur atom (structure of tiopronin shown in Figure 3.46). Ag-S bond enthalphies (217 kJ mol^{-1}) are lower than their Ag-O and Au-O counterparts (238 and 223 kJ mol^{-1} respectively).[336] Citrate ions coordinating through an oxygen atom readily undergo ligand exchange with dye molecules to give destabilised particles and agglomeration in the case of citrate stabilised particles. As the Ag-S bond energy is lower even than Au-O we would expect the dye molecules, coordinating through the amine group, to be able to displace tiopronin from the surface of the nanoparticles. However, the chains of particles that form on sonication are held together by hydrogen bonding between deprotonated carboxylate groups on the tiopronin molecules.[325] It is perhaps the case that the energy required to overcome the hydrogen bonding between tiopronin molecules is sufficient to discourage ligand exchange and to produce the results obtained here, where no interaction was seen with either positive or negatively charged dyes.

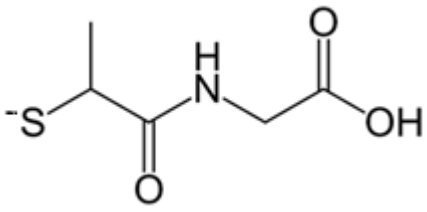

Figure 3.46 The structure of 2-mercaptopropionylglycine (tiopronin).

3.4.2 Particle size measurements for citrate-capped gold nanoparticles: TEM studies and Zetasizer

Particle size studies before, during and after titration were performed for citrate stabilised gold particles due to the emergence of a UV-vis absorption at large red shifts, indicative of aggregation. TEM images of other particles can be found in Chapter 2.

TEM studies of the citrate-capped gold nanoparticles on their own showed well-formed, spherical particles arranged singly or in small groups of 2 - 5 (Figure 3.47). The diameter of the particles largely fell between 10 – 15 nm, skewed towards the smaller end of the scale. Average particle diameter was found to be 11 nm. This corresponds well with dynamic light scattering (DLS) studies on a solution of the gold particles, where the average hydrodynamic diameter was observed to be 20.5 nm. The hydrodynamic diameter takes the capping and solvent layers into consideration and is typically twice that of the inorganic core, thus a hydrodynamic diameter of this size agrees well with the observed average particle size of approximately 11 nm.

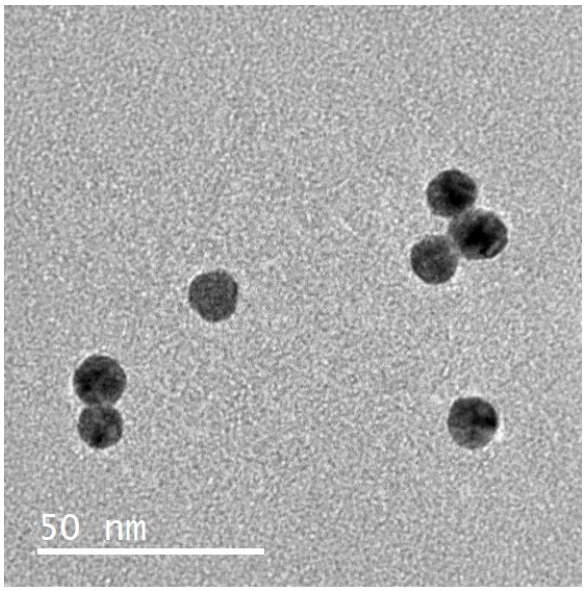

Figure 3.47 TEM image showing gold nanoparticles synthesised by the Turkevich method

TEM images of gold nanoparticle samples after cationic dye solutions had been added showed some significant differences to those of the nanoparticles alone. Images taken of a gold nanoparticle solution to which 4 mL of toluidine blue had been added (corresponding to a dye concentration of 1 µM) showed significant aggregation of the particles (Figure 3.48b). Arrays expanded over several hundred nanometres and consisted of discrete particles in close proximity to each other, though there were still particles in smaller groups and indeed found singly. Increasing dye concentration to 1.2 µM by adding 5 mL of toluidine blue increased the size of the arrays to several micrometres in diameter with very few particles found outside the aggregates (Figure 3.48c). Increasing the dye concentration further to 1.4 µM (6 mL added; the critical concentration at which enhanced maximum absorption is observed in the UV-vis) yielded larger, multi-micrometre aggregates in which the particles had begun to disintegrate into smaller fragments (Figure 3.48d). This differs from the discrete, well-formed spherical particles in the previous three images. The broken down particles form a large globular matrix surrounding particles which have not yet disintegrated, vastly increasing perceived particle size. This correlates excellently with the data from the Zetasizer measurements on the toluidine blue – gold nanoparticle system (Figure 3.52; blue

line), which showed a sudden increase in hydrodynamic radius of the particles after 5 mL toluidine blue had been added to the system.

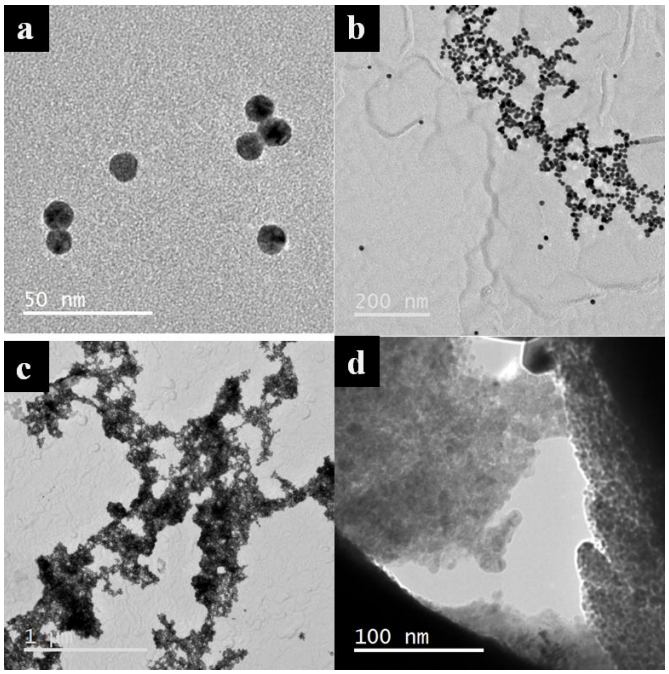

Figure 3.48 TEM images showing (a) gold nanoparticles made by the Turkevich method before dye solutions were added; (b) gold nanoparticles to which 4 mL of toluidine blue had been added; (c) gold nanoparticles to which 5 mL toluidine blue had been added; (d) gold nanoparticles to which 6 mL toluidine blue had been added.

Studies on the crystal violet-gold nanoparticle system showed similar results. Below the critical concentration particles are arranged singly or in small clusters of <5 (Figure 3.49a). Close to the critical concentration we start to see aggregation into chain-like arrays (Figure 3.49b). Typically these arrays were 200-300 nm in length. Increasing the concentration of the dye to well above critical resulted in continued aggregation into micrometre-scale, multidirectional arrays. As in the toluidine blue experiments the particles start to break down and/or grow together and become much less well-formed, resulting in cloudy areas on the TEM images. This series of TEM images showing increase in effective particle size from 5 mL crystal violet added onwards corroborates closely with the Zetasizer data gathered on the same system (Figure 3.52; purple line).

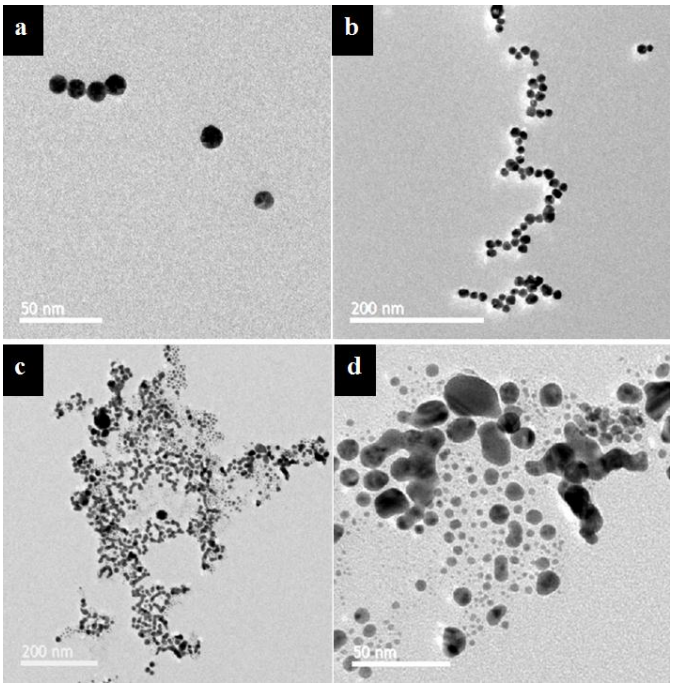

Figure 3.49 TEM images showing the formation of aggregates as crystal violet is added to a solution of gold nanoparticles: (a) 3 mL crystal violet added; (b) 6 mL crystal violet added; (c) and (d) 10 mL crystal violet added.

Acridine orange yields analogous results. From a well-dispersed starting point (Figure 3.50a), at the critical concentration of 3.2 μM (3 mL acridine orange added) particles aggregated into micron-scale arrays (Figure 3.50b). Increasing dye concentration past the critical point caused the breakdown of particles into fragments and a degree of particle growth (Figure 3.50c and 3.50d). Zetasizer studies showed increase in hydrodynamic radius over the course of the experiment (Figure 3.52; orange line), agreeing well with the TEM images in Figure 3.52.

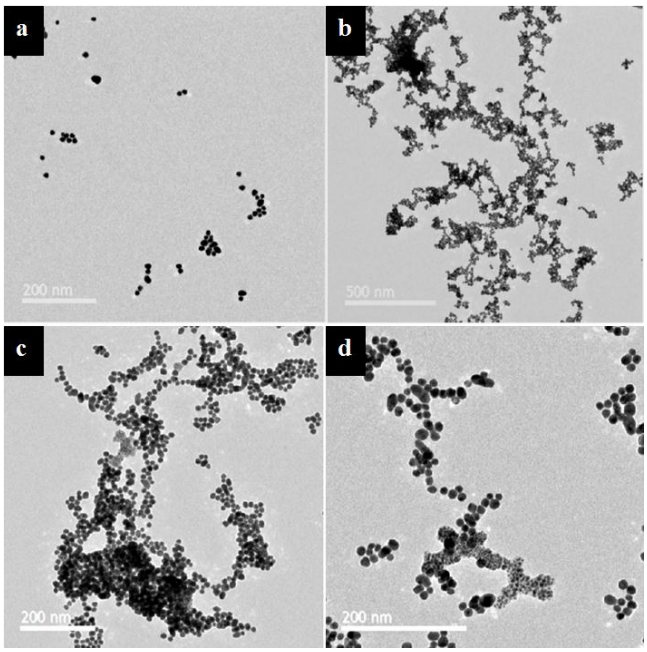

Figure 3.50 TEM images showing the formation of aggregates of nanoparticles as acridine orange was added to a solution of gold nanoparticles: (a) 1 mL acridine orange added; (b) 3 mL acridine orange added; (c) 7 mL acridine orange added; (d) 10 mL acridine orange added.

A potential reason for the disintegration and globularisation of the nanoparticles at high dye concentrations is ligand exchange. Loss of the citrate shell as the particles undergo ligand exchange with the dye molecules could cause destabilisation of the surface and consequent fusion of the nanoparticles in an effort to reduce surface area and thus surface energy.

Experiments with malachite green and gold nanoparticles follow a similar pattern but to a lesser degree (Figure 3.51). This supports UV-vis data from this study which showed a small shoulder corresponding to aggregation rather than a large, well-defined peak. Zetasizer data also supported this (Figure 3.52; green line), as a much lower degree of aggregation was detected for malachite green than any of the other cationic dyes: 583nm, compared to 1654, 1382 and 2230 nm for toluidine blue, crystal violet and acridine orange respectively. It is unclear why malachite green aggregates to a lesser extent than the other cationic dyes used; this would be the subject of further work.

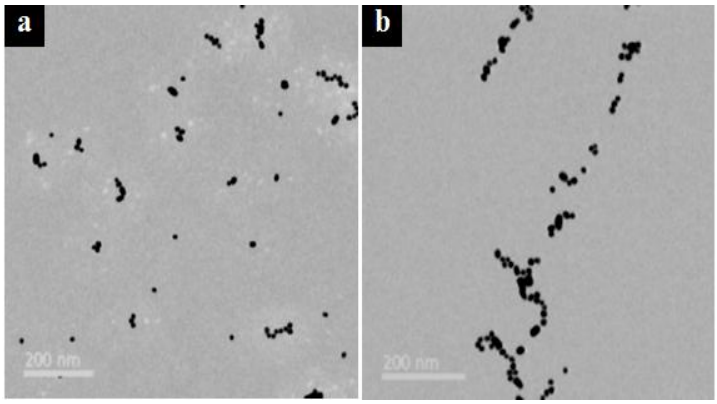

Figure 3.51 TEM images showing the formation of aggregates as malachite green was added to a solution of gold nanoparticles: (a) 3 mL malachite green added; (b) 6 mL malachite green added.

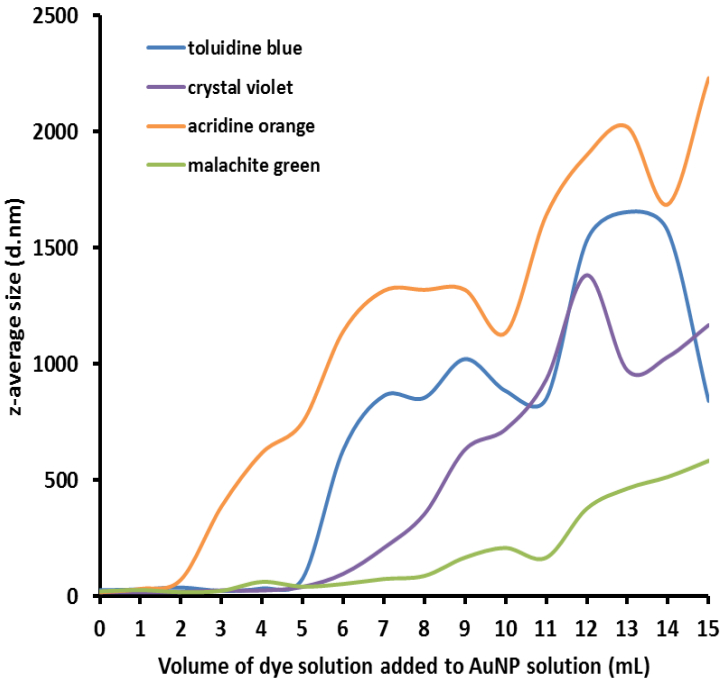

Figure 3.52 Graph showing the increase in observed hydrodynamic radius of gold nanoparticles as dyes are added to the nanoparticle solution.

To the best of our knowledge TEM and Zetasizer analysis of the interaction of dyes with gold nanoparticles and observation of the aggregation that occurs had not been reported previously.

3.5 Conclusions

It was shown that citrate-stabilised gold nanoparticles interact strongly with cationic dyes and trigger agglomeration of the nanoparticles into large, micrometre-scale arrays. This is

accompanied by a new peak developing on the UV-vis spectra at a large red shift, concurrent with increasing effective particle size. Enhanced absorption of this peak was observed for toluidine blue (previously reported[43]), crystal violet and acridine orange. This phenomenon has not, to the best of our knowledge, been reported for crystal violet or acridine orange. From the results obtained it is unclear why this effect is seen for acridine orange, crystal violet and toluidine blue but not malachite green, a structurally similar like-charge dye. From our results it is not clear why this is the case; future work concerning the nature of the interaction between the dyes and nanoparticle surface such as time-correlated single photon counting (TCSPC) and DFT could help to elucidate the reasons behind this.

None of the anionic dyes tested produced aggregation or enhanced absorption. As anionic dyes failed to cause aggregation in the same manner as cationic it is clear that agglomeration of the particles is not solely due to an increase in the ionic strength of the solution as previously asserted in the literature. The charge present on the dyes plays an important part in aggregation due to electrostatic attraction or repulsion between the dye molecules and the citrate shell. Silver nanoparticles made by analogous methods to the gold samples showed no interaction with either anionic or cationic dyes. It is thought that lower gold-oxygen bond energies compared to silver-oxygen cause citrate to be more weakly bonded to the surface of the gold particles. Combined with the low affinity of amine groups for silver compared with the gold, it is thought that ligand exchange is favourable with amine-containing dyes on gold particles but not silver. Bimetallic particles synthesised in an analogous way behaved erratically, with no predictable pattern to the results. It is suggested that the erratic behaviour of the silver-gold alloyed particles is a result of the variation in size, shape and surface composition obtained using this synthesis.

In the case of zero interaction being recorded for tiopronin-capped silver particles it is postulated that the extra energy required to overcome hydrogen bonding between tiopronin

molecules in the thiolate chains makes ligand exchange unfavourable. Branched gold nanocrystals also showed no interaction with either class of dye, which is thought to be a consequence of strong Au-S covalent bonds present between the surface of the particles and the HEPES molecules. CTAB-stabilised gold nanorods showed no interaction with cationic dyes but a small different in the spectrum when titrated with anionic naphthol green, suggesting the net-positively charged CTAB sheath plays a role in allowing the interaction.

CHAPTER 4 : THE ANTIMICROBIAL CAPACITY OF CITRATE-STABILISED GOLD AND SILVER NANOPARTICLE-DYE CONJUGATES IN POLYURETHANE

4.1 Aims

This chapter presents the functional testing of some of the nanoparticle-dye conjugates seen in Chapter 3. Citrate-stabilised gold and silver nanoparticles were used with acridine orange, crystal violet and malachite green. The combinations were incorporated into polyurethane and the antimicrobial properties of the resultant surfaces evaluated. Excellent results against both gram positive and gram negative bacteria were seen for gold and silver particles with crystal violet and acridine orange. Acridine orange with citrate-stabilised silver nanoparticles, a previously unreported combination, outperformed all other samples, effecting total kill of *S. aureus* and *E. coli* within five hours in both light and dark conditions. The rapidity and potency of the photobactericidal response combined with excellent dark kill ability makes this an exciting possibility for fabrication of commercial self-sterilising surfaces.

4.2 Introduction and motivations

4.2.1 Nosocomial infections

Nosocomial infections – that is, infections which are acquired in hospital - affect an estimated 9% of all hospital patients and represent 50% of all hospitalization complications.[288] These preventable infections are a huge drain on health care resources worldwide, costing an estimated £1 billion per year in the UK alone.[289] The emergence of drug-resistant strains of common pathogens as a consequence of antibiotic overprescription has added a new dimension to this struggle as we race to find new, novel treatments where conventional antibiotic therapy fails.[341]

It is estimated that 8/10 nosocomial infections are transmitted by touch. Though high standards of personal hygiene are recommended in hospitals, compliance with recommended protocol is low among staff, patients and visitors alike.[287,292,342] Frequently touched surfaces in hospitals (such as door handles, bed rails, surgical trays, telephones) can act as 'reservoirs' for pathogenic bacteria to be spread around.[343] Infections of staff and other personnel by direct contact with patients is much less likely than by contact with a colonised surface. Thus, if surfaces can be made self-sterilising the rate of nosocomial infections could be significantly reduced.

4.2.2 Light activated antimicrobial surfaces

A possible simple method to achieve this aim is to fabricate reservoir surfaces out of photosensitizer-impregnated polymers. Photosensitizers are light activated antimicrobial agents (LAAA) which can be used for PDT, which has been proposed as a promising alternative to antibiotics to treat common bacterial infections.[248] This novel process uses a photosensitizer (most commonly a dye) to kill bacteria *via* the production of singlet oxygen.[344] Mechanistically, there are three phases of PDT: excitation of the photosensitizing molecule, generation of cytotoxic oxygen species, followed by cell death. In the first phase the photosensitizer is exposed to light (either white or of a target wavelength) and absorbs a photon of specific frequency, promoting the dye molecule to a high-energy triplet state. The second stage sees interaction of the excited state with molecular O_2, producing either a reactive oxygen species (ROS) or singlet oxygen. Both of these species are highly cytotoxic and induce cell death by destroying vital cell features such as mitochondria, lysosomes, cell walls, membranes and by attacking DNA.[345] This process is summarised in Scheme 4.1. It is believed that the likelihood of microbes developing a resistance to this treatment is extremely low, as singlet oxygen utilises a non-specific, multi-site mechanistic mode of destroying microorganisms.[301,304,346]

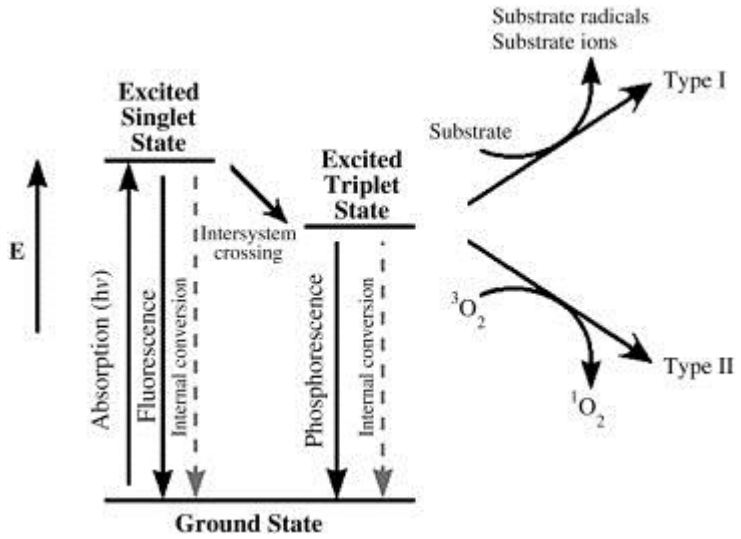

Scheme 4.1 Illustration showing the mechanism of photodynamic therapy

Incorporation of these LAAAs into surfaces could therefore have great benefit in reducing the numbers of bacteria present on commonly handled objects and surfaces. The concept of self-sterilising surfaces is one which has gathered a lot of momentum in recent years as PDT has becoming increasingly widely studied. Inorganic surfaces such as titania,[347,348] glass[349,350] and polymers[298,351] have been investigated for this application, but impregnation of polymers with LAAAs offers one of the most facile and versatile solutions to the problem due to the flexibility and relative cheapness of the material, durability and ability to choose which LAAAs are required for a certain application. A range of polymers such as cellulose acetate[295,351,352], polymer resins[353] and silicone[354] have been utilised for this purpose, combined with many different dyes from both the triarylmethyl[61,355,356] and phenothiazine families.[295,301,352,357] General photobactericidal effect was found to be good, with a more efficacious kill (in terms of rapidity and reducing number of viable counts) observed against gram positive pathogens than gram negative. Gram positive bacteria are differentiated from gram negative by a difference in cell wall structure: gram positive species have a thick peptidoglycan cell wall, whereas gram negative cell walls contain a thin peptidoglycan layer enveloped in a thick plasma membrane.[358] This protective plasma membrane affords additional protection to

gram negative organisms and renders them harder to kill by both PDT and traditional antibiotic methods.

4.2.3 Conjugation of LAAAs and nanomaterials

The potency of the LAAAs can be increased by conjugation with a nanomaterial. Solution studies have shown that combining toluidine blue with gold nanoparticles (2 nm and 15 nm) can enhance bacterial kill rates by an order of one log10 compared to toluidine blue alone.[282] In polymers, a combination of methylene blue with size-specific gold nanoparticles has been shown to enhance photobactericidal kill against both gram positive and gram negative bacteria compared to methylene blue-impregnated polymers only.[298,305,306] Seemingly the size of nanoparticle incorporated into the polymer-dye system is vital: incorporation of gold nanoparticles over 20 nm in diameter showed a decrease in the antibacterial activity of methylene blue-silicone samples against gram-positive and negative bacteria.[305] 5 nm diameter gold particles in the same methylene blue-silicone system produced no noticeable enhancement of bacterial kill against *E. coli* compared to methylene blue alone, but did show an enhancement (ca. 0.3 log) when assays against *S. epidermis* were carried out. Smaller particles ~2 nm in diameter gave even greater activity, increasing bacterial kill by one log10 against *E. coli* and reducing bacterial numbers to below the detection limit (≥ 4 log reduction; ≥99.99% kill) for *S. epidermis*.[305] 2 nm gold particles were successfully used to enhance the inactivation of both *E. coli* and *S. epidermis* by significant amounts.[301,306] Silicone containing 2 nm gold particles alone did not show any photobactericidal ability,[306] thus the enhancement of bacterial kill rates observed on the addition of these particles to methylene blue-containing polymers was deduced to be as a result of a synergic interaction between the dye molecule and nanoparticle. Metal oxide particles have also been shown to have a potent light activated antimicrobial effect when combined with gold nanoparticles.[308] More specialised pre-clinical studies found that a 50% reduction in *S. epidermis* biofilm was

achieved using methylene blue and nanogold-impregnated silicone treated with laser illumination for 10 minutes per hour.[307]

Activation of the polymers can either be of short duration, using laser illumination,[309] or of longer duration under standard white lighting.[359] For self-sterilising surfaces it is advantageous that the photobactericidal effect is triggered under normal light conditions to circumvent the need for specialist equipment and to make them useful in a wider variety of situations.

To be of use as self-sterilising surfaces the modified polymers must fulfil a number of additional criteria: they must be non-toxic to humans, not leach out as a consequence of routine washing, be durable and also be environmentally benign. Though covalent attachment of dyes to the surface of polymers can be achieved,[360] a simple swell-encapsulation-shrink method has been used extensively to great effect.[309,359] As noted previously, the latter process immerses a polymer in a swelling solution containing a solvent (such as acetone) and the molecule or particle to be encapsulated. The solvent causes the polymer matrix to expand, allowing diffusion of the dye or particle into the bulk of the substrate. After the desired time frame, the polymer is removed from the swelling solution and allowed to dry. The solvent evaporates and allows the polymer matrix to return to its original size, immobilising the dye molecules or nanoparticles in the sample. Thus trapped, the target molecules should remain within the polymer and be resistant to leaching. This is highly important if the polymers are to be used in healthcare settings, either *in vivo* or not.

Concerning toxicity towards humans, studies have shown that antimicrobial PDT systems which show good photobactericidal ability do not result in cytotoxicity towards mammalian cells.[361,362] Mammalian cells are larger than bacterial, thus a higher concentration of photosensitizing molecules and longer illumination times are required produce sufficient singlet oxygen/ROS to induce cell death.[346] These levels are not necessary for bacterial cells,

thus concentrations of photosensitizers able to kill bacteria effectively are non-toxic to humans.[363] Advantageously, due to their greater susceptibility it has been shown to be possible to kill bacteria not only on the surface of the LAAA-modified polymer, but also up to 0.65 mm away from it.[359] This has great potential in healthcare situations to reduce biofilm formation on reservoir surfaces.

In this work, we report the lethal sensitization of *E. coli* and *S. aureus* by polyurethane impregnated with a range of dyes and either gold or silver nanoparticles using the aforementioned swell-encapsulation-shrink method. The nanoparticles were synthesised using the citrate-reduction method. These bacterial species were chosen as representative of common nosocomial pathogenic species (*S. aureus* accounts for 16% of all nosocomial infections [29% of which were found to have resistance to methicillin] and *E. coli* is particularly prevalent in obstetrics[364]). It was found that polyurethane embedded with gold nanoparticles showed no intrinsic toxicity towards either species. Silvernanoparticle-only samples showed good activity against gram negative *E. coli* but failed to induce kill against *S. aureus*. Addition of gold and silver nanoparticles showed enhancement of the antimicrobial properties of the dyes. Addition of silver nanoparticles to crystal violet and acridine orange resulted in excellent photobactericidal ability against both gram-positive and gram-negative organisms, both giving total kill over five hours under white light. Both systems also showed good dark kill ability (acridine orange and silver nanoparticles induced complete kill against *E. coli* in five hours) giving them huge promise as antimicrobial surfaces. Despite the antibacterial effects of silver nanoparticles being well-known,[365–369] to the best of our knowledge this is the first reported incidence of using silver nanoparticles in conjunction with LAAAs to fabricate self-sterilising surfaces. It is also the first report of acridine orange being used for such a purpose, and the potency of its bactericidal effects when combined with noble metal nanoparticles is highly exciting.

4.3 Experimental methods

4.3.1 Synthesis of nanoparticles

4.3.1.1 Synthesis of gold and silver citrate stabilised nanoparticles.

Nanoparticles of gold and silver were synthesised using the same modified Turkevich method described in Sections 2.3.1.1 and 2.3.1.2 respectively.

4.3.1.2 Nanoparticle characterisation techniques

UV-vis absorption spectra of nanoparticle and dye solutions were recorded using a Shimadzu UV-1800 Spectrophotometer. Plastic cuvettes with a light path length of 10 mm were used. Absorption was measured over the spectral range 200 – 1000 nm.

TEM micrographs were taken using a Jeol 200 kV TEM. Samples of the particles without dyes were prepared by evaporating drops of the aqueous nanoparticle solution onto carbon coated copper grids.

4.3.2 Preparation of dye solutions

Two methods of incorporating dyes into the polymer samples were used. Malachite green and crystal violet were post-coated onto the surface of the polymer samples; acridine orange and naphthol green were swell encapsulated into the polymer matrix. The dyes used in this work are shown with their structures in Table 4.1.

Post-coating solutions were made up by dissolving solid dye in deionised water to make 1 mM solutions.

Swell encapsulation solutions were created by making a 9:1 acetone:water solution then saturating it with solid dye.

Table 4.1 The names and structures of the dyes used in the antimicrobial investigation

Dye	Structure
	Cationic dyes

Malachite green	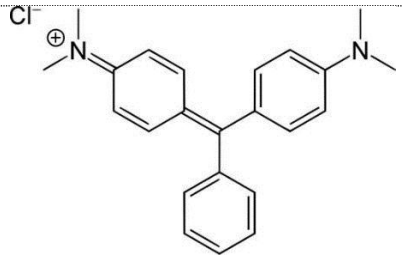
Crystal violet	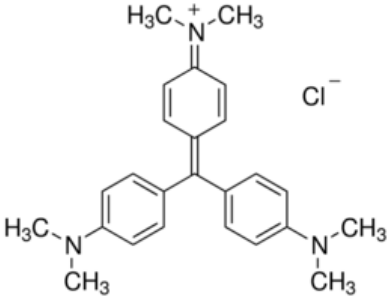
Acridine Orange	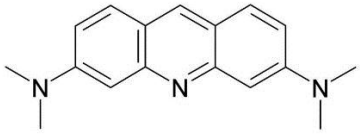
	Anionic dyes
Naphthol green B	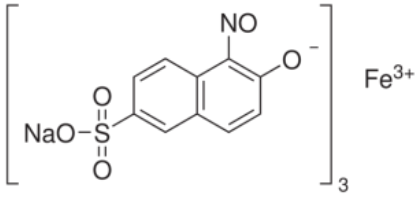

4.3.3 Polymer samples for antimicrobial testing

All synthetic work used medical grade flat polyurethane sheets (thickness 0.8 mm; purchased from American Polyfilm Inc) as the substrate. The sheet polyurethane was cut into approximately 10x10 mm squares.

The following samples were made up for antimicrobial testing:

1. Control samples. Treated in a 9:1 acetone to water swelling solution for 24 hours then dried overnight.

2. Citrate-capped gold nanoparticle treated samples. Treated in 9:1 acetone to gold nanoparticle solution for 24 hours, then dried overnight. These were split into five sub-categories:
    i. Gold-only. No further treatment
    ii. Gold-crystal violet. Samples post-coated with 1 mM aqueous crystal violet solution for 24 h, then dried overnight.
    iii. Gold-naphthol green. Samples post-coated with 1 mM aqueous naphthol green solution for 24 h, then dried overnight.
    iv. Gold-acridine orange. Samples treated with acridine orange-saturated 9:1 acetone to water solution for 24 h, then dried overnight.
    v. Gold-malachite green. Samples treated with malachite green-saturated 9:1 acetone to water solution for 24 h, then dried overnight
3. Citrate-capped silver nanoparticle treated samples. Treated in 9:1 acetone to silver nanoparticle solution for 24 hours, then dried overnight. These were split into five sub-categories:
    i. Silver-only. No further treatment
    ii. Silver-crystal violet. Samples post-coated with 1 mM aqueous crystal violet solution for 24 h, then dried overnight.
    iii. Silver-naphthol green. Samples post-coated with 1 mM aqueous naphthol green solution for 24 h, then dried overnight.
    iv. Silver-acridine orange. Samples treated with acridine orange-saturated 9:1 acetone to water solution for 24 h, then dried overnight.
    v. Silver-malachite green. Samples treated with malachite green-saturated 9:1 acetone to water solution for 24 h, then dried overnight.
4. Dye-only samples. These were created by taking control samples with no nanoparticles. The four dye-only samples were as follows:

i. Crystal violet. Samples post-coated with 1 mM aqueous crystal violet solution for 24 h, then dried overnight.

ii. Naphthol green. Samples post-coated with 1 mM aqueous naphthol green solution for 24 h, then dried overnight.

iii. Acridine orange. Samples treated with acridine orange-saturated 9:1 acetone to water solution for 24 h, then dried overnight.

iv. Malachite green. Samples treated with malachite green-saturated 9:1 acetone to water solution for 24 h, then dried overnight.

The full range of samples used is summarised in **Table 4.2.**

All samples were treated and handled in ambient temperatures and light conditions. Samples were dried in covered transparent petri dishes to ensure minimal contamination of the sample surface.

Table 4.2 A summary of the polyurethane samples used in antimicrobial testing. Control indicates sample treated with solvent only. Au- and Ag only refer to samples containing either citrate-capped gold or silver nanoparticles exclusively. CV, AO, MG and NG-only denotes samples treated with crystal violet, acridine orange, malachite green or naphthol green dyes only. Au-CV refers to samples containing both gold nanoparticles and crystal violet, Ag-CV to silver nanoparticles and crystal violet. Other dye-nanoparticle combinations are denoted similarly.

	Control	**Gold NPS**	**Silver NPs**
Control	Control	Au only	Ag only
Crystal violet	CV only	Au-CV	Ag-CV
Acridine orange	AO only	Au-AO	Ag-AO
Malachite green	MG only	Au-MG	Ag-MG
Naphthol green	NG only	Au-NG	Ag-NG

4.3.3.1 Characterisation of polymer samples

UV-vis absorption measurements were taken on a Lambda 950 spectrophotometer over the spectral range 800-200 nm. Water contact angle measurements of a ~5 µL drop of deionised

water were obtained using a FTA 1000 Drop Shape instrument. Droplets were dispensed by a gauge 30 needle with a side-photographing camera. Data were analysed using FTA32 software.

4.3.4 Antimicrobial activity assays

The antibacterial activity of all samples was tested against *S. aureus* 8325-4 and *E. coli* ATCC 25922. These bacteria were stored in a Brain-Heart-Infusion broth (BHI, Oxoid) containing 20% glycerol by volume and were kept at a temperature of -70 °C. *S. aureus* was propagated onto Mannitol Salt agar (MSA, Oxoid) whereas *E. coli* was propagated on MacConkey agar (MAC, Oxoid). In both cases there was a maximum of 2 subcultures at intervals of 14 days.

The procedure used is an adaptation of that used by Noimark *et al.* at the Materials Chemistry Research Centre at University College London.[309] BHI broth was inoculated with a single colony before being cultured in air at 37 °C for 18 hours with shaking at 200 rpm. The mixture was centrifuged and the pellet recovered and washed in PBS (10 mL). Further centrifugation recovered the pellet again before the bacteria were re-suspended in PBS (10 mL). Thousand-fold dilution of this suspension produced an inoculum of approx. 10^{-6} cfu mL^{-1}. The inoculum was confirmed by plating 10-fold serial dilutions on agar for viable counts.

Duplicates of each polymer sample type were inoculated with 25 mL of inoculum and covered by a sterile cover slip. Samples were then either irradiated by white light (General Electric 28 W Misert T5 2D compact fluorescent lamp) or maintained in the dark for the same duration. The light source emitted an average of 6600 ± 990 lux and was set a distance of 0.25 m away from the samples.

Once irradiation was complete the samples and cover slips were added to PBS (450 mL) and vortexed (20 s). The resultant suspension and 10-fold serial dilutions were plated on agar for viable counts. Aerobic incubation of the plates at 37 °C for either 48 or 24 hours (*S. aureus* and *E. coli* respectively) was carried out.

Each experiment used at least two technical replicates and was repeated three times.

Bacterial kill rates are expressed as a log reduction, where 1 log reduction = 90% bacteria killed; 2 log reduction = 99% bacteria killed; 3 log reduction = 99.9% bacteria killed etc. The statistical significance of the nanoparticle, dye and dye-nanoparticle samples vs. control in both light and dark conditions was analysed in SPSS (IBM) using the Mann–Whitney U test.

4.4 Results and discussion

4.4.1 Nanoparticle synthesis

Gold and silver nanoparticles were synthesised by a modified Turkevich method. Gold particles produced by this method were predominantly spherical in shape, well-formed and regular. Particle size ranged from 8 nm-15 nm, with the average particle diameter found to be 11 nm. Silver nanoparticles formed by analogous methodology were slightly larger on average (~20 nm, though particles were not uniformly spherical) and occupied a much larger range of particle diameters (5 – 40 nm). This disparity of size and shape between gold and silver citrate-capped particles has been previously reported in literature.[370] TEM images of both citrate capped metallic nanoparticles are shown in Figure 4.1.

The gold nanoparticle solution produced using the citrate reduction method had a characteristic deep red colouration. Silver nanoparticle solutions were a slightly cloudy yellow. UV-vis studies on the solutions showed SPR peaks at 402 nm for silver and 519 nm for gold (Figure 4.2).

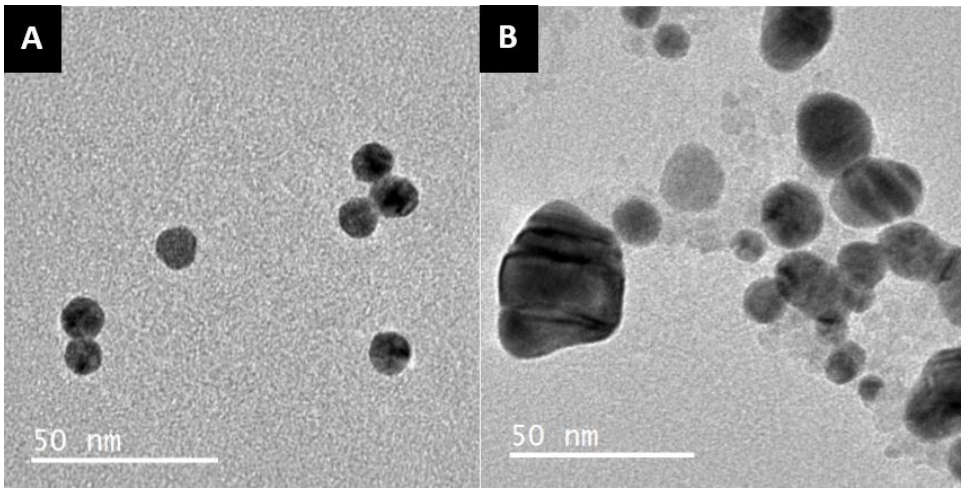

Figure 4.1 TEM images showing A) citrate capped gold nanoparticles showing good uniformity of size and shape, and B) citrate-capped silver nanoparticles produced by the same method showing a greater spread of particle sizes and less regular shape.

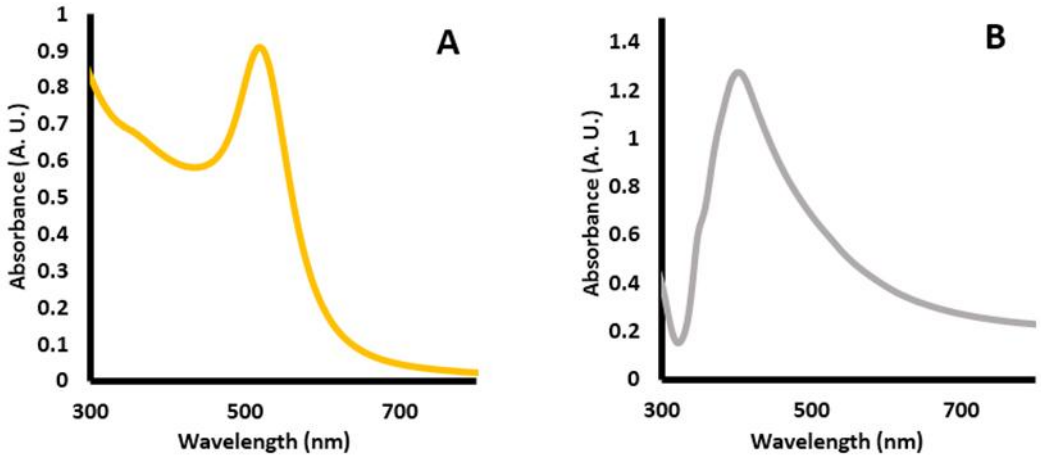

Figure 4.2 Graphs showing the UV-vis spectra of A) citrate-capped gold nanoparticles, showing characteristic SPR band at 519 nm, and B) citrate-capped silver nanoparticles showing SPR band at 402 nm.

4.4.2 Polymer samples

10 x 10 mm squares of medical grade polyurethane were exposed to swelling solutions containing a 9:1 ratio of acetone to aqueous nanoparticle solution. The polymer samples were left in the swelling solution for 24 h, allowing the polymer matrix to expand and the nanoparticles to diffuse into the bulk. Samples were allowed to dry at room temperature in ambient light. Samples exposed to an acetone-gold nanoparticle swelling solution exhibited a change in colour from translucent creamy white to pinkish, indicating successful

incorporation of the nanoparticles into the polymer. Silver analogues showed very slight yellow colouration after swelling, though the change was not as noticeable most likely due to the similarity in colour between the nanoparticles and polymer. UV-vis studies of these changes are shown in Section 4.4.2.1.

Dyes were incorporated into the nanoparticle-doped polyurethane samples *via* either a second swell-encapsulation-shrink step or post-coating. Acridine orange and naphthol green were both incorporated using a second swelling step. A 9:1 acetone to saturated aqueous dye solution mixture was used, forcing the polyurethane to re-expand and allowing dye molecules to diffuse into the polyurethane matrix. Samples were placed in these second swelling solutions for a further 24 h before being air dried, washed with water, and dried again. Samples treated with acridine orange showed successful incorporation of the dye as the samples were a uniform dark orange. Naphthol green did not successfully incorporate into the polymer, leaving only blotchy green residue on the surface of the polyurethane after air drying. The washing step removed this to a great degree. As such, the samples using naphthol green were discounted from the antibacterial investigation as such instability is unacceptable for clinical uses.

Postcoating samples was carried out using crystal violet and malachite green. Solutions of 0.001 M were used as these have been previously reported to be the most efficacious for maximising uptake of the dye.[308] Samples were exposed to a postcoating solution for 24 h before being air dried, washed and then dried again. Both malachite green and crystal violet showed good uptake, producing strongly coloured polymer samples after washing.

4.4.2.1 UV-vis studies

Polyurethane samples impregnated with the stated nanoparticle and dye combinations were analysed on a Lamda 950 spectrometer over the spectral range 800-200 nm. The spectra of polyurethane both alone and with the three types of nanoparticles used are shown in Figure

4.3. Addition of gold nanoparticles to the polyurethane substrate resulted in a defined, broad peak forming at ~540 nm. This peak was found at a clear red shift (~20 nm) to the peak observed in the UV-vis absorption spectrum of the same gold nanoparticles in solution, and was also significantly broader. Addition of citrate-capped silver nanoparticles to polyurethane increased absorption almost uniformly across all wavelengths but without changing the shape of the absorption spectrum – no characteristic SPR peak was observed (Figure 4.3; AgNPs, grey line).

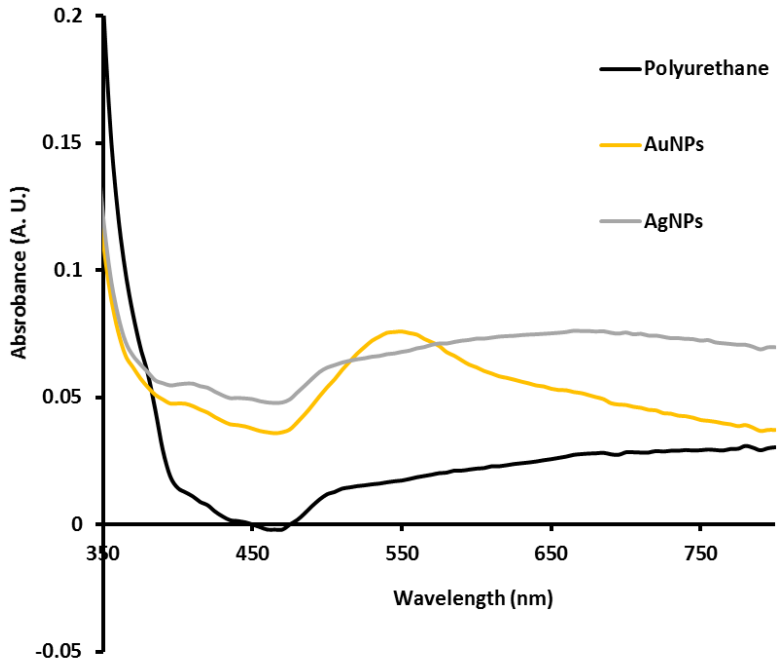

Figure 4.3 Graph showing the UV-vis absorption spectra of (i) solvent-treated polyurethane, (ii) polyurethane with citrate-capped gold nanoparticles and (iii) polyurethane with citrate-capped silver nanoparticles.

Addition of dyes to polyurethane was either by a second swell-encapsulation-shrink step (acridine orange; naphthol green) or by post-coating the samples in aqueous 0.1 M dye solution (crystal violet; malachite green). Naphthol green failed to diffuse into the bulk of the polymer; what little colouration was achieved was blotchy, sat on the surface of the polyurethane square and was removed during the washing step. UV-vis analysis of polyurethane treated with naphthol green showed no significant changes in the UV-vis spectrum compared to polyurethane alone (Figure 4.4, pale green line). Conversely, samples

treated analogously but using acridine orange produced very strongly coloured polymer squares. UV-vis on these samples showed a single broad absorption which peaked at 495 nm with a slight shoulder observed at 465 nm (Figure 4.4). These spectral features agree closely with those seen when the spectrum of aqueous acridine orange is taken. Post-coating solvent-treated polyurethane with 0.1 M malachite green and crystal violet resulted in intense absorptions with maxima at 635 and 590 nm respectively (Figure 4.4). The spectrum of malachite green with polyurethane showed a second, much less intense absorption at ~435 nm, agreeing with the aqueous spectrum of malachite green.

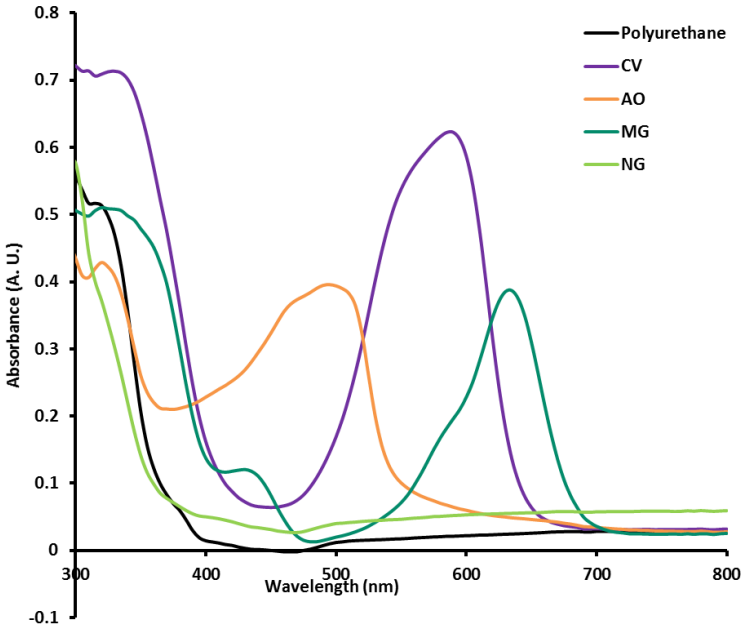

Figure 4.4 Graph showing the UV-vis absorption spectra of (i) solvent-treated polyurethane, (ii) polyurethane post-coated with 0.1 M aqueous crystal violet (CV), (iii) polyurethane treated with solvent and acridine orange (AO), (iv) polyurethane post-coated with 0.1 M aqueous malachite green (MG), (v) polyurethane treated with solvent and naphthol green (NG).

UV-vis studies of combinations of gold nanoparticles and naphthol green in the polyurethane substrate gave little difference compared to gold nanoparticles alone, indicating little to no uptake of naphthol green (Figure 4.5; AuNG). Some broadening of the acridine orange absorption peak was observed when gold nanoparticles were present in the polymer (Figure 4.5; AuAO), indicating the inclusion of gold nanoparticles affects uptake of the dye. The peak still exhibited a maximum at 495 nm, though the intensity of absorption was increased by

approximately 0.75 A. U. Citrate-capped gold nanoparticles were shown to increase the absorption of acridine orange in Chapter 3. Little difference was observed in the UV-vis absorption spectrum of gold nanoparticle and crystal violet-modified polymers (Figure 4.5; AuCV) compared to crystal violet-only samples (Figure 4.4; CV): maximum absorbance was still located at 590 nm, no increase in maximum intensity was seen and peak morphology remained very similar. Gold nanoparticle and malachite green-modified polyurethane (Figure 4.5; AuMG) too showed no shifting of the absorption peak compared to malachite green only samples, but a large increase in maximum absorption (~0.2 A. U.) was observed.

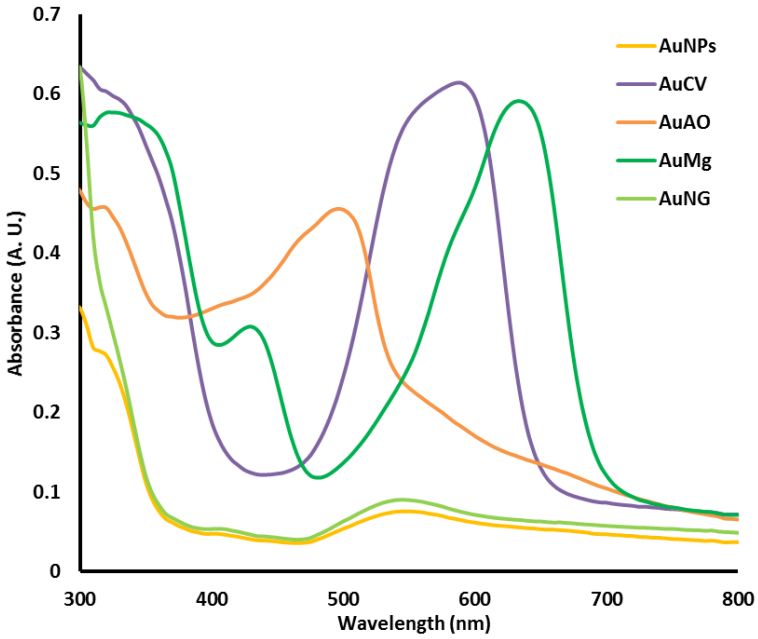

Figure 4.5 Graph showing the UV-vis absorption spectra of (i) solvent-treated polyurethane with citrate-capped gold nanoparticles (AuNPs), (ii) polyurethane embedded with gold nanoparticles and post-coated with 0.1 M aqueous crystal violet (AuCV), (iii) polyurethane embedded with gold nanoparticles then treated with solvent and acridine orange (AuAO), (iv) polyurethane embedded with gold nanoparticles then post-coated with 0.1 M aqueous malachite green (AuMG), (v) polyurethane embedded with gold nanoparticles treated with solvent and naphthol green (AuNG).

UV-vis studies of silver nanoparticle embedded polymers with dyes showed similar results. Broadening of the acridine orange peak around the expected maximum of 495 nm was seen when combined with silver nanoparticles (Figure 4.6; AgAO), though no enhancement in the absorption was recorded. The crystal violet and silver nanoparticle sample (Figure 4.6; AgCV) showed the expected peak at 590 nm with little to no change in peak shape. Silver

nanoparticles and malachite green in polyurethane (Figure 4.6; AgMG) did not show enhanced absorption of the dye as the analogous sample with gold nanoparticles did. Naphthol green again failed to be taken into the silver-modified polymer and exhibited no spectral changes compared to silver-polyurethane samples alone.

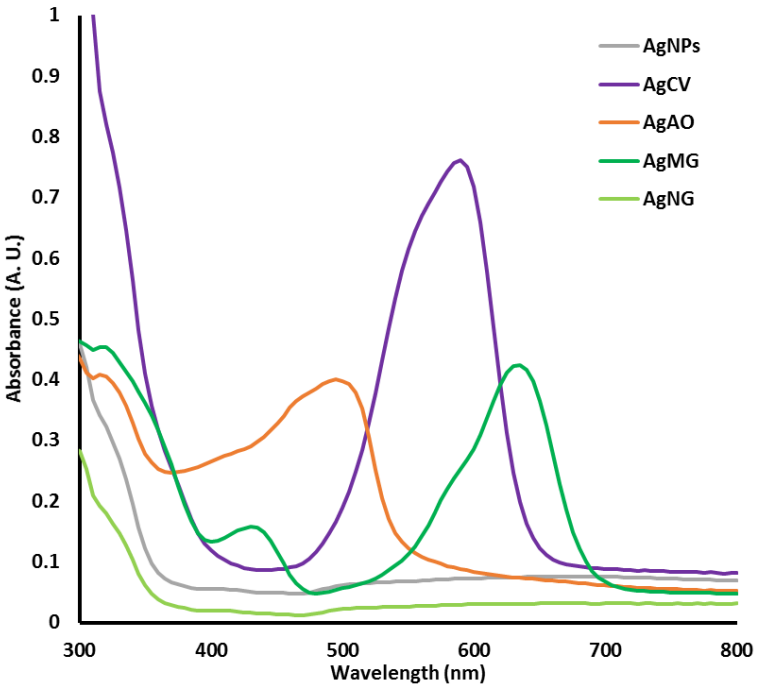

Figure 4.6 Graph showing the UV-vis absorption spectra of (i) solvent-treated polyurethane with citrate-capped silver nanoparticles (AuNPs), (ii) polyurethane embedded with silver nanoparticles and post-coated with 0.1 M aqueous crystal violet (AgCV), (iii) polyurethane embedded with silver nanoparticles then treated with solvent and acridine orange (AgAO), (iv) polyurethane embedded with silver nanoparticles then post-coated with 0.1 M aqueous malachite green (AgMG), (v) polyurethane embedded with silver nanoparticles treated with solvent and naphthol green (AgNG).

4.4.2.2 Water contact angle measurements

Only slight variation in water contact angles was observed on addition of dyes and nanoparticles to polyurethane. Solvent-treated polyurethane (control) samples with no additions gave a water contact angle of 98.6° (Figure 4.7a). The variation in angle ranged from 99.3° for polyurethane containing silver particles and naphthol green (+0.7°; Figure 4.7b) to 81.8° for samples containing silver-citrate particles and malachite green (-16.8°; Figure 4.7c), a total range of 17.5°. Though variation of the contact angles was small, the trend was for a decrease in hydrophobicity on the addition of nanoparticles and dyes.

Such small variations in hydrophobicity are unlikely to adversely affect the tribological properties of the polymers.[371]

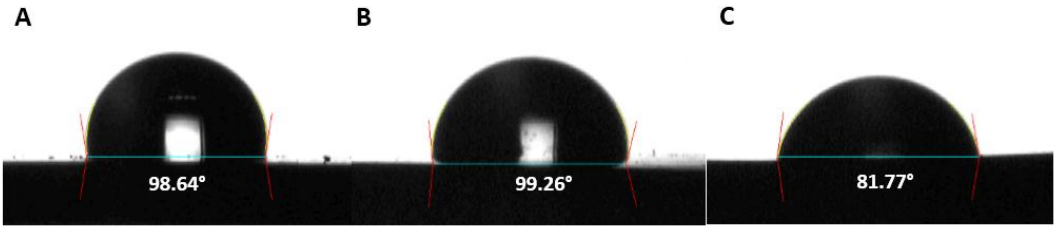

Figure 4.7 Images showing the water contact angles achieved on (a) solvent treated polyurethane; (b) polyurethane containing silver particles and naphthol green; (c) polyurethane containing citrate-capped silver particles and malachite green.

4.4.3 Antibacterial testing

The antibacterial capabilities of the samples were tested against both *E. coli* (gram negative) and *S. aureus* (gram positive), which were chosen as representative of common nosocomial pathogens. The polymer samples were exposed to broad spectrum white light to imitate the non-specific lighting found in an average hospital. Experiments were either 5 or 2 hours in duration, and a set of identical samples was incubated for the same time frame in the dark to provide a control. A summary of the samples used in this investigation can be found above in Table 4.2.

4.4.3.1 Staphylococcus aureus

Figure 4.8 shows the lethal sensitization of *S. aureus* over five hours when exposed to polyurethane samples containing i) nothing (control), ii) acridine orange, iii) malachite green and iv) crystal violet. The black bar represents the initial bacterial count for reference. The subsequent four bars represent the bacterial count after incubation of the samples in the dark; the latter four (in repeated colours) the same four samples exposed to a white light source for the same duration. It is clear that neither the control polymer nor any of the samples with incorporated dyes achieved any bacterial kill when incubated in the dark. There

is a very slight reduction in bacterial numbers for the same samples exposed to the light source, but the changes are so small as to be insignificant.

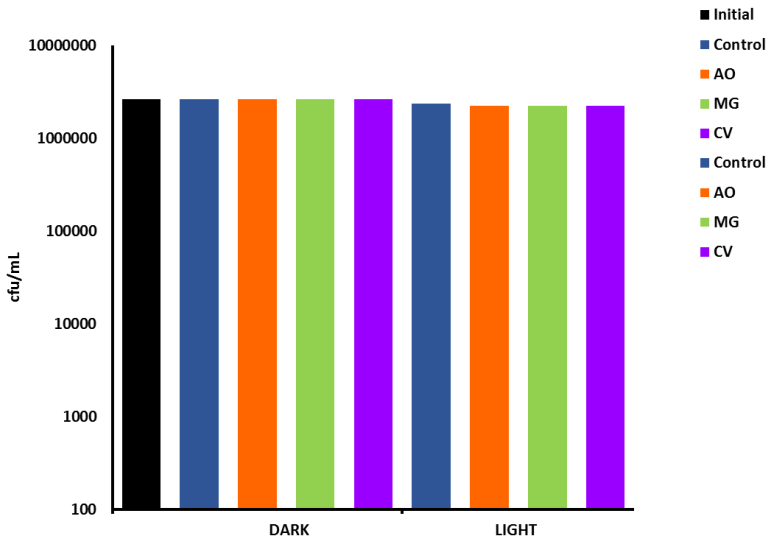

Figure 4.8 Graph showing viable counts of *S. aureus* after a 5 hour incubation on dye-modified polyurethane, incubated either in the dark or illuminated by a white light source (of 6600 ± 990 lux at a distance of 25 cm).

Incorporation of gold nanoparticles into the polyurethane samples gave more noticeable results (Figure 4.9). Again, we see no bactericidal activity for the control polymer in either dark or light conditions. Incorporation of gold nanoparticles into the polyurethane (yellow bar; 'Au only') also showed no significant change in bacterial numbers in either condition. Polyurethane containing a combination of gold nanoparticles with acridine orange (orange bar; 'AuAO'), however, showed a significant (p = 0.05, analysed using the Mann-Whitney U test in SPSS) 1.5 log reduction of *S. aureus* when incubated in the dark for five hours. Incubation of this sample under the white light source for the same duration reduced the colony forming units per mL (cfu/mL) to below the detection limit of 100, inducing total kill (p = 0.037). Samples containing gold nanoparticles and crystal violet (purple bar; 'AuCV') also showed good photobactericidal activity, giving 1.2 log reduction in dark conditions and a highly significant 2.5 log reduction under the light source over five hours. For both samples p= 0.05. No reduction in bacterial numbers was observed for gold nanoparticles and malachite green (green bar, 'AuMG') either in the light or dark.

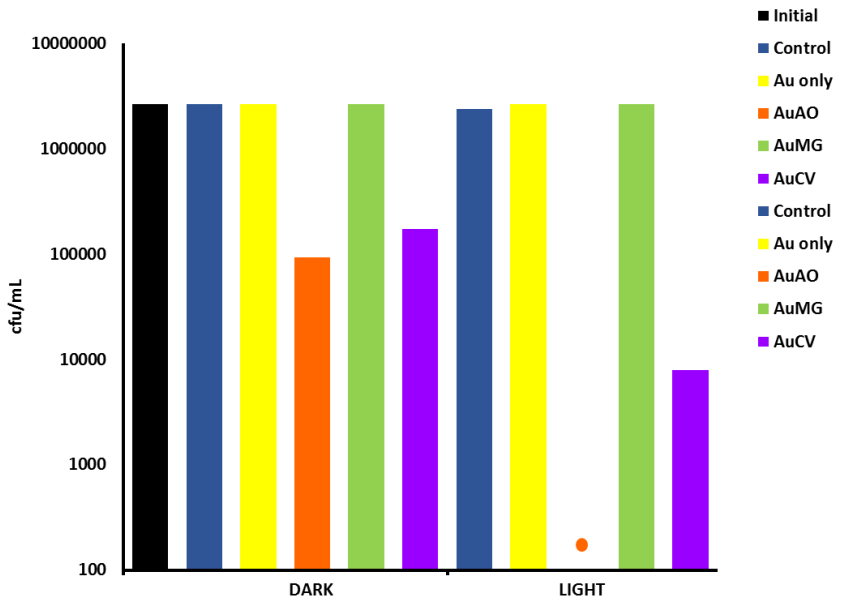

Figure 4.9 Graph showing viable counts of *S. aureus* after a 5 hour incubation on gold nanoparticle and dye-modified polyurethane, incubated either in the dark or illuminated by a white light source (of 6600 ± 990 lux at a distance of 25 cm.). A dot indicates that the bacterial numbers were reduced below the detection limit of 100 cfu/mL for that sample.

A similar sample set but using silver nanoparticles rather than gold yielded even better bactericidal results over five hours (Figure 4.10). Silver nanoparticles alone (grey bar; 'Ag') showed no kill in either dark or light conditions. Combination of silver nanoparticles with acridine orange, however, exhibited total kill (> 4 log reduction) in both dark and light. Silver nanoparticles and crystal violet gave ~1.5 log reduction in the dark and total kill when exposed to the white light source, p = 0.05 and 0.037 respectively. In stark contrast to the analogous gold sample, malachite green and silver nanoparticles also showed photobactericidal capabilities: 0.8 and 1.2 log reductions were recorded in the dark and light respectively, both representing statistically significant results (p = 0.05 for both).

The bactericidal capabilities of the silver nanoparticle-acridine orange combination was so marked that a 2 hour study was carried out, the results of which are shown in Figure 4.11. Over a two hour experiment a significant (p = 0.05) 1.8 log reduction was achieved in the dark, whilst total kill was again achieved by AgAO samples under the white light source. To the best of our knowledge, the use of acridine orange in to kill bacteria has not been reported

before. Limited studies have shown the promise of acridine orange mediated PDT to treat certain cancers,[372–374] but no use of AO in antimicrobial surfaces is found in the literature. The novelty, rapidity and efficacy of this system, therefore, presents a potentially excellent option to fabricate commercial bactericidal polymers for medical usage.

Whilst excellent bactericidal results of dye-nanoparticle combinations under a white light source are expected when using a photosensitizing dye, the significant reduction of bacterial numbers in the dark is less easy to explain. In the case of silver nanoparticles being present it is likely that the release of silver ions from the nanoparticle surface causes the cytotoxic effect. Silver ion release is a well-studied phenomenon and destroys cells by the interaction of Ag^+ ions with thiol-containing groups and thus deactivates enzymes which are vital to the cell's survival and replication.[284] Regarding gold, it is unclear why dark kill is observed with certain dyes. Gold is not, to the best of our knowledge, known to undergo ion release in the manner of silver. It is possible that the stronger interaction observed between gold nanoparticles and cationic dyes (seen in Chapter 3) activates the dye in some way by producing reactive sites, rendering the dye cytotoxic independently of photoactivity. Future work on this topic could involve investigation of the bactericidal polymer after antimicrobial assays were carried out to assess any changes to particle morphology that could give any mechanistic clues. It is also potentially useful to repeat the antimicrobial testing with gold-dye conjugates whilst making more efforts to block photons of all frequencies. It is feasible that, though isolation from visible photons that would usually induce the expected photochemical response was achieved, photons outside this portion of the spectrum could still be impinging upon the gold-dye modified polymers. Increased isolation of the samples from all frequencies of photons could establish whether introducing the gold nanoparticle to the dye allows absorption of photons outside the visible spectrum which then produces a similar singlet oxygen induced kill, or if the mechanism of dark kill in the gold-dye conjugates is entirely unrelated to that phenomenon.

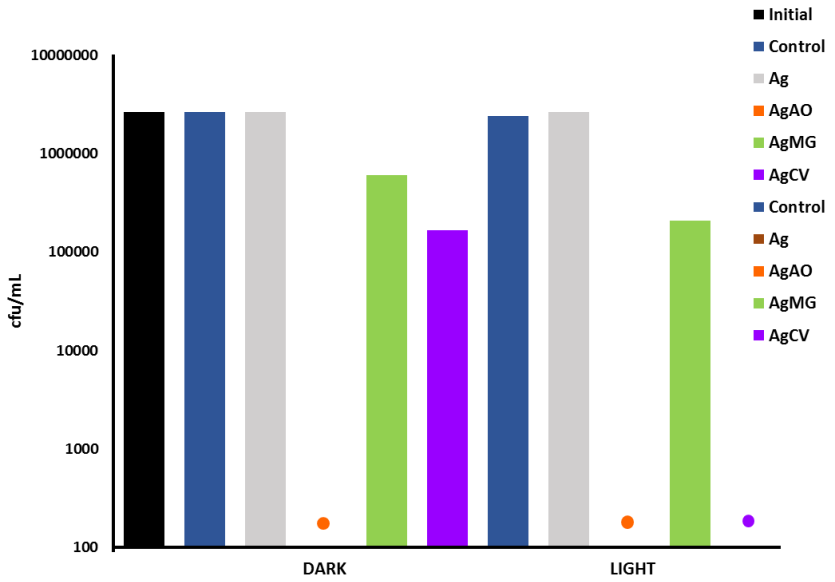

Figure 4.10 Graph showing viable counts of *S. aureus* after a 5 hour incubation on silver nanoparticle and dye-modified polyurethane, incubated either in the dark or illuminated by a white light source (of 6600 ± 990 lux at a distance of 25 cm.). A dot indicates that the bacterial numbers were reduced below the detection limit of 100 cfu/mL for that sample.

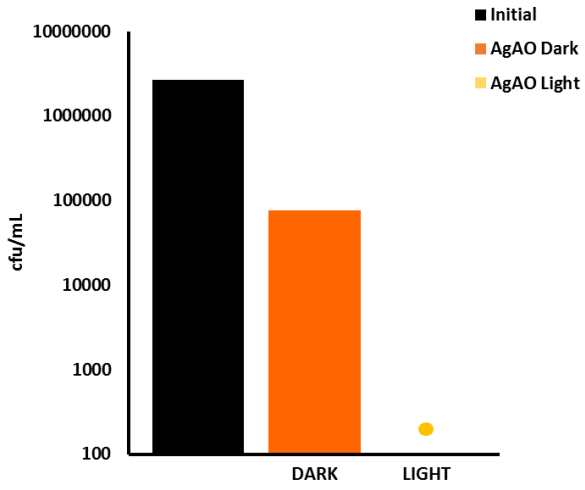

Figure 4.11 Graph showing viable counts of *S. aureus* after a 2 hour incubation on silver nanoparticle and acridine orange-modified polyurethane, incubated either in the dark or illuminated by a white light source (of 6600 ± 990 lux at a distance of 25 cm.). A dot indicates that the bacterial numbers were reduced below the detection limit of 100 cfu/mL for that sample.

4.4.3.2 E. coli

An identical sample set was tested against the gram-negative bacterium *E. coli*., as it is important for potential bactericidal systems to be able to kill bacteria with both cell wall types.

Figure 4.12 shows the lethal sensitization of *E. coli* over five hours when exposed to polyurethane samples containing dyes alone. As before, the black bar represents the initial bacterial count of the inoculum to give a reference point. Very little change in bacterial numbers was observed for the control polymer, acridine orange or malachite green in either dark or light conditions after a five hour incubation period. Crystal violet showed no bactericidal capability in the dark, but when incubated in the light we observed a significant ~1.4 log reduction in viable *E. coli* counts (p =0.05).

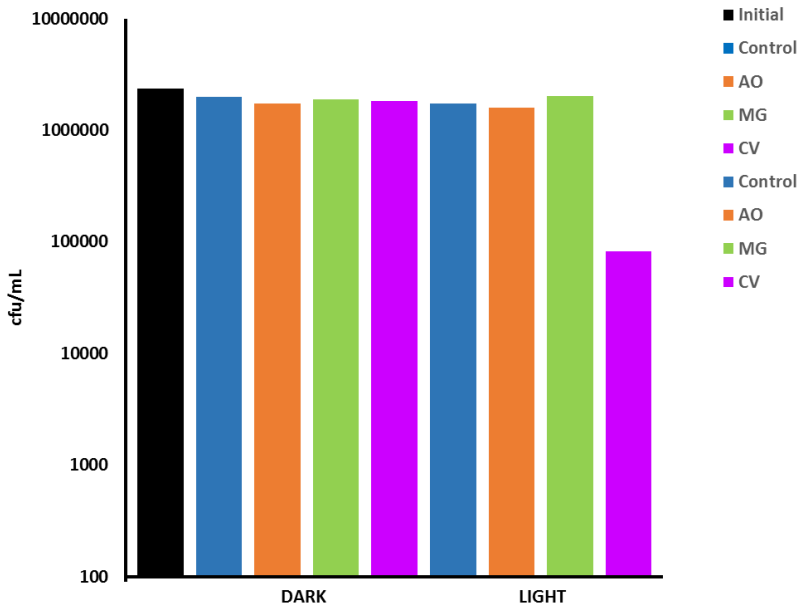

Figure 4.12 Graph showing viable counts of *E. coli* after a 5 hour incubation on dye-modified polyurethane, incubated either in the dark or illuminated by a white light source (of 6600 ± 990 lux at a distance of 25 cm).

Introducing gold nanoparticles into the polymer with the dyes makes little different to samples incubated in dark conditions (Figure 4.13). No significant reduction in viable *E. coli* counts is observed for either gold nanoparticle-modified polymer or any of the gold

nanoparticle and dye-modified samples. Five hours' incubation under a light source again gave no significant change for gold particles alone or gold nanoparticles and malachite green. We see a significant reduction in bacterial count for gold and crystal violet (~0.5 log reduction; p = 0.05), though it is not large enough to be of substantial clinical use. Acridine orange and gold nanoparticles shows the greatest bactericidal effect of this sample set, showing a 1.1 log reduction in bacterial numbers (p = 0.05).

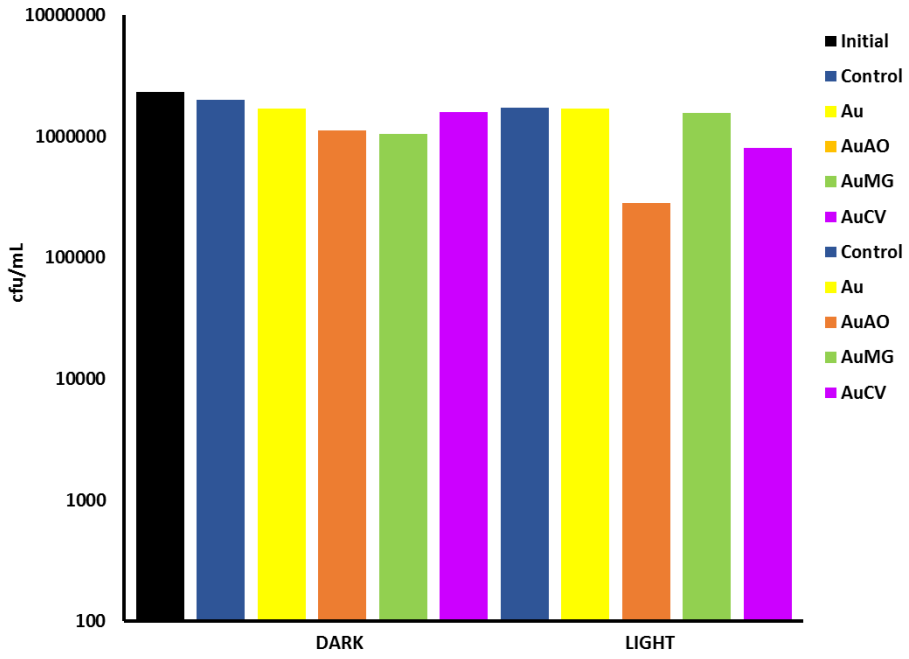

Figure 4.13 Graph showing viable counts of *E. coli* after a 5 hour incubation on gold nanoparticle and dye-modified polyurethane, incubated either in the dark or illuminated by a white light source (of 6600 ± 990 lux at a distance of 25 cm).

Silver nanoparticles in conjunction with the dyes gave excellent results after five hours (Figure 4.14). Silver nanoparticle-modified polymer samples gave ~2.2 and 2.3 log reduction in viable *E. coli* counts in the dark and light respectively. Combination of malachite green with silver particles yielded a 2 log reduction in the dark and matched silver alone in the light, reducing bacterial numbers by 2.3 log. Polymer samples containing silver nanoparticles and crystal violet showed good activity in the dark (2.1 log reduction) and reduced the *E. coli* cfu/mL to undetectable levels when exposed to a white light source. Acridine orange and silver nanoparticle modified polyurethane was found to be capable of inducing total kill in

both dark and light conditions, a superb result that has not, to our knowledge, been reported before. All samples modified with silver nanoparticles and any of the dyes in this study gave a *p* value ≤0.05, indicating all results were statistically significant.

On the strength of the results for silver nanoparticles and both crystal violet and acridine orange, a second antibacterial investigation was carried out with a shorter 2 hour duration in order to assess the rapidity of the photobactericidal effect. The results of this are shown in Figure 4.15. Though total kill was not achieved for either dye-silver particle combination, significant kill rates were observed. Crystal violet and silver nanoparticles was observed to give 1.3 and 2 log reduction in the dark and light respectively ($p = 0.05$). Acridine orange and silver again exhibited excellent bactericidal activity, reducing viable *E. coli* counts by 1.3 log after incubation in the dark and an impressive 3 log on exposure to the white light source for 2 hours ($p = 0.05$).

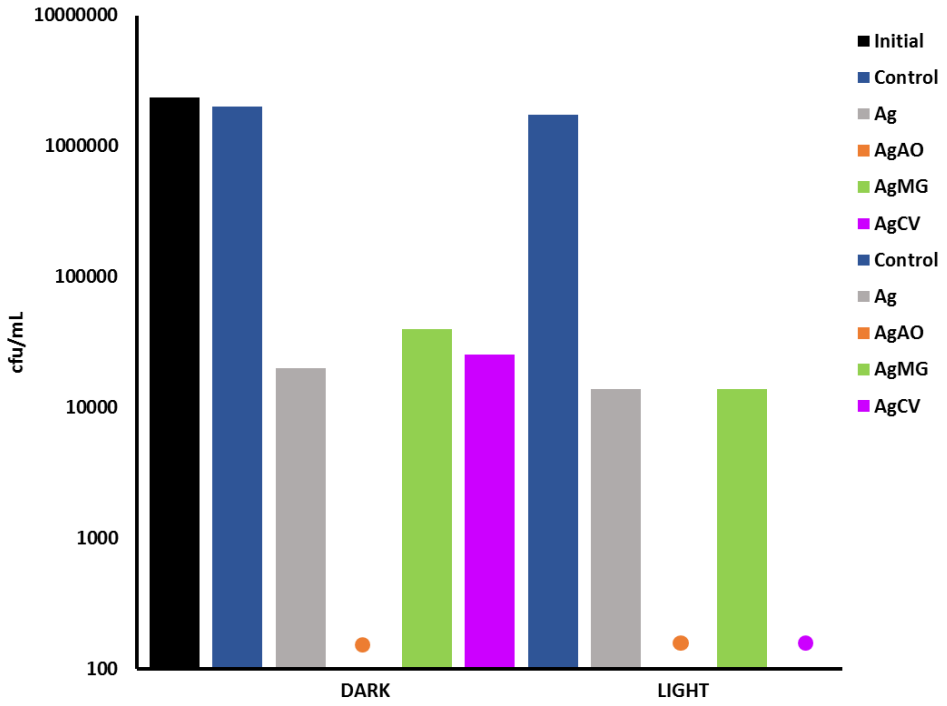

Figure 4.14 Graph showing viable counts of *E. coli* after a 5 hour incubation on silver nanoparticle and dye-modified polyurethane, incubated either in the dark or illuminated by a white light source (of 6600 ± 990 lux at a distance of 25 cm.). A dot indicates that the bacterial numbers were reduced below the detection limit of 100 cfu/mL for that sample.

If issues of potential toxicity can be satisfactorily addressed, acridine orange and silver nanoparticle impregnated polymers could offer powerful assistance in maintaining low bacterial counts on 'reservoir' surfaces in hospitals, cutting the risk of spreading nosocomial infections. Not only would this represent large monetary savings for the healthcare industry it would help to reduce the need to prescribe large quantities of antibiotics, helping to slow the rate of antibiotic-resistant mutations occurring in common pathogens. Their non-specificity in terms of light source makes them good candidates for installation in the average hospital, as previous antibacterial polymers have required laser illumination to induce significant bacterial kill. The potent dark kill exhibited by the system also makes them an option to be utilised in devices such as catheters, where formation of a biofilm on the device-body interface is responsible for large numbers of infections.[307,375]

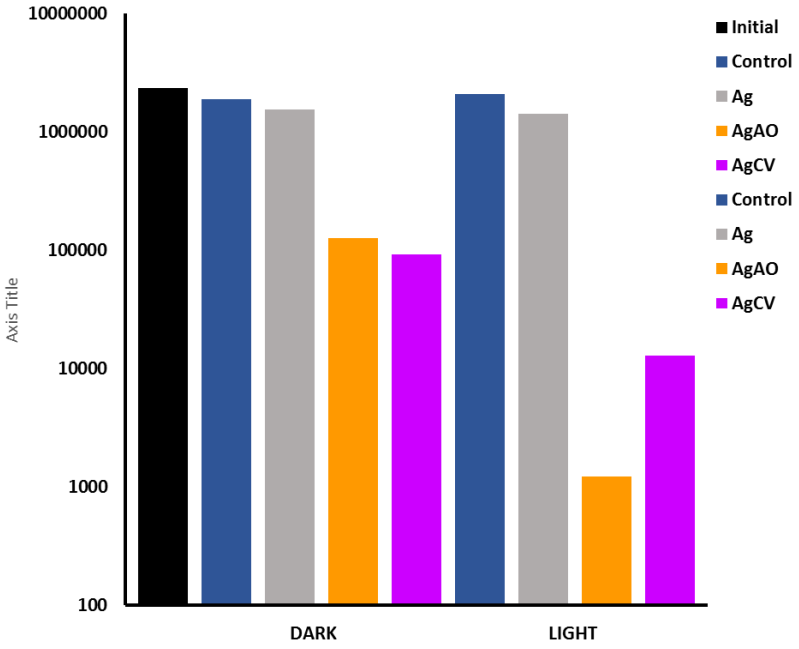

Figure 4.15 Graph showing viable counts of *E. coli* after a 2 hour incubation on silver nanoparticle and dye-modified polyurethane, incubated either in the dark or illuminated by a white light source (of 6600 ± 990 lux at a distance of 25 cm.).

4.5 Conclusions

Gold and silver nanoparticles were successfully synthesised *via* a modified Turkevich synthesis. These nanoparticles were incorporated into 10 x 10 mm squares of medical-grade

polyurethane using a swell-encapsulation-shrink method. Dyes were added to the samples either by a second swell-encapsulation-shrink step (acridine orange and naphthol green) or by postcoating (malachite green and crystal violet). Naphthol green failed to incorporate into the polyurethane samples, but the other three dyes studied gave good colouration as studied by UV-vis. Water contact angle measurements showed that the wetting properties of the polymers remained largely unchanged after incorporation of nanoparticles and dyes.

Antibacterial testing of all samples was carried out against gram negative *E. coli* and gram positive *S. aureus*. The presence of dyes only in the polymer was insufficient to induce bacterial kill in either dark or light conditions against *S. aureus* or *E. coli*. Gold nanoparticle-only samples failed to show any activity against either bacterium. Silver nanoparticle-only samples showed good (2.2 log reduction over 5 hours) activity against gram negative *E. coli* but failed to induce kill against *S. aureus*.

Combination of dyes with nanoparticles, however, gave good antimicrobial results. Crystal violet with silver nanoparticles induced 1.5 log reduction of *S. aureus* in the dark and total kill under a light source after five hours. The same sample produced a 2 log reduction in the dark against *E. coli* and total kill in light. Crystal violet has been previously reported to be an excellent LAAA and has been successfully incorporated into polymers previously, though to the best of our knowledge has not been combined with silver nanoparticles for this purpose.

Acridine orange in combination with gold nanoparticles gave 1.5 log reduction of viable *S. aureus* counts in the dark after 5 hours, and total kill in the same time frame under a white light source. 1.1 log reduction in the light was seen for AuAO samples against *E. coli.* Combination of acridine orange with silver nanoparticles gave total kill against *S. aureus* and *E. coli* in both light and dark conditions within 5 hours. Moreover, further investigations on AgAO samples over a shorter 2 hour time frame gave reductions in bacterial numbers of 1.2 and 1.8 log in the dark and 3 log and total kill in the light against *E. coli* and *S. aureus*

respectively. To the best of our knowledge, this is the first reported incidence of acridine orange being used to make antimicrobial polymers, either in combination with nanoparticles or alone. The rapidity and strength of the demonstrated photobactericidal effect combined with good dark kill ability makes the combination of silver nanoparticles with acridine orange a powerful option for potential applications in the healthcare sector, where promptness of bactericidal response and ability to remain functional in sub-optimal, non-specialised lighting conditions is paramount.

CHAPTER 5 : CONCLUDING REMARKS

5.1 Synthesis of gold and silver nanoparticles

Successful synthesis of gold and silver citrate-stabilised nanoparticles was achieved using a Turkevich method. Gold nanoparticles synthesised in this manner were regular in shape and size, forming defined spheres with an average diameter of 11 nm, recorded using TEM and Zetasizer measurements. Particle size varied across the range 10-15 nm and the solutions had the characteristic deep red colour of gold colloids. Silver nanoparticles synthesised by this method were less regular, being mostly spherical but with some ellipsoids and non-spherical particles too. The range of particle sizes was much greater than gold, ranging from 5-40 nm. Solutions were a pale yellow. The less well-formed particles and larger variation for silver particles synthesised in this way agrees with literature, which records a less tightly grouped range of sizes for silver nanoparticles made using the citrate reduction method than gold.[324] Citrate-capped silver-gold particles of varying molar ratios were successfully synthesised by the same method. Though facile, the synthesis of these particles showed disparity in colour of resultant solutions of the same molar ratios and variation in the position of the SPR bands. No relationship between the ratio of gold to silver and position of the SPR band was drawn, indicating the particles were neither a true alloy nor had a true core-shell structure.

Synthesis of tiopronin-capped silver particles *via* a borohydride was also achieved. Particles obtained using this methodology were small (average diameter 6 nm) and spherical, though variation in size of particles was observed. High aspect ratio chains of these nanoparticles were obtained by sonication of small quantities of the dried nanoparticle powder (0.5 mg/mL) in deionised water for 2 hours upwards. Particles in chains were smaller on average

(~4 nm) and had a narrower size distribution than in the as-prepared samples, a phenomenon attributed to digestive ripening during the sonication step.

CTAB-stabilised gold nanorods were synthesised, though average aspect ratio was quite short (<2). Nevertheless the rods showed defined cylindrical shape and definite anisotropic growth patterns.

5.2 Interaction of gold and silver nanoparticles with anionic and cationic dyes

It was shown that gold nanoparticles interact strongly with all the cationic dyes used in this study. Titration of cationic dyes and gold particles triggered aggregation of the nanoparticles into large arrays spanning hundreds of nanometres across. This physical observation was accompanied by a new peak developing on the UV-vis spectra of the dye-nanoparticle mixture at a large red shift characteristic of increasing effective particle size. In three cases enhanced absorption of this new peak was observed: for gold-toluidine blue (which was reported in literature),[43] gold-crystal violet and gold-acridine orange systems. This phenomenon has not been previously reported in literature for these combinations to the best of our knowledge.

Titration of anionic dyes with gold nanoparticles failed to produce similar results – no aggregation was observed, the red shifted peak did not appear on the UV-vis spectra during titration experiments and no enhanced absorption was seen. It is clear then that the assertion in literature that aggregation of the nanoparticles when dyes are added is a function of the ionic strength of the solution is not true. This was supported by the titration of isomolar potassium chloride with nanoparticles in place of the dyes, resulting in no aggregation. The charge on the dye molecules is therefore crucial in triggering or preventing aggregation due to electrostatic repulsion or attraction between the dye molecule and the negatively charged citrate shell surrounding the particle.

Silver nanoparticles made by the citrate reduction method showed no interaction with cationic or anionic dyes when titrated against them. It is postulated that the lower affinity of gold for oxygen (Au-O bond energy is 223 kJ mol^{-1} compared to 238 kJ mol^{-1} for Ag-O) results in the capping citrate ligands, which coordinate through an oxygen atom, to be less strongly bound to the surface of the gold particles than the silver. Thus it is probable that ligand exchange with amine group containing dyes is favourable for gold particles but not for silver, causing silver not to exhibit the aggregation behaviour observed with cationic dyes and gold particles.

Bimetallic particles synthesised in an analogous way behaved unpredictably, with no observable pattern to the obtained results. It is suggested that the erratic behaviour of the silver-gold particles is a result of the variation in size, shape and surface composition obtained using this synthesis.

Tiopronin-capped silver particles showed no interaction with either anionic or cationic dyes. It is suggested that the additional energy required to overcome hydrogen bonding between the structural thiolate chains makes ligand exchange unfavourable. Branched gold nanocrystals also failed to interact with either dye type, thought to be a result of strong covalent gold-sulphur bonds present between the directing HEPES molecules and the gold surface. Nanorods failed to interact with cationic dyes but showed marginal interaction with anionic naphthol green, likely a result of the positively-charged CTAB capping layer allowing interaction between negatively charged naphthol green molecules and the surface.

5.3 Incorporation of dyes and nanoparticles into polyurethane for antimicrobial surfaces

Successful incorporation of citrate capped gold and silver nanoparticles and tiopronin-capped silver nanoparticles into medical grade polyurethane was achieved *via* a swell-encapsulation-shrink method. These samples were then either postcoated with crystal violet

or malachite green or underwent a second swell-encapsulation-shrink step to incorporate acridine orange or naphthol green into the polymer matrix. Crystal violet, malachite green and acridine orange were successfully introduced into the polyurethane, whereas naphthol green failed to incorporate, forming faint greenish blotches on the surface which were removed in the washing step. UV-vis studies showed clear peaks at the characteristic wavelengths of the three former dyes. Water contact angle measurements showed that the tribological properties of the polyurethane remained largely the same after treatment with nanoparticles and dyes, an important result if the polymers are potentially to be used in applications which necessitate contact with the body such as catheters.

Antimicrobial testing of these samples was carried out against both gram negative *E. coli* and gram positive *S. aureus*. Samples of polyurethane containing dyes only did not induce bacterial kill against either organism in either light or dark conditions. Samples containing citrate capped gold nanoparticles only also did not record any antibacterial activity. Citrate capped silver nanoparticles, however, showed a 2.2 log reduction of bacterial numbers against gram negative *E. coli* over a period of five hours though failed to kill *S. aureus*.

Conversely, combination of citrate capped nanoparticles with the dyes gave good bacterial kill. Polyurethane containing crystal violet and silver nanoparticles gave 1.5 log reduction in *S. aureus* numbers in the dark and complete kill under a white light source over a five hour time span. The same combination gave a 2 log reduction in the dark and complete kill in the light against *E. coli*. Though crystal violet is a well-known photosensitizer and has been added to polymers for medical applications before,[309] to the best of our knowledge this is the first time it has been combined with silver nanoparticles for antimicrobial purposes.

Excellent results were obtained using acridine orange with citrate-capped particles. Conjugation with gold particles gave total kill and 1.5 log reduction against *S. aureus* in five hours under dark and light conditions respectively. ~1 log reduction of viable *E. coli* counts

was observed for the same sample under white light. Acridine orange and silver nanoparticles, however, gave total kill against both bacterial species in both light and dark conditions in five hours. Excitingly, total kill was also achieved by this sample over just two hours against *S. aureus*. 1.8 log reduction was seen in the dark. Good kills of 1.2 and 3 log in the dark and light respectively was observed for AgAO samples against *E. coli*. This represents the first report of acridine orange being used to make antimicrobial surfaces, either with or without nanoparticles. The rapidity of the effect – achieving excellent kills over just two hours under a normal white light source – and the potent dark kill ability of this combination offers an excellent tool in medical settings, where its demonstrated power for killing both gram negative and gram positive organisms under non-specialised lighting could be of great use.

5.4 Future work

Though a commonly used biological stain, relatively little is known about the toxicity of acridine orange to humans. It is classified as 'harmful by contact, ingestion and inhalation', though little is known about any possible mutagenic and teratogenic effects. As such, it is crucial to perform extensive leaching testing on polymers impregnated with acridine orange that are intended for any use where they will be in contact with humans.

Further antimicrobial testing against other common nosocomial pathogens should be undertaken to ensure that silver-acridine orange modified polyurethane presents a broad spectrum solution to fabrication of antimicrobial surfaces. Work pertaining to the origin of dark kill seen in gold samples – such as isolation of the samples from a greater range of photons and investigation of the samples post-bacterial kill – should be undertaken to ascertain the mechanism at work.

Further work would be useful to optimise the size of the nanoparticles incorporated into the polymers before adding dyes. Studies have shown that the size of the nanoparticle conjugated with the dye can have significant effects of the activity of the system as a

whole.[305] Studies by Noimark *et al*. suggest that 2 nm gold particles are optimal for enhancing the photoactivity of crystal violet.[309] Such small particles are harder to make and less stable than their larger cousins, used here for ease of synthesis. However, if the activity of the silver-acridine orange system could be enhanced to show total kill against gram-positive and gram-negative pathogens within 2 hours in ambient lighting, it would certainly present a strong competitor for fabrication of bactericidal surfaces.

High resolution XRD could be used to elucidate the true structure of the gold-silver hybrid particles obtained *via* the citrate reduction method. Understanding of the structures obtained on an atomic level could help tailor future syntheses to produce the desired result.

Work to investigate the nature of the dye-nanoparticle interaction and therefore the origin of enhanced absorption of some dyes vs. others should be undertaken. DFT calculations could provide insight into the dye-nanoparticles bond, whereas more work on TCSPC could show how combination of a nanoparticle with a dye alters the excitement and relaxation of the dye in question. Understanding the nature of this interaction would enable theoretical prediction of dyes that exhibit such behaviour and potential tuning of the interactions observed.

Bibliography

1 M. Auffan, J. Rose, J.-Y. Bottero, G. V. Lowry, J.-P. Jolivet and M. R. Wiesner, *Nat. Nanotechnol.*, 2009, **4**, 634–641.

2 G. Walters, I. P. Parkin, R. Palgrave, I. P. Parkin, S. W. Han, C. Goyes, Y. Jestin, M. L. Mattarelli, M. Montagna, G. N. Conti, S. Pelli, G. C. Righini, C. Tosello and K. C. Vishunubhatla, *J. Mater. Chem.*, 2009, **19**, 574–590.

3 J.-Y. Bottero, J. Rose and M. R. Wiesner, *Integr. Environ. Assess. Manag.*, 2006, **2**, 391–395.

4 D. F. Emerich and C. G. Thanos, *Biomol. Eng.*, 2006, **23**, 171–184.

5 A. K. Gupta and M. Gupta, *Biomaterials*, 2005, **26**, 3995–4021.

6 J. Jolivet, C. Froidefond and A. Pottier, *J. Mater.*, 2004.

7 E. Baudrin, S. Cassaignon, M. Koelsch, J.-P. Jolivet, L. Dupont and J.-M. Tarascon, 2006.

8 R. Lamber, S. Wetjen and N. I. Jaeger, *Phys. Rev. B*, 1995, **51**, 10968–10971.

9 P. Ayyub, V. R. Palkar, S. Chattopadhyay and M. Multani, *Phys. Rev. B*, 1995.

10 M. Zhang, M. Y. Efremov, F. Schiettekatte, E. A. Olson, A. T. Kwan, S. L. Lai, T. Wisleder, J. E. Greene and L. H. Allen, *Phys. Rev. B*, 2000, **62**, 10548–10557.

11 S. L. Lai, J. Y. Guo, V. Petrova, G. Ramanath and L. H. Allen, *Phys. Rev. Lett.*, 1996, **77**, 99–102.

12 Z. X. Tang, C. M. Sorensen, K. J. Klabunde and G. C. Hadjipanayis, *Phys. Rev. Lett.*, 1991, **67**, 3602–3605.

13 S. M. Selbach, T. Tybell, M.-A. Einarsrud and T. Grande, *Chem. Mater.*, 2007, **19**, 6478–6484.

14 S. Shetty, V. R. Palkar and R. Pinto, in *Pramana - Journal of Physics*, 2002.

15 R. Narayanan and M. A. El-Sayed, *J. Phys. Chem. B*, 2005, **109**, 12663–12676.

16 E. Hao, G. C. Schatz and J. T. Hupp, *J. Fluoresc.*, 2004, **14**, 331–341.

17 S. Eustis and M. A. El-Sayed, *Chem. Soc. Rev.*, 2006, **35**, 209–217.

18 B. Khlebtsov, V. Zharov, A. Melnikov, V. Tuchin and N. Khlebtsov, *Nanotechnology*, 2006, **17**, 5167.

19 S. Link and M. A. El-Sayed, *J. Phys. Chem. B*, 1999, **103**, 4212–4217.

20 X. Huang and M. A. El-Sayed, *J. Adv. Res.*, 2010, **1**, 13–28.

21 X. Liu, M. Atwater, J. Wang and Q. Huo, *Colloids Surfaces B Biointerfaces*, 2007, **58**, 3–7.

22 M. H. V. Werts, M. Lambert, J.-P. Bourgoin and M. Brust, *Nano Lett.*, 2002, **2**, 43–47.

23 P. M. Mendes, S. Jacke, K. Critchley, J. Plaza, Y. Chen, K. Nikitin, R. E. Palmer, J. A. Preece, S. D. Evans and D. Fitzmaurice, *Langmuir*, 2004, **20**, 3766–3768.

24 J. Li, K. Kamata and T. Iyoda, *Thin Solid Films*, 2008, **516**, 2577–2581.

25 S. Sun, P. Mendes, K. Critchley, S. Diegoli, M. Hanwell, S. D. Evans, G. J. Leggett, J. A. Preece and T. H. Richardson, *Nano Lett.*, 2006, **6**, 345–350.

26 C. L. Haynes and R. P. Van Duyne, *J. Phys. Chem. B*, 2001, **105**, 5599–5611.

27 E. M. Hicks, S. Zou, G. C. Schatz, K. G. Spears, R. P. Van Duyne, L. Gunnarsson, T. Rindzevicius, B. Kasemo and M. Käll, *Nano Lett.*, 2005, **5**, 1065–1070.

28 J. Kimling, M. Maier, B. Okenve, V. Kotaidis, H. Ballot and A. Plech, *J. Phys. Chem. B*, 2006, **110**, 15700–15707.

29 J. Zhou, J. Ralston, R. Sedev and D. A. Beattie, *J. Colloid Interface Sci.*, 2009, **331**, 251–

262.

30 Y. Sun and Y. Xia, *Science*, 2002, **298**, 2176–9.

31 B. Nikoobakht and M. A. El-Sayed, *Chem. Mater.*, 2003, **15**, 1957–1962.

32 F. Kim, S. Connor, H. Song, T. Kuykendall and P. Yang, *Angew. Chemie*, 2004, **116**, 3759–3763.

33 Y. Kondo and K. Takayanagi, *Science*, 2000, **289**, 606–8.

34 R. T. Senger, S. Dag and S. Ciraci, *Phys. Rev. Lett.*, 2004, **93**, 196807.

35 P. Senthil Kumar, I. Pastoriza-Santos, B. Rodríguez-González, F. Javier García de Abajo and L. M. Liz-Marzán, *Nanotechnology*, 2008, **19**, 15606.

36 J. Turkevich, P. C. Stevenson and J. Hillier, *J. Phys. Chem.*, 1953, **57**, 670–673.

37 Z. S. Pillai and P. V Kamat, *J. Phys. Chem. B*, 2003, **108**, 945–951.

38 A. Rohiman, I. Anshori, A. Surawijaya, I. Idris, F. Iskandar and M. Abdullah, in *THE 4TH NANOSCIENCE AND NANOTECHNOLOGY SYMPOSIUM (NNS2011): An International Symposium*, AIP Publishing, 2011, vol. 1415, pp. 39–42.

39 X. Ji, X. Song, J. Li, Y. Bai, W. Yang and X. Peng, *J. Am. Chem. Soc.*, 2007, **129**, 13939–13948.

40 G. Frens, *Kolloid-Zeitschrift und Zeitschrift für Polym.*, 1972, **250**, 736–741.

41 J. W. Slot and H. J. Geuze, *Eur. J. Cell Biol.*, 1985, **38**, 87–93.

42 C. J. Sandroff and D. R. Herschbach, *Langmuir*, 1985, **1**, 131–135.

43 N. Narband, M. Uppal, C. W. Dunnill, G. Hyett, M. Wilson and I. P. Parkin, *Phys. Chem. Chem. Phys.*, 2009, **11**, 10513–10518.

44 C. J. Murphy, T. K. Sau, A. M. Gole, C. J. Orendorff, J. Gao, L. Gou, S. E. Hunyadi and T.

Li, *J. Phys. Chem. B*, 2005, **109**, 13857–13870.

45 A. Gole and C. J. Murphy, *Chem. Mater.*, 2004, **16**, 3633–3640.

46 C. J. Johnson, E. Dujardin, S. A. Davis, C. J. Murphy and S. Mann, *J. Mater. Chem.*, 2002, **12**, 1765–1770.

47 M. Brust, M. Walker, D. Bethell, D. J. Schiffrin and R. Whyman, *J. Chem. Soc., Chem. Commun.*, 1994, **0**, 801–802.

48 K. L. Kelly, E. Coronado, L. L. Zhao and G. C. Schatz, *J. Phys. Chem. B*, 2003, **107**, 668–677.

49 L. Guo, S. Yang, C. Yang, P. Yu, J. Wang, W. Ge and G. K. L. Wong, *Appl. Phys. Lett.*, 2000, **76**, 2901.

50 I. O. Sosa, C. Noguez and R. G. Barrera, *J. Phys. Chem. B*, 2003, **107**, 6269–6275.

51 W. P. Zhou, A. Lewera, R. Larsen, R. I. Masel, P. S. Bagus and A. Wieckowski, *J. Phys. Chem. B*, 2006, **110**, 13393–8.

52 S.-J. Park, A. A. Lazarides, C. A. Mirkin, P. W. Brazis, C. R. Kannewurf and R. L. Letsinger, *Angew. Chemie*, 2000, **39**, 3845–3848.

53 D. L. Leslie-Pelecky and R. D. Rieke, *Chem. Mater.*, 1996, **8**, 1770–1783.

54 M.-C. Daniel, J. Ruiz and D. Astruc, *J. Am. Chem. Soc.*, 2003, **125**, 1150–1.

55 Z.-J. Jiang, C.-Y. Liu and L.-W. Sun, *J. Phys. Chem. B*, 2005, **109**, 1730–5.

56 R. M. Rioux, H. Song, M. Grass, S. Habas, K. Niesz, J. D. Hoefelmeyer, P. Yang and G. A. Somorjai, *Top. Catal.*, 2006, **39**, 167–174.

57 C. B. Murray, C. R. Kagan and M. G. Bawendi, *Annu. Rev. Mater. Sci.*, 2000, **30**, 545–610.

58 C. P. Collier, T. Vossmeyer and J. R. Heath, *Annu. Rev. Phys. Chem.*, 1998, **49**, 371–404.

59 M. P. Pileni, *J. Phys. Chem. B*, 2001, **105**, 3358–3371.

60 N. A. Kotov, F. C. Meldrum, C. Wu and J. H. Fendler, *J. Phys. Chem.*, 1994, **98**, 2735–2738.

61 J. Hu, T. W. Odom and C. M. Lieber, *Acc. Chem. Res.*, 1999, **32**, 435–445.

62 S. A. Maier, P. G. Kik, H. A. Atwater, S. Meltzer, E. Harel, B. E. Koel and A. A. G. Requicha, *Nat. Mater.*, 2003, **2**, 229–232.

63 S. A. Maier, M. L. Brongersma, P. G. Kik, S. Meltzer, A. A. G. Requicha, B. E. Koel and H. A. Atwater, *Adv. Mater.*, 2003, **15**, 562.

64 J.-Y. Bigot, J.-Y. Merle, O. Cregut and A. Daunois, *Phys. Rev. Lett.*, 1995, **75**, 4702–4705.

65 G. H. Chan, J. Zhao, E. M. Hicks, G. C. Schatz and R. P. Van Duyne, *Nano Lett.*, 2007, **7**, 1947–1952.

66 T. R. Jensen, M. D. Malinsky, C. L. Haynes and R. P. Van Duyne, *J. Phys. Chem. B*, 2000, **104**, 10549–10556.

67 L. J. Sherry, S.-H. Chang, G. C. Schatz, R. P. Van Duyne, B. J. Wiley and Y. Xia, *Nano Lett.*, 2005, **5**, 2034–2038.

68 B. J. Wiley, S. H. Im, Z.-Y. Li, J. McLellan, A. Siekkinen and Y. Xia, *J. Phys. Chem. B*, 2006, **110**, 15666–15675.

69 L. J. Sherry, R. Jin, C. A. Mirkin, G. C. Schatz and R. P. Van Duyne, *Nano Lett.*, 2006, **6**, 2060–5.

70 T. Klar, M. Perner, S. Grosse, G. Von Plessen, W. Spirkl and J. Feldmann, *Phys. Rev. Lett.*, 1998, **80**, 4249–4252.

71 M. Perner, P. Bost, U. Lemmer, G. Von Plessen, J. Feldmann, U. Becker, M. Mennig, M. Schmitt and H. Schmidt, *Phys. Rev. Lett.*, 1997, **78**, 2192–2195.

72 T. Shimada, K. Ookubo, N. Komuro, T. Shimizu and N. Uehara, *Langmuir*, 2007, **23**, 11225–32.

73 S. K. Ghosh and T. Pal, *Chem. Rev.*, 2007, **107**, 4797–862.

74 Z. Nie, A. Petukhova and E. Kumacheva, *Nat. Nanotechnol.*, 2010, **5**, 15–25.

75 E. M. Conwell, *Proc. Natl. Acad. Sci. U. S. A.*, 2005, **102**, 8795–9.

76 N. C. Seeman, *Nature*, 2003, **421**, 427–31.

77 J. Richter, *Phys. E Low-dimensional Syst. Nanostructures*, 2003, **16**, 157–173.

78 A. P. Alivisatos, K. P. Johnsson, X. Peng, T. E. Wilson, C. J. Loweth, M. P. Bruchez and P. G. Schultz, 1996.

79 Z. Deng, Y. Tian, S.-H. Lee, A. E. Ribbe and C. Mao, *Angew. Chemie*, 2005, **117**, 3648–3651.

80 D. Liu, S. L. Daubendiek, M. A. Zillman, K. Ryan and E. T. Kool, *J. Am. Chem. Soc.*, 1996, **118**, 1587–1594.

81 E. Braun, Y. Eichen, U. Sivan and G. Ben-Yoseph, *Nature*, 1998, **391**, 775–778.

82 K. Keren, M. Krueger, R. Gilad, G. Ben-Yoseph, U. Sivan and E. Braun, *Science (80-.).*, 2002, **297**, 72–75.

83 D. Coomber, D. Bartczak, S. R. Gerrard, S. Tyas, A. G. Kanaras and E. Stulz, *Langmuir*, 2010, **26**, 13760–13762.

84 W. Cheng, M. J. Campolongo, J. J. Cha, S. J. Tan, C. C. Umbach, D. A. Muller and D. Luo, *Nat. Mater.*, 2009, **8**, 519–525.

85 W. E. Ford, O. Harnack, A. Yasuda and J. M. Wessels, *Adv. Mater.*, 2001, **13**, 1793–1797.

86 K. Nguyen, M. Monteverde, A. Filoramo, L. Goux-Capes, S. Lyonnais, P. Jegou, P. Viel, M. Goffman and J.-P. Bourgoin, *Adv. Mater.*, 2008, **20**, 1099–1104.

87 J. D. Le, Y. Pinto, N. C. Seeman, K. Musier-Forsyth, T. A. Taton and R. A. Kiehl, *Nano Lett.*, 2004, **4**, 2343–2347.

88 Y. Y. Pinto, J. D. Le, N. C. Seeman, K. Musier-Forsyth, T. A. Taton and R. A. Kiehl, *Nano Lett.*, 2005, **5**, 2399–402.

89 J. D. Le, Y. Pinto, N. C. Seeman, K. Musier-Forsyth, T. A. Taton and R. A. Kiehl, *Nano Lett.*, 2004, **4**, 2343–2347.

90 T. Ohshiro, T. Zako, R. Watanabe-Tamaki, T. Tanaka and M. Maeda, *Chem. Commun.*, 2010, **46**, 6132–6134.

91 X. Fu, Y. Wang, L. Huang, Y. Sha, L. Gui, L. Lai and Y. Tang, *Adv. Mater.*, 2003, **15**, 902–906.

92 M. G. Ryadnov and D. N. Woolfson, *J. Am. Chem. Soc.*, 2004, **126**, 7454–7455.

93 D. Walsh, L. Arcelli, T. Ikoma, J. Tanaka and S. Mann, *Nat. Mater.*, 2003, **2**, 386–390.

94 X. Fu, Y. Wang, L. Huang, Y. Sha, L. Gui, L. Lai and Y. Tang, *Adv. Mater.*, 2003, **15**, 902–906.

95 E. Dujardin, C. Peet, G. Stubbs, J. N. Culver and S. Mann, *Nano Lett.*, 2003, **3**, 413–417.

96 Y. Huang, C.-Y. Chiang, S. K. Lee, Y. Gao, E. L. Hu, J. De Yoreo and A. M. Belcher, *Nano Lett.*, 2005, **5**, 1429–1434.

97 C. Mao, C. E. Flynn, A. Hayhurst, R. Sweeney, J. Qi, G. Georgiou, B. Iverson and A. M.

Belcher, *Proc. Natl. Acad. Sci. U. S. A.*, 2003, **100**, 6946–51.

98 S.-W. Lee, C. Mao, C. E. Flynn and A. M. Belcher, *Science*, 2002, **296**, 892–5.

99 O. K. Zahr and A. S. Blum, *Nano Lett.*, 2012, **12**, 629–33.

100 R. Djalali, Y. Chen and H. Matsui, *J. Am. Chem. Soc.*, 2002, **124**, 13660–13661.

101 S. Behrens, K. Rahn, W. Habicht, K.-J. Böhm, H. Rösner, E. Dinjus and E. Unger, *Adv. Mater.*, 2002, **14**, 1621–1625.

102 S. Drescher, G. Hempel, W. H. Binder, B. Dobner, A. Blume and A. Meister, *Langmuir*, 2012, **28**, 11615–24.

103 C. Mao, D. J. Solis, B. D. Reiss, S. T. Kottmann, R. Y. Sweeney, A. Hayhurst, G. Georgiou, B. Iverson and A. M. Belcher, *Science*, 2004, **303**, 213–7.

104 T. Scheibel, R. Parthasarathy, G. Sawicki, X.-M. Lin, H. Jaeger and S. L. Lindquist, *Proc. Natl. Acad. Sci. U. S. A.*, 2003, **100**, 4527–32.

105 J. He, T. Kunitake and A. Nakao, *Chem. Mater.*, 2003, **15**, 4401–4406.

106 S. Iijima and T. Ichihashi, *Nature*, 1993, **363**, 603–605.

107 S. C. Tsang, Y. K. Chen, P. J. F. Harris and M. L. H. Green, *Nature*, 1994, **372**, 159–162.

108 D. Ugarte, T. Stöckli, J. M. Bonard, A. Châtelain and W. A. de Heer, *Appl. Phys. A Mater. Sci. Process.*, 1998, **67**, 101–105.

109 S. Fullam, D. Cottell, H. Rensmo and D. Fitzmaurice, *Adv. Mater.*, 2000, **12**, 1430–1432.

110 M. J. Moghaddam, S. Taylor, M. Gao, S. Huang, L. Dai and M. J. McCall, *Nano Lett.*, 2004, **4**, 89–93.

111 A. V. Ellis, K. Vijayamohanan, R. Goswami, N. Chakrapani, L. S. Ramanathan, P. M. Ajayan and G. Ramanath, *Nano Lett.*, 2003, **3**, 279–282.

112 M. Quintana, X. Ke, G. Van Tendeloo, M. Meneghetti, C. Bittencourt and M. Prato, *ACS Nano*, 2010, **4**, 6105–13.

113 Y.-P. Sun, W. Huang, Y. Lin, K. Fu, A. Kitaygorodskiy, L. A. Riddle, Y. J. Yu and D. L. Carroll, *Chem. Mater.*, 2001, **13**, 2864–2869.

114 S. Hrapovic, Y. Liu, K. B. Male and J. H. T. Luong, *Anal. Chem.*, 2004, **76**, 1083–8.

115 M. Endo, Y. A. Kim, M. Ezaka, K. Osada, T. Yanagisawa, T. Hayashi, M. Terrones and M. S. Dresselhaus, *Nano Lett.*, 2003, **3**, 723–726.

116 Y. Mu, H. Liang, J. Hu, L. Jiang and L. Wan, *J. Phys. Chem. B*, 2005, **109**, 22212–6.

117 L.-M. Ang, T. S. A. Hor, G.-Q. Xu, C. Tung, S. Zhao and J. L. S. Wang, *Chem. Mater.*, 1999, **11**, 2115–2118.

118 K. B. Male, S. Hrapovic, Y. Liu, D. Wang and J. H. . Luong, *Anal. Chim. Acta*, 2004, **516**, 35–41.

119 R. Giordano, P. Serp, P. Kalck, Y. Kihn, J. Schreiber, C. Marhic and J.-L. Duvail, *Eur. J. Inorg. Chem.*, 2003, **2003**, 610–617.

120 R. Larciprete, S. Lizzit, L. Petaccia and A. Goldoni, *Appl. Phys. Lett.*, 2006, **88**, 243111.

121 B. M. Quinn, C. Dekker and S. G. Lemay, *J. Am. Chem. Soc.*, 2005, **127**, 6146–6147.

122 M. Ding, D. C. Sorescu, G. P. Kotchey and A. Star, *J. Am. Chem. Soc.*, 2012, **134**, 3472–9.

123 T. O. Hutchinson, Y.-P. Liu, C. Kiely, C. J. Kiely and M. Brust, *Adv. Mater.*, 2001, **13**, 1800–1803.

124 E. Fort, C. Ricolleau and J. Sau-Pueyo, *Nano Lett.*, 2003, **3**, 65–67.

125 E. C. Walter, B. J. Murray, F. Favier, G. Kaltenpoth, M. Grunze and R. M. Penner, *J.*

Phys. Chem. B, 2002, **106**, 11407–11411.

126 W. Luo, W. van der Veer, P. Chu, D. L. Mills, R. M. Penner and J. C. Hemminger, *J. Phys. Chem. C*, 2008, **112**, 11609–11613.

127 A. Fukuoka, T. Higuchi, T. Ohtake, T. Oshio, J. Kimura, Y. Sakamoto, N. Shimomura, S. Inagaki and M. Ichikawa, *Chem. Mater.*, 2006, **18**, 337–343.

128 M. H. Huang, A. Choudrey and P. Yang, *Chem. Commun.*, 2000, 1063–1064.

129 Y.-J. Han, J. M. Kim and G. D. Stucky, *Chem. Mater.*, 2000, **12**, 2068–2069.

130 K. Lee, S. Lee and J. Cheon, *Adv. Mater.*, 2001, **13**, 517–520.

131 Q. Dai, J. G. Worden, J. Trullinger and Q. Huo, *J. Am. Chem. Soc.*, 2005, **127**, 8008–9.

132 K. Takagi and T. Ishiwatari, *Chem. Lett.*, 2002, 990–991.

133 D.-F. Zhang, L.-Y. Niu, L. Jiang, P.-G. Yin, L.-D. Sun, H. Zhang, R. Zhang, L. Guo and C.-H. Yan, *J. Phys. Chem. C*, 2008, **112**, 16011–16016.

134 X. Shen, L. Chen, D. Li, L. Zhu, H. Wang, C. Liu, Y. Wang, Q. Xiong and H. Chen, *ACS Nano*, 2011, **5**, 8426–33.

135 D. Coursault, J. Grand, B. Zappone, H. Ayeb, G. Lévi, N. Félidj and E. Lacaze, *Adv. Mater.*, 2012, **24**, 1461–5.

136 J.-Y. Chang, B. Lo, M. Jeng, S.-H. Tzing and Y.-C. Ling, *Appl. Phys. Lett.*, 2004, **85**, 2613.

137 A. Cabañas, J. A. Darr, E. Lester and M. Poliakoff, *J. Mater. Chem.*, 2001, **11**, 561–568.

138 J. D. Holmes, *Science (80-.).*, 2000, **287**, 1471–1473.

139 J.-Y. Chang, J.-J. Chang, B. Lo, S.-H. Tzing and Y.-C. Ling, *Chem. Phys. Lett.*, 2003, **379**, 261–267.

140 J. Liao, Y. Zhang, W. Yu, L. Xu, C. Ge, J. Liu and N. Gu, *Colloids Surfaces A Physicochem.*

Eng. Asp., 2003, **223**, 177–183.

141 X. Han, J. Goebl, Z. Lu and Y. Yin, *Langmuir*, 2011, **27**, 5282–9.

142 A. Gangula, J. Chelli, S. Bukka, V. Poonthiyil, R. Podila, R. Kannan and A. M. Rao, *J. Mater. Chem.*, 2012, **22**, 22866.

143 S. Lin, M. Li, E. Dujardin, C. Girard and S. Mann, *Adv. Mater.*, 2005, **17**, 2553–2559.

144 A. Y. Sinyagin, A. Belov, Z. Tang and N. A. Kotov, *J. Phys. Chem. B*, 2006, **110**, 7500–7.

145 M. Yang, G. Chen, Y. Zhao, G. Silber, Y. Wang, S. Xing, Y. Han and H. Chen, *Phys. Chem. Chem. Phys.*, 2010, **12**, 11850–60.

146 H. Zhang, K.-H. Fung, J. Hartmann, C. T. Chan and D. Wang, *J. Phys. Chem. C*, 2008, **112**, 16830–16839.

147 K. Butter, P. H. H. Bomans, P. M. Frederik, G. J. Vroege and A. P. Philipse, *Nat. Mater.*, 2003, **2**, 88–91.

148 Z. Jian, H. Liqing, W. Yongchang and L. Yimin, *Phys. E Low-dimensional Syst. Nanostructures*, 2004, **25**, 114–118.

149 G. A. Devries, M. Brunnbauer, Y. Hu, A. M. Jackson, B. Long, B. T. Neltner, O. Uzun, B. H. Wunsch and F. Stellacci, *Science*, 2007, **315**, 358–61.

150 I. Hussain, M. Brust, J. Barauskas and A. I. Cooper, *Langmuir*, 2009, **25**, 1934–1939.

151 K. K. Caswell, J. N. Wilson, U. H. F. Bunz and C. J. Murphy, *J. Am. Chem. Soc.*, 2003, **125**, 13914–13915.

152 L. Zhu, D. Xue and Z. Wang, *Langmuir*, 2008, **24**, 11385–11389.

153 C. Shi, L. Tian, L. Wu and J. Zhu, *J. Phys. Chem. C*, 2007, **111**, 1243–1247.

154 R. Sardar and J. S. Shumaker-Parry, *Nano Lett.*, 2008, **8**, 731–736.

155 T. Shirman, T. Arad and M. E. van der Boom, *Angew. Chem. Int. Ed. Engl.*, 2010, **49**, 926–9.

156 L. Polavarapu and Q.-H. Xu, *Nanotechnology*, 2008, **19**, 75601.

157 Y. Tan, L. Jiang, Y. Li and D. Zhu, *J. Phys. Chem. B*, 2002, **106**, 3131–3138.

158 H. Kitching, M. J. Shiers, A. J. Kenyon and I. P. Parkin, *J. Mater. Chem. A*, 2013, **1**, 6985.

159 M. V Walter, N. Cheval, O. Liszka, M. Malkoch and A. Fahmi, *Langmuir*, 2012, **28**, 5947–55.

160 Z. Zhu, W. Liu, Z. Li, B. Han, Y. Zhou, Y. Gao and Z. Tang, *ACS Nano*, 2012, **6**, 2326–32.

161 M. Grzelczak, J. Vermant, E. M. Furst and L. M. Liz-Marzán, *ACS Nano*, 2010, **4**, 3591–605.

162 T. P. Huelser, H. Wiggers, P. Ifeacho, O. Dmitrieva, G. Dumpich and A. Lorke, *Nanotechnology*, 2006, **17**, 3111–3115.

163 A. Hucht, S. Buschmann and P. Entel, *Europhys. Lett.*, 2007, **77**, 57003.

164 R. L. Penn, *J. Phys. Chem. B*, 2004, **108**, 12707–12712.

165 V. M. Yuwono, N. D. Burrows, J. A. Soltis and R. L. Penn, *J. Am. Chem. Soc.*, 2010, **132**, 2163–5.

166 R. L. Penn, *Science (80-.).*, 1998, **281**, 969–971.

167 G. Viau, J.-Y. Piquemal, M. Esparrica, D. Ung, N. Chakroune, F. Warmont and F. Fievet, *Chem. Commun.*, 2003, 2216.

168 M. Giersig, I. Pastoriza-Santos and L. M. Liz-Marzan, *J. Mater. Chem.*, 2004, **14**, 607.

169 O. Taratula, A. M. Chen, J. Zhang, J. Chaudry, L. Nagahara, I. Banerjee and H. He, *J. Phys. Chem. C*, 2007, **111**, 7666–7670.

170 L. Manna, D. J. Milliron, A. Meisel, E. C. Scher and A. P. Alivisatos, *Nat. Mater.*, 2003, **2**, 382–5.

171 Z. A. Peng and X. Peng, *J. Am. Chem. Soc.*, 2001, **123**, 183–184.

172 Q. Lu, F. Gao and D. Zhao, *Nano Lett.*, 2002, **2**, 725–728.

173 J. Polleux, N. Pinna, M. Antonietti and M. Niederberger, *Adv. Mater.*, 2004, **16**, 436–439.

174 Y. Sun, Y. Yin, B. T. Mayers, T. Herricks and Y. Xia, *Chem. Mater.*, 2002, **14**, 4736–4745.

175 R. F. W. Pease, *Contemp. Phys.*, 2006, **22**, 265–290.

176 J. C. Hulteen, *J. Vac. Sci. Technol. A Vacuum, Surfaces, Film.*, 1995, **13**, 1553.

177 X. Zhang, E. M. Hicks, J. Zhao, G. C. Schatz and R. P. Van Duyne, *Nano Lett.*, 2005, **5**, 1503–1507.

178 T. Bhuvana and G. U. Kulkarni, *ACS Nano*, 2008, **2**, 457–62.

179 D. Yin, S. Horiuchi, M. Morita and A. Takahara, *Langmuir*, 2005, **21**, 9352–8.

180 L. Zhang and A. Eisenberg, *Macromolecules*, 1996, **29**, 8805–8815.

181 Y. Kang, K. J. Erickson and T. A. Taton, *J. Am. Chem. Soc.*, 2005, **127**, 13800–1.

182 H. Wang, L. Chen, X. Shen, L. Zhu, J. He and H. Chen, *Angew. Chem. Int. Ed. Engl.*, 2012, **51**, 8021–5.

183 Z. Nie, D. Fava, E. Kumacheva, S. Zou, G. C. Walker and M. Rubinstein, *Nat. Mater.*, 2007, **6**, 609–614.

184 Z. Tang and N. A. Kotov, *Adv. Mater.*, 2005, **17**, 951–962.

185 L. Zhao, K. L. Kelly and G. C. Schatz, *J. Phys. Chem. B*, 2003, **107**, 7343–7350.

186 S. A. Maier and H. A. Atwater, *J. Appl. Phys.*, 2005, **98**, 11101.

187 E. Ozbay, *Science*, 2006, **311**, 189–93.

188 M. Rycenga, C. M. Cobley, J. Zeng, W. Li, C. H. Moran, Q. Zhang, D. Qin and Y. Xia, *Chem. Rev.*, 2011, **111**, 3669–712.

189 W. L. Barnes, A. Dereux and T. W. Ebbesen, *Nature*, 2003, **424**, 824–30.

190 B. Wiley, Y. Sun and Y. Xia, *Acc. Chem. Res.*, 2007, **40**, 1067–76.

191 A. L. Pyayt, B. Wiley, Y. Xia, A. Chen and L. Dalton, *Nat. Nanotechnol.*, 2008, **3**, 660–665.

192 M. Rang, A. C. Jones, F. Zhou, Z.-Y. Li, B. J. Wiley, Y. Xia and M. B. Raschke, *Nano Lett.*, 2008, **8**, 3357–63.

193 M. Quinten, A. Leitner, J. R. Krenn and F. R. Aussenegg, *Opt. Lett.*, 1998, **23**, 1331.

194 H. Ditlbacher, A. Hohenau, D. Wagner, U. Kreibig, M. Rogers, F. Hofer, F. R. Aussenegg and J. R. Krenn, *Phys. Rev. Lett.*, 2005, **95**, 257403.

195 H.-S. Chu, W.-B. Ewe, E.-P. Li and R. Vahldieck, *Opt. Express*, 2007, **15**, 4216.

196 A. W. Sanders, D. A. Routenberg, B. J. Wiley, Y. Xia, E. R. Dufresne and M. A. Reed, *Nano Lett.*, 2006, **6**, 1822–6.

197 Y. Fang, Z. Li, Y. Huang, S. Zhang, P. Nordlander, N. J. Halas and H. Xu, *Nano Lett.*, 2010, **10**, 1950–4.

198 A. L. Falk, F. H. L. Koppens, L. Y. Chun, K. Kang, N. de Leon Snapp, A. V Akimov, M.-H. Jo, M. D. Lukin and H. Park, *Nat. Phys.*, 2009, **5**, 475–479.

199 W. M. Saj, *Opt. Express*, 2005, **13**, 4818.

200 S. A. Maier, P. G. Kik and H. A. Atwater, *Phys. Rev. B*, 2003, **67**, 205402.

201 S. Link and M. A. El-Sayed, *J. Phys. Chem. B*, 1999, **103**, 8410–8426.

202 S. A. Maier, M. L. Brongersma, P. G. Kik and H. A. Atwater, *Phys. Rev. B*, 2002, **65**, 193408.

203 S. A. Maier, P. G. Kik and H. A. Atwater, *Appl. Phys. Lett.*, 2002.

204 W. Chen, A. Bian, A. Agarwal, L. Liu, H. Shen, L. Wang, C. Xu and N. A. Kotov, *Nano Lett.*, 2009, **9**, 2153–9.

205 J. K. Gansel, M. Thiel, M. S. Rill, M. Decker, K. Bade, V. Saile, G. von Freymann, S. Linden and M. Wegener, *Science*, 2009, **325**, 1513–5.

206 M. Février, P. Gogol, G. Barbillon, A. Aassime, R. Mégy, B. Bartenlian, J.-M. Lourtioz and B. Dagens, *Opt. Express*, 2012, **20**, 17402–17409.

207 S. L. D. Solis Jr, B. Willingham, S. L. Nauert, L. S. Slaughter, J. Olson, P. Swanglap, A. Paul, W.-S. Chang, *Nano Lett.*, 2012, **12**, 1349–1353.

208 C. Petit, V. Russier and M. P. Pileni, *J. Phys. Chem. B*, 2003, **107**, 10333–10336.

209 C.-M. Liu, L. Guo, R.-M. Wang, Y. Deng, H.-B. Xu and S. Yang, *Chem. Commun. (Camb).*, 2004, 2726–7.

210 W. Zhou, L. He, R. Cheng, L. Guo, C. Chen and J. Wang, *J. Phys. Chem. C*, 2009, **113**, 17355–17358.

211 A. N. Rudenko, V. V. Mazurenko, V. I. Anisimov and A. I. Lichtenstein, *Phys. Rev. B*, 2009, **79**, 144418.

212 S. A. Corr, S. J. Byrne, R. Tekoriute, C. J. Meledandri, D. F. Brougham, M. Lynch, C. Kerskens, L. O'Dwyer and Y. K. Gun'ko, *J. Am. Chem. Soc.*, 2008, **130**, 4214–4215.

213 M. Klaui, J. Rothman, L. Lopez-Diaz, C. A. F. Vaz, J. A. C. Bland and Z. Cui, *Appl. Phys.*

Lett., 2001, **78**, 3268–3270.

214 S. L. Tripp, R. E. Dunin-Borkowski and A. Wei, *Angew. Chemie Int. Ed.*, 2003, **42**, 5591–5593.

215 S. Si, A. Kotal and T. K. Mandal, *J. Phys. Chem. C*, 2007, **111**, 1248–1255.

216 C. Leiterer, S. Berg, A.-P. Eskelinen, A. Csaki, M. Urban, P. Törmä and W. Fritzsche, *Sensors Actuators B Chem.*, 2013, **176**, 368–373.

217 F. Yang, D. K. Taggart and R. M. Penner, *Nano Lett.*, 2009, **9**, 2177–82.

218 C.-M. Chang, M.-H. Hon and I.-C. Leu, *RSC Adv.*, 2012, **2**, 2469.

219 W. Si, G. Yu, B. Zhou, Y. Ouyang and L. Qiao, *Sens. Lett.*, 2012, **10**, 26–32.

220 E. García-Berríos, T. Gao, M. D. Woodka, S. Maldonado, B. S. Brunschwig, M. W. Ellsworth and N. S. Lewis, *J. Phys. Chem. C*, 2010, **114**, 21914–21920.

221 S. M. Joun Lee Carlos M. Hangarter, Ashok Mulchandani, Wilfred Chen, Nosang V. Myung*, *Electroanalysis*, 2011, **23**, 2623–2628.

222 A. M. Jackson, J. W. Myerson and F. Stellacci, *Nat. Mater.*, 2004, **3**, 330–6.

223 K. G. Thomas, S. Barazzouk, B. I. Ipe, S. T. S. Joseph and P. V. Kamat, *J. Phys. Chem. B*, 2004, **108**, 13066–13068.

224 B. Spellberg, R. Guidos, D. Gilbert, J. Bradley, H. W. Boucher, W. M. Scheld, J. G. Bartlett and J. Edwards, *Clin. Infect. Dis.*, 2008, **46**, 155–64.

225 M. Unemo and R. A. Nicholas, *Future Microbiol.*, 2012, **7**, 1401–1422.

226 M. Sebaihia, B. W. Wren and P. Mullany, *Nat. Genet.*, 2006, **38**, 779–86.

227 F. F. Reinthaler, J. Posch, G. Feierl, G. Wüst, D. Haas, G. Ruckenbauer, F. Mascher and E. Marth, *Water Res.*, 2003, **37**, 1685–90.

228 A. C. Fluit, *FEMS Immunol. Med. Microbiol.*, 2005, **43**, 1–11.

229 *Antimicrobial resistance surveillance in Europe*, 2010.

230 T. J. Dougherty, C. J. Gomer, B. W. Henderson, G. Jori, D. Kessel, M. Korbelik, J. Moan and Q. Peng, *J. Natl. Cancer Inst.*, 1998, **90**, 889–905.

231 M. D. Daniell and J. S. Hill, *ANZ J. Surg.*, 1991, **61**, 340–348.

232 R. Bonnett, *Chemical Aspects of Photodynamic Therapy*, CRC Press, 2000.

233 R. Roelandts, *J. Am. Acad. Dermatol.*, 2002, **46**, 926–930.

234 R. J. Cremer, P. W. Perryman and D. H. Richards, *Lancet*, 1958, **271**, 1094–1097.

235 M. D. D. and J. S. Hill, *Aust. N. Z. J. Surg.*, 1991, **61**, 340–348.

236 D. F. & R. K. J. Dennis E.J.G.J. Dolmans, *Nat. Rev. cancer*, 2003, **3**, 380–387.

237 H. F. BLUM, *Ann. Intern. Med.*, 1933, **6**, 877–884.

238 B. C. Wilson and M. S. Patterson, *Phys. Med. Biol.*, 1986, **31**, 327–360.

239 M. DeRosa, *Coord. Chem. Rev.*, 2002, **233**–**234**, 351–371.

240 G. Bertoloni, F. M. Lauro, G. Cortella and M. Merchat, *Biochim. Biophys. Acta - Gen. Subj.*, 2000, **1475**, 169–174.

241 R. R. Allison, G. H. Downie, R. Cuenca, X.-H. Hu, C. J. Childs and C. H. Sibata, *Photodiagnosis Photodyn. Ther.*, 2004, **1**, 27–42.

242 J. J. Lopez, M. A. G. Carter, Y. P. Tsentalovich, O. B. Morozova, A. V Yurkovskaya and P. J. Hore, *Photochem. Photobiol.*, 2002, **75**, 6–10.

243 K. König, V. Bockhorn, W. Dietel and H. Schubert, *J. Cancer Res. Clin. Oncol.*, 1987, **113**, 301–303.

244 F. S. De Rosa and M. V. L. B. Bentley, *Pharm. Res.*, **17**, 1447–1455.

245 P. S. Zolfaghari, S. Packer, M. Singer, S. P. Nair, J. Bennett, C. Street and M. Wilson, *BMC Microbiol.*, 2009, **9**, 27.

246 J. S. Bellin, L. Lutwick and B. Jonas, *Arch. Biochem. Biophys.*, 1969, **132**, 157–164.

247 K. Orth, G. Beck, F. Genze and A. Rück, *J. Photochem. Photobiol. B Biol.*, 2000, **57**, 186–192.

248 I. Diamond, A. Mcdonagh, C. Wilson, S. Granelli, S. Nielsen and R. Jaenicke, *Lancet*, 1972, **300**, 1175–1177.

249 T. J. Dougherty, *J. Natl. Cancer Inst.*, 1974, **52**, 1333–1336.

250 S. H. Tomson, E. A. Emmett and S. H. Fox, *Cancer Res.*, 1974, **34**, 3124–3127.

251 T. J. Dougherty, J. E. Kaufman, A. Goldfarb, K. R. Weishaupt, D. Boyle and A. Mittleman, *Cancer Res.*, 1978, **38**, 2628–2635.

252 O. J. Balchum, D. R. Doiron and G. C. Huth, *Prog. Clin. Biol. Res.*, 1984, **170**, 727–45.

253 H. Kato, *J. Photochem. Photobiol. B Biol.*, 1998, **42**, 96–99.

254 J. F. Kelly, M. E. Snell and M. C. Berenbaum, *Br. J. Cancer*, 1975, **31**, 237.

255 G. R. Prout Jr, C.-W. Lin, R. Benson Jr, U. O. Nseyo, J. J. Daly, P. P. Griffin, J. Kinsey, M. Tian, Y. Lao and Y. Mian, *N. Engl. J. Med.*, 1987, **317**, 1251–1255.

256 D. E. Schuller, J. S. McCaughan and R. P. Rock, *Arch. Otolaryngol. - Head Neck Surg.*, 1985, **111**, 351–355.

257 J. Feyh, A. Goetz, W. Müller, R. Königsberger and E. Kastenbauer, *J. Photochem. Photobiol. B Biol.*, 1990, **7**, 353–358.

258 S. S. Stylli, A. H. Kaye, L. MacGregor, M. Howes and P. Rajendra, *J. Clin. Neurosci.*, 2005,

12, 389–98.

259 A. H. Kaye and J. S. Hill, *Ann. Acad. Med. Singapore*, 1993, **22**, 470.

260 B. W. Henderson, T. M. Busch, L. A. Vaughan, N. P. Frawley, D. Babich, T. A. Sosa, J. D. Zollo, A. S. Dee, M. T. Cooper and D. A. Bellnier, *Cancer Res.*, 2000, **60**, 525–529.

261 V. X. D. Yang, P. J. Muller, P. Herman and B. C. Wilson, *Lasers Surg. Med.*, 2003, **32**, 224–232.

262 X.-Y. He, R. A. Sikes, S. Thomsen, L. W. K. Chung and S. L. Jacques, *Photochem. Photobiol.*, 1994, **59**, 468–473.

263 B. F. Overholt, K. K. Wang, J. S. Burdick, C. J. Lightdale, M. Kimmey, H. R. Nava, M. V Sivak, N. Nishioka, H. Barr and N. Marcon, *Gastrointest. Endosc.*, 2007, **66**, 460–468.

264 A. Sharwani, W. Jerjes, V. Salih, A. J. MacRobert, M. El-Maaytah, H. S. M. Khalil and C. Hopper, *J. Photochem. Photobiol. B Biol.*, 2006, **83**, 27–33.

265 O. Driemel, M. Kunkel, M. Hullmann, F. von Eggeling, U. Müller-Richter, H. Kosmehl and T. E. Reichert, *J. Dtsch. Dermatol. Ges.*, 2007, **5**, 1095–100.

266 L. E. Bockstahler, T. P. Coohill, K. B. Hellman, C. David Lytle and J. E. Roberts, *Pharmacol. Ther.*, 1979, **4**, 473–499.

267 J. Marotti, A. C. C. Aranha, C. D. P. Eduardo and M. S. Ribeiro, *Photomed. Laser Surg.*, 2009, **27**, 357–63.

268 B. Lambrecht, H. Mohr, J. Knüver-Hopf and H. Schmitt, *Vox Sang.*, 1991, **60**, 207–213.

269 B. Bachmann, J. Knüver-Hopf, B. Lambrecht and H. Mohr, *J. Med. Virol.*, 1995, **47**, 172–178.

270 Z. Smetana, Z. Malik, A. Orenstein, E. Mendelson and E. Ben-Hur, *Lasers Surg. Med.*,

1997, **21**, 351–358.

271 C. Propst and L. Lubin, *Infect. Immun.*, 1978, **20**, 136–141.

272 M. Wilson and N. Mia, *J. Oral Pathol. Med.*, 1993, **22**, 354–357.

273 M. C. Teichert, J. W. Jones, M. N. Usacheva and M. A. Biel, *Oral Surgery, Oral Med. Oral Pathol. Oral Radiol. Endodontology*, 2002, **93**, 155–160.

274 T. Burns, M. Wilson and G. J. Pearson, *J. Dent.*, 1994, **22**, 273–278.

275 A. Pfitzner, B. W. Sigusch, V. Albrecht and E. Glockmann, *J. Periodontol.*, 2004, **75**, 1343–9.

276 S. A. G. Lambrechts, T. N. Demidova, M. C. G. Aalders, T. Hasan and M. R. Hamblin, *Photochem. Photobiol. Sci.*, 2005, **4**, 503–509.

277 T. Dai, G. P. Tegos, T. Zhiyentayev, E. Mylonakis and M. R. Hamblin, *Lasers Surg. Med.*, 2010, **42**, 38–44.

278 M. L. Embleton, S. P. Nair, B. D. Cookson and M. Wilson, *Microb. Drug Resist.*, 2004, **10**, 92–7.

279 B. Zeina, J. Greenman, W. M. Purcell and B. Das, *Br. J. Dermatol.*, 2001, **144**, 274–278.

280 A. C. Khazraji, S. Hotchandani, S. Das and P. V Kamat, *J. Phys. Chem. B*, 1999, **103**, 4693–4700.

281 A. Khdair, B. Gerard, H. Handa, G. Mao, M. P. V Shekhar and J. Panyam, *Mol. Pharm.*, 2008, **5**, 795–807.

282 N. Narband, S. Tubby, I. Parkin, J. Gil-Tomas, D. Ready, S. Nair and M. Wilson, *Curr. Nanosci.*, 2008, **4**, 409–414.

283 M. Rai, A. Yadav and A. Gade, *Biotechnol. Adv.*, 2009, **27**, 76–83.

284 J. Liu and R. H. Hurt, *Environ. Sci. Technol.*, 2010, **44**, 2169–2175.

285 S. Noimark, C. W. Dunnill and I. P. Parkin, *Adv. Drug Deliv. Rev.*, 2013, **65**, 570–580.

286 J. M. Bartley and R. N. Olmsted, *Clin. Microbiol. Newsl.*, 2008, **30**, 113–117.

287 R. A. Weinstein and B. Hota, *Clin. Infect. Dis.*, 2004, **39**, 1182–1189.

288 Robert P. Gaynes, *Infect. Control Hosp. Epidemiol.*, 1997, **18**, 475–478.

289 House of Commons Public Accounts Committee, *Reducing Healthcare Associated Infection in Hospitals in England*, London, 2009.

290 K. Page, R. G. Palgrave, I. P. Parkin, M. Wilson, S. L. P. Savin and A. V. Chadwick, *J. Mater. Chem.*, 2007, **17**, 95–104.

291 P. Evans and D. W. Sheel, *Surf. Coatings Technol.*, 2007, **201**, 9319–9324.

292 K. Page, M. Wilson and I. P. Parkin, *J. Mater. Chem.*, 2009, **19**, 3819.

293 B. Gottenbos, H. C. van der Mei, F. Klatter, P. Nieuwenhuis and H. J. Busscher, *Biomaterials*, 2002, **23**, 1417–1423.

294 A. E. Madkour, J. M. Dabkowski, K. Nüsslein and G. N. Tew, *Langmuir*, 2009, **25**, 1060–1067.

295 V. Decraene, J. Pratten and M. Wilson, *Appl. Environ. Microbiol.*, 2006, **72**, 4436–4439.

296 S. Gemili, A. Yemenicioğlu and S. A. Altınkaya, *J. Food Eng.*, 2009, **90**, 453–462.

297 S. L. Haynie, G. A. Crum and B. A. Doele, *Antimicrob. Agents Chemother.*, 1995, **39**, 301–307.

298 A. J. T. Naik, S. Ismail, C. Kay, M. Wilson and I. P. Parkin, *Mater. Chem. Phys.*, 2011, **129**, 446–450.

299 J.-P. Guggenbichler, M. Böswald, S. Lugauer and T. Krall, *Infection*, 1999, **27**, S16–S23.

300 U. Makal, L. Wood, D. E. Ohman and K. J. Wynne, *Biomaterials*, 2006, **27**, 1316–1326.

301 S. Perni, P. Prokopovich, C. Piccirillo, J. Pratten, I. P. Parkin and M. Wilson, *J. Mater. Chem.*, 2009, **19**, 2715.

302 T. Maisch, C. Bosl, R.-M. Szeimies, N. Lehn and C. Abels, *Antimicrob. Agents Chemother.*, 2005, **49**, 1542–1552.

303 M. Soncin, C. Fabris and A. Busetti, *Photochem. Photobiol. Sci.*, 2002, **1**, 815–819.

304 M. A. Kohanski, D. J. Dwyer, B. Hayete, C. A. Lawrence and J. J. Collins, *Cell*, 2007, **130**, 797–810.

305 S. Perni, C. Piccirillo, A. Kafizas, M. Uppal, J. Pratten, M. Wilson and I. P. Parkin, *J. Clust. Sci.*, 2010, **21**, 427–438.

306 S. Perni, C. Piccirillo, J. Pratten, P. Prokopovich, W. Chrzanowski, I. P. Parkin and M. Wilson, *Biomaterials*, 2009, **30**, 89–93.

307 S. Perni, P. Prokopovich, I. P. Parkin, M. Wilson and J. Pratten, *J. Mater. Chem.*, 2010, **20**, 8668.

308 Sehmi, S. K., Noimark, S., Bear, J. C., Peveler, W. J., Bovis, M., Allan, E., MacRobert, A. J. and Parkin, I. P., *J. Mater. Chem. B*, 2015, 6490–6500.

309 S. Noimark, M. Bovis, A. J. MacRobert, A. Correia, E. Allan, M. Wilson and I. P. Parkin, *RSC Adv.*, 2013, **3**, 18383.

310 V. J. Gandubert and R. B. Lennox, *Langmuir*, 2005, **21**, 6532–6539.

311 S. Jaiswal, B. Duffy, A. K. Jaiswal, N. Stobie and P. McHale, *Int. J. Antimicrob. Agents*, 2010, **36**, 280–283.

312 A. A. El-Kheshen and S. F. Gad El-Rab, 2012, **4**, 53–65.

313 S. S. Shankar, S. Bhargava and M. Sastry, .

314 H. J. Wang, C. Y. Xue, R. Chen and W. D. Zhang, *Adv. Mater. Res.*, 2010, **152–153**, 600–604.

315 C.-H. Kuo and M. H. Huang, *Langmuir*, 2005, **21**, 2012–2016.

316 H.-Y. Wu, M. Liu and M. H. Huang, *J. Phys. Chem. B*, 2006, **110**, 19291–19294.

317 E. Hao, R. C. Bailey, G. C. Schatz, J. T. Hupp and S. Li, *Nano Lett.*, 2004, **4**, 327–330.

318 M. Yamamoto, Y. Kashiwagi, T. Sakata, H. Mori and M. Nakamoto, *Chem. Mater.*, 2005, **17**, 5391–5393.

319 O. M. Bakr, B. H. Wunsch and F. Stellacci, *Chem. Mater.*, 2006, **18**, 3297–3301.

320 J. Xie, J. Y. Lee and D. I. C. Wang, *Chem. Mater.*, 2007, **19**, 2823–2830.

321 B. Rodríguez-González, A. Burrows, M. Watanabe, C. J. Kiely and L. M. Liz Marzán, *J. Mater. Chem.*, 2005, **15**, 1755.

322 M. A. Uppal, M. B. Ewing and I. P. Parkin, *Eur. J. Inorg. Chem.*, 2011, **2011**, 4534–4544.

323 S. Link, Z. L. Wang and M. A. El-Sayed, *J. Phys. Chem. B*, 1999, **103**, 3529–3533.

324 Z. S. Pillai and P. V. Kamat, *J. Phys. Chem. B*, 2004, **108**, 945–951.

325 M. J. Shiers, R. Leech, C. J. Carmalt, I. P. Parkin and A. J. Kenyon, *Adv. Mater.*, 2012, **24**, 5227–35.

326 Y. H. Su, S.-L. Tu, S.-W. Tseng, Y.-C. Chang, S.-H. Chang, W.-M. Zhang, F. Hao, Y. Sonnefraud, P. Van Dorpe, S. A. Maier, N. J. Halas, P. Nordlander, J. Maly, H. Lampova, A. Semeradtova, M. Stofik, L. Kovacik, J. P. Camden, J. A. Dieringer, Y. Wang, D. J. Masiello, L. D. Marks, G. C. Schatz, R. P. Van Duyne, M. Zhu, C. M. Aikens, F. J. Hollander, G. C. Schatz, R. Jin, H. B. Li, F. Y. Li, C. P. Han, Z. M. Cui, G. Y. Xie, A. Q. Zhang,

F. Z. Henari, A. A. Dakhel, X. Y. Hu, Z. Y. Wang, T. C. Zhang, X. Y. Zeng, W. Xu, J. X. Zhang, J. Yan, J. P. Zhang, L. D. Zhang, A. Bouhelier, R. Bachelot, G. Lerondel, S. Kostcheev, P. Royer, G. P. Wiederrecht1, Y. Bao, C. Zhong, D. M. Vu, J. P. Temirov, R. B. Dyer, J. S. Martinez, J. Zheng, C. W. Zhang, R. M. Dickson, D. J. Roaf, C. T. Yuan, W. C. Chou, J. Tang, C. A. Lin, W. H. Chang, J. L. Shen, D. S. Chuu, P. Frantsuzov, M. Kuno, B. Janko, R. A. Marcus, B. N. Khlebtsov, V. A. Khanadeev, N. G. Khlebtsov, H. L. Wu, C. H. Chen, M. H. Huang, L. Wang, S. J. Guo, J. F. Zhai, S. J. Dong, S. J. Guo, L. Wang, S. J. Dong, E. K. Wang, P. Zhou, Z. H. Dai, M. Fang, X. H. Huang, J. C. Bao, J. F. Gong, K. F. Yu, K. L. Kelly, N. Sakai, T. Tatsuma, Y. H. Su, W. H. Lai, W. Y. Chen, M. H. Hon, S.-H. Chang, O. M. Bakr, B. H. Wunsch, F. Stellacci, G. H. Jeong, Y. W. Lee, M. Kim, S. W. Han, C. L. Nehl, J. H. Hafner, Y. H. Su, L. G. Teoh, S.-L. Tu, J.-H. Lee, M. H. Hon, L. Frolov, Y. Rosenwaks, S. Richter, C. Carmeli, I. Carmeli, C. Curutchet, A. Franceschetti, A. Zunger, G. D. Scholes, Y. H. Su, W. H. Lai, S.-H. Chang, M. H. Hon, M. Zhu, C. M. Aikens, F. J. Hollander, G. C. Schatz, R. Jin, H. Kawasaki, H. Yamamoto, H. Fujimori, R. Arakawa, Y. Iwasaki, M. Inada, M. Kuno, D. P. Fromm, H. F. Hamann, A. Gallagher, D. J. Nesbitt, T. Ozaki, H. Kino, B. Mahler, P. Spinicelli, S. Buil, X. Quelin, J.-P. Hermier, B. Dubertret1, T. Ming, L. Zhao, Z. Yang, H. J. Chen, L. D. Sun, J. F. Wang, C. H. Yan, Z. Yang, W. H. Ni, X. S. Kou, S. Z. Zhang, Z. H. Sun, L.-D. Sun, J. F. Wang and C.-H. Yan, *Nanoscale*, 2010, **2**, 2639.

327 B. Spellberg, R. Guidos, D. Gilbert, J. Bradley, H. W. Boucher, W. M. Scheld, J. G. Bartlett, J. Edwards and the I. D. S. of America, *Clin. Infect. Dis.*, 2008, **46**, 155–164.

328 M. D. Iseman and L. A. Madsen, *Clin. Chest Med.*, 1989, **10**, 341–53.

329 T. Maisch, *Lasers Med. Sci.*, 2007, **22**, 83–91.

330 J. P. Tardivo, A. Del Giglio, C. S. de Oliveira, D. S. Gabrielli, H. C. Junqueira, D. B. Tada, D. Severino, R. de Fátima Turchiello and M. S. Baptista, *Photodiagnosis Photodyn.*

Ther., 2005, **2**, 175–191.

331 S. T. Naima Narband Ivan P. Parkin, Jesús Gil-Tomás, Derren Ready, Sean P. Nair and Michael Wilson, *Curr. Nanosci.*, 2008, **4**, 409–414.

332 Y. Wang, G. Chen, M. Yang, G. Silber, S. Xing, L. H. Tan, F. Wang, Y. Feng, X. Liu and S. Li, *Nat. Commun.*, 2010, **1**, 87.

333 D. V Leff, L. Brandt and J. R. Heath, *Langmuir*, 1996, **12**, 4723–4730.

334 S. L. Westcott, S. J. Oldenburg, T. R. Lee and N. J. Halas, *Langmuir*, 1998, **14**, 5396–5401.

335 S. Bharathi, N. Fishelson and O. Lev, *Langmuir*, 1999, **15**, 1929–1937.

336 Y.-R. Luo, *Comprehensive Handbook of Chemical Bond Energies*, CRC Press, Taylor & Francis Group, 2007.

337 T. Konno, M. Usami, A. Toyota, M. Hirotsu and T. Kawamoto, *Chem. Lett.*, 2005, **34**, 1146–1147.

338 N. Gonzalez-Lakunza, N. Lorente and A. Arnau, *J. Phys. Chem. C*, 2007, **111**, 12383–12390.

339 D. R. Whitcomb and M. Rajeswaran, *J. Coord. Chem.*, 2006, **59**, 1253–1260.

340 F. Chen, X. Li, J. Hihath, Z. Huang and N. Tao, *J. Am. Chem. Soc.*, 2006, **128**, 15874–15881.

341 A.-P. Magiorakos, A. Srinivasan, R. B. Carey, Y. Carmeli, M. E. Falagas, C. G. Giske, S. Harbarth, J. F. Hindler, G. Kahlmeter, B. Olsson-Liljequist, D. L. Paterson, L. B. Rice, J. Stelling, M. J. Struelens, A. Vatopoulos, J. T. Weber and D. L. Monnet, *Clin. Microbiol. Infect.*, 2012, **18**, 268–281.

342 D. Pittet, *Infect. Control Hosp. Epidemiol.*, 2000, **21**, 381–386.

343 E. R. Goodman, R. Platt, R. Bass, A. B. Onderdonk, D. S. Yokoe and S. S. Huang, *Infect. Control Hosp. Epidemiol.*, 2008, **29**, 593–599.

344 H. I. Pass, *JNCI J. Natl. Cancer Inst.*, 1993, **85**, 443–456.

345 D. E. J. G. J. Dolmans, D. Fukumura and R. K. Jain, *Nat. Rev. Cancer*, 2003, **3**, 380–7.

346 S. Noimark, C. W. Dunnill, M. Wilson and I. P. Parkin, *Chem. Soc. Rev.*, 2009, **38**, 3435–48.

347 Y. Sekiguchi, Y. Yao, Y. Ohko, K. Tanaka, T. Ishido, A. Fujishima and Y. Kubota, *Int. J. Urol.*, 2007, **14**, 426–430.

348 Y. Ohko, Y. Utsumi, C. Niwa, T. Tatsuma, K. Kobayakawa, Y. Satoh, Y. Kubota and A. Fujishima, *J. Biomed. Mater. Res.*, 2001, **58**, 97–101.

349 C. W. Dunnill, K. Page, Z. A. Aiken, S. Noimark, G. Hyett, A. Kafizas, J. Pratten, M. Wilson and I. P. Parkin, *J. Photochem. Photobiol. A Chem.*, 2011, **220**, 113–123.

350 Z. A. Aiken, G. Hyett, C. W. Dunnill, M. Wilson, J. Pratten and I. P. Parkin, *Chem. Vap. Depos.*, 2010, **16**, 19–22.

351 V. Decraene, J. Pratten and M. Wilson, *Infect. Control Hosp. Epidemiol.*, 2008, **29**, 1181–1184.

352 M. Wilson, *Infect. Control Hosp. Epidemiol.*, 2003, **24**, 782–784.

353 M. Wainwright, M. N. Byrne and M. A. Gattrell, *Phenothiazinium-based photobactericidal materials*, 2006, vol. 84.

354 M. Wainwright, D. A. Phoenix, P. B. Nickson and G. Morton, *Biofouling*, 2002, **18**, 247–249.

355 R. Hachem, R. Reitzel, A. Borne, Y. Jiang, P. Tinkey, R. Uthamanthil, J. Chandra, M. Ghannoum and I. Raad, *Antimicrob. Agents Chemother.*, 2009, **53**, 5145–5149.

356 D. P. Camacho, A. Gasparetto and T. I. E. Svidzinski, *Mycopathologia*, 2007, **163**, 261–266.

357 V. Decraene, J. Pratten and M. Wilson, *Curr. Microbiol.*, 2008, **57**, 269–273.

358 I. Sondi and B. Salopek-Sondi, *J. Colloid Interface Sci.*, 2004, **275**, 177–182.

359 S. Noimark, E. Allan and I. P. Parkin, *Chem. Sci.*, 2014, **5**, 2216.

360 C. Piccirillo, S. Perni, J. Gil-Thomas, P. Prokopovich, M. Wilson, J. Pratten and I. P. Parkin, *J. Mater. Chem.*, 2009, **19**, 6167.

361 B. Zeina, J. Greenman, D. Corry and W. M. Purcell, *Br. J. Dermatol.*, 2003, **148**, 229–232.

362 B. Zeina, J. Greenman, D. Corry and W. M. Purcell, *Br. J. Dermatol.*, 2002, **146**, 568–573.

363 B. Zeina, J. Greenman, W. M. Purcell and B. Das, *Br. J. Dermatol.*, 2001, **144**, 274–278.

364 M. B. Edmond, S. E. Wallace, D. K. McClish, M. A. Pfaller, R. N. Jones and R. P. Wenzel, *Clin. Infect. Dis.*, 1999, **29**, 239–244.

365 A. Panáček, L. Kvítek, R. Prucek, M. Kolář, R. Večeřová, N. Pizúrová, V. K. Sharma, T. Nevěčná and R. Zbořil, *J. Phys. Chem. B*, 2006, **110**, 16248–16253.

366 I. Sondi and B. Salopek-Sondi, *J. Colloid Interface Sci.*, 2004, **275**, 177–182.

367 M. Rai, A. Yadav and A. Gade, *Biotechnol. Adv.*, 2009, **27**, 76–83.

368 S. Pal, Y. K. Tak and J. M. Song, *Appl. Environ. Microbiol.*, 2007, **73**, 1712–1720.

369 C.-N. Lok, C.-M. Ho, R. Chen, Q.-Y. He, W.-Y. Yu, H. Sun, P. K.-H. Tam, J.-F. Chiu and C.-

M. Che, *JBIC J. Biol. Inorg. Chem.*, 2007, **12**, 527–534.

370 P. C. Lee and D. Meisel, *J. Phys. Chem.*, 1982, **86**, 3391–3395.

371 P. Prokopovich, S. Perni, C. Piccirillo, J. Pratten, I. P. Parkin and M. Wilson, *J. Mater. Sci. Mater. Med.*, 2010, **21**, 815–821.

372 K. Kusuzaki, K. Aomori, T. Suginoshita, G. Minami, H. Takeshita, H. Murata, S. Hashiguchi, T. Ashihara and Y. Hirasawa, *Oncology*, 2000, **59**, 174–180.

373 K. Kusuzaki, H. Murata, T. Matsubara, S. Miyazaki, A. Okamura, M. Seto, A. Matsumine, H. Hosoi, T. Sugimoto and A. Uchida, *Anticancer Res.*, 2005, **25**, 1225–35.

374 K. Kusuzaki, H. Murata, T. Matsubara, S. Miyazaki, K. Shintani, M. Seto, A. Matsumine, H. Hosoi, T. Sugimoto and A. Uchida, *Photochem. Photobiol.*, 2005, **81**, 705.

375 J. W. Costerton, P. S. Stewart and E. P. Greenberg, *Science*, 1999, **284**, 1318–22.